

# **HIGH-QUALITY COMPUTED TOMOGRAPHY USING ADVANCED MODEL-BASED ITERATIVE RECONSTRUCTION**

by  
Steven Tilley II

A dissertation submitted to Johns Hopkins University in conformity with  
the requirements for the degree of Doctor of Philosophy

Baltimore, Maryland  
January, 2019

© 2019 by Steven Tilley II  
All rights reserved

# Abstract

Computed Tomography (CT) is an essential technology for the treatment, diagnosis, and study of disease, providing detailed three-dimensional images of patient anatomy. While CT image quality and resolution has improved in recent years, many clinical tasks require visualization and study of structures beyond current system capabilities. Model-Based Iterative Reconstruction (MBIR) techniques offer improved image quality over traditional methods by incorporating more accurate models of the imaging physics. In this work, we seek to improve image quality by including high-fidelity models of CT physics in a MBIR framework. Specifically, we measure and model spectral effects, scintillator blur, focal-spot blur, and gantry motion blur, paying particular attention to shift-variant blur properties and noise correlations. We derive a novel MBIR framework that is capable of modeling a wide range of physical effects, and use this framework with the physical models to reconstruct data from various systems. Physical models of varying degrees of accuracy are compared with each other and more traditional techniques. Image quality is assessed with a variety of metrics, including bias, noise, and edge-response, as well as task specific metrics such as segmentation quality and material density accuracy. These results show that improving the model accuracy generally improves image quality, as the measured data is used more efficiently. For example, modeling focal-spot blur, scintillator blur, and noise

correlations enables more accurate trabecular bone visualization and trabecular thickness calculation as compared to methods that ignore blur or model blur but ignore noise correlations. Additionally, MBIR with advanced modeling typically outperforms traditional methods, either with more accurate reconstructions or by including physical effects that cannot otherwise be modeled, such as shift-variant focal-spot blur. This work provides a means to produce high-quality and high-resolution CT reconstructions for a wide variety of systems with different hardware and geometries, providing new tradeoffs in system design, enabling new applications in CT, and ultimately improving patient care.

## Thesis Committee Members

J. Webster Stayman, Ph.D. (Advisor)

Assistant Professor, Department of Biomedical Engineering

Johns Hopkins University

Jeffrey H. Siewerdsen, Ph.D.

Professor, Department of Biomedical Engineering

Johns Hopkins University

Jerry L. Prince, Ph.D.

Professor, Department of Electrical and Computer Engineering

Johns Hopkins University

Katsuyuki Taguchi, Ph.D.

Associate Professor, Department of Radiology and Radiological Science

Johns Hopkins University



# Acknowledgments

As with all research, this work would not have been possible without the help and support of many people. First, I'd like to thank my advisor, Web Stayman, for being an excellent mentor. Throughout my time in his lab, Web has provided fantastic guidance while giving me the freedom to explore my own ideas. He has been an invaluable advisor, colleague, and friend.

I would also like to thank Jeff Siewerdsen and Wojtek Zbijewski, who have likewise been patient sources of much assistance and insight. Thanks also to Jerry Prince and Katsuyuki Taguchi, who have provided extremely valuable guidance over the years. I'd like to thank Chris Schaffer and Nozomi Nishimura at Cornell University, who first started me on the researcher's path.

A big thanks to the members of the AIAI and I-STAR labs, whose combined expertise and skills provide for an excellent and unique research environment. They have been and will continue to be excellent colleagues and friends, and I'll miss our daily lunches taking up a considerable portion of the daily grind and consuming vast quantities of food-truck meals.

A huge thanks and much love to my parents, Steven and Patricia, and my brother, Michael, who have fostered in me the curiosity and drive that made this work possible. Thank you for the unending love, encouragement, and support.

I would also like to express my gratitude and love to my wife, Heather, who has been a constant source of support, encouragement, and companionship throughout this process. Having met her just after graduate student orientation, it feels truly special to have gone on this journey with her from beginning to end, and I look forward to our next journey together.

This work used some fantastic open sourced software, including Python (python.org), SciPy [1], and Matplotlib [2]. It also made use of algorithm implementations written by Ali Uneri and Yoshito Otake. Much of this work was conducted using computational resources at the Maryland Advanced Research Computing Center (MARCC).

This dissertation was supported in part by NIH grants R21 EB014964, T32 EB010021, R01 EB018896, F31 EB023783, R01 EB025470, and R21 EB026849, as well as academic-industry partnerships with Varian Medical Systems (Palo Alto, CA), and Carestream (Rochester, NY). Thanks to Sungwon Yoon and Kevin Holt from Varian for their insights.

*Dedicated to my parents*

# Table of Contents

<b>Table of Contents</b>	<b>viii</b>
<b>List of Tables</b>	<b>xiv</b>
<b>List of Figures</b>	<b>xv</b>
<b>List of Acronyms</b>	<b>xxx</b>
<b>1 Introduction</b>	<b>1</b>
<b>2 Background</b>	<b>5</b>
2.1 CT physics . . . . .	5
2.1.1 The X-ray source . . . . .	6
2.1.2 X-ray attenuation . . . . .	14
2.1.3 X-ray detection . . . . .	16
2.2 CT image reconstruction . . . . .	20
2.2.1 Analytic reconstruction . . . . .	21
2.2.2 Model-based iterative reconstruction . . . . .	25
2.2.2.1 PL derivation example: post-log Gaussian model . .	30
2.2.3 Advanced modeling in MBIR: overview and prior work . . . .	32

2.2.3.1	Fidelity term . . . . .	34
2.2.3.2	Prior/penalty term . . . . .	35
<b>3</b>	<b>A general model-based iterative reconstruction framework</b>	<b>38</b>
3.1	Forward model and objective function . . . . .	39
3.2	Optimization strategies . . . . .	40
3.2.1	Separable quadratic surrogates optimizer . . . . .	40
3.2.1.1	Optimum curvature derivation . . . . .	46
3.2.1.2	Ordered subsets and Nesterov acceleration . . . . .	48
3.2.1.3	Useful approximations . . . . .	50
3.2.2	Staged linearized optimizer . . . . .	51
3.2.2.1	Line integral covariance matrix derivation . . . . .	57
3.3	Accommodation of an isotropic Huber penalty . . . . .	58
<b>4</b>	<b>Relative effects of shift-invariant source and detector blur with a linearized model</b>	<b>64</b>
4.1	Introduction . . . . .	65
4.2	Methods . . . . .	68
4.2.1	Simulation studies . . . . .	72
4.2.2	Bench characterization . . . . .	78
4.2.3	Test-bench data reconstructions . . . . .	80
4.3	Results . . . . .	82
4.3.1	Simulation studies . . . . .	82
4.3.2	Bench characterization . . . . .	91
4.3.3	Test-bench data reconstructions . . . . .	95

4.4	Discussion . . . . .	100
<b>5</b>	<b>Shift-invariant source and detector blur with a nonlinear forward model</b>	<b>104</b>
5.1	Introduction . . . . .	104
5.2	Methods . . . . .	106
5.2.1	Comparison with linearized method . . . . .	107
5.2.2	System characterization of a high-resolution prototype extremities scanner . . . . .	108
5.2.3	Simulation study . . . . .	110
5.2.3.1	Parameter sweep . . . . .	113
5.2.3.2	Algorithm comparison . . . . .	113
5.2.4	Extremities prototype experiment . . . . .	114
5.3	Results . . . . .	116
5.3.1	Comparison with linearized method . . . . .	116
5.3.2	System characterization of a high-resolution prototype extremities scanner . . . . .	118
5.3.3	Simulation study . . . . .	120
5.3.3.1	Parameter sweep . . . . .	120
5.3.3.2	Algorithm comparison . . . . .	121
5.3.4	Extremities prototype experiment . . . . .	124
5.4	Discussion . . . . .	128
<b>6</b>	<b>Shift-variant focal-spot blur and gantry-motion blur</b>	<b>131</b>
6.1	Introduction . . . . .	132

6.2	Focal-spot blur modeling . . . . .	134
6.2.1	Methods . . . . .	134
6.2.1.1	Projection Domain blur modeling . . . . .	134
6.2.1.1.1	Mathematical derivation . . . . .	134
6.2.1.1.2	Simulation study . . . . .	136
6.2.1.1.3	Focal-spot measurement . . . . .	139
6.2.1.1.4	Resolution phantom study . . . . .	140
6.2.1.2	Trabecular probe study . . . . .	140
6.2.1.2.1	Phantom and data generation . . . . .	141
6.2.1.2.2	Reconstruction . . . . .	143
6.2.1.3	Bench data reconstructions with full sourcelets model	146
6.2.1.3.1	Focal-spot modeling and measurement . . .	147
6.2.1.3.2	Multiresolution forward model . . . . .	149
6.2.1.3.3	Reconstruction . . . . .	151
6.2.2	Results . . . . .	154
6.2.2.1	Projection Domain blur modeling . . . . .	154
6.2.2.1.1	Simulation study . . . . .	154
6.2.2.1.2	Focal-spot measurement . . . . .	157
6.2.2.1.3	Resolution phantom study . . . . .	158
6.2.2.2	Trabecular probe study . . . . .	160
6.2.2.2.1	FDK short scan maps . . . . .	160
6.2.2.2.2	MBIR . . . . .	163
6.2.2.3	Bench data reconstructions with full sourcelets model	169
6.2.2.3.1	Focal-spot modeling and measurement . . .	169

6.2.2.3.2	Reconstruction . . . . .	173
6.3	Gantry motion blur modeling . . . . .	179
6.3.1	Methods . . . . .	179
6.3.1.1	Model . . . . .	179
6.3.1.2	Simulation study . . . . .	180
6.3.1.3	Test bench study . . . . .	181
6.3.2	Results . . . . .	183
6.3.2.1	Simulation study . . . . .	183
6.3.2.2	Test bench study . . . . .	185
6.4	Discussion . . . . .	186
<b>7</b>	<b>Model-based material decomposition</b>	<b>189</b>
7.1	Introduction . . . . .	190
7.2	Methods . . . . .	193
7.2.1	Reconstruction algorithm . . . . .	193
7.2.2	Image domain decomposition . . . . .	197
7.2.3	Water/calcium simulation study . . . . .	198
7.2.4	Iodine sensitivity simulation study . . . . .	201
7.2.5	Kilovolt-switching with split-filtration simulation studies . . .	202
7.2.6	Kilovolt-switching with filtration physical test bench studies .	205
7.3	Results . . . . .	208
7.3.1	Water/calcium simulation study . . . . .	208
7.3.2	Iodine sensitivity simulation study . . . . .	208
7.3.3	Kilovolt-switching with split-filtration simulation studies . . .	214
7.3.4	Kilovolt-switching with filtration physical test bench studies .	217



7.4	Discussion . . . . .	218
<b>8</b>	<b>Conclusion</b>	<b>221</b>
8.1	Summary . . . . .	221
8.2	Future work . . . . .	223
	<b>Appendix A Test-Bench Gain Estimation</b>	<b>226</b>
	<b>Appendix B Sourcelet Projector</b>	<b>228</b>
B.1	Derivation . . . . .	229
B.2	Algorithm . . . . .	233
B.3	Jacobian Calculation . . . . .	235
B.3.1	Transaxial coordinate system . . . . .	236
B.3.2	Axial coordinate system . . . . .	237

# List of Tables

2.1	Notation conventions . . . . .	25
4.1	Systems with varying degrees of source and detector blur were simulated to investigate reconstruction performance over a range of scenarios. These scenarios are lettered a–g and permit two experiments where (1) the total blur is constant and the proportion of source and detector blur is varied; and (2) the proportion of source and detector blur is constant and the total blur is varied. Note that scenario d appears in both experiments. . . . .	76
5.1	Trabecular bone metric results. © 2017 IEEE . . . . .	128
6.1	Summary of blur models . . . . .	145
6.2	Noise levels in each of the four reconstructions in Figure 6.23 . . . . .	173
7.1	Notation summary. . . . .	195

# List of Figures

2.1	Schematic of a MDCT system showing the X-ray source and detector. X-ray photons are generated at the source, travel through the patient/object (in this case a box), and then are absorbed by the detector. Both the source and detector are fixed to a gantry (not shown) that rotates about the $y$ axis along the path indicated by the dotted line. The direction indicated by $y$ is referred to as to axial direction. .	6
2.2	Schematic of a FP CBCT system. As compared to the MDCT system in Figure 2.1, FP CBCT systems have a flat detector and often have smaller pixels. Flat panel detectors are usually more square then MDCT detectors, leading to a larger cone angle in the axial direction but less lateral coverage. . . . .	7
2.3	Schematic from Figure 2.2 viewed from the side. The dotted line is the axis of rotation, and $y$ is the same as in Figure 2.2. The cone angle is indicated by $\gamma$ . . . . .	7
2.4	Schematic of the anode and cathode inside an X-ray tube. The anode is rotated about the axis indicated with the dashed line. An X-ray photon shown is traveling along the central ray, towards the patient. .	8

2.5	X-ray focal spot appearance from different positions. In the center image the viewing angle is aligned with the central ray, or $z$ axis in this figure. The other positions correspond to shifting the viewing angle $5^\circ$ about the $x$ and/or $y$ axes. In this example the anode angle is $11.3^\circ$ . . . . .	11
2.6	Example X-ray spectrum with 120 kVp. The peaks are due to characteristic X-ray photons. . . . .	13
2.7	Mass attenuation coefficients of water, calcium, and iodine. . . . .	15
2.8	Schematic of X-ray detection process. An X-ray photon enters the scintillator and is converted into multiple visible light photons, which are then detected by the photodiodes on right of each image. Subfigure A shows a pixelated scintillator, as is common in MDCT detectors. The light photons reflect off the septa and only hit one photodiode. Subfigure B shows a non-pixelated scintillator, where the light photons can spread to multiple detector photodiodes. This schematic assumes a 100% fill factor for simplicity. . . . .	17
2.9	Parallel beam geometry. The detector is rotated about an angle $\theta$ from the $y$ axis. The integration path for measurement $y(s, \theta)$ is indicated by the thick line . . . . .	21

2.10	Example of FBP (with a fan beam geometry). A simple truth image (A) is forward projected to calculate the sinogram (B). Backprojecting a single angle effectively “smears” the projection back across the volume (C). Repeating for all angles results in a blurry reconstruction (D), while filtering prior to backprojecting results in an accurate reconstruction (E). . . . .	24
2.11	Gaussian and Poisson distributions with mean and variance equal to 1, 10, and 20. . . . .	28
2.12	Comparison of different potential functions. The vertical line indicates the value of $\delta$ for the Huber penalty. The quadratic penalty is scaled to ease comparison. . . . .	37
3.1	Representation of deblur masking. The original blur (a) tends towards zero at higher frequencies. To account for this, those frequencies are masked. Subfigure (a) shows $\mathbf{b}^+$ from equation (3.51) and (b) shows $\mathbf{b}^-$ from equation (3.49). . . . .	55

4.1	Model for the mean (bottom) and covariance (top) of quanta at various stages. (1) After X-ray photon generation, quanta are independent with a variance equal to the mean. (2) When X-ray photons are attenuated by the object, the spatial distribution of the mean and variance change, but remain equal and independent. An operator that includes source blur is also included. (3) In the scintillator, X-ray photons interact with a scintillating material creating many light photons which spread spatially, blurring the mean distribution and adding correlation to the noise. (4) Photodiodes detect the light photons with possible additive readout noise. . . . .	69
4.2	Digital phantom used in simulation studies emulating an extremity imaging scan with (i) fat, (ii) muscle, (iii) bone, (iv) line pairs, and (v) a uniform disc. For noise evaluations, sample variance was calculated in the disc interior indicated with a circle. Spatial resolution was estimated using the edge response between the disc and fat background.	73
4.3	Test bench with flat panel detector (left) and X-ray source (right). The wrist phantom used is shown at the axis of rotation. . . . .	77

4.4	Spatial resolution-variance tradeoff for different reconstructions in a simulated tomographic system with a 0.34 mm FWHM scintillator blur and a 0.70 mm FWHM source blur. Variance and spatial resolution are shown for MBIR reconstructions using the correlated and uncorrelated noise models and FDK with no deblurring, PD deblurring, and ID deblurring. The square data points are either noise-matched or resolution-matched to the square data point in the correlated model dataset. . . . .	83
4.5	(a) Reconstructions from the simulation study corresponding to the noise-matched and resolution-matched data points in Figure 4.4. (b) Difference images show the difference between the reconstruction and truth. Zoomed images focus on the bone in the center of the phantom, with the line pairs inset in the lower right. . . . .	85
4.6	Evaluation of reconstruction algorithms for systems with differing source and detector blur. The schematic (top) illustrates the different imaging system scenarios with varying amounts of source and detector blur. These scenarios have a constant total system blur and a varying blur distribution — from detector-dominated (point a) to source-dominated (point e). The subfigures (a-e) show the resolution-variance tradeoff for each of the systems with blur scenarios corresponding to points a-e in the schematic. Note that the correlated noise model shows the greatest advantage over the uncorrelated noise model for the scenario where source blur dominates. . . . .	86

4.7	Performance evaluation of reconstructions under varying total blur conditions. The points in the left figure show three different system scenarios, each with the same ratio of source to scintillator blur. The different total system blur conditions represented by points f, d, and g correspond to the resolution-variance plots on the right. . . . .	87
4.8	(a) Detector MTF measurements and parameterized fit. The model used for fitting was a Gaussian multiplied by a sinc function. (b) Focal spot image from the CBCT test-bench. (c) A source MTF derived from the focal spot image approximately scaled for focal spot blur at the center of rotation. (d) Trans-axial, axial, and 45° profiles of the pinhole-derived source MTF. (e) Source MTFs as estimated from edge responses at the center of rotation. (f) Zoomed version of (e), with solid lines indicating the corresponding profiles of the parameterized fit. . . . .	90
4.9	This figure shows horizontal, vertical, and 45° slices of the 2D measured NPS at the center of the detector, along with the theoretical 1D NPS (assuming radial symmetry). . . . .	93
4.10	Horizontal and vertical NPS slices for NPSs acquired at different positions on the detector, indicated by distance from the center in the horizontal direction. . . . .	94



4.11	Test-bench data reconstructions. (a) High resolution reference image. The large box denotes the ROI used for (b-f). (b) FDK reconstruction. (c) FDK reconstruction on deblurred data. (d) High resolution reference image with an arrow indicating cartilage-equivalent plastic. (e) Reconstruction obtained using the uncorrelated noise model. (f) Reconstruction obtained using the correlated noise model and noise matched with (e). . . . .	96
4.12	Difference images between the high-resolution reference image and the various reconstruction methods: (a) FDK; (b) PD deblur + FDK; (c) uncorrelated MBIR; and (d) correlated MBIR (corresponding to b, c, e, and f in Figure 4.11). The smallest differences from the high-resolution reference are observed in the correlated MBIR reconstruction. . . . .	98
4.13	(a) Blurred high-resolution reference image. (b) correlated MBIR reconstruction. (c) Difference image between (a) and (b). . . . .	99
5.1	Digital phantom with line pairs and bone inserts. The background attenuation value in the oval is $0.019 \text{ mm}^{-1}$ and the bone attenuation is $0.060 \text{ mm}^{-1}$ . The line pair attenuation values are either $0.060 \text{ mm}^{-1}$ (left and center) or $0.019 \text{ mm}^{-1}$ (right). The line pair frequency is $2.38 \text{ mm}^{-1}$ . © 2017 IEEE . . . . .	110
5.2	Resolution-variance tradeoff of the nonlinear and the linear reconstruction methods. . . . .	117

5.3	System characterization results. A: Measured axial and trans-axial MTF slices derived from tungsten edge responses. Inset: Pinhole image of the X-ray focal spot, resampled to match the PSF of the focal-spot blur experienced by an object at isocenter. B: MTF models. The detector model has the form given in (5.6). The isocenter models are slices of the MTF derived from the final PSF multiplied by the detector MTF model. © 2017 IEEE . . . . .	119
5.4	Parameter sweep results. Each point is the maximum mJac over $\beta$ for a given $\delta$ , reconstruction method, and noise realization. The left column is MBIR-I and the right column is MBIR-BC. The top row is the low photon flux results and the bottom row is the high photon flux results. © 2017 IEEE . . . . .	120
5.5	Bias/noise (A) and mJac (B) plots. The large markers in (A) correspond to the maximum mJacs in (B). The frequency cutoffs for the dFeldkamp-Davis-Kress (FDK) data in B (x-axis) are indicated at the top of the plot. © 2017 IEEE . . . . .	121
5.6	The center line pairs from the reconstructions in Figure 5.5. Each row corresponds to a different reconstruction method. Note that different values of $\beta$ were used for different MBIR methods. The reconstructions with the red border correspond to the ones with the maximum mJac in Figure 5.5(B). The lower half of each image shows the best segmentation for that $\beta$ /cutoff (i.e., the one resulting in the maximum Jaccard index over threshold values). © 2017 IEEE . . . . .	122

5.7	Maximum Jaccard (mJac) for each reconstruction method and regularization strength for the test bench-data. © 2017 IEEE . . . . .	124
5.8	Axial slice of trabecular bone reconstructions. Rows correspond to different reconstruction methods. The red background in the $\mu$ CTmv segmentation image indicates a slice of the mask used for registration and metric calculation. Note the attenuation values of the $\mu$ CT and $\mu$ CTmv scans are arbitrary and do not correspond to the gray-level map on the bottom. © 2017 IEEE . . . . .	125
5.9	Trans-axial slice of trabecular bone reconstructions. $\mu$ CT and $\mu$ CTmv attenuation units are arbitrary. © 2017 IEEE . . . . .	126
6.1	Geometry used to calculate the focal-spot blur impulse response. The focal spot is represented by the bold line on the side of the anode. All coordinates are in detector coordinates. The origin of the anode coordinate system is at $(u_0, v_0, SDD)$ . . . . .	136
6.2	Digital extremities phantom with medial (c) and lateral (d) bones, line pairs (a), and a uniform disc (b). . . . .	137
6.3	Axial (A) and Coronal (B) slice of trabecular bone phantom. The phantom consists of bone ( $0.060 \text{ mm}^{-1}$ ) surrounded by fat ( $0.019 \text{ mm}^{-1}$ ).141	
6.4	Focal spot model for data generation. Each pixel represents a sourcelet, and the relative intensity indicates the relative weight of that sourcelet's measurements. Due to the anode angle, fewer samples were required along the long axis of the focal spot, resulting in anisotropic sourcelets. . . . .	142

6.5	Sourcelet modeling illustration with two different types of projector. On the left, the sourcelets are modeled as point sources, and the voxels as rectangles/cubes. On the right, the sourcelets are modeled as lines/rectangles, and the voxels are modeled as points. . . . .	147
6.6	Demonstration of the line-pair contrast calculation. The reconstruction was averaged over slices to reduce noise (left). The rows were averaged between the dotted lines, resulting in the profile on the right. The mean of the peak values (triangles) and trough values (squares) were found and subtracted to get the final contrast measurement. A slice of the mask used for noise calculation is shown in red. . . . .	153
6.7	Best mutual overlap versus $\beta$ . A) Medial and B) Lateral bone. . . . .	154
6.8	Reconstructions of the medial bone with the highest mutual overlap over all thresholds and $\beta$ 's. The top half of each reconstruction is thresholded at the optimum threshold value. . . . .	156
6.9	MTFs and fits for the detector and the detector+source blur at different displacements from the center of rotation. . . . .	157
6.10	Physical CBCT reconstructions. Each subfigure shows a portion of the phantom from the edge to one of the line pairs. Each reconstruction has approximately the same noise level (indicated in each subplot in units of $\text{mm}^{-1}$ and denoted by $\sigma$ ). . . . .	159

6.11	A: Schematic of the Field of View (FOV) sampling. Each ring was sampled using the FDK algorithm. For a given sample point (for example the red dot), the phantom was placed at that location and scanned using a short scan with the source centered at (0, 0, 381.0) and the detector centered at (0, 0, -132.0). The angular range covered by the source is represented by the red arc. The data were then reconstructed using FDK. B-G: Root Mean Squared Error (RMSE) of FDK reconstructions for each sample point. Data at a constant radius corresponds to sampling along one of the black circles in A. The red dots indicate the corresponding location in A. . . . .	161
6.12	Example $\beta$ sweep results at the red dot in Figure 6.11A with a transaxial focal-spot orientation. . . . .	163
6.13	Minimum RMSE from each $\beta$ sweep along with the FDK RMSE values. Data is wrapped around at $360^\circ$ (i.e., the $360^\circ$ data are the same as the $0^\circ$ data). Subfigures A-D correspond to B-E, respectively, in Figure 6.11.	164
6.14	Axial slices of reconstructions. Each set of 16 reconstruction corresponds to a X-ray tube orientation (columns) and plane in the FOV (rows). Within each set, columns correspond to the location of the phantom (in degrees rotated about the $y$ axis) and rows to reconstruction method. . . . .	165
6.15	Coronal slices of reconstructions. Images are arranged as in Figure 6.14.	166
6.16	Simple 1D focal-spot distribution used to test focal-spot sampling properties with different projectors. . . . .	169

6.17	Simulated impulse responses using the focal spot in Figure 6.16 and either the separable footprints projector (blue) or the proposed separable sourcelets projector (orange). For each plot a different number of sourcelets were sampled from the distribution in Figure 6.16 (indicated at the top of each plot). . . . .	170
6.18	Pinhole measurements at different positions on the detector with the axial bench. There are some residual artifacts (vertical streaks) due to bad pixels. Approximate position relative to the piercing point (the point on the detector closest to the focal spot) is given in mm. . . .	171
6.19	Focal spot model for the axial bench. Each pixel in the image is a sourcelet and represents an area on the anode that emits X-rays, The intensity of each pixel indicates the relative intensity of the corresponding sourcelet. The coordinates indicate the position on the anode surface.	172
6.20	Simulated pinhole measurements for the axial bench based on the focal-spot model and separable sourcelets projector. . . . .	174
6.21	Focal spot model for the transaxial bench. . . . .	175
6.22	SI blur kernel for the transaxial bench. . . . .	175
6.23	Reconstructions from each scan type (rows) and blur model (columns) for the transaxial bench. The reconstructions are approximately noise matched. The noise for each reconstruction is give in Table 6.2. . . .	176
6.24	Contrast-noise plots for each scan type and reconstruction method for the transaxial bench reconstructions. . . . .	178

6.25	The digital phantom used in the motion blur study. The ROI indicated by the orange box in the left image is shown on the right. The left most circle in this ROI is at the center of the phantom. The circles are separated by 20 mm. . . . .	180
6.26	“Harp” phantom containing 25 spans of wire (labeled 1–25). The phantom was positioned off-center, with the center of rotation indicated by the star. . . . .	182
6.27	Bias/noise curves (top) and reconstructions (bottom) for each ROI in Figure 6.25. Each column corresponds to a distance from the center of rotation. The top row reconstructions use the identity model and the bottom row reconstructions use the gantry motion blur model. . . . .	184
6.28	“Harp” phantom reconstructions for the identity model (left) and blur model (right). Each ROI corresponds to one of the wires in Figure 6.26.	185
7.1	Iodine sensitivity phantom. The numbers indicate the iodine concentration in each adjacent ROI in $\text{mg mL}^{-1}$ . ROI specific CNR was calculated as the ratio of the mean in the regions indicated by the circles along the edge of the phantom to the standard deviation in the inner circle. . . . .	200
7.2	Schematic of the kV-switching/split-filter acquisition protocol. The kVp was switched every projection (i.e., every $1^\circ$ ). . . . .	203
7.3	Digital water, iodine, and gadolinium phantom. Inserts are numbered in the iodine image, and corresponding Regions of Interest (ROIs) for metric evaluation are indicated with circles. Iodine and gadolinium concentrations are next to each ROI in $\text{mg mL}^{-1}$ . . . . .	203

7.4	(a) Mass attenuation coefficients. (b) Spectral responses ( $S$ ) for the kV-switching/split-filter simulation study. . . . .	204
7.5	(a) Iodine/gadolinium phantom. Each vial contains different mixtures of iodine- and gadolinium-based contrast agents. In (b) and (c) we show a schematic of the phantom identifying insert/ROI labels. The concentration of iodine in each vial is indicated in (b), and the concentration of gadolinium in each vial is in (c). . . . .	206
7.6	Schematic of tiled filter acquisition. The filter was translated each frame to improve sampling (not shown). . . . .	207
7.7	Water/calcium simulation reconstructions. The insert ROIs are numbered from top to bottom. The standard deviations of the calcium concentrations in insert 1 are $7.82 \text{ mg mL}^{-1}$ for IDD KV1:1, $12.41 \text{ mg mL}^{-1}$ for PDD KV1:1, $8.11 \text{ mg mL}^{-1}$ for MBMD KV1:1, $8.42 \text{ mg mL}^{-1}$ for Image Domain Decomposition (IDD) KV10:10, and $8.71 \text{ mg mL}^{-1}$ for MBMD KV10:10. The percentages indicate the root mean squared fractional errors in the calcium ROIs. . . . .	209
7.8	Average concentration in each insert in Figure 7.7 for water (left) and calcium (right). . . . .	210
7.9	RMSE for each penalty strength combination for the (a) IDD and (b) Model-Based Material Decomposition (MBMD) methods. The minimum RMSE in each plot is indicated with a star. . . . .	210



7.10	IDD (top) and MBMD (bottom) reconstructions of water (left) and iodine (middle and right) concentrations. The right column is the same as the center but with a tighter window to better visualize the low concentration ROIs. . . . .	212
7.11	CNR values in each ROI from the optimal reconstruction with each method. . . . .	213
7.12	Digital iodine/gadolinium phantom reconstructions. Each column is a different material density image. . . . .	214
7.13	Concentrations of each material (columns) and ROI in the digital iodine/gadolinium phantom. The true concentrations are indicated by vertical lines. ROI numbers correspond to those in Figure 7.3. . . . .	215
7.14	Iodine and gadolinium estimates for the physical test bench experiment. The top row shows the split filter results and the bottom shows the tiled filtered results. . . . .	216
7.15	Concentration values for each material and ROI in the physical iodine/gadolinium phantom. Insert/ROI locations are indicated in Figure 7.5. . . . .	217
B.1	Geometry and coordinates for a transaxial oriented x-ray source. . . .	228

# List of Acronyms

**BMD** Bone Mineral Density

**BV/TV** Bone Volume to Total Volume

**CBCT** Cone-Beam CT

**CG** Conjugate Gradient

**CNR** Contrast-to-Noise Ratio

**CsI** Cesium Iodide

**CT** Computed Tomography

**ESF** Edge Spread Function

**FBP** Filtered Backprojection

**FDK** Feldkamp-Davis-Kress

**FP** Flat Panel

**FPD** Flat Panel Detector

**FOV** Field of View

**FWHM** Full Width at Half Maximum

**GPU** Graphics Processing Unit

**I** Identity

**ID** Image Domain

**IDD** Image Domain Decomposition

**MAP** Maximum *A Posteriori*

**MBIR** Model-Based Iterative Reconstruction

**MBMD** Model-Based Material Decomposition

**MBSR** Model-Based Sinogram Restoration

**MDCT** Multi-Detector CT

**mJac** maximum Jaccard index

**MTF** Modulation Transfer Function

**mv** matched voxel size

**NPS** Noise Power Spectrum

**PET** Positron Emission Tomography

**PD** Projection Domain

**PDD** Projection Domain Decomposition

**PL** Penalized-Likelihood

**PSF** Point Spread Function

**qCBCT** quantitative CBCT

**ROI** Region of Interest

**RMSE** Root Mean Squared Error

**SI** Shift Invariant

**SNR** Signal-to-Noise Ratio

**SQS** Separable Quadratic Surrogates

**SV** Shift Variant

**Tb.Sp.** Trabecular Spacing

**Tb.Th.** Trabecular Thickness

**TV** Total Variation

**μCT** micro CT

# Chapter 1

## Introduction

Since its invention in 1972 [3, 4], Computed Tomography (CT) has been an invaluable clinical and research tool. Prior to the adoption of CT, X-ray imaging was focused on projection images. While projection images are useful, they contain overlapping biological structures and limited soft tissue visualization. Conventional tomography [5] mitigates this overlap by “blurring out” structures outside of a single plane with X-ray source and detector motion. In contrast to projection imaging, modern CT is capable of rapidly imaging multiple slices of the patient to produce three-dimensional images. Additionally, these images may be used for soft tissue differentiation. Since their inception, CT hardware and software have improved dramatically, decreasing scan time and increasing spatial and temporal resolution.

Most medical CT scanners can be classified as either Multi-Detector CT (MDCT) (i.e., multi-slice CT) or Flat Panel (FP) Cone-Beam CT (CBCT). MDCT scanners are general-purpose machines capable of rapidly acquiring large images of patients. Currently available commercial systems have reported resolutions of approximately 0.23 mm to 0.7 mm [6–8], with one state-of-the-art system (Canon’s Precision Aquilion) reporting a resolution of 0.15 mm [9]. In contrast, FP CBCT scanners are gen-

erally higher resolution (0.18 mm to 0.5 mm [10]), but have longer scan times and are more application specific (e.g., extremities imaging [11], dental imaging [12], and radiotherapy [13]).

Many imaging tasks and biological structures lie below this resolution. For example, visualization of trabecular bone (0.05 mm to 0.15 mm [14]) is important in osteoarthritis and fracture healing studies and detection and classification of microcalcifications ( $<0.1$  mm [15]) are important in mammography. An increase in spatial resolution has the potential to dramatically improve the research and treatment of various diseases, particularly those that are currently just below current resolution limits. Improved resolution may also improve feature extraction in radiomics [16] potentially leading to more accurate tumor characterization.

Another critical component of image quality is quantitative accuracy (e.g., the accuracy of attenuation values or derived quantities). This is particularly important in applications such as Bone Mineral Density (BMD) measurement [17] and material decomposition, which seek accurate density values to assess bone health and to determine the concentration of specific materials in the body, respectively.

The data processing chain used to generate the final image can have a dramatic effect on image quality. The raw data measured by a CT scanner are projections of the patient, from which the slice or volume image is reconstructed. Reconstruction algorithms vary dramatically in complexity, making different assumptions and tradeoffs depending on the CT system, computation constraints, and imaging task. Recently, Model-Based Iterative Reconstruction (MBIR) algorithms have become increasingly popular for CT reconstruction. These algorithms rely on accurate physical and statistical measurement models for the CT scanner to derive an objective function, or

goodness-of-fit metric. The reconstruction is the optimum of this objective function. MBIR methods generally offer improved image quality over traditional methods, and provide an excellent opportunity to further improve resolution and quantitative accuracy by increasing the fidelity of these physical and statistical models.

This dissertation seeks to **improve image quality and accuracy using MBIR with high-fidelity system and noise models**, and consists of three aims:

- Aim 1. develop a generalized MBIR framework capable of incorporating a wide range of physical effects including realistic noise models;
- Aim 2. characterize different physical effects and the resulting noise properties on multiple CT devices and designs, and develop mathematical and computational models of those effects; and
- Aim 3. incorporate these models into the MBIR framework to improve image quality, and assess image quality improvements in simulation and physical data studies.

This dissertation is organized by the physical effects being modeled instead of following the order of the above aims.

**Chapter 2** presents the relevant background information for this work. It contains an overview of the CT imaging chain, focusing on the physical effects that will be modeled in later chapters. It then provides an overview of CT reconstruction, including Filtered Backprojection (FBP) and MBIR, followed by a brief overview of previous high-fidelity modeling in CT reconstruction.

**Chapter 3** presents the generalized MBIR framework and derives associated optimization algorithms (Aim 1). The MBIR framework permits modeling of many physical effects without changing the underlying optimizer.

**Chapters 4 and 5** address Aims 2 and 3 for focal-spot and scintillator blur as well as noise correlations using a Shift Invariant (SI) model. Focal-spot blur, scintillator blur, and noise correlations are measured and modeled for multiple systems. The models are incorporated into the MBIR framework to improve image quality, which is assessed using a variety of metrics.

**Chapter 6** addresses Aims 2 and 3 for Shift Variant (SV) focal-spot blur and SV gantry motion blur. Both types of blur are location and orientation dependent, requiring more complicated mathematical modeling. This chapter presents a general strategy for measuring SV focal-spot blur and models blur in a manner consistent with the developed MBIR framework. The effects of these types of blur and the image quality improvements due to the resulting MBIR algorithm are studied with multiple simulated systems as well as physical experiments.

**Chapter 7** demonstrates that the generalized MBIR framework is capable of modeling the polyenergetic properties of CT acquisition, and exploits this to perform Model-Based Material Decomposition (MBMD) in multiple challenging data acquisition scenarios. Spectral properties are measured and modeled (Aim 2) and used with the MBIR framework to improve image quality (Aim 3), specifically by removing artifacts and providing accurate density measurements for improved quantification.

**Chapter 8** concludes with additional observations and proposals for future work.



# Chapter 2

## Background

This chapter begins with an overview of CT imaging. The measurement process from X-ray generation to detection is explained, with an emphasize on the aspects that will be modeled in later chapters. Next, an overview of the reconstruction process is provided, focusing on MBIR methods.

### 2.1 CT physics

A typical CT image is an estimate of the internal X-ray attenuation properties of a patient. A CT scanner measures the degree of X-ray attenuation along various paths through the patient, with each path corresponds to a particular detector pixel and gantry position. These measurements are then used to reconstruct the final image. Figures 2.1 and 2.2 show the source and detector configuration of a MDCT and FP CBCT scanner, respectively. X-ray photons are generated at the X-ray source which then travel through the patient. The X-ray beam is attenuated as it travels through the patient, and then unattenuated X-ray photons are detected and converted into a digital signal at the detector. This section provides a brief overview of this imaging

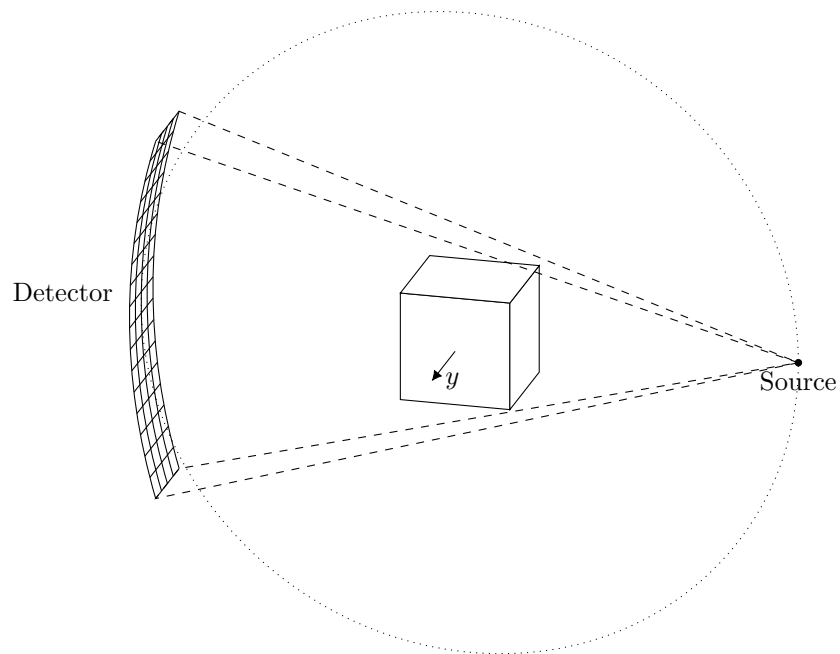


Figure 2.1: Schematic of a MDCT system showing the X-ray source and detector. X-ray photons are generated at the source, travel through the patient/object (in this case a box), and then are absorbed by the detector. Both the source and detector are fixed to a gantry (not shown) that rotates about the  $y$  axis along the path indicated by the dotted line. The direction indicated by  $y$  is referred to as axial direction.

process. More detailed descriptions may be found in Prince and Links [18], Hsieh [19], and Bushberg et al. [20].

### 2.1.1 The X-ray source

The X-ray source produces photons at the desired energy and fluence from a small area called the focal spot. The properties of the focal spot and of the X-ray beam can

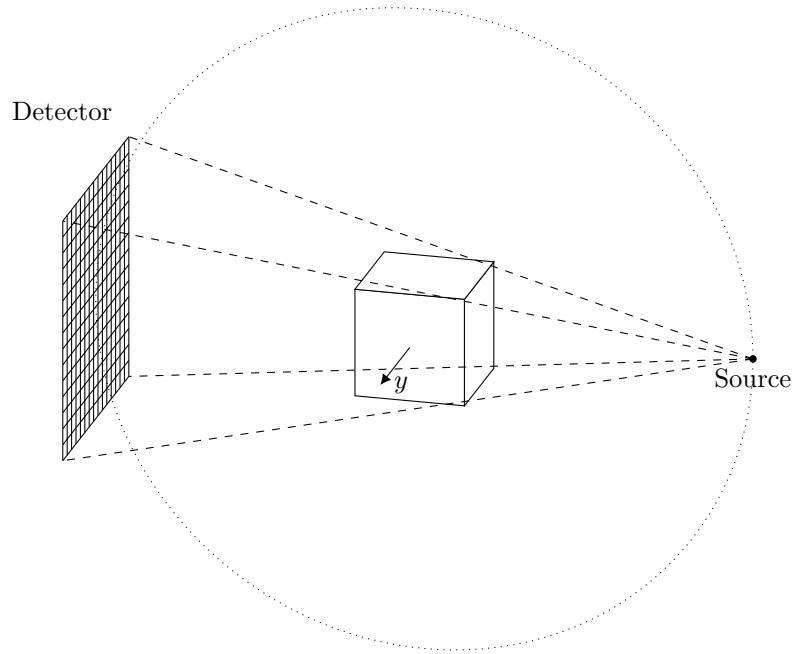


Figure 2.2: Schematic of a FP CBCT system. As compared to the MDCT system in Figure 2.1, FP CBCT systems have a flat detector and often have smaller pixels. Flat panel detectors are usually more square then MDCT detectors, leading to a larger cone angle in the axial direction but less lateral coverage.

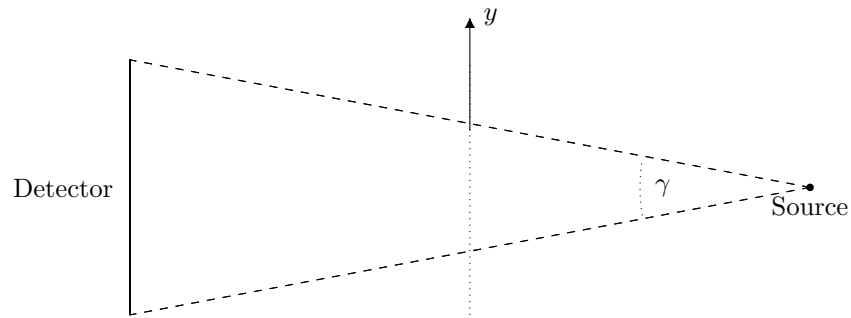


Figure 2.3: Schematic from Figure 2.2 viewed from the side. The dotted line is the axis of rotation, and  $y$  is the same as in Figure 2.2. The cone angle is indicated by  $\gamma$ .

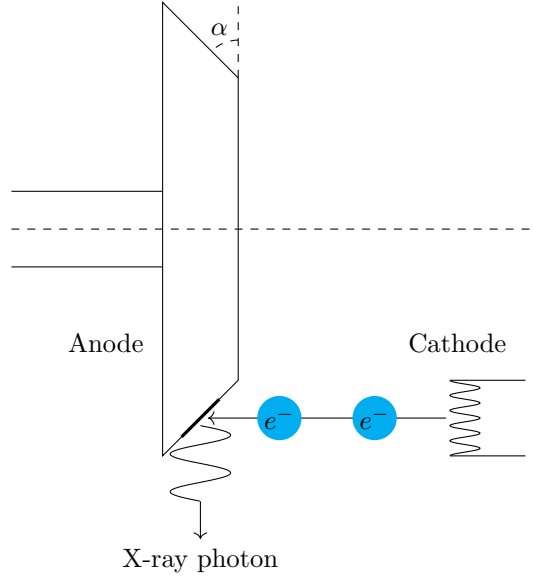


Figure 2.4: Schematic of the anode and cathode inside an X-ray tube. The anode is rotated about the axis indicated with the dashed line. An X-ray photon shown is traveling along the central ray, towards the patient.

dramatically effect image quality. This section discusses these properties and how they are determined by X-ray source.

The primary component of an X-ray source is the X-ray tube, a glass vacuum tube containing a tungsten anode and cathode. To generate X-ray photons, an electric current (typically  $\leq 7$  A [20]) is passed through the cathode, heating it and releasing electrons via thermionic emission. When a voltage difference is applied between the anode and cathode, these electrons are accelerated towards the positively charged anode. This voltage difference is usually in the range of 60 kV to 140 kV, and may be continuous or pulsed to produce either a continuous or pulsed X-ray beam. (A pulsed X-ray beam may also be controlled using a grid [21] or by applying a pulsed

current.) When the electrons collide with the anode, some are decelerated by the atomic nuclei, causing them to shed energy in the form of X-ray photons. This is known as “Bremsstrahlung,” or breaking radiation. Electrons may also transfer their energy to an inner shell electron, ejecting that electron from the atom. When an outer shell electron takes its place, a characteristic X-ray photon is released, with an energy equal to the energy difference between the inner and outer shells. The area where electrons interact with the anode to release X-ray photons is the focal spot. A focusing cup around the cathode helps direct the electrons to the focal spot, although the spatial electron distribution (and hence, focal-spot distribution) is generally not uniform. The three main parameters defining an imaging technique are the voltage, which determines the energy of the X-ray photons; the pulse time (for pulsed sources); and the current flow of electrons from cathode to anode, which determines the rate of X-ray photon generation (fluence). The current is controlled by changing the current through the cathode.

The conversion of electrons to X-ray photons is very inefficient, and most of the energy released by the bombarding electrons is converted to heat. To reduce heat buildup, many X-ray sources feature a rotating anode, such as the one in Figure 2.4. By rotating the anode about its central axis, any given area of the anode is only bombarded with electrons for a small fraction of its rotational period, giving time for heat to dissipate. Note that while the focal spot moves relative to the surface of the anode, it remains fixed<sup>1</sup> relative to the X-ray tube and the system as a whole. A large focal spot area also improves heat dissipation but larger focal spots will degrade

---

<sup>1</sup>The focal-spot can be shifted slightly throughout a scan, for example to reduce gantry motion artifacts. Additionally, the focal-spot may experience small perturbations in position, although these are typically much smaller than the focal-spot size.

resolution. To address this, focal spots are often designed long and narrow, with a relatively steep angle ( $\alpha$  in Figure 2.4) between the anode surface and the central ray (the direction the X-ray photon is traveling in Figure 2.4). This allows the focal spot to be relatively large, while appearing small from a point along the central ray. The non-zero size of the focal spot causes its apparent size and shape to change based on location in the imaging volume (illustrated in Figure 2.5). In other words, the impulse response of the focal spot is position dependent, leading to a Shift Variant (SV) blur. In Chapters 4 and 5 the focal-spot blur is modeled using a Shift Invariant (SI) approximation. In Chapter 6 the SV effects on image quality are explored, along with proper modeling and reconstruction techniques to mitigate these effects.

There is inherent randomness associated with X-ray generation, causing Poisson noise, or shot noise, in measurements. The probability distribution of a given number of X-ray photons emitted in a given time period is modeled by a Poisson distribution, with a probability density function given by

$$p[y = k] = \frac{\exp(-n) n^k}{k!} \quad (2.1)$$

where  $y$  is the emitted number of X-ray photons, and  $n$  is the theoretical mean number of emitted photons [22]. A random variable with a Poisson distribution has a mean equal to its variance. Therefore the Signal-to-Noise Ratio (SNR), calculated as the mean divided by the standard deviation, increases as the square root of the mean. In other words, in order to double SNR, the X-ray beam intensity must be increased by a factor of four.

The energy of the X-ray photons produced by the source is determined by the voltage difference between the anode and cathode. The individual photon energies

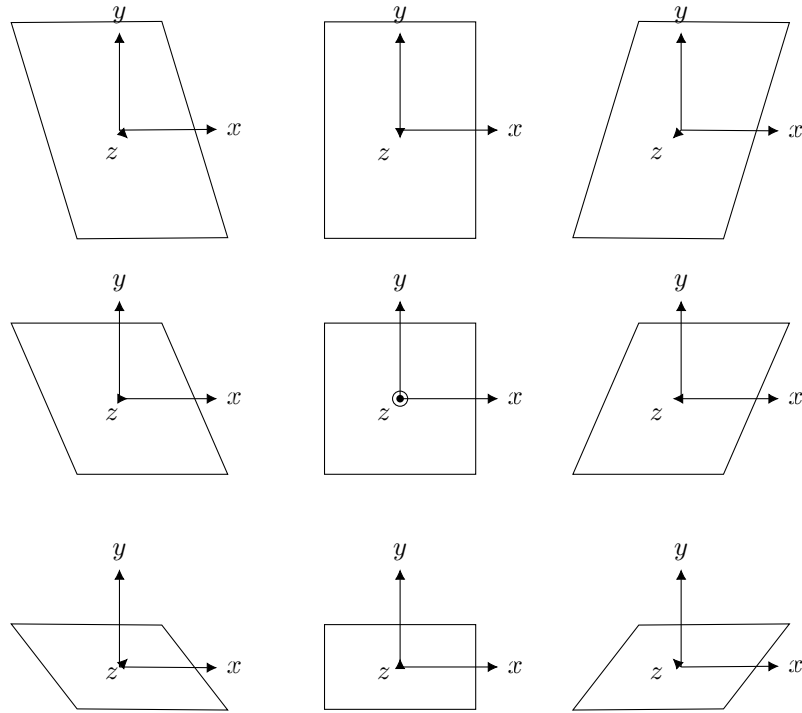


Figure 2.5: X-ray focal spot appearance from different positions. In the center image the viewing angle is aligned with the central ray, or  $z$  axis in this figure. The other positions correspond to shifting the viewing angle  $5^\circ$  about the  $x$  and/or  $y$  axes. In this example the anode angle is  $11.3^\circ$ .

are not constant, but follow a distribution from 0 keV to the applied voltage difference in eV (electron volts). For example, applying a 120 kV potential produces X-ray photons with an energy range of 0 keV to 120 keV. An electron which is completely decelerated by an atomic nucleus in the anode will produce a 120 kV photon, while an electron which is only partially decelerated will produce a lower energy photon. For this reason, the voltage difference is referred to as kVp for kilovolt peak. The lower energy photons ( $<10$  keV) are almost entirely attenuated by inherent filtration in the system (e.g., the glass of the X-ray tube) or additional filtration outside the X-ray tube. If these lower energy, or “soft,” X-ray photons were not filtered out, they would be almost completely absorbed in the patient, increasing radiation dose without adding any signal. The process of filtering lower energy photons is referred to as “hardening” the beam, and results in a distribution with more higher energy, or “hard,” photons. An example spectrum (computed using Spektr [23]) is shown in Figure 2.6.

Most reconstruction techniques assume the X-ray beam is monoenergetic. Unless this discrepancy is accounted for, either with preprocessing or advanced reconstruction techniques, the reconstruction may exhibit beam hardening artifacts. These artifacts arise because the patient hardens the X-ray beam by preferentially attenuating softer X-ray photons. This results in a higher energy X-ray spectrum at the detector, and more photons being detected than would be expected with a monoenergetic assumption. Therefore, the reconstructed attenuation values are underestimated to account for the increase in detected photons. This underestimation is most pronounced along paths of high attenuation through the patient. This work addresses beam hardening as part of the material decomposition studies in Chapter 7.



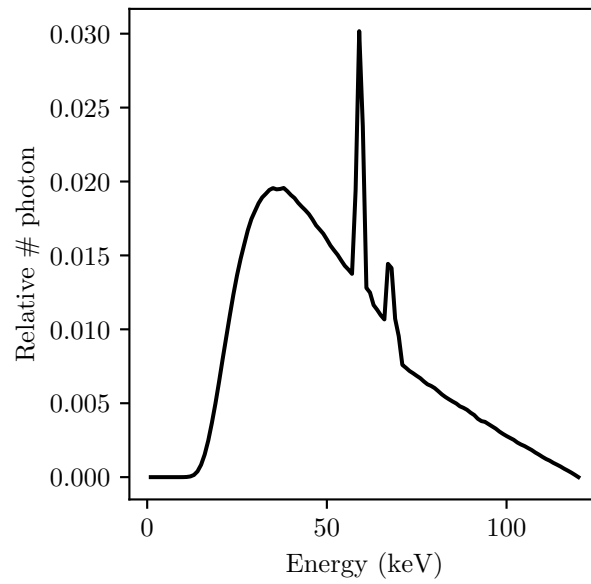


Figure 2.6: Example X-ray spectrum with 120 kVp. The peaks are due to characteristic X-ray photons.

### 2.1.2 X-ray attenuation

Contrast in CT is due to attenuation differences between different materials/tissue types and different local material densities. Transmissivity is a measure of the fraction of X-ray photons that are transmitted through an object along a particular path, and is given by

$$y_0 = \exp(-\mu\ell) \quad (2.2)$$

for a uniform object, where  $y_0$  is transmissivity,  $\mu$  is the attenuation coefficient of the object (in units of inverse distance), and  $\ell$  is the length of the path. Water has an attenuation coefficient of about  $0.018 \text{ mm}^{-1}$ , while cortical bone is about  $0.044 \text{ mm}^{-1}$  at 80 kVp [24, 25]. Attenuation coefficients are energy dependent, generally with higher attenuation at lower energies. This, combined with the polyenergetic source spectrum, leads to the beam hardening artifacts discussed in §2.1.1. Attenuation is often given as the mass attenuation coefficient, which is the attenuation coefficient of a material normalized by density. Mass attenuation curves of select materials are shown in Figure 2.7. Heavier elements, such as iodine, often have a K-edge, or a sharp increase in attenuation at a specific energy (specifically, the energy required to eject an electron from the K-shell).

The fact that materials have different mass attenuation curves may be exploited to separate, or decompose, materials with similar overall attenuation. For example, iodine and calcium have similar overall attenuations at diagnostic energies, but different energy-dependent properties due to the iodine K-edge. Material decomposition requires measurements with different spectral properties (e.g., measurements acquired at different kVp). Material decomposition is the topic of Chapter 7.

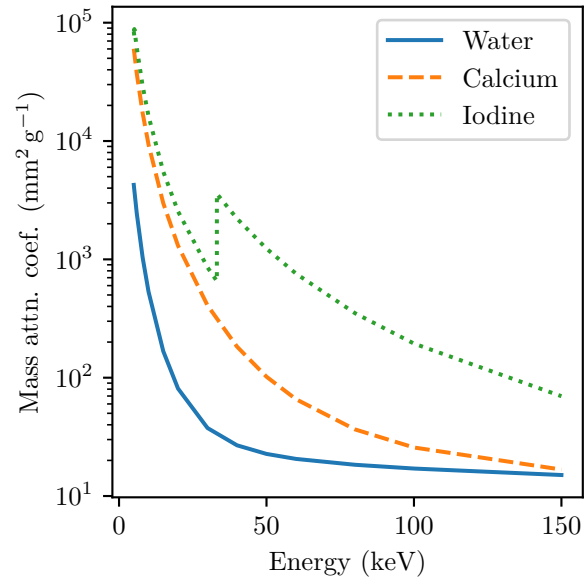


Figure 2.7: Mass attenuation coefficients of water, calcium, and iodine.

The predominant mechanisms of X-ray attenuation at CT energies are the photoelectric effect and Compton scattering. For the photoelectric effect, all of the X-ray energy is absorbed and an electron is released from the atom. With Compton scattering, an incoming X-ray photon imparts some energy in deflecting an electron, and the remainder is released as a scattered X-ray photon. This scattered photon has lower energy and a different trajectory than the initial photon. Scattered photons may still be detected, but because their paths through the object cannot be determined, the signal cannot be used for traditional attenuation estimation. (The fact that the initial photon was scattered in the first place *is* useful, and is part of the overall attenuation.) Detected scatter is a low frequency effect which may effect quantification and cause “cupping” artifacts. With small cone angles scatter effects are minimal, as a scattered photon must remain within the slice to be detected. (Cone angle is described in Figure 2.3.) However, MDCT scanners with many detector slices and FP CBCT systems may have large cone angles, and as such are more susceptible to scatter. This work largely assumes that X-ray scatter is either negligible or can be corrected for prior to reconstruction.

### 2.1.3 X-ray detection

A CT detector absorbs X-ray photons and converts them to an electronic signal. There are many types of detectors with different physical properties and trade-offs. MDCT scanners use a curved array of pixels with the X-ray focal spot at the center of curvature (Figure 2.1). In contrast the Flat Panel Detectors (FPDs) used in FP CBCT systems typically have smaller pixels and are generally longer in the axial

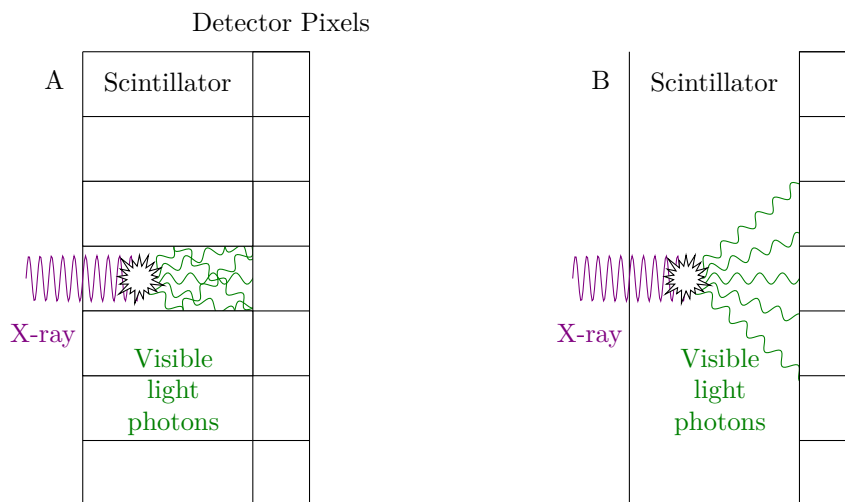


Figure 2.8: Schematic of X-ray detection process. An X-ray photon enters the scintillator and is converted into multiple visible light photons, which are then detected by the photodiodes on right of each image. Subfigure A shows a pixelated scintillator, as is common in MDCT detectors. The light photons reflect off the septa and only hit one photodiode. Subfigure B shows a non-pixelated scintillator, where the light photons can spread to multiple detector photodiodes. This schematic assumes a 100% fill factor for simplicity.

direction but shorter in the trans-axial dimension as compared to MDCT detectors (Figure 2.2). This results in a larger cone angle (Figure 2.3) in FP CBCT.

The term CBCT refers to systems with a large cone angle (i.e., a large detector extent in the axial direction). Traditionally only FP systems met this criteria. However, as MDCT scanners add wider detectors, the distinction is more ambiguous. In this work we use CBCT to specifically refer to FP CBCT.

Both MDCT and CBCT typically use indirect detectors, where the X-ray photons first interact with a scintillating material which converts them to many visible light photons. These light photons, or secondary photons, are then detected by photodiodes which convert them into an electronic signal. (In a direct detector, the X-ray photons are directly converted into an electronic signal.) A typical detector has one photodiode per pixel. A schematic of this process is shown in Figure 2.8. The light photons spread from the point of X-ray interaction before being detected by the photodiode. In CBCT (Figure 2.8B) this may result in a single X-ray photon being detected at multiple pixels, causing scintillator blur. Cesium Iodide (CsI) is often used as a scintillating material in CBCT because it can be manufactured with a columnar structure, which reduces scintillator blur by discouraging light spreading outside the columns [26]. MDCT scanners generally avoid much of the scintillator blur by using a pixelated detector, which divides the scintillator with a reflective coating (Figure 2.8A). However, there is still some optical crosstalk between detector elements [27]. Because multiple visible light photons are generated from a single X-ray photon, they are statistically dependent. Scintillator blur also correlates the noise. The noise properties of scintillator blur are explored in Chapters 4 and 5. A thorough exploration of FPD noise properties can be found in Siewerdsen et al. [28].

The visible light photons are converted to an electronic signal in each pixel. Each photodiode integrates the signal over its aperture into a single value. Mathematically, this results in a blurring and then sampling of the signal. The photodiode aperture is often smaller than full extent of the pixel, with the ratio between aperture area and pixel area referred to as the fill factor. A fill factor less than one results in signal loss as X-ray photons that fall outside the aperture are not detected. Typical fill factors are 60 % to 70 % [29, 30] for FPDs. The sampling step may result in aliasing of higher frequencies. In most CBCT scanners, system blur usually modulates any aliasing frequencies to low levels. Finally, the signal stored in each pixel is read out and stored in a computer. The photodiode and readout electronics can add (potentially correlated [31]) electronic noise, or readout noise, to the signal.

Most detectors integrate the incoming signal over a period of time before it is read out to the computer. On a system with a continuously rotating source and detector this leads to a type of motion blur, where the source and detector are moving during the integration time. Such blur appears in the azimuthal direction in the reconstructed image. In MDCT systems, integration times are around 0.2 ms to 0.5 ms [20], while for CBCT they are approximately 5 ms to 25 ms [30, 32]. Gantry motion may be reduced by operating in step-and-shoot mode, where the gantry is stationary during X-ray exposure and signal integration, or by using short X-ray pulses. Additionally, some MDCT systems shift the focal spot during an exposure to offset the gantry rotation.

CT detectors are also susceptible to detector lag and afterglow, where the signal is “trapped” in the detector during one exposure and then counted as signal in subsequent exposures. Lag is primarily due to the detector electronics, while afterglow

is the delayed release of optical light photons in the scintillator. These are usually subtle effects, but can last for many frames. Because these are one-sided projection domain convolutions, they can easily be corrected for in preprocessing [33].

An increasingly popular class of detector is the photon counting detector. These are typically direct detectors which are capable of detecting individual X-ray photons. Because these detectors are not integrating the signal from multiple photons over time, each signal corresponds to a single X-ray photon, and the strength of that signal can often be related to the photon energy. This additional energy information enables spectral CT and material decomposition. While this work does not deal with photon counting detectors directly, the material decomposition method in Chapter 7 may be applied to data collected with such detectors.

In this section we provided an overview of many physical effects present in CT systems. In later chapters we will present mathematical models of these effects for incorporation into reconstruction algorithms.

## 2.2 CT image reconstruction

CT image reconstruction is the process of using the projection data from the X-ray detector to form an image of attenuation values<sup>2</sup> in the patient. Reconstruction algorithms may be divided into one of two classes, analytic methods which are based on the Radon transform, and model-based methods which are often based on statistical

---

<sup>2</sup>As will be shown in Chapter 7, one can reconstruct other properties instead of attenuation values.



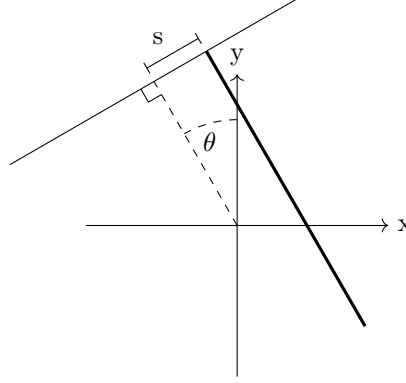


Figure 2.9: Parallel beam geometry. The detector is rotated about an angle  $\theta$  from the  $y$  axis. The integration path for measurement  $y(s, \theta)$  is indicated by the thick line

likelihood functions. Because model-based methods are typically solved iteratively, they are often referred to as Model-Based Iterative Reconstruction (MBIR) methods. Hybrid methods also exist, where data is preprocessed with model-based algorithms prior to analytic reconstruction.

### 2.2.1 Analytic reconstruction

Most analytic reconstruction techniques are variations of FBP. Basic FBP is derived using a two-dimensional parallel-beam geometry where each integration path is perpendicular to the detector (Figure 2.9). Modern implementations (e.g., for fan beam and cone beam systems) can be thought of as modifications of parallel beam Filtered Backprojection (FBP). In this section we show a derivation of parallel FBP. More detailed derivations may be found in Prince and Links [18] and Kak and Slaney [34].

The signal detected at a point on the X-ray detector may be modeled by:

$$y(s, \theta) = g(s) \exp(-\ell(s, \theta)) \quad (2.3)$$

$$\ell(s, \theta) = \int_{x=-\infty}^{\infty} \int_{y=-\infty}^{\infty} \mu(x, y) \delta(s - y \sin(\theta) - x \cos(\theta)) dy dx \quad (2.4)$$

where  $y$  is the measured data,  $s$  is the position along the detector,  $\theta$  is the gantry rotation angle,  $g(s)$  is the bare beam photon flux at location  $s$ , and  $\mu$  is a function describing the map of attenuation values. The integral sums the attenuation values along a line perpendicular to the detector that intersects at point  $s$  (Figure 2.9). Equation (2.4) is also known as the Radon transform. Analytic methods tend to use the line integrals ( $\ell$ ) instead of the measurements ( $y$ ), which can be estimated by

$$\hat{\ell}(s, \theta) = -\log\left(\frac{y(s, \theta)}{g(s)}\right). \quad (2.5)$$

Taking the Fourier transform of  $\ell$  with respect to  $s$  yields

$$L(\rho, \theta) \triangleq \mathcal{F}_{1D}(\ell(s, \theta)) = \int_{s=-\infty}^{\infty} \exp(-2\pi i s \rho) \ell(s, \theta) ds \quad (2.6)$$

$$= \int_{x=-\infty}^{\infty} \int_{y=-\infty}^{\infty} \exp(-2\pi i \rho(x \cos(\theta) + y \sin(\theta))) \mu(x, y) dy dx \quad (2.7)$$

$$= \mathcal{F}_{2D}(\mu)(u, v) \quad (2.8)$$

where

$$u \triangleq \rho \cos(\theta) \quad (2.9)$$

$$v \triangleq \rho \sin(\theta). \quad (2.10)$$

This results state that the one-dimensional Fourier transform of  $\ell$  at a given angle is equivalent to a one-dimensional slice of the two-dimensional Fourier transform of  $\mu$ . This is known as the Fourier Slice Theorem. One could therefore calculate  $\mu$  by Fourier transforming the line integrals, arranging them in the correct slice, and then inverse Fourier transforming the results. In practice, a more computationally efficient technique is used, which is derived starting with a rewritten form of the Fourier Slice Theorem:

$$\mu(x, y) = \int_{u=-\infty}^{\infty} \int_{v=-\infty}^{\infty} \exp(2\pi i(ux + vy)) L(\rho, \theta) du dv \quad (2.11)$$

$$\mu(x, y) = \int_{\theta=0}^{2\pi} \int_{\rho=0}^{\infty} \exp(2\pi i \rho t) L(\rho, \theta) \rho d\rho d\theta \quad (2.12)$$

where

$$t \triangleq (x \cos(\theta) + y \sin(\theta)) \quad (2.13)$$

$$\mu(x, y) = \int_{\theta=0}^{\pi} \int_{\rho=0}^{\infty} \exp(2\pi i \rho t) L(\rho, \theta) \rho d\rho d\theta \quad (2.14)$$

$$+ \int_{\theta=0}^{\pi} \int_{\rho=0}^{\infty} \exp(-2\pi i \rho t) L(\rho, \theta + \pi) \rho d\rho d\theta \quad (2.15)$$

$$\mu(x, y) = \int_{\theta=0}^{\pi} \int_{\rho=0}^{\infty} \exp(2\pi i \rho t) L(\rho, \theta) \rho d\rho d\theta \quad (2.16)$$

$$+ \int_{\theta=0}^{\pi} \int_{\rho'=0}^{-\infty} -\exp(2\pi i \rho' t) L(-\rho', \theta + \pi) (-\rho') d\rho' d\theta \quad (2.17)$$

$$\mu(x, y) = \int_{\theta=0}^{\pi} \int_{\rho=0}^{\infty} \exp(2\pi i \rho t) L(\rho, \theta) \rho d\rho d\theta \quad (2.18)$$

$$+ \int_{\theta=0}^{\pi} \int_{\rho'=-\infty}^0 \exp(2\pi i \rho' t) L(-\rho', \theta + \pi) (-\rho') d\rho' d\theta. \quad (2.19)$$

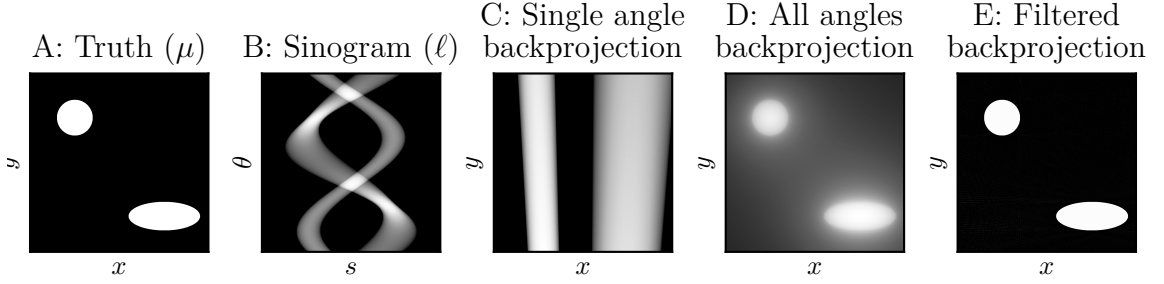


Figure 2.10: Example of FBP (with a fan beam geometry). A simple truth image (A) is forward projected to calculate the sinogram (B). Backprojecting a single angle effectively “smears” the projection back across the volume (C). Repeating for all angles results in a blurry reconstruction (D), while filtering prior to backprojecting results in an accurate reconstruction (E).

Using the facts that  $L(p, \theta) = L(-p, \theta)$  and  $L(\rho, \theta) = L(\rho, \theta + \pi)$

$$\mu(x, y) = \int_{\theta=0}^{\pi} \int_{\rho=-\infty}^{\infty} \exp(2\pi i \rho t) L(\rho, \theta) |\rho| d\rho d\theta \quad (2.20)$$

$$\mu(x, y) = \int_{\theta=0}^{\pi} f(t, \theta) d\theta \quad (2.21)$$

where

$$f(t, \theta) = \int_{\rho=-\infty}^{\infty} \exp(2\pi i \rho t) L(\rho, \theta) |\rho| d\rho \quad (2.22)$$

is the line integrals filtered with ramp filter  $|\rho|$ . Equation 2.21 is the backprojection operation, and may be visualized as “smearing”  $f$  back across the volume. This is illustrated in Figure 2.10. Note that backprojecting without filtering (Figure 2.10D) results in a blurred reconstruction (specifically a  $|\rho^{-1}|$  blur).

Table 2.1: Notation conventions

Description	Format	Example
Matrix	Bold, upright, uppercase	<b>A</b>
Vector	Bold, italic, lowercase	<b><i>a</i></b>
Matrix Element at i, j	Subscripted, bold, upright, uppercase	<b>A<sub>ij</sub></b>
Vector Element at i	Subscripted, bold, italic, lowercase	<b><i>a<sub>i</sub></i></b>

This parallel beam FBP algorithm may be modified for fan beam and cone-beam systems [35]. While this section doesn't go into detail describing these algorithms, the basic principle is the same (i.e., high pass filtering followed by backprojection).

### 2.2.2 Model-based iterative reconstruction

While FBP algorithms are based on an analytic solution to the Radon transform, MBIR methods are based on optimizing an objective function which is a goodness-of-fit measure for an image estimate based on the measured data. A forward model is a mathematical description of the imaging chain, and describes the mean and statistical properties of the measured data for a given image of attenuation values. It is used to derive the objective function. The reconstruction process is then finding an image which minimizes this objective function, e.g., finding the most likely image given the measured data.

MBIR methods are based on discrete system models. Equations (2.3,2.4) can be approximated in a discrete form as

$$\bar{\mathbf{y}} = \mathbf{D}\{\mathbf{g}\} \exp(-\ell) \quad (2.23)$$

$$\ell = \mathbf{A}\boldsymbol{\mu}. \quad (2.24)$$

Table 2.1 lists the matrix and vector notation used throughout this work (unless otherwise noted). Vector  $\boldsymbol{\mu}$  is a discretization of  $\mu$  using some basis function  $b$ . In three dimensions

$$\boldsymbol{\mu}_{kN_xN_y+jN_x+i} \triangleq \iiint \mu(x, y, z) b(x, y, z; i, j, k, \Delta_x, \Delta_y, \Delta_z) dz dy dx \quad (2.25)$$

where  $\Delta_x$  is the sampling period and  $N_x$  is the number of samples in the  $x$  direction (likewise defined for the  $y$  and  $z$  directions). The most common basis functions are boxes, given by

$$b(x, y, z; i, j, k, \Delta_x, \Delta_y, \Delta_z) \triangleq \text{rect}\left(\frac{i\Delta_x - x}{\Delta_x}\right) \text{rect}\left(\frac{j\Delta_y - y}{\Delta_y}\right) \text{rect}\left(\frac{k\Delta_z - z}{\Delta_z}\right). \quad (2.26)$$

Vectors  $\boldsymbol{\ell}$  and  $\boldsymbol{y}$  are defined similarly. Discretizing  $\boldsymbol{\mu}$  and  $\boldsymbol{\ell}$  allows the integral in (2.4) to be represented as a matrix multiplication. The matrix,  $\mathbf{A}$ , is referred to as the system matrix. The exponential in (2.23) is applied element-wise.  $\text{D}\{\cdot\}$  creates a diagonal matrix with its argument on the diagonal. For example,  $\text{D}\{\boldsymbol{g}\}$  is the gain term with the gain for each measurement (i.e. the number of photons detected by the pixel during a bare-beam scan) given by vector  $\boldsymbol{g}$ . For CT sized problems, the matrices  $\mathbf{A}$  and  $\text{D}\{\boldsymbol{g}\}$  are typically too large to be formed and stored on a computer, and are instead applied functionally.

MBIR algorithms may use either pre-log data ( $\boldsymbol{y}$ ) or post-log data ( $\boldsymbol{\ell}$ ) as an input. As previously, post-log data may be estimated as

$$\hat{\boldsymbol{\ell}} = -\log\left(\text{D}\{\boldsymbol{g}^{-1}\}\boldsymbol{y}\right). \quad (2.27)$$

Note that (2.23) models the *mean* measurements ( $\bar{\mathbf{y}}$ ) in contrast to the actual observed measurements ( $\mathbf{y}$ ). The observed measurements are modeled as a random variable. The two most common models are independent Poisson and independent Gaussian, given by:

$$\mathbf{y}_i \sim \text{Poisson}(\bar{\mathbf{y}}_i), \quad (2.28)$$

$$\mathbf{y} \sim \mathcal{N}(\bar{\mathbf{y}}, \text{D}\{\bar{\mathbf{y}}\}), \quad (2.29)$$

or

$$\hat{\ell} \sim \mathcal{N}(\bar{\ell}, \text{D}\{\bar{\mathbf{y}}^{-1}\}) \quad (2.30)$$

where  $\mathcal{N}$  is a multivariate Gaussian distribution. Equation 2.30 operates in the post-log domain. The Poisson model is based on the fact that the predominant source of noise in CT measurements is quantum noise, which follows a Poisson distribution. The Gaussian model uses the same variance as the Poisson model, and is a good approximation to the Poisson model except for very low photon count rates (Figure 2.11). For (2.30), the variance is estimated with a Taylor expansion about  $\bar{y}$  [36]:

$$-\log\left(\frac{x}{g}\right) \approx -\log\left(\frac{\bar{y}}{g}\right) - x \frac{1}{\bar{y}} \quad (2.31)$$

$$\text{var}\left(-\log\left(\frac{x}{g}\right)\right) \approx \frac{\text{var } x}{\bar{y}^2} = \frac{\bar{y}}{\bar{y}^2} = \frac{1}{\bar{y}}. \quad (2.32)$$

Likelihood based MBIR methods seek the most likely  $\boldsymbol{\mu}$  given the measured  $\mathbf{y}$  (or  $\hat{\ell}$  if operating in the post-log domain):

$$\hat{\boldsymbol{\mu}} = \arg \max_{\boldsymbol{\mu}} P(\boldsymbol{\mu}|\mathbf{y}) \quad (2.33)$$

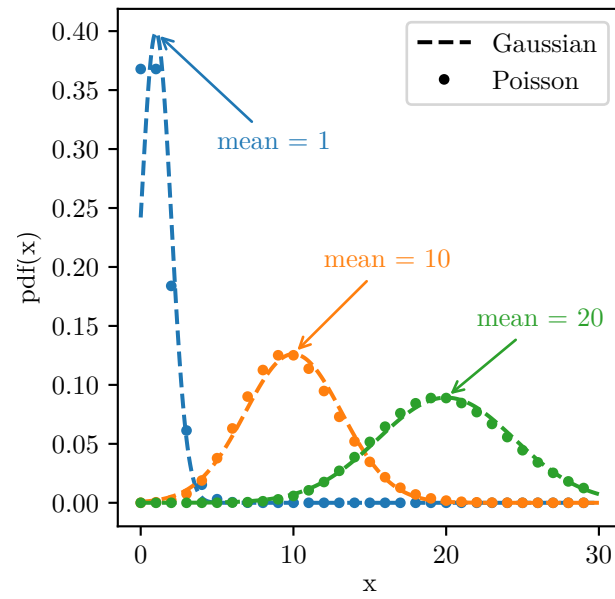


Figure 2.11: Gaussian and Poisson distributions with mean and variance equal to 1, 10, and 20.



where  $\hat{\boldsymbol{\mu}}$  is the reconstruction. Using Bayes theorem, this may be rewritten as

$$\hat{\boldsymbol{\mu}} = \arg \max_{\boldsymbol{\mu}} \frac{P(\mathbf{y}|\boldsymbol{\mu})P(\boldsymbol{\mu})}{P(\mathbf{y})}. \quad (2.34)$$

Because the log function increases monotonically, the log of the probability has the same optimum. Taking the negative log yields

$$\hat{\boldsymbol{\mu}} = \arg \min_{\boldsymbol{\mu}} \psi(\boldsymbol{\mu}) \quad (2.35)$$

$$\psi(\boldsymbol{\mu}) \triangleq -\log(P(\mathbf{y}|\boldsymbol{\mu})) - \log(P(\boldsymbol{\mu})) + \log(P(\mathbf{y})). \quad (2.36)$$

$\psi$  is the general negative log likelihood objective function, and has three terms. The first term is a fidelity term, and measures the likelihood of the measurements given a particular reconstruction. The second is the prior term, and is a measure of the likelihood of a given reconstruction independent of measurements. For example, a smoothness penalty is a means of saying that smooth reconstructions are more likely than non-smooth reconstructions. The last term is a constant (independent of  $\boldsymbol{\mu}$ ) and therefore doesn't effect the location of the optima.

The minimum of  $\psi$  is often referred to as the Maximum *A Posteriori* (MAP) estimator for  $\boldsymbol{\mu}$ . However, in practice the prior term is usually a form of roughness penalty, often implicitly assuming a Gibbs prior distribution [37, 38]. Samples of these distributions do not resemble medical images [39], suggesting the assumed distributions are not true priors of the data. Therefore, these estimators are typically referred to as Penalized-Likelihood (PL) estimators instead of MAP estimators.

CT objective functions are high-dimensional and may require complex optimization algorithms to minimize. These algorithms are often derived for specific classes

of objective functions. A major contribution of this work is the derivation of an optimization algorithm that is applicable to a large class of objective functions. This algorithm is derived in Chapter 3.

### 2.2.2.1 PL derivation example: post-log Gaussian model

In this section we derive the objective function for the post-log forward model with a Gaussian noise model (2.30). While this is the arguably the simplest model, it illustrates the process of deriving a MBIR algorithm.

The probability density function for  $\hat{\ell}$  is

$$P(\hat{\ell}|\boldsymbol{\mu}) = k \exp\left(-\frac{1}{2}(\boldsymbol{\ell} - \bar{\boldsymbol{\ell}})^T \mathbf{D}\{\bar{\mathbf{y}}\}(\boldsymbol{\ell} - \bar{\boldsymbol{\ell}})\right) \quad (2.37)$$

where  $k$  is a constant which normalizes the distribution. Substituting this into (2.36) and dropping constants yields the following penalized least-squares objective function

$$\psi(\boldsymbol{\mu}) = \frac{1}{2}(\hat{\boldsymbol{\ell}} - \mathbf{A}\boldsymbol{\mu})^T \mathbf{D}\{\bar{\mathbf{y}}\}(\hat{\boldsymbol{\ell}} - \mathbf{A}\boldsymbol{\mu}) + \beta \mathbf{R}(\boldsymbol{\mu}) \quad (2.38)$$

where the prior term has been replaced by the penalty function  $\mathbf{R}$  multiplied by constant  $\beta$ . This is equivalent to assuming a prior distribution given by

$$P(\boldsymbol{\mu}) \propto \exp(-\beta \mathbf{R}(\boldsymbol{\mu})). \quad (2.39)$$

These distributions often take the form of a Gibbs prior distribution which describes a Markov random field [37, 38, 40]. The simplest common penalty is a quadratic

penalty  $R_q$ :

$$R_q = \frac{1}{4} \sum_j \sum_{k \in \mathcal{N}_j} (\mu_k - \mu_j)^2 \quad (2.40)$$

where  $\mathcal{N}_j$  is the set of voxel indices in some neighborhood of  $j$ . This penalizes differences between neighboring pixels, enforcing smoothness. This may be rewritten in matrix form

$$R_q = \frac{1}{2} \boldsymbol{\mu}^T \mathbf{Q} \boldsymbol{\mu} \quad (2.41)$$

where

$$Q_{ij} = \begin{cases} \text{size}(\mathcal{N}_i) & \text{if } i = j \\ -1 & \text{if } j \in \mathcal{N}_i \\ 0 & \text{otherwise.} \end{cases} \quad (2.42)$$

When a quadratic penalty is used the solution may be rewritten as

$$\hat{\boldsymbol{\mu}} = \arg \min_{\boldsymbol{\mu}} \psi(\boldsymbol{\mu}) \quad (2.43)$$

where

$$\psi(\boldsymbol{\mu}) = \frac{1}{2} \tilde{\boldsymbol{\ell}}^T \mathbf{D}\{\bar{\mathbf{y}}\} \hat{\boldsymbol{\ell}} + \frac{1}{2} \boldsymbol{\mu}^T \mathbf{A}^T \mathbf{D}\{\bar{\mathbf{y}}\} \mathbf{A} \boldsymbol{\mu} - \boldsymbol{\mu}^T \mathbf{A}^T \mathbf{D}\{\bar{\mathbf{y}}\} \boldsymbol{\ell} + \frac{1}{2} \beta \boldsymbol{\mu}^T \mathbf{Q} \boldsymbol{\mu} \quad (2.44)$$

which may be simplified to

$$\hat{\boldsymbol{\mu}} = \arg \min_{\boldsymbol{\mu}} \frac{1}{2} \boldsymbol{\mu}^T [\mathbf{A}^T \mathbf{D}\{\bar{\mathbf{y}}\} \mathbf{A} + \beta \mathbf{Q}] \boldsymbol{\mu} - \boldsymbol{\mu}^T \mathbf{A}^T \mathbf{D}\{\bar{\mathbf{y}}\} \boldsymbol{\ell}. \quad (2.45)$$

Using the fact that the gradient of  $\psi$  equals zero at  $\hat{\boldsymbol{\mu}}$  yields

$$\nabla\psi = [\mathbf{A}^T \mathbf{D}\{\bar{\mathbf{y}}\} \mathbf{A} + \beta \mathbf{Q}] \hat{\boldsymbol{\mu}} - \mathbf{A}^T \mathbf{D}\{\bar{\mathbf{y}}\} \boldsymbol{\ell} = 0 \quad (2.46)$$

$$\hat{\boldsymbol{\mu}} = [\mathbf{A}^T \mathbf{D}\{\bar{\mathbf{y}}\} \mathbf{A} + \beta \mathbf{Q}]^{-1} \mathbf{A}^T \mathbf{D}\{\bar{\mathbf{y}}\} \hat{\boldsymbol{\ell}}. \quad (2.47)$$

The matrix inverse in (2.47) is generally too expensive to be calculated directly. Thus,  $\hat{\boldsymbol{\mu}}$  is usually estimated iteratively, for example with the Conjugate Gradient (CG) method in Hestenes and Stiefel [41].

### 2.2.3 Advanced modeling in MBIR: overview and prior work

Measurements on real systems may deviate from the presented forward models in a variety of ways (see §2.1). Discrepancies between the model assumptions and reality may lead to image degradation, such as blur or loss of quantitative accuracy. MBIR offers a natural way to mitigate this degradation by incorporating additional physical effects in the forward model. For example, including a scintillator blur in the forward model will enable the MBIR algorithm to invert/deblur the data as part of the reconstruction process.

Other techniques to improve image quality rely on either preprocessing or postprocessing steps (e.g., deblurring the projection data prior to FBP, or deblurring an FBP reconstruction). These methods require that the physical effect can be accurately modeling in either the measurement domain (preprocessing) or image domain (postprocessing). Complicated effects such as SV focal-spot blur can only be approximated in these domains, and accurate modeling requires a full MBIR approach. For example, depth dependent focal-spot blur depends on both the location within the

volume (not available in preprocessing) and the gantry angle (not available in post-processing). Additionally, such processing steps are often ill-conditioned and therefore require regularization, which may require more degrees of freedom (e.g., regularization strength). In contrast, the regularization in MBIR applies to both the reconstruction and any implicit processing (e.g. deblurring) simultaneously. This regularization also occurs within the domain of interest (the final image), which is often advantageous. Nevertheless, pre/postprocessing methods are often very effective, providing adequate image quality and fast computation time. Some preprocessing methods are formulated similarly to MBIR, estimating ideal line integrals using mean and noise models [42]. In this work these techniques are referred to as Model-Based Sinogram Restoration (MBSR). One can also model the effects of the preprocessing step itself, and incorporate these effects into a subsequent MBIR method. For example, the noise properties of various artifact correction techniques may be used to change the data weights in MBIR [36].

Advanced modeling in MBIR was first applied to nuclear imaging (e.g., SPECT, PET) [43–47]. Nuclear imaging modalities have a linear forward model, allowing much of the advanced modeling to be incorporated into the system matrix. In contrast, the exponential operation due to Beer’s Law in CT makes the forward model nonlinear, complicating blur modeling. While operating in the post-log domain linearizes CT reconstruction, much of the effects (e.g., scintillator blur) exist in the pre-log domain. The size of CT images and measurements are also much larger than those of nuclear imaging, making high-fidelity modeling and MBIR, in general, more computationally demanding. However, with the ever increasing power of computing hardware, high-fidelity modeling and MBIR have increasingly been applied to CT.

Most MBIR algorithms include a noise model and a penalty term. This leads to more efficient use of the measurement data as compared to FBP and therefore better image quality [48]. More advanced penalties/priors and forward models may be incorporated into MBIR to further improve image quality.

### 2.2.3.1 Fidelity term

The fidelity term has two components, the mean model and the noise model. The mean model may be modified to include blur and spectral effects, allowing the MBIR algorithm to deblur data or decompose materials during the reconstruction process. Changing the noise model effects the relative weights of different measurements in determining the final reconstruction.

The most common blur modeled in MBIR is pixel aperture blur, which is usually part of the projector derivation [49, 50]. In this case, the blur is applied as part of the system matrix, although it would be more accurate to model it outside the exponential. However, in general, this is a reasonable approximation [51], the exception being nonlinear partial volume effects [52] (i.e., when the projections contain sharp contrast within a pixel)<sup>3</sup>. Additional system blur may be modeled in the system matrix as well, e.g. by overestimating the size of the voxels [53]. MBIR methods have been developed to include measurement (pre-log) domain blur [54] such as scintillator blur, SV focal-spot blur [51, 55, 56], SV gantry motion blur [57], and spectral effects [58–65].

---

<sup>3</sup>While not a focus of this work, nonlinear partial volume effects may be modeled with the techniques presented here by oversampling the number of pixels and binning the results, similar to the gantry motion model in §6.3.1.1.

SV focal-spot blur and gantry motion blur are addressed in Chapter 6, and spectral effects are addressed in Chapter 7.

The noise model may also be modified to improve image quality. Most noise models either assume *independent* Poisson noise or *independent* Gaussian noise. A Poisson noise model assumes all of the noise is due to quantum noise, and ignores effects such as readout noise and noise due to the visible light conversion in the scintillator. A Gaussian noise model may easily accommodate many different types of noise, so long as they may all be approximated as Gaussian. This is less accurate at low photon counts, where the Poisson nature of quantum noise is more apparent. Ding et al. [66] have developed an MBIR method that uses a Poisson plus Gaussian noise model to capture both low dose quantum statistics and readout noise, and other modifications on the standard Poisson assumption exist to accurately model low photon counts and other effects [67]. Noise correlations may also be modeled, in which case the covariance matrix is non-diagonal. Noise correlations have been modeled in MBSR [68] and in tomosynthesis [69]. Correlated noise modeling is a major component of Chapters 4 and 5.

### 2.2.3.2 Prior/penalty term

Many common prior terms penalize roughness. These typically take the difference between neighboring pixels, apply a one-dimensional potential function, and sum the results. Mathematically,

$$R(\boldsymbol{\mu}) = \frac{1}{2} \sum_i \sum_{j \in \mathcal{N}_i} \phi(\boldsymbol{\mu}_i - \boldsymbol{\mu}_j). \quad (2.48)$$

For example, the penalty in §2.2.2.1 used  $\phi(t) = 0.5t^2$ . Another popular potential function is the absolute value function, resulting in a Total Variation (TV) penalty [70] which tends to enforce piece-wise constant images. Many researchers view CT reconstruction in terms of a compressed sensing problem, in which case the TV penalty encourages sparse solutions for the image gradient. The absolute value function is non-differentiable at zero, complicating optimization. A compromise is the Huber penalty [71], which is quadratic for arguments and linear for larger arguments

$$\phi(t; \delta) = \begin{cases} \frac{t^2}{2\delta} & \text{if } |t| \leq \delta \\ |t| - \frac{\delta}{2} \text{sign } t & \text{otherwise.} \end{cases} \quad (2.49)$$

Different potential functions are compared in Figure 2.12.

More advanced penalties may further improve image quality. Advanced penalties include dictionary based methods [72], roughness penalties with spatially varying  $\beta$  [73], and neural network derived auto encoders [74]. In many cases a prior scan of the patient may exist, such as in follow-up studies. In these scenarios, the previous scan may be used as prior information by penalizing the difference between the new reconstruction and the previous scan [75–77]. By incorporating this patient specific prior information, dose can be considerably reduced while maintaining image quality.



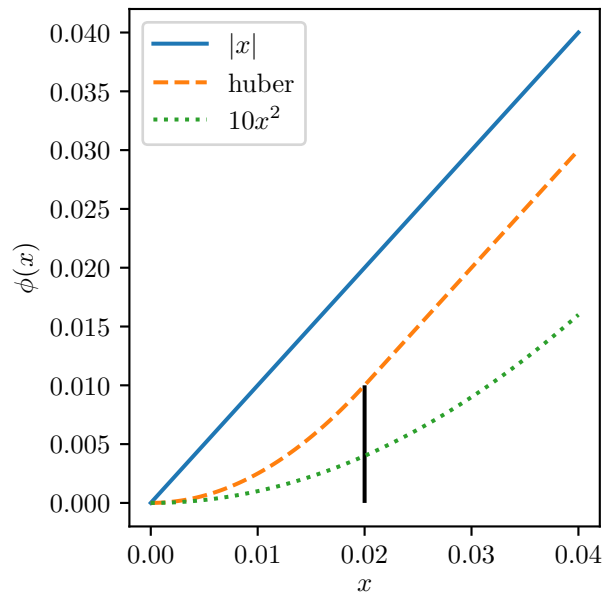


Figure 2.12: Comparison of different potential functions. The vertical line indicates the value of  $\delta$  for the Huber penalty. The quadratic penalty is scaled to ease comparison.

# Chapter 3

## A general model-based iterative reconstruction framework

This chapter contains work originally published in

Steven Tilley II, Jeffrey H. Siewerdsen, and J. Webster Stayman. “Model-Based Iterative Reconstruction for Flat-Panel Cone-Beam CT with Focal Spot Blur, Detector Blur, and Correlated Noise”. In: *Physics in Medicine and Biology* 61.1 (2016), p. 296. ISSN: 0031-9155. DOI: 10.1088/0031-9155/61/1/296. URL: <http://stacks.iop.org/0031-9155/61/i=1/a=296> (visited on 12/09/2015)

and

S. Tilley II et al. “Penalized-Likelihood Reconstruction with High-Fidelity Measurement Models for High-Resolution Cone-Beam Imaging”. In: *IEEE Transactions on Medical Imaging* 37.4 (Dec. 4, 2017), pp. 988–999. ISSN: 0278-0062. DOI: 10.1109/TMI.2017.2779406. URL: <https://ieeexplore.ieee.org/document/8125700/>.

Portions of this chapter are © 2017 IEEE. Reproduced here with permission.

This chapter derives the MBIR framework used in the rest of this work. A forward model and associated objective function is defined which is capable of modeling a wide range of physical effects. Two different reconstruction strategies are then derived, offering different tradeoffs between model assumptions, algorithm complexity, and reconstruction time.

### 3.1 Forward model and objective function

In this work we use the following forward model

$$\bar{\mathbf{y}} = \mathbf{B} \exp(-\mathbf{A}\boldsymbol{\mu}) \quad (3.1)$$

$$\mathbf{y} \sim \mathcal{N}(\bar{\mathbf{y}}, \mathbf{K}_Y). \quad (3.2)$$

This differs from a common Gaussian forward model (2.23, 2.24, 2.29) by replacing the gain term  $D\{\mathbf{g}\}$  with a general matrix  $\mathbf{B}$ , and permitting a general covariance matrix  $\mathbf{K}_Y$  instead of a diagonal matrix. As will be seen in later chapters, these changes permit modeling of many physical effects, including scintillator blur (with correlated noise), focal-spot blur, gantry motion blur, and multienergy acquisitions.

A Gaussian noise model was chosen over a Poisson noise model because it more naturally accommodates a non-diagonal covariance matrix. This is an acceptable approximation for all but highly photon starved measurements.

The negative log likelihood objective function for this forward model is

$$\psi(\boldsymbol{\mu}) = \frac{1}{2} [\mathbf{y} - \mathbf{B} \exp(-\mathbf{A}\boldsymbol{\mu})]^T \mathbf{W} [\mathbf{y} - \mathbf{B} \exp(-\mathbf{A}\boldsymbol{\mu})] + \beta R(\boldsymbol{\mu}) \quad (3.3)$$

where

$$\mathbf{W} \triangleq \mathbf{K}_Y^{-1}. \quad (3.4)$$

This objective function is nonconvex and nonlinear, making optimization particularly challenging. Additionally, it contains a matrix inversion in the objective function  $\mathbf{K}_Y^{-1}$ , which may potentially require a separate iterative solver.

## 3.2 Optimization strategies

Two optimization strategies are discussed. The first is a novel Separable Quadratic Surrogates (SQS) optimizer, and is used for most reconstructions in this dissertation. The second uses preprocessing to derive a linearized objective function while keeping track of noise correlations. This objective function may be minimized using standard linear solvers (e.g., the CG method [41]).

### 3.2.1 Separable quadratic surrogates optimizer

This section contains work originally published in

S. Tilley II et al. “Penalized-Likelihood Reconstruction with High-Fidelity Measurement Models for High-Resolution Cone-Beam Imaging”. In: *IEEE Transactions on Medical Imaging* 37.4 (Dec. 4, 2017), pp. 988–999. ISSN: 0278-0062. DOI: 10.1109/TMI.2017.2779406. URL: <https://ieeexplore.ieee.org/document/8125700/>.

Reproduced here with permission.

The objective function (3.3) is equivalent (within an additive constant) to

$$\psi_2 = \theta + \beta R(\boldsymbol{\mu}), \quad (3.5)$$

where

$$\theta \triangleq \frac{1}{2}[\mathbf{x}]^T \mathbf{B}^T \mathbf{K}_Y^{-1} \mathbf{B} \mathbf{x} - \mathbf{y}^T \mathbf{K}_Y^{-1} \mathbf{B} \mathbf{x}. \quad (3.6)$$

$$\mathbf{x} \triangleq \exp(-\mathbf{A}\boldsymbol{\mu}). \quad (3.7)$$

$$(3.8)$$

We derive an algorithm to optimize (3.5) in a manner similar to that of [80], i.e., minimizing a separable quadratic surrogate of the objective function at each iteration. Each surrogate matches the objective function in value and first derivative at an operating point, and otherwise majorizes the objective function. Surrogate functions are chosen such that their optima have closed form solutions, in contrast to the objective function which may be difficult to minimize. To minimize the objective function, we therefore minimize successive surrogate functions. Such an optimization approach is desirable since the separability of the surrogates permits a high degree of parallelization (e.g., facilitating implementation on high-performance Graphics Processing Units (GPUs)), while the surrogates framework can guarantee monotonicity. However, there is a classic trade-off between parallel algorithms, which require many fast iterations, and sequential algorithms, which require fewer slow iterations. A separable/parallel algorithm is well suited to GPU hardware. In [80], separable surrogate functions are found for the data fit term and the penalty term (in this work given by  $\theta$  and  $\beta R$ , respectively). The same formulation may be used for the penalty term

surrogate, but a new formulation for the data fit term surrogate is required. A series of surrogates are calculated for (3.6):  $Q$ ,  $Q_2$ , and  $Q_3$ .  $Q$  is a surrogate to  $\theta$  which is separable in an intermediate term,  $Q_2$  is a quadratic surrogate to  $Q$ , and  $Q_3$  is a surrogate to  $Q_2$  which is both separable in  $\boldsymbol{\mu}$  and quadratic, and can thus be easily minimized. Each surrogate function has the same function value and first derivative as  $\theta$  at the current iterate  $(\boldsymbol{\mu}^{(n)})$ . Therefore, minimizing the final surrogate at every iteration will monotonically decrease  $\theta$  [81]. Throughout this chapter, a lower case superscript in parenthesis denotes the current iteration. For example  $\boldsymbol{\mu}^{(n)}$  is the value of  $\boldsymbol{\mu}$  at iteration  $n$ .

To aid in deriving surrogates matched at the current iterate,  $\theta$  may be expressed as

$$\theta = \frac{1}{2}(\mathbf{x} - \mathbf{x}^{(n)})^T \mathbf{B}^T \mathbf{W} \mathbf{B} (\mathbf{x} - \mathbf{x}^{(n)}) + [\mathbf{x}^{(n)}]^T \mathbf{B}^T \mathbf{W} \mathbf{B} \mathbf{x} - \mathbf{y}^T \mathbf{W} \mathbf{B} \mathbf{x} - \frac{1}{2}[\mathbf{x}^{(n)}]^T \mathbf{B}^T \mathbf{W} \mathbf{B} \mathbf{x}^{(n)}. \quad (3.9)$$

A separable surrogate to  $\theta$  may be found by replacing the Hessian  $(\mathbf{B}^T \mathbf{W} \mathbf{B})$  with  $\mathbf{D}\{\boldsymbol{\eta}\}$  where

$$\boldsymbol{\eta} \triangleq \mathbf{B}^T \mathbf{W} \mathbf{B} \mathbf{1} \quad (3.10)$$

and  $\mathbf{1}$  is a vector of ones [80, 82, 83]. The quadratic surrogate may be expressed as

$$Q_X^{(n)}(\mathbf{x}) \triangleq \sum_i^{N_y} \left( \frac{1}{2} \mathbf{x}_i^2 \boldsymbol{\eta}_i + \boldsymbol{\rho}_i^{(n)} \mathbf{x}_i \right) + \xi^{(n)} \quad (3.11)$$

where

$$\boldsymbol{\rho}^{(n)} \triangleq \mathbf{B}^T \mathbf{W} \mathbf{B} \mathbf{x}^{(n)} - \mathbf{D}\{\boldsymbol{\eta}\} \mathbf{x}^{(n)} - \mathbf{B}^T \mathbf{W} \mathbf{y} \quad (3.12)$$

$$\xi^{(n)} \triangleq \frac{1}{2} \left[ [\mathbf{x}^{(n)}]^T \left( \mathbf{D}\{\boldsymbol{\eta}\} - \mathbf{B}^T \mathbf{W} \mathbf{B} \right) \mathbf{x}^{(n)} \right] \quad (3.13)$$

and  $N_y$  is the number of measurements. Note that  $\xi^{(n)}$  is a constant, which can be ignored for the purposes of optimization. Equation (3.11) is written using summation notation to highlight its separability. The first surrogate function,  $Q$ , is  $Q_X$  expressed as a function of the line integrals  $\boldsymbol{\ell}$ :

$$Q^{(n)}(\boldsymbol{\ell}) \triangleq Q_X^{(n)}(\exp(-\boldsymbol{\ell})) = \sum_i^{N_y} Q_i^{(n)} = \sum_i^{N_y} \frac{1}{2} \exp(-2\boldsymbol{\ell}_i) \boldsymbol{\eta}_i + \exp(-\boldsymbol{\ell}_i) \boldsymbol{\rho}_i^{(n)} + \xi^{(n)} \quad (3.14)$$

where

$$\boldsymbol{\ell} \triangleq \mathbf{A} \boldsymbol{\mu}. \quad (3.15)$$

$Q_i^{(n)}$  is analogous to the marginal negative log-likelihood functions in [81, Eq. 2].

A quadratic surrogate to  $Q_i^{(n)}$  is

$$Q_{2,i}^{(n)}(\boldsymbol{\ell}_i) = Q_i^{(n)}(\boldsymbol{\ell}_i^{(n)}) + (\boldsymbol{\ell}_i - \boldsymbol{\ell}_i^{(n)}) \frac{dQ^{(n)}}{d\boldsymbol{\ell}_i} \Big|_{\boldsymbol{\ell}_i^{(n)}} + \frac{1}{2} (\boldsymbol{\ell}_i - \boldsymbol{\ell}_i^{(n)})^2 \mathbf{c}_i^{(n)}. \quad (3.16)$$

The curvatures  $\mathbf{c}_i^{(n)}$  should be as small as possible while preserving the majorization property of the surrogate. A small curvature results in a wider surrogate function and therefore a larger step size and faster convergence. Erdoğan and Fessler [81] derived the optimum curvatures for a class of functions, taking advantage of the nonnegativity of  $\boldsymbol{\ell}$ . In §3.2.1.1 we show that (3.16) is one of these functions when  $\boldsymbol{\eta}$  is positive. Thus,

the optimal curvatures are [81, Eq. 28]

$$\mathbf{c}_i^{(n)} = \begin{cases} \left[ 2 \frac{Q_i^{(n)}(0) - Q_i^{(n)}(\ell_i^{(n)}) + \ell_i^{(n)} \frac{dQ_i^{(n)}}{d\ell_i}(\ell_i^{(n)})}{(\ell_i^{(n)})^2} \right]_+ & \ell_i^{(n)} > 0 \\ \left[ \frac{d^2 Q_i^{(n)}}{d\ell_i^2}(0) \right]_+ & \ell_i^{(n)} = 0 \end{cases} \quad (3.17)$$

where the  $[\cdot]_+$  operator returns the element-wise maximum of its argument and zero.

Finally, a surrogate to  $Q_2^{(n)}$  can be defined in a similar manner to  $Q_X^{(n)}$  (3.11) and as shown in [80]:

$$Q_2^{(n)}(\ell) = \sum_i^{N_y} Q_{2,i}^{(n)} \left( \sum_j^{N_\mu} \mathbf{A}_{ij} \mu_j \right) \leq Q_3(\mu) \quad (3.18)$$

where

$$Q_3^{(n)}(\mu) \triangleq \sum_i^{N_y} \sum_j^{N_\mu} \frac{\mathbf{A}_{ij}}{\gamma_i} Q_{2,i}^{(n)}(\gamma_i(\mu_j - \mu_j^{(n)})) + \sum_j^{N_\mu} \mathbf{A}_{ij} \mu_j^{(n)} \quad (3.19)$$

$$\gamma \triangleq \mathbf{A} \mathbf{1} \quad (3.20)$$

and  $N_\mu$  is the number of elements in  $\mu$ . This new function  $Q_3^{(n)}$  is quadratic, separable with respect to  $\mu$ , and matches  $\theta$  in function value and derivative for  $\mu = \mu^{(n)}$ .

After obtaining a separable surrogate  $\Phi$  for the penalty function  $R$  using [80] and [81], the combined surrogate of the full objective function (3.5) may be minimized.



Using the following definitions for compactness:

$$\mathbf{f}_j^{(n)} \triangleq \left. \frac{dQ_{3,j}^{(n)}}{d\boldsymbol{\mu}_j} \right|_{\boldsymbol{\mu}=\boldsymbol{\mu}^{(n)}} \quad (3.21)$$

$$\mathbf{h}_j^{(n)} \triangleq \left. \frac{d^2Q_{3,j}^{(n)}}{d\boldsymbol{\mu}_j^2} \right|_{\boldsymbol{\mu}=\boldsymbol{\mu}^{(n)}} \quad (3.22)$$

$$\mathbf{r}_j^{(n)} \triangleq \left. \frac{d\Phi_j^{(n)}}{d\boldsymbol{\mu}_j} \right|_{\boldsymbol{\mu}=\boldsymbol{\mu}^{(n)}} \quad (3.23)$$

$$\mathbf{s}_j^{(n)} \triangleq \left. \frac{d^2\Phi_j^{(n)}}{d\boldsymbol{\mu}_j^2} \right|_{\boldsymbol{\mu}=\boldsymbol{\mu}^{(n)}} \quad (3.24)$$

the minimization is given by

$$\arg \min_{\boldsymbol{\mu}_j \geq 0} Q_{3,j}^{(n)}(\boldsymbol{\mu}_j) + \beta \Phi_j^{(n)}(\boldsymbol{\mu}_j) = \left[ \boldsymbol{\mu}_j^{(n)} - \frac{\mathbf{f}_j^{(n)} + \beta \mathbf{r}_j^{(n)}}{\mathbf{h}_j^{(n)} + \beta \mathbf{s}_j^{(n)}} \right]_+ . \quad (3.25)$$

Note that  $\boldsymbol{\mu}$  is constrained to physically realistic nonnegative values by the  $[\cdot]_+$  operator. All derivatives are evaluated at  $\boldsymbol{\mu}_j = \boldsymbol{\mu}_j^{(n)}$ , yielding

$$\mathbf{f}_j^{(n)} = \sum_i^{N_y} \mathbf{A}_{ij} \left. \frac{dQ_{2,i}^{(n)}}{d\boldsymbol{\ell}_i} \right|_{\boldsymbol{\ell}_i=\boldsymbol{\ell}_i^{(n)}} \quad (3.26)$$

$$\mathbf{f} = \mathbf{A}^T \left( \mathbf{D}\{\boldsymbol{\eta}\} \exp(-2\mathbf{A}\boldsymbol{\mu}^{(n)}) - \mathbf{D}\{\boldsymbol{\rho}^{(n)}\} \exp(-\mathbf{A}\boldsymbol{\mu}^{(n)}) \right) \quad (3.27)$$

$$\mathbf{h}_j^{(n)} = \sum_i^{N_y} \mathbf{A}_{ij} \gamma_i \left. \frac{d^2Q_{2,i}^{(n)}}{d\boldsymbol{\ell}_i^2} \right|_{\boldsymbol{\ell}_i=\boldsymbol{\ell}_i^{(n)}} \quad (3.28)$$

$$\mathbf{h} = \mathbf{A}^T \mathbf{D}\{\boldsymbol{\gamma}\} \mathbf{c}^{(n)} \quad (3.29)$$

where  $\boldsymbol{\eta}$ ,  $\boldsymbol{\rho}$ ,  $\boldsymbol{\gamma}$ , and  $\mathbf{c}$  are given in (3.10), (3.12), (3.20), and (3.17), respectively.

Because  $Q_3^{(n)}$  is separable in  $\boldsymbol{\mu}$ , each  $\boldsymbol{\mu}_j$  can be updated simultaneously. This update step is the core iterative estimator shown in Algorithm 1. It can be shown

that the surrogate is jointly continuous in  $\boldsymbol{\mu}$  and  $\boldsymbol{\mu}^{(n)}$ . Therefore, if the sequence  $\{\boldsymbol{\mu}^{(n)}\}$  generated using this update step has a limit, that limit is a stationary point of the objective function (3.3) [84, Thm. 4.1].

### 3.2.1.1 Optimum curvature derivation

Erdoğan and Fessler [81] have shown that (3.17) is the optimum curvature for a function  $Q(\ell)$  (see Appendix of [81]) if:

1. (a)  $\ddot{Q} > 0$  when  $\ell \geq 0$ .  
 (b)  $\ddot{Q} < 0$  when  $\ell \geq 0$ .
2. OR  
 (a)  $Q \in \mathbb{C}^2$ .  
 (b)  $\dot{Q}(\ell^*)$  is a local maximum of  $\dot{Q}$ .  
 (c)  $\ell^*$  is the only critical point of  $\dot{Q}$ .  
 (d)  $\ddot{Q} < 0$  when  $\ell < \ell^*$ .  
 (e)  $\ddot{Q} > 0$  when  $\ell < \ell^*$ .

We use dot notation to indicate derivatives with respect to  $\ell$ .

In this section,  $Q$  refers to  $Q_i^{(n)}$  in (3.14). Without the subscripts and superscripts,

$$Q(\ell) = \frac{1}{2}\eta \exp(-2\ell) + \rho \exp(-\ell) + k. \quad (3.30)$$

**Algorithm 1** Algorithm to minimize (3.3), with ordered subsets and optional Nesterov acceleration (§3.2.1.2). The number of iterations is given by  $P$  and the number of ordered subsets by  $M$ . The combined iteration and subset index is given by a fractional value,  $n$ . For Nesterov acceleration, use *both* initialization columns and the *right* update column. Otherwise, use the *left* initialization column and the *left* update column. Element-wise multiplication is denoted by the  $\circ$  operator. The  $[\cdot]_+$  operator returns the (element-wise) maximum of its argument and 0.

Common Initialization	AND	Nesterov Initialization
Initialize $\boldsymbol{\mu}^{(0)}$ $\boldsymbol{\eta} \leftarrow \mathbf{B}^T \mathbf{W} \mathbf{B} \mathbf{1}$ $\boldsymbol{\gamma} \leftarrow \mathbf{A} \mathbf{1}$ Calculate $\mathbf{B}^T \mathbf{W} \mathbf{y}$		$\mathbf{z} \leftarrow \boldsymbol{\mu}^{(0)}, \quad \mathbf{w} \leftarrow \mathbf{0}$ $t^{(0)} \leftarrow 1, \quad t_{sum} \leftarrow t^{(0)}$
<hr/> for $p \leftarrow 0..P - 1$ do for $m \leftarrow 0..M - 1$ do $n \leftarrow p + m/M$ $\mathbf{l}^{(n)} \leftarrow \mathbf{A}_{(m)} \boldsymbol{\mu}^{(n)}$ $\mathbf{x}^{(n)} \leftarrow \exp(-\mathbf{l}^{(n)})$ $\boldsymbol{\rho}^{(n)} \leftarrow [\mathbf{B}^T \mathbf{W} \mathbf{B}]_{(m)} \mathbf{x}^{(n)} - [\mathbf{B}^T \mathbf{W} \mathbf{y}]_{(m)} - \boldsymbol{\eta}_{(m)} \circ \mathbf{x}^{(n)}$ $\mathbf{f}^{(n)} \leftarrow M \mathbf{A}_{(m)}^T [-\boldsymbol{\eta}_{(m)} \circ \mathbf{x}^{(n)} \circ \mathbf{x}^{(n)} - \boldsymbol{\rho}^{(n)} \circ \mathbf{x}^{(n)}]$ $\mathbf{c}_i^{(n)} = \begin{cases} \left[ 2 \frac{0.5\eta_i + \rho_i^{(n)} - 0.5\eta_i(x_i^{(n)})^2 - x_i^{(n)}\rho_i^{(n)} - \ell_i^{(n)}(\eta_i(x_i^{(n)})^2 + \rho_i^{(n)}x_i^{(n)})}{(\ell_i^{(n)})^2} \right]_+ & \ell_i^{(n)} > 0 \\ [2\eta_i + \rho_i^{(n)}]_+ & \ell_i^{(n)} = 0 \end{cases}$ $\mathbf{h}^{(n)} \leftarrow M \mathbf{A}_{(m)}^T (\boldsymbol{\gamma}_{(m)} \circ \mathbf{c}^{(n)})$ Calculate penalty surrogate gradient ( $\mathbf{r}^{(n)}$ ) and curvature ( $\mathbf{s}^{(n)}$ ) $\Delta \boldsymbol{\mu} \leftarrow \frac{\mathbf{f}^{(n)} + \mathbf{r}^{(n)}}{\mathbf{h}^{(n)} + \mathbf{s}^{(n)}}$		
Normal Update	OR	Nesterov Update
$\boldsymbol{\mu}^{(n+1/M)} \leftarrow [\boldsymbol{\mu}^{(n)} - \Delta \boldsymbol{\mu}]_+$		$t^{(n+1/M)} \leftarrow \frac{1}{2}(1 + \sqrt{1 + 4(t^{(n)})^2})$ $t_{sum} \leftarrow t_{sum} + t^{(n+1/M)}$ $\mathbf{z} \leftarrow [\boldsymbol{\mu}^{(n)} - \Delta \boldsymbol{\mu}]_+$ $\mathbf{w} \leftarrow \mathbf{w} + t^{(n)} \Delta \boldsymbol{\mu}$ $\mathbf{v} \leftarrow [\boldsymbol{\mu}^{(0)} - \mathbf{w}]_+$ $\boldsymbol{\mu}^{(n+1/M)} \leftarrow \mathbf{z} + t^{(n+1/M)} t_{sum}^{-1} (\mathbf{v} - \mathbf{z})$

The first, second, and third derivatives are given by

$$\dot{Q} = -\eta \exp(-2\ell) - \rho \exp(-\ell) \quad (3.31)$$

$$\ddot{Q} = 2\eta \exp(-2\ell) + \rho \exp(-\ell) \quad (3.32)$$

$$\dddot{Q} = -4\eta \exp(-2\ell) - \rho \exp(-\ell). \quad (3.33)$$

If either  $\eta$  or  $\rho$  is zero, or both  $\eta$  and  $\rho$  are positive, 1 is true.

We will show that if  $\rho$  is negative and  $\eta$  is positive, 2 is true. By definition, 2a is true.  $\ddot{Q}(\ell)$  is 0 only when

$$\ell = \ell^* \triangleq -\log\left(\frac{-\rho}{2\eta}\right), \quad (3.34)$$

satisfying 2c.

$$\ddot{Q}(\ell^*) = \frac{-\rho^2}{2\eta} < 0, \quad (3.35)$$

implying  $\dot{Q}(\ell^*)$  is a maximum, and therefore 2b.  $\ddot{Q}$  only has one root at  $\ell = -\log(-\rho/4\eta)$ , which is greater than  $\ell^*$ . This combined with the fact that  $\ddot{Q}(\ell^*) < 0$  implies 2d. Finally, because  $\ell^*$  is the only root of  $\ddot{Q}$  and  $\ddot{Q}(\ell^*) < 0$ , 2e is satisfied.

### 3.2.1.2 Ordered subsets and Nesterov acceleration

Additional modifications to the underlying update in (3.25) are also shown in Algorithm 1. Specifically, the algorithm uses the ordered-subsets approach [80] to accelerate estimation. With ordered subsets, the gradient and curvature of the fidelity term are calculated using only a subset of the projection angles (e.g., every 10<sup>th</sup> projection angle). This is repeated for each set of projection angles until every angle is used. The ordered-subsets approach takes advantage of the fact that subsequent

projections contain similar information. Using  $M$  ordered subsets (where each subset uses every  $M^{\text{th}}$  projection angle) decreases computation time by about a factor of  $M$ . The variable  $m$  in Algorithm 1 denotes the subset index and subscripts in parentheses indicate that the argument is modified for the corresponding subset (e.g.  $\mathbf{A}_{(m)}\boldsymbol{\mu}$  is a forward projection of  $\boldsymbol{\mu}$  using only the projection angles in the  $m^{\text{th}}$  subset). While  $p$  indexes the outer loop of iterations using all of the data, the current iterate  $n$  is permitted to take on fractional values indicating progress through the inner loop of ordered-subsets updates.

Algorithm 1 also includes a second column of calculations to optionally apply Nesterov acceleration [83, 85] to further improve the rate of convergence. Nesterov acceleration is a momentum based acceleration approach, where a weighted average of previously calculated updates is used to modify the current update.

Note that using ordered subsets or acceleration results in an algorithm that might not converge. Ordered-subsets may result in a limit cycle, and acceleration is only guaranteed to preserve convergence when the objective function is convex. Combining ordered-subsets and acceleration can also result in instability. However, in practice the number of subsets can be chosen such that updates are well-behaved. Additionally, ordered subsets and acceleration can be used to get close to the solution, followed by several iterations without subsets or acceleration. The sequence of iterates in [83] with the desired convergence properties corresponds to  $\mathbf{z}^{(n)}$  in Algorithm 1. However, Algorithm 1 only returns  $\boldsymbol{\mu}^{(n)}$  at each iteration, which simplifies implementation.

### 3.2.1.3 Useful approximations

Algorithm 1 requires one application of  $\mathbf{B}^T \mathbf{W} \mathbf{B}$  each iteration. In cases where noise correlation is modeled, calculating  $\mathbf{W}$  (i.e.,  $\mathbf{K}_Y^{-1}$ ) is nontrivial, and may require an iterative method. However, physical effects in tomography often fit the following model:

$$\mathbf{B} \triangleq \mathbf{B}_c \mathbf{B}_n \mathbf{D}\{\mathbf{g}\} \quad (3.36)$$

$$\mathbf{K}_Y \triangleq \mathbf{B}_c \mathbf{D}\{\mathbf{q}\} \mathbf{B}_c^T + \mathbf{K}_{ro} \quad (3.37)$$

where  $\mathbf{B}_c$  is a correlating blur,  $\mathbf{B}_n$  is a non-correlating blur,  $\mathbf{g}$  is a vector of gain terms,  $\mathbf{q}$  is a vector of quantum noise (pre-correlating blur) variance, and  $\mathbf{K}_{ro}$  is the readout noise covariance matrix. The physical justification for this model will be discussed in chapter 4. When readout noise is much less than quantum noise

$$\mathbf{K}_Y \approx \mathbf{B}_c \mathbf{D}\{\mathbf{q}\} \mathbf{B}_c^T \quad (3.38)$$

$$\mathbf{K}_Y^{-1} \approx [\mathbf{B}_c^T]^{-1} \mathbf{D}\{\mathbf{q}^{-1}\} \mathbf{B}_c^{-1} \quad (3.39)$$

$$\mathbf{B}^T \mathbf{W} \mathbf{B} \approx \mathbf{D}\{\mathbf{g}\} \mathbf{B}_n^T \mathbf{B}_c^T [\mathbf{B}_c^T]^{-1} \mathbf{D}\{\mathbf{q}^{-1}\} \mathbf{B}_c^{-1} \mathbf{B}_c \mathbf{B}_n \mathbf{D}\{\mathbf{g}\} \quad (3.40)$$

$$\mathbf{B}^T \mathbf{W} \mathbf{B} \approx \mathbf{D}\{\mathbf{g}\} \mathbf{B}_n^T \mathbf{D}\{\mathbf{q}^{-1}\} \mathbf{B}_n \mathbf{D}\{\mathbf{g}\}. \quad (3.41)$$

Thus, the only inversion in this approximation is a diagonal matrix, which may be computed explicitly. In the case where  $\mathbf{K}_{ro}$  is not negligible, but is diagonal, the readout noise improves the condition number of  $\mathbf{K}_Y$  and allows the inversion to be solved with relatively few iterations.

### 3.2.2 Staged linearized optimizer

This section derives a staged, linearized optimizer for a simplified forward model. Specifically

$$\bar{\mathbf{y}} = \mathbf{B}_c \mathbf{B}_n \mathbf{D}\{\mathbf{g}\} \exp(-\mathbf{A}\boldsymbol{\mu}) \quad (3.42)$$

$$\mathbf{y} \sim \mathcal{N}(\bar{\mathbf{y}}, \mathbf{K}_Y) \quad (3.43)$$

$$\mathbf{K}_Y = \mathbf{B}_c \mathbf{D}\{\mathbf{B}_n \mathbf{D}\{\mathbf{g}\} \exp(-\mathbf{A}\boldsymbol{\mu})\} \mathbf{B}_c^T + \mathbf{D}\{\boldsymbol{\sigma}^2\}. \quad (3.44)$$

Where  $\mathbf{B}_c$  is a correlating blur,  $\mathbf{B}_n$  is a non-correlating blur,  $\mathbf{g}$  is a vector of measurement gains, and  $\boldsymbol{\sigma}$  is a vector of readout noise standard deviations for each measurement (the square in (3.44) is applied element-wise). For convenience, the total blur is defined as

$$\mathbf{B}_t \triangleq \mathbf{B}_c \mathbf{B}_n. \quad (3.45)$$

The overall strategy is to define an estimate for the line integrals ( $\boldsymbol{\ell} = \mathbf{A}\boldsymbol{\mu}$ ), and track the resulting noise properties of that estimate for input into a subsequent linear reconstruction. The estimate and covariance matrix are then used to derive a linear least squares objective function with a non-diagonal weighting matrix.

The line integrals may be estimated as

$$\hat{\boldsymbol{\ell}} = \log \left( \mathbf{D}\{\mathbf{g}^{-1}\} \mathbf{C}' \mathbf{y} \right) \quad (3.46)$$

where we introduce a general data deblurring operation,  $\mathbf{C}' \approx \mathbf{B}_t^{-1}$ . We note that an exact inversion of  $\mathbf{B}_t$  may not be desirable or even possible depending on the form of

the total system blur. This will be discussed in greater detail below. Naturally, the transformation in (3.46) changes the covariance structure. One can show that the covariance for the line integrals may be approximated as:

$$\mathbf{K}_L \approx \mathbf{D}\left\{\frac{1}{\mathbf{C}'\bar{\mathbf{y}}}\right\}\mathbf{C}'\mathbf{K}_Y[\mathbf{C}']^T\mathbf{D}\left\{\frac{1}{\mathbf{C}'\bar{\mathbf{y}}}\right\}. \quad (3.47)$$

This approximate form is derived using a Taylor approximation and is described in detail in §3.2.2.1. It is this expression that we will use for noise modeling in a statistical reconstruction method.

One must take care in choosing the exact form for the deblur operator  $\mathbf{C}'$ . If  $\mathbf{B}_t$  is not full rank, then there is a null space that cannot be recovered. Similarly, if  $\mathbf{B}_t$  is highly ill-conditioned with near zero singular values, extreme noise amplification and sensitivity to finite precision computing may occur. To avoid these scenarios, we introduce a modified deblur operator below that avoids these undesirable features.

For this algorithm, we assume the system blur is shift-invariant, which allows blurring and deblurring operations to be performed using Fourier methods. In this case, zero or near zero singular values associated with null-spaces and ill-conditioning can be identified at specific spatial frequencies in the transfer function, since Fourier operators diagonalize the circulant system blur operator,  $\mathbf{B}_t$ . Thus, one simple solution is to mask the nulled or near null frequencies. If  $\mathbf{b}$  is the unmodified Fourier transfer function such that

$$\mathbf{F}^*\mathbf{D}\{\mathbf{b}\}\mathbf{F} = \mathbf{B}_t \quad (3.48)$$



where  $\mathbf{F}$  is the discrete Fourier transform, then we may apply a modified deblur operator with threshold parameter  $\epsilon$  as

$$\mathbf{C}' \triangleq \mathbf{F}^* \mathbf{D}\{\mathbf{b}^-\} \mathbf{F} \quad (3.49)$$

where

$$\mathbf{b}_i^- \triangleq \begin{cases} 0 & \text{if } \left| \frac{\mathbf{b}_i}{\mathbf{b}_0} \right| < \epsilon \\ \frac{1}{\mathbf{b}_i} & \text{otherwise.} \end{cases} \quad (3.50)$$

where  $\mathbf{b}_i$  are individual frequency components of the blur, and  $\mathbf{b}_0$  is the zero frequency component (unity for an energy preserving blur). Similarly, we may define an approximate inverse to this thresholded deblur operation as

$$[\mathbf{C}']^{-1} \triangleq \mathbf{C} \triangleq \mathbf{F}^* \mathbf{D}\{\mathbf{b}^+\} \mathbf{F} \quad (3.51)$$

where

$$\mathbf{b}_i^+ \triangleq \begin{cases} 0 & \text{if } \left| \frac{\mathbf{b}_i}{\mathbf{b}_0} \right| < \epsilon \\ \mathbf{b}_i & \text{otherwise.} \end{cases} \quad (3.52)$$

The masked deblur and blur transfer functions are illustrated in Figure 3.1. A representation of (3.51) is shown in Figure 3.1(a), which is a blur transfer function with the high frequencies masked out, as indicated by the gray hatched area. A representation of (3.49) is shown in figure Figure 3.1(b), which is an inversion of (3.51) within the unmasked region, and zero otherwise.

The diagonal terms in (3.47) can easily be inverted by inverting each element on the diagonal. This fact and (3.51) give expressions for the inverse of each term in

(3.47) except  $\mathbf{K}_Y$ . The inverse of (3.47) can therefore be written as:

$$\mathbf{K}_L^{-1} \approx \mathbf{D}\{\mathbf{C}'\bar{\mathbf{y}}\}\mathbf{C}^T\mathbf{K}_Y^{-1}\mathbf{C}\mathbf{D}\{\mathbf{C}'\bar{\mathbf{y}}\}. \quad (3.53)$$

$\mathbf{K}_Y$  is approximated as:

$$\mathbf{K}_Y \approx \mathbf{C}_c\mathbf{D}\{\mathbf{C}'\mathbf{y}\}\mathbf{C}_c^T + \mathbf{D}\{\boldsymbol{\sigma}^2\} \quad (3.54)$$

where  $\mathbf{C}_c$  is a thresholded correlating blur. This thresholded blur is defined in (3.51), using  $\mathbf{B}_d$  instead of  $\mathbf{B}_t$ . The term  $\mathbf{D}\{\mathbf{B}_n\mathbf{D}\{\mathbf{g}\}\exp(-\mathbf{A}\boldsymbol{\mu})\}$  from equation 3.44 requires unavailable mean pre-detection data, and is estimated by the deblurred measurement data.

With the previously described processing in (3.46) which linearizes the system model, and the presumption of Gaussian distributed noise with zero mean and known covariance, we may form an objective function. Under these assumptions the implicitly defined objective is a generalized least-squares fit with a weighting by the inverse of the covariance matrix. Specifically, we may write

$$\hat{\boldsymbol{\mu}} = \arg \min_{\boldsymbol{\mu}} \frac{1}{2} [\boldsymbol{\ell} - \mathbf{A}\boldsymbol{\mu}]^T \mathbf{K}_L^{-1} [\boldsymbol{\ell} - \mathbf{A}\boldsymbol{\mu}] + \beta \mathbf{R}(\boldsymbol{\mu}). \quad (3.55)$$

As discussed in §2.2.2.1, when a quadratic penalty is used the solution is

$$\hat{\boldsymbol{\mu}} = [\mathbf{A}^T\mathbf{K}_L^{-1}\mathbf{A} + \beta\mathbf{Q}]^{-1}\mathbf{A}^T\mathbf{K}_L^{-1}\hat{\boldsymbol{\ell}}. \quad (3.56)$$

where  $\mathbf{Q}$  is defined in (2.42).

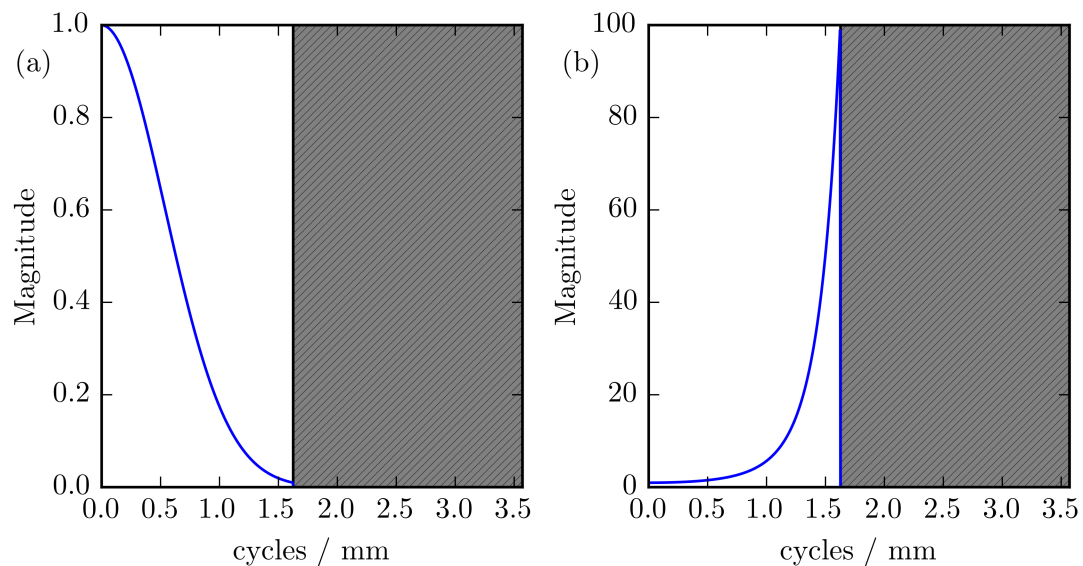


Figure 3.1: Representation of deblur masking. The original blur (a) tends towards zero at higher frequencies. To account for this, those frequencies are masked. Subfigure (a) shows  $\mathbf{b}^+$  from equation (3.51) and (b) shows  $\mathbf{b}^-$  from equation (3.49).

Sauer and Bouman [86] derived this general form (with a diagonal weighting matrix) using a second order Taylor series approximation to a fidelity term based on a Poisson noise model and a Gaussian Markov random field prior. Fessler [87] modified the derivation to include scatter, and used a more general penalty term.

Beside the additional deblurring step in (3.46), the key difference between equation (3.56) and the work of Sauer, Bouman, and Fessler, is the use of a non-diagonal weighting matrix—the inverse of  $\mathbf{K}_L$ —which may not necessarily exist. For the formulation used above, the masked frequencies in  $\mathbf{C}$  result in a degenerate  $\mathbf{K}_L$  which cannot be inverted (i.e. information at certain frequencies cannot be recovered). If we replace the inverse in (3.55) with a generalized inverse, the unregularized solution to (3.55) is the maximum-likelihood solution in the span of  $\mathbf{K}_L$ . For line integral frequencies in the null space, the fidelity term evaluates to zero and the reconstruction relies only on the penalty function. For this algorithm, we will use inverse notation to mean generalized inverse where appropriate. See Rao [88] for a detailed explanation of Gaussian density functions with degenerate covariance matrices.

Equation (3.56) can be logically separated into two sections (see Algorithm 2). The preprocessing section requires estimating the line integrals, applying the inverse covariance matrix, and backprojecting (applying  $\mathbf{A}^T$ ) the result. The application of the inverse covariance matrix is performed in steps in accordance with (3.53). The iterative section involves two iterative optimization algorithms, the “outer” system algorithm, which solves for  $\hat{\boldsymbol{\mu}}$ , and the “inner” inversion of  $\mathbf{K}_Y$  within  $\mathbf{K}_L^{-1}$ . The inversions of  $\mathbf{K}_Y$  and  $(\mathbf{A}^T \mathbf{K}_L^{-1} \mathbf{A} + \beta \mathbf{Q})$  can be performed using a variety of solvers, such as LSQR( $\mathbf{A}^{-1}$ ) [89], a momentum based approach [83, 85], or the CG method [41].

---

**Algorithm 2** Overview and pseudocode for the proposed linearized algorithm.

---

```

 $\mathbf{y}_{db} \leftarrow \mathbf{C}'\mathbf{y}$  ▷ Start of preprocessing section
 $\hat{\ell} \leftarrow -\log(\mathbf{D}\{\mathbf{g}^{-1}\}\mathbf{y}_{db})$ 
 $\mathbf{z} \leftarrow \text{APPLY\_INV\_COV}(\hat{\ell})$ 
 $\mathbf{b} \leftarrow \mathbf{A}^T\mathbf{z}$ 
 $\hat{\mu} \leftarrow \text{APPLY\_INV}(\mathbf{b})$  ▷ Iterative section
function  $\text{APPLY\_INV\_COV}(\hat{\ell})$ 
   $\mathbf{p} \leftarrow \mathbf{C}^T\mathbf{D}\{\mathbf{y}_{db}\}\hat{\ell}$ 
  Solve  $\mathbf{K}_Y\mathbf{a} = \mathbf{p}$  for  $\mathbf{a}$  ▷ Inner loop
  return  $\mathbf{D}\{\mathbf{y}_{db}\}\mathbf{C}\mathbf{a}$ 
function  $\text{APPLY\_INV}(\mathbf{b})$ 
  Solve  $[\mathbf{A}^T\mathbf{K}_L^{-1}\mathbf{A} + \beta\mathbf{Q}]\hat{\mu} = \mathbf{b}$  for  $\hat{\mu}$  ▷ Outer loop

```

---

### 3.2.2.1 Line integral covariance matrix derivation

We show how the preprocessing steps transform the covariance matrix of the data. We start with the mean ( $\bar{\mathbf{y}}$ ) and covariance ( $\mathbf{K}_Y$ ) of the measurement data. The deblurring and normalization steps are represented by the linear operators  $\mathbf{C}'$  and  $\mathbf{D}\{\mathbf{g}^{-1}\}$ , respectively, resulting in deblurred normalized data ( $\mathbf{y}_{dbn}$ ) with mean and covariance given in (3.57) and (3.58) respectively.

$$\bar{\mathbf{y}}_{dbn} = \mathbf{D}\{\mathbf{g}^{-1}\}\mathbf{C}'\bar{\mathbf{y}} \quad (3.57)$$

$$\mathbf{K}_{Y_{dbn}} = \mathbf{D}\{\mathbf{g}^{-1}\}\mathbf{C}'\mathbf{K}_Y[\mathbf{C}']^T\mathbf{D}\{\mathbf{g}^{-1}\} \quad (3.58)$$

To calculate the effects of the log transform on the covariance matrix, we estimate  $\log(x)$  as a linear function using a Taylor series expansion about  $x_0$ .

$$\log(x) \approx \log(x_0) + \frac{x - x_0}{x_0} \quad (3.59)$$

For each element of  $\mathbf{y}_{dbn}$  we expand about its current value. For some input  $\mathbf{a}$

$$\log(\mathbf{a}_i) \approx \log(\mathbf{y}_{dbn,i}) + \frac{\mathbf{a}_i - \mathbf{y}_{dbn,i}}{\mathbf{y}_{dbn,i}} \quad (3.60)$$

$$\log(\mathbf{a}) \approx \log(\mathbf{y}_{dbn}) + \mathbf{D}\{\mathbf{y}_{dbn}^{-1}\}\mathbf{a} - 1. \quad (3.61)$$

Addition of constants does not affect the covariance matrix, so the alterations to the covariance simply involve two multiplications by the diagonal matrix in the middle term in (3.61). The covariance of the line integral estimates is therefore

$$\mathbf{K}_L = \mathbf{D}\{\mathbf{y}_{dbn}^{-1}\} \mathbf{D}\{\mathbf{g}^{-1}\} \mathbf{C}' \mathbf{K}_Y [\mathbf{C}']^T \mathbf{D}\{\mathbf{g}^{-1}\} \mathbf{D}\{\mathbf{y}_{dbn}^{-1}\}. \quad (3.62)$$

Because

$$\mathbf{D}\{\mathbf{y}_{dbn}^{-1}\} = \mathbf{D}\{\mathbf{g}\} \mathbf{D}\left\{\frac{1}{\mathbf{C}'\mathbf{y}}\right\} \quad (3.63)$$

equation 3.62 can be reduced to

$$\mathbf{K}_L = \mathbf{D}\left\{\frac{1}{\mathbf{C}'\mathbf{y}}\right\} \mathbf{C}' \mathbf{K}_Y [\mathbf{C}']^T \mathbf{D}\left\{\frac{1}{\mathbf{C}'\mathbf{y}}\right\}. \quad (3.64)$$

### 3.3 Accommodation of an isotropic Huber penalty

An isotropic Huber penalty is used in some studies in this work. Erdoğan and Fessler [80, 81] present a general strategy for obtaining surrogates to penalties with the form of (2.48). However, the isotropic Huber penalty does not fit this form. The isotropic penalty does not prefer gradients with particular orientations. In contrast, the Huber penalty using the form of (2.48) and the eight nearest voxel neighborhood tends to

prefer gradients oriented with the voxel grid. This chapter derives the surrogates, gradient, and curvature approximations for the isotropic Huber penalty.

We define the penalty as

$$R(\boldsymbol{\mu}) = R_1(\boldsymbol{\mu}) + R_2(\boldsymbol{\mu}) \quad (3.65)$$

$$R_1(\boldsymbol{\mu}) = \sum_i \phi(\mathbf{g}_i(\boldsymbol{\mu})) \quad (3.66)$$

$$R_2(\boldsymbol{\mu}) = \sum_i \phi(\mathbf{g}_i^*(\boldsymbol{\mu})) \quad (3.67)$$

$$(3.68)$$

where  $\mathbf{g}_i$  and  $\mathbf{g}_i^*$  are different calculations of the gradient of  $\boldsymbol{\mu}$  at index  $i$  and  $\phi$  is the Huber function (2.49). Specifically,

$$\mathbf{g}_i(\boldsymbol{\mu}) = \sqrt{(\boldsymbol{\mu}_i - \boldsymbol{\mu}_{i-s_x})^2 + (\boldsymbol{\mu}_i - \boldsymbol{\mu}_{i-s_y})^2 + (\boldsymbol{\mu}_i - \boldsymbol{\mu}_{i-s_z})^2} \quad (3.69)$$

$$\mathbf{g}_i^*(\boldsymbol{\mu}) = \sqrt{(\boldsymbol{\mu}_i - \boldsymbol{\mu}_{i+s_x})^2 + (\boldsymbol{\mu}_i - \boldsymbol{\mu}_{i+s_y})^2 + (\boldsymbol{\mu}_i - \boldsymbol{\mu}_{i+s_z})^2} \quad (3.70)$$

$$(3.71)$$

where  $s_x$ ,  $s_y$ , and  $s_z$  are the offsets to move one element in that direction. If using the indexing scheme in (2.25), the values of  $s_x$ ,  $s_y$ , and  $s_z$  are 1,  $N_x$ , and  $N_x N_y$ , respectively, where  $N_x$  is the number of elements in the  $x$  direction, etc. By defining  $N_i$  as the set  $\{i - s_x, i - s_y, i - s_z\}$  and  $N_i^* = \{i + s_x, i + s_y, i + s_z\}$ ,  $\mathbf{g}_i$  and  $\mathbf{g}_i^*$  can be

written as

$$\mathbf{g}_i(\boldsymbol{\mu}) = \sqrt{\sum_{j \in N_i} (\boldsymbol{\mu}_i - \boldsymbol{\mu}_j)^2} \quad (3.72)$$

$$\mathbf{g}_i^*(\boldsymbol{\mu}) = \sqrt{\sum_{j \in N_i^*} (\boldsymbol{\mu}_i - \boldsymbol{\mu}_j)^2}. \quad (3.73)$$

If any element of  $N_i$  or  $N_i^*$  is not in the image (i.e.,  $i$  is a boundary point), that element is dropped from the set.

We seek a surrogate function for  $R$  that is greater than or equal to  $R$  everywhere and matches  $R$  in value and derivative at a point  $\hat{t}$ . We derive this specifically for  $R_1$ , as the derivation for  $R_2$  is similar.

From Erdoğan and Fessler [81] we define this function as

$$\hat{\phi}(t; \hat{t}) = \phi(\hat{t}) + \dot{\phi}(\hat{t})(t - \hat{t}) + \dot{\phi}(\hat{t}) \frac{(t - \hat{t})^2}{2\hat{t}} \quad (3.74)$$

which can be simplified to

$$\hat{\phi}(t) = \dot{\phi}(\hat{t}) \frac{t^2}{2\hat{t}} + k \quad (3.75)$$

$$k = \phi(\hat{t}) - \dot{\phi}(\hat{t}) \left( \frac{3\hat{t}}{2} \right). \quad (3.76)$$

We therefore define a surrogate penalty function at point  $\boldsymbol{\mu}^{(n)}$  as

$$Q^{(n)}(\boldsymbol{\mu}) = \sum_i \hat{\phi}(\mathbf{g}_i(\boldsymbol{\mu}); \boldsymbol{\mu}^{(n)}) = \sum_i \alpha_i^{(n)} \mathbf{g}_i(\boldsymbol{\mu})^2 + k \geq R_1(\boldsymbol{\mu}) \quad (3.77)$$

$$\alpha_i^{(n)} = \frac{1}{2} \frac{\dot{\phi}(\mathbf{g}_i(\boldsymbol{\mu}^{(n)}))}{\mathbf{g}_i(\boldsymbol{\mu}^{(n)})}. \quad (3.78)$$



Substituting  $\mathbf{g}$  yields

$$Q^{(n)}(\boldsymbol{\mu}) = \sum_i \sum_{j \in N_i} \alpha_i^{(n)} (\boldsymbol{\mu}_i - \boldsymbol{\mu}_j)^2 + k. \quad (3.79)$$

From this point we drop  $k$  because it does not effect the derivative of the result.

Using the technique in Lange and Fessler [90, Eq. 12]

$$Q_2^{(n)}(\boldsymbol{\mu}) = \sum_i \left[ \sum_{j \in N_i} \frac{\alpha_i^{(n)}}{2} (2\boldsymbol{\mu}_i - \boldsymbol{\mu}_j^{(n)} - \boldsymbol{\mu}_i^{(n)})^2 + \sum_{j \in N_i} \frac{\alpha_i^{(n)}}{2} (2\boldsymbol{\mu}_j - \boldsymbol{\mu}_j^{(n)} - \boldsymbol{\mu}_i^{(n)})^2 \right] \geq Q(\boldsymbol{\mu}). \quad (3.80)$$

$$Q_2^{(n)}(\boldsymbol{\mu}) = \sum_i \left[ \sum_{j \in N_i} \frac{\alpha_i^{(n)}}{2} (2\boldsymbol{\mu}_i - \boldsymbol{\mu}_j^{(n)} - \boldsymbol{\mu}_i^{(n)})^2 + \sum_{j \in N_i^*} \frac{\alpha_j^{(n)}}{2} (2\boldsymbol{\mu}_i - \boldsymbol{\mu}_j^{(n)} - \boldsymbol{\mu}_i^{(n)})^2 \right] \geq Q(\boldsymbol{\mu}). \quad (3.81)$$

Repeating the above process for  $R_2$  and adding the surrogates together yields

$$T^{(n)}(\boldsymbol{\mu}) = \sum_i \left[ \sum_{j \in N_i} \left[ \frac{\alpha_i^{(n)}}{2} (2\boldsymbol{\mu}_i - \boldsymbol{\mu}_j^{(n)} - \boldsymbol{\mu}_i^{(n)})^2 + \frac{\gamma_j^{(n)}}{2} (2\boldsymbol{\mu}_i - \boldsymbol{\mu}_j^{(n)} - \boldsymbol{\mu}_i^{(n)})^2 \right] + \sum_{j \in N_i^*} \left[ \frac{\alpha_j^{(n)}}{2} (2\boldsymbol{\mu}_i - \boldsymbol{\mu}_j^{(n)} - \boldsymbol{\mu}_i^{(n)})^2 + \frac{\gamma_i^{(n)}}{2} (2\boldsymbol{\mu}_i - \boldsymbol{\mu}_j^{(n)} - \boldsymbol{\mu}_i^{(n)})^2 \right] \right] \quad (3.82)$$

where

$$\gamma_i^{(n)} = \frac{1}{2} \frac{\dot{\phi}(\mathbf{g}_i^*(\boldsymbol{\mu}^{(n)}))}{\mathbf{g}_i^*(\boldsymbol{\mu}^{(n)})}. \quad (3.83)$$

The first and second derivatives at  $\boldsymbol{\mu}^{(n)}$  needed for optimization are

$$\begin{aligned} \dot{T}^{(n)}(\boldsymbol{\mu}^{(n)}) = & \sum_{j \in N_i} 2(\boldsymbol{\alpha}_i^{(n)} + \boldsymbol{\gamma}_j^{(n)}) (\boldsymbol{\mu}_i^{(n)} - \boldsymbol{\mu}_j^{(n)}) + \\ & \sum_{j \in N_i^*} 2(\boldsymbol{\alpha}_j^{(n)} + \boldsymbol{\gamma}_i^{(n)}) (\boldsymbol{\mu}_i^{(n)} - \boldsymbol{\mu}_j^{(n)}) \end{aligned} \quad (3.84)$$

$$\ddot{T}^{(n)} = \sum_{j \in N_i} 4(\boldsymbol{\alpha}_i + \boldsymbol{\gamma}_j) + \sum_{j \in N_i^*} 4(\boldsymbol{\alpha}_j + \boldsymbol{\gamma}_i) \quad (3.85)$$

The calculation is summarized in Algorithms 3 and 4.

---

**Algorithm 3** Algorithm for the isotropic Huber penalty gradient ( $\mathbf{r}$ ) and curvature ( $\mathbf{s}$ ) calculation.

---

```

 $\boldsymbol{\alpha} \leftarrow \text{CALC\_ALPHA}(\boldsymbol{\mu}^{(n)}, \delta)$ 
 $\boldsymbol{\gamma} \leftarrow \text{CALC\_GAMMA}(\boldsymbol{\mu}^{(n)}, \delta)$ 
for  $i = 0..\text{length}(\boldsymbol{\mu}^{(n)}) - 1$  do
     $\mathbf{r}_i \leftarrow 0$  ▷ Gradient at  $i$ 
     $\mathbf{s}_i \leftarrow 0$  ▷ Curvature at  $i$ 
    for  $s \in \{s_x, s_y, s_z\}$  do
         $j \leftarrow i - s$ 
        if  $j \geq 0$  then
             $\mathbf{r}_i \leftarrow \mathbf{r}_i + 2(\boldsymbol{\alpha}_i + \boldsymbol{\gamma}_j)(\boldsymbol{\mu}_i^{(n)} - \boldsymbol{\mu}_j^{(n)})$ 
             $\mathbf{s}_i \leftarrow \mathbf{s}_i + 4(\boldsymbol{\alpha}_i + \boldsymbol{\gamma}_j)$ 
         $j \leftarrow i + s$ 
        if  $j < N_i$  then
             $\mathbf{r}_i \leftarrow \mathbf{r}_i + 2(\boldsymbol{\alpha}_j + \boldsymbol{\gamma}_i)(\boldsymbol{\mu}_i^{(n)} - \boldsymbol{\mu}_j^{(n)})$ 
             $\mathbf{s}_i \leftarrow \mathbf{s}_i + 4(\boldsymbol{\alpha}_j + \boldsymbol{\gamma}_i)$ 

```

---

---

**Algorithm 4** Functions used by Algorithm 3

---

```

function CALC_ALPHA( $\boldsymbol{\mu}^{(n)}$ ,  $\delta$ )
  for  $i = 0..\text{length}(\boldsymbol{\mu}^{(n)}) - 1$  do
     $g \leftarrow 0$ 
    for  $s \in \{s_x, s_y, s_z\}$  do
      if  $i - s \geq 0$  then
         $g \leftarrow g + (\boldsymbol{\mu}_i^{(n)} - \boldsymbol{\mu}_{i-s}^{(n)})^2$ 
     $g \leftarrow \sqrt{g}$ 
     $\alpha_i \leftarrow \text{PHIPRIME\_G\_OVER\_G}(g, \delta)$ 
  return  $\alpha$ 

function CALC_GAMMA( $\boldsymbol{\mu}^{(n)}$ ,  $\delta$ )
  for  $i = 0..\text{length}(\boldsymbol{\mu}^{(n)}) - 1$  do
     $g \leftarrow 0$ 
    for  $s \in \{s_x, s_y, s_z\}$  do
      if  $i + s < \text{length}(\boldsymbol{\mu}^{(n)})$  then
         $g \leftarrow g + (\boldsymbol{\mu}_i^{(n)} - \boldsymbol{\mu}_{i+s}^{(n)})^2$ 
     $g \leftarrow \sqrt{g}$ 
     $\gamma_i \leftarrow \text{PHIPRIME\_G\_OVER\_G}(g, \delta)$ 
  return  $\gamma$ 

function PHIPRIME_G_OVER_G( $g, \delta$ )
  if  $g \leq \delta$  then
    return  $(2\delta)^{-1}$ 
  else
    return  $(2g)^{-1}$ 

```

---

# Chapter 4

## Relative effects of shift-invariant source and detector blur with a linearized model

This chapter contains work originally published in

Steven Tilley II, Jeffrey H. Siewerdsen, and J. Webster Stayman. “Model-Based Iterative Reconstruction for Flat-Panel Cone-Beam CT with Focal Spot Blur, Detector Blur, and Correlated Noise”. In: *Physics in Medicine and Biology* 61.1 (2016), p. 296. ISSN: 0031-9155. DOI: 10.1088/0031-9155/61/1/296. URL: <http://stacks.iop.org/0031-9155/61/i=1/a=296> (visited on 12/09/2015)

and

Steven Tilley II, Jeffrey H Siewerdsen, and J Webster Stayman. “Iterative CT Reconstruction Using Models of Source and Detector Blur and Correlated Noise”. In: *Proc. 3rd Intl. Mtg. on Image Formation in X-Ray CT*. 2014, pp. 363–367. URL: <http://www.ucair.med.utah.edu/CTmeeting/ProceedingsCTMeeting2014.pdf>.

Reproduced here with permission. Preliminary work was also presented in

J Webster Stayman et al. “Generalized Least-Squares CT Reconstruction with Detector Blur and Correlated Noise Models”. In: *Proc. SPIE*. San Diego, CA, 2014, pp. 903335–903335–6. ISBN: 4-10-955111-0. DOI: 10.1117/12.2043067. URL: <http://dx.doi.org/10.1117/12.2043067>

and

Steven Tilley II, Jeffrey H Siewerdsen, and J Webster Stayman. “Iterative CT Reconstruction Using Models of Source and Detector Blur and Correlated Noise”. In: *Proc. 3rd Intl. Mtg. on Image Formation in X-Ray CT*. 2014, pp. 363–367. URL: <http://www.ucair.med.utah.edu/CTmeeting/ProceedingsCTMeeting2014.pdf>.

## 4.1 Introduction

CBCT is a promising modality for many clinical applications due, in large part, to its adaptable open geometry and capacity for high, isotropic spatial resolution. A broad variety of geometries exist, each driven by application requirements as well as tradeoffs between X-ray scatter (favoring greater object-detector distance) and spatial resolution. In some cases, the extended system geometry increases the influence of focal spot blur. Many CBCT systems would benefit from even greater resolution capabilities. Clinical examples in which improved spatial resolution is required include the detection of microcalcifications in CBCT mammography [15, 93] and the characterization of trabecular structure in CBCT extremities imaging [94]. In both of these cases, there are important image features that are just beyond the typical spatial

resolution of CBCT systems. While the image quality (including the spatial resolution) of current CBCT systems can be improved through hardware changes (smaller detector pixels, thinner scintillator, smaller X-ray source focal spot, etc.) and the redesign of other system characteristics (increased magnification, increased exposure, etc.), improved reconstruction algorithms can also lead to dramatic improvements in image quality. Moreover, improvements to the data processing pipeline have the potential to alter traditional tradeoffs in the design of new systems.

Much work on improved data processing in CBCT has concentrated on improved system modeling for reconstruction. This includes models for data corrections to account for scatter, beam hardening, and source and detector effects [42, 68, 95–99] as well as changes to the reconstruction algorithm [36, 100, 101]. MBIR algorithms have demonstrated higher image quality than traditional analytical approaches like FBP in both multi-detector CT [48] as well as CBCT [36, 102–104]. Much of this success comes from an accurate statistical model of measurement noise. Typically, statistical approaches model the data-dependent variance of measurements and implicitly or explicitly weigh the relative contributions of data with differing noise levels. Nearly all MBIR methods have made the assumption that the measurements are statistically independent. However, a few counterexamples can be found in the literature in Fourier rebinned Positron Emission Tomography (PET) [105], multienergy CT reconstruction [106–108], and tomosynthesis [69]. While the independence assumption may be appropriate for some MDCT systems, CBCT data can exhibit significant spatial noise correlation due to the detection process (e.g. as part of the indirect X-ray detection and light spread in the scintillator). In this chapter we discuss and model the effect

of noise correlation and use the results of chapter 3 to integrate the effect of noise correlation in the reconstruction algorithm.

For high spatial resolution reconstructions, accurate modeling of system blur is also potentially important. System blur modeling has been used extensively in MBIR for nuclear imaging to achieve higher spatial resolution reconstructions [43, 54, 56, 109]. Such methods have also been attempted in MDCT; however, it should be noted that in many cases, sophisticated blur modeling does not yield significant improvements. For example, Hofmann, Knaup, and Kachelrieß [110] showed that, under typical diagnostic CT conditions (0.5 mm to 2.0 mm focal spot size, 1.3 mm detector pixel size), modeling the effects of an extended source focal spot was not beneficial. However, there is a large opportunity for improvement in CBCT systems that often have smaller detector pixel pitches, larger (fixed anode) X-ray focal spots, and more varied geometries than clinical MDCT.

Previous work to improve the accuracy of the system model has accounted for blur in the reconstruction algorithm but without modeling noise correlation [54, 56]. Other staged reconstruction approaches perform a sinogram restoration step to account for system blur, [42] and noise correlation [68, 111]. In this chapter we present a forward model that includes source and scintillator blur and is compatible with the reconstruction algorithm developed in §3.2.2. This reconstruction algorithm tracks noise correlation through a deblurring step and incorporates this correlation in an iterative optimization algorithm. We evaluate the method by comparing reconstructions using the correlated noise model with results obtained using a model that assumes spatially independent noise. We evaluate the performance of the MBIR algorithm developed in §3.2.2 under different noise model assumptions and compare reconstructed

image quality in a digital extremities phantom in a variety of system configurations with different combinations of source and detector blur sizes. The MBIR algorithms are also compared with FBP with Projection Domain (PD) deblurring, Image Domain (ID) deblurring, and no deblurring. Additionally, we demonstrate performance advantages using the proposed approach in physical CBCT data of an anthropomorphic wrist phantom from an X-ray test bench for which we have measured system blur associated with both the X-ray source and the detector.

This chapter uses a SI assumption for both scintillator blur and focal-spot blur. While this is usually accurate for scintillator blur, focal-spot blur may exhibit strong shift-variant properties depending on the focal spot and the system geometry. However, for a small Field of View (FOV) and low magnification, the SI approximation is reasonably accurate. The SV nature of focal-spot blur is explored in chapter 6.

## 4.2 Methods

In Figure 4.1 we present an idealized model of a CBCT system. The measurements are modeled as a random vector which has undergone a series of transformations as the signal propagates through the system. We presume that the statistical distribution of quanta at each stage is approximately Gaussian and concentrate only on the first- and second-order statistics of this random vector. In each of four stages of the CBCT system we identify the mean (across the bottom of the figure) and the covariance matrix (top) for this random vector.

In the first stage, we presume the X-ray tube generates a spatial distribution of X-ray photons with a mean vector  $\mathbf{g}$ . These primary quanta are independent with



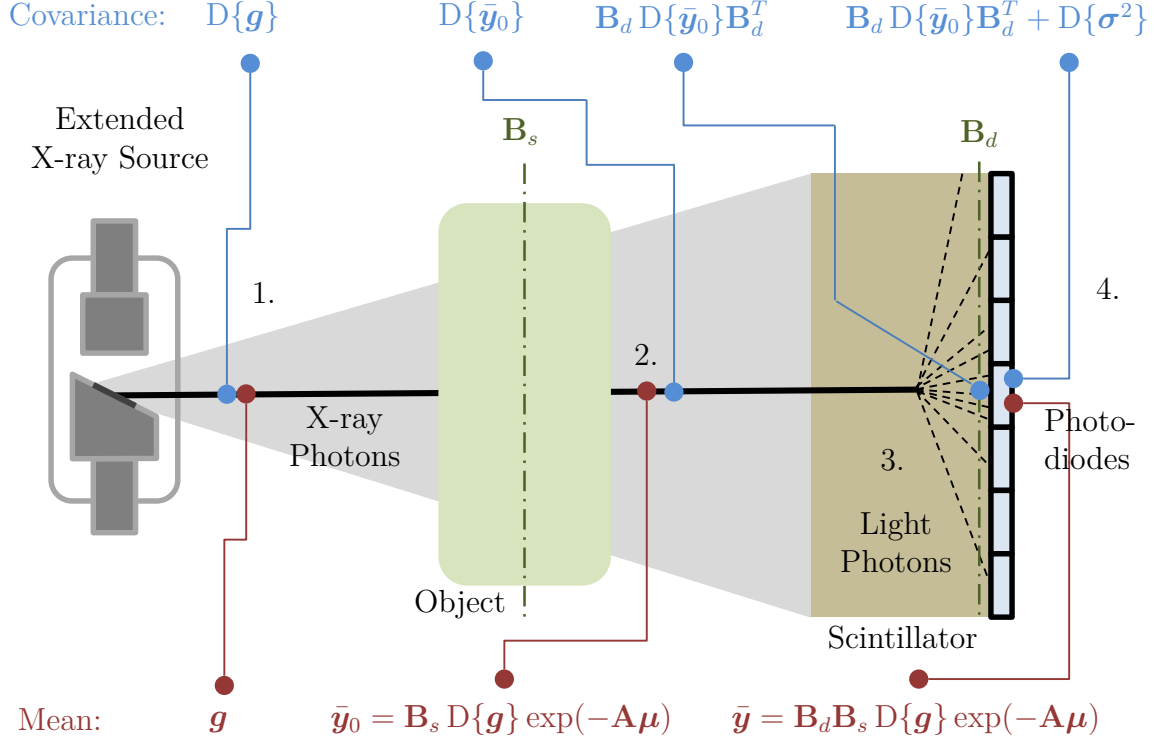


Figure 4.1: Model for the mean (bottom) and covariance (top) of quanta at various stages. (1) After X-ray photon generation, quanta are independent with a variance equal to the mean. (2) When X-ray photons are attenuated by the object, the spatial distribution of the mean and variance change, but remain equal and independent. An operator that includes source blur is also included. (3) In the scintillator, X-ray photons interact with a scintillating material creating many light photons which spread spatially, blurring the mean distribution and adding correlation to the noise. (4) Photodiodes detect the light photons with possible additive readout noise.

a Poisson distribution. Thus, the covariance is given by a diagonal matrix with the vector  $\mathbf{g}$  on the diagonal.

At the second stage, X-ray photons have been attenuated by the object in accordance with Beer's law and the signal has been blurred by the extended X-ray source. The pre-detection mean distribution of X-ray photons is given by the vector  $\bar{\mathbf{y}}_0$ . Similarly, since source blur does not correlate noise [112], the covariance matrix remains diagonal with values updated to match the mean vector. The mean vector  $\bar{\mathbf{y}}_0$  is modeled using Beer's law along line integrals obtained by applying a forward projection operator ( $\mathbf{A}$ ) to the vector of attenuation values ( $\boldsymbol{\mu}$ ). A scaling by the primary quanta distribution is also applied ( $\mathbf{D}\{\mathbf{g}\}$ ).

Focal spot blur is modeled as a linear operator ( $\mathbf{B}_s$ ) on the (unblurred) transmission values. Ideally, this focal-spot blur might be modeled by an integration of transmission values over a fine sampling of rays distributed over the extended focal spot, which would accommodate the depth-dependent blur associated with the source. However, while the above mathematical model is general, a model with very fine sampling is expensive to compute. In this chapter we presume that the object being scanned has a small width relative to the source-detector distance (i.e., that magnification is fairly constant throughout the object) so that  $\mathbf{B}_s$  may be approximated as a single convolutional blur function acting within the object plane (at the source-object distance). (More advanced focal-spot modeling is addressed in chapter 6.) This blur is applied for each projection using a system model with the number of rays equal to the number of detector elements. Moreover, we choose a separable footprints projector/backprojector pair [50] that explicitly models the detector aperture and cubic voxels. This approximation moves the physical integration over the

detector aperture (ideally modeled in  $\mathbf{B}_s$  or  $\mathbf{B}_d$ ) inside the exponential (as part of  $\mathbf{A}$ ). While not strictly correct, this approximation accounts for a degree of blur due to the detector aperture at reduced computational cost.

In the detector scintillator (stage 3), individual X-ray photons are converted into many visible light photons with a broad angular distribution in trajectories. This results in a single X-ray photon contributing signal to multiple pixels. This is modeled as a second blurring operator ( $\mathbf{B}_d$ ) which modifies the mean vector. Because of the one-to-many conversion of primary to secondary quanta in the detector, the scintillator also correlates the noise associated with each X-ray quanta, resulting in a non-diagonal covariance matrix. In this chapter, it is assumed that any blur associated with the pixel aperture is negligible compared to scintillator blur and that aliasing is not a dominating effect.

At the final stage (position 4), we include additional zero-mean electronic readout noise associated with the detector. This is modeled by adding the readout noise covariance matrix  $\mathbf{D}\{\boldsymbol{\sigma}^2\}$  to the current covariance matrix, where  $\boldsymbol{\sigma}$  is a vector of the readout noise standard deviation for each measurement. Thus, the final mean and covariance of the measurement random vector are given by equations (4.1) and (4.2).

$$\bar{\mathbf{y}} = \mathbf{B}_d \mathbf{B}_s \mathbf{D}\{\mathbf{g}\} \exp(-\mathbf{A}\boldsymbol{\mu}) \quad (4.1)$$

$$\mathbf{K}_Y = \mathbf{B}_d \mathbf{D}\{\mathbf{B}_s \mathbf{D}\{\mathbf{g}\} \exp(-\mathbf{A}\boldsymbol{\mu})\} \mathbf{B}_d^T + \mathbf{D}\{\boldsymbol{\sigma}^2\}. \quad (4.2)$$

For convenience, the total blur is defined as

$$\mathbf{B}_t \triangleq \mathbf{B}_d \mathbf{B}_s. \quad (4.3)$$

The linear reconstruction model (§3.2.2) was used with  $\mathbf{B}_c = \mathbf{B}_d$ ,  $\mathbf{B}_n = \mathbf{B}_s$ , and  $\mathbf{K}_Y$  approximated as in (3.54). The same method was used but without correlated noise modeling for comparison. Specifically,

$$\mathbf{K}_L^{\text{uncorr}} = \mathbf{D} \left\{ \frac{1}{\mathbf{C}'_y + \sigma^2} \right\}. \quad (4.4)$$

Additionally, for comparison with traditional FBP, reconstructions were performed on both deblurred and non-deblurred data using the Feldkamp-Davis-Kress (FDK) algorithm [35] using an unapodized ramp filter with a cutoff at the Nyquist frequency. FDK on deblurred data is referred to as Projection Domain (PD) deblurring.

The actions of  $\mathbf{A}$  and  $\mathbf{A}^T$  were performed on a GPU using the separable footprints algorithm [50] and an in-house CUDA [113] library.

### 4.2.1 Simulation studies

Simulation studies were conducted using the digital phantom illustrated in Figure 4.2. This phantom contains a number of different regions that include the following tissue types and attenuation values: (i) fat ( $\mu = 0.01875 \text{ mm}^{-1}$ ); (ii) muscle ( $\mu = 0.02150 \text{ mm}^{-1}$ ); and (iii) bone ( $\mu = 0.06044 \text{ mm}^{-1}$ ). There are additional features for qualitative and quantitative performance analysis, including a medium-contrast (v) disc and (iv) line pairs ( $\mu = 0.03 \text{ mm}^{-1}$ ). Simulated mean projection data were generated for a C-arm geometry (120 cm source detector distance and 60 cm source axis distance) with a 1D detector with 1750 pixels and a 0.14 mm pixel pitch. To approximate a continuous domain projection operator, line integrals were obtained by projecting a high resolution version of the phantom ( $4000 \times 4000$  with 0.025 mm

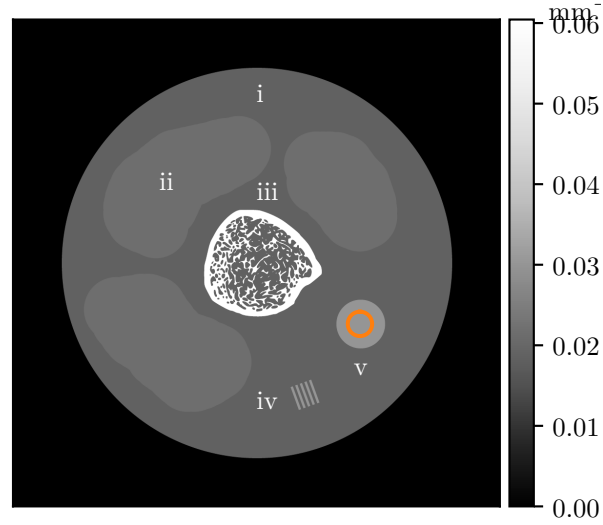


Figure 4.2: Digital phantom used in simulation studies emulating an extremity imaging scan with (i) fat, (ii) muscle, (iii) bone, (iv) line pairs, and (v) a uniform disc. For noise evaluations, sample variance was calculated in the disc interior indicated with a circle. Spatial resolution was estimated using the edge response between the disc and fat background.

voxels) onto a subsampled detector (7000 pixels with 0.035 mm pixel pitch) followed by an integration in the line-integral domain (over four detector sub-elements) to match the detector grid.

Noisy projection measurements were generated using Gaussian noise. The readout noise ( $\sigma$ ) was 1.9 equivalent photons and the bare-beam fluence was a constant  $10^6$  photons per detector element. Noiseless projection data were blurred by applying  $\mathbf{B}_s$  to obtain an intermediate mean vector  $\bar{\mathbf{y}}_0$ . This vector was then blurred by applying  $\mathbf{B}_d$  to obtain the noiseless measurement data. Quantum noise was modeled as zero mean Gaussian noise with variance equal to  $\bar{\mathbf{y}}_0$ . This noise was blurred by  $\mathbf{B}_d$  to add correlations and then added to the mean vector. Lastly, zero mean Gaussian readout noise with a variance of  $\sigma^2$  was added to yield the noisy measurement data.

Data were reconstructed into a  $1000 \times 1000$  2D image volume with 0.1 mm voxels for each of the three reconstruction methods: MBIR with the proposed correlated noise model, MBIR with the uncorrelated noise model, and FDK. In the preprocessing section  $\mathbf{K}_L^{-1}$  was applied using 1000 iterations of the CG method [41], and in the iterative section  $\mathbf{K}_L^{-1}$  was applied with 100 iterations (inner loop). The outer loop used 100 iterations of CG. The CG method was terminated early if the residual vector reached zero. Before deblurring, the data were padded with  $I_0$ . Both  $\mathbf{C}_c$ ,  $\mathbf{C}$ , and  $\mathbf{C}'$  had a threshold ( $\epsilon$ ) equal to  $10^{-2}$ . When performing covariance operations, padding prior to blur operations was performed using nearest neighbor extrapolation.

FDK reconstructions were also deblurred using a Image Domain (ID) Wiener deblur filter for comparison. Specifically, the deblur transfer function in the Fourier

domain was

$$\frac{H}{H^2 + \lambda \mathcal{F}(\mathbf{Q})}. \quad (4.5)$$

$H$  is a Gaussian transfer function with the width parameter found by fitting an error function to the disc (v. in Figure 4.2) edge response in a noiseless FDK reconstruction.  $\mathbf{Q}$  is defined in (2.42), and the Fourier transform is

$$\mathcal{F}(\mathbf{Q}) = (4 - 2 \cos(2\pi f_x) - 2 \cos(2\pi f_y)) \quad (4.6)$$

where  $f_x$  and  $f_y$  are the frequencies in the  $x$  and  $y$  directions. The regularization strength is given by  $\lambda$ . This assumes the same prior distribution on  $\boldsymbol{\mu}$  as a quadratic penalty and that the image noise is white.

For performance assessment in simulation studies, noise-resolution tradeoffs were investigated for each MBIR reconstruction and the ID deblurring. Specifically, resolution-variance curves were obtained by sweeping the regularization parameter ( $\beta$  or  $\lambda$ ) across a range of values (e.g. lower  $\beta/\lambda$  induces a higher resolution image with more noise, higher  $\beta/\lambda$  yields an image with lower resolution and less noise). To quantify resolution, the width of the edge response of the disc (Figure 4.2) was estimated using an error function fit. Specifically, attenuation values,  $\boldsymbol{\mu}_j$ , from a noiseless reconstruction were fit to the following equation which is a function of distance,  $\mathbf{x}_j$ , from the center of the disc in the phantom (from 0.1 mm to 10.0 mm):

$$\boldsymbol{\mu}_j(\mathbf{x}_j) = a + b \operatorname{erf} \left( \frac{2\sqrt{\log(2)}(\mathbf{x}_j - d)}{\text{FWHM}} \right) \quad (4.7)$$

Experiment	System Scenario	Scintillator Blur ( $\mathbf{B}_d$ ) FWHM (mm)	Source Blur ( $\mathbf{B}_s$ ) FWHM (mm)
Constant Total Blur	a	0.77	0.00
	b	0.70	0.34
	c	0.55	0.55
	d	0.34	0.70
	e	0.00	0.77
Constant Blur Ratio	d	0.34	0.70
	f	0.25	0.52
	g	0.42	0.88

Table 4.1: Systems with varying degrees of source and detector blur were simulated to investigate reconstruction performance over a range of scenarios. These scenarios are lettered a–g and permit two experiments where (1) the total blur is constant and the proportion of source and detector blur is varied; and (2) the proportion of source and detector blur is constant and the total blur is varied. Note that scenario d appears in both experiments.

The Full Width at Half Maximum (FWHM) is derived from this fitting operation. Noise was quantified as the sample variance of attenuation values inside the disc (within a 2.5 mm radius indicated in Figure 4.2) for a noisy data reconstruction.

To assess how performance varies with different blur properties, data generation and reconstruction were performed with Gaussian source blur and scintillator blur of various sizes (Table 4.1). Seven scenarios were chosen, five in which the total system blur was constant and three in which the ratio of the types of blur was constant (with one scenario belonging to both groups). Evaluation of systems with constant total blur and varying levels of source and detector blur permits an investigation into the relative performance of methods under varying levels of noise correlation.



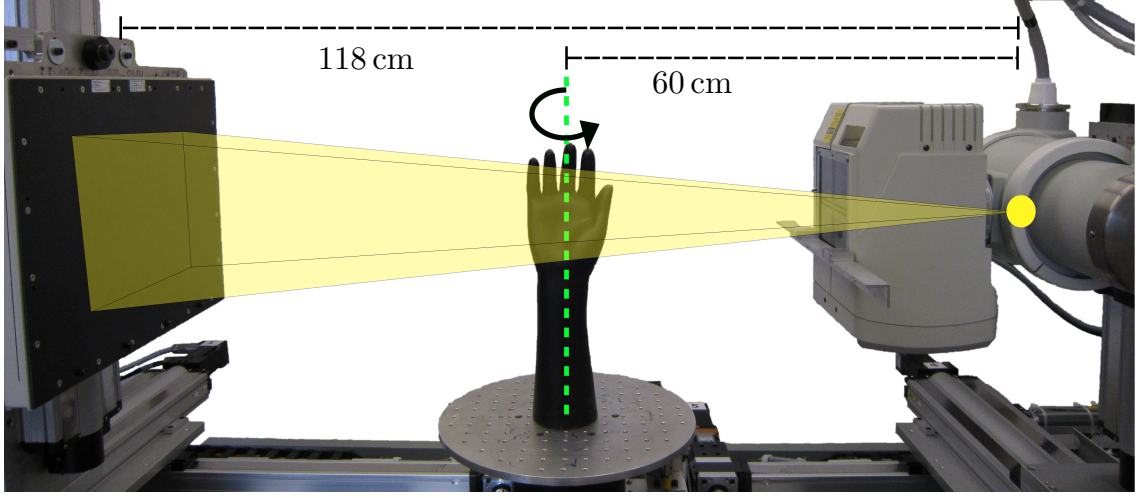


Figure 4.3: Test bench with flat panel detector (left) and X-ray source (right). The wrist phantom used is shown at the axis of rotation.

(Recall that source blur does not introduce noise correlation, whereas detector blur does impart correlation). The constant blur ratio scenarios permit investigation of performance when the total amount of blur is varied. In all studies, for all deblurring and reconstructions, blur models were matched with those used in data generation (except for ID deblurring which was in a different domain).

The original  $4000 \times 4000$  voxel phantom was downsampled by a factor of four in both dimensions to obtain a truth image with the same dimensions as the reconstructions. This truth image was used to generate difference images to visualize the accuracy of different reconstructions.

### 4.2.2 Bench characterization

To apply the proposed methodology to physical data, a system characterization was necessary to estimate system blur. The experimental setup and CBCT test-bench used for investigations is illustrated in Figure 4.3. This system is composed of a flat-panel detector (4030CB, Varian, Palo Alto CA) and an X-ray tube (Rad-94, Varian, Salt Lake City UT). Modulation Transfer Function (MTF) measurements were acquired using a technique similar to that of Samei, Flynn, and Reimann [114]. Multiple projections (720) of a tungsten edge were acquired and gain/offset corrected. These projections were then averaged to reduce noise. The location of the edge was found by fitting error functions to the pixel values along either rows or columns, and fitting a line to the center points of the error functions. The location of this edge was then used to extract the Edge Spread Function (ESF), which was then binned, differentiated, and Fourier transformed to obtain the MTF.

Both detector and source MTFs were computed. The detector MTF was acquired by placing the tungsten edge on the face of the FPD. The MTF was modeled as a Gaussian (scintillator) multiplied by a sinc. This model was fit to the measured MTF by varying the width of the Gaussian. It was assumed that the scintillator blur is radially symmetric, so only one edge orientation was needed. The source MTF was acquired by placing the tungsten edge at isocenter, and rotating the edge about the source-detector axis to measure different slices of the MTF. The edge was (approximately) oriented to obtain an edge response along the axis of rotation (axial), perpendicular to the axis of rotation (trans-axial), and at  $45^\circ$  to the axis of rotation. These experiments yielded the composition of both source and detector blur.

Thus, to find the source blur, the combined source and detector MTF was divided by the detector MTF. Gaussians were fit to the main lobe of the axial and trans-axial slices of the source MTF, and combined into a separable 2D MTF estimate in the reconstruction algorithm.

As an additional check on the nature of the source blur, focal spot images were obtained. A pinhole image of the focal spot was taken using a large source-detector distance to obtain a source magnification of approximately 14. Multiple projections (100) were acquired and averaged. The background of the pinhole image was detrended by fitting a paraboloid to the background and subtracting it from the entire image. This removes low frequency effects (e.g. off-focal radiation) that are not particularly important for resolution recovery. Fourier transforming the pinhole image permitted profiles of the 2D MTF to be compared with the measurements obtained using the tungsten edge.

Noise Power Spectrum (NPS) measurements were acquired to validate the correlated noise model and the SI scintillator blur assumption. These measurements were performed on a different test bench, with a different, but similar, detector (4343CB, Varian, Palo Alto CA). The measured NPS was compared with the theoretical NPS calculated with a detector blur measurement. The NPS was also measured at multiple locations to determine if the scintillator blur is SV. The local NPS at a location on the detector was calculated with a  $201 \text{ pixel} \times 201 \text{ pixel}$  square centered at that location and 500 gain and offset corrected exposures. Dead pixel values were replaced with the average value of the neighboring working pixels. The NPS calculation was [115]

$$NPS = \text{mean}_i(|(\mathcal{F}(\mathbf{y}_i - \bar{\mathbf{y}}_i))^2|) \Delta_u \Delta_v (201 \times 201)^{-1} I_0^{-1} \quad (4.8)$$

where  $I_0$  is the estimated photon flux,  $\mathbf{y}_i$  is a single cropped and corrected exposure multiplied by  $I_0$  (i.e., in photon units), and  $\Delta_u$  and  $\Delta_v$  are the column and row pixel pitches, respectively. Note that  $\mathbf{y}_i$  here refers to a vector of measurements at frame  $i$ , not a single element of  $\mathbf{y}$ . Assuming pixel aperture blur is negligible compared to scintillator blur and that obliquity effects are small, the theoretical NPS is approximately radially symmetric, with the 1D slice given by

$$NPS_{\text{theoretical}} = MTF_{\text{detector}}^2 \Delta_u \Delta_v k \quad (4.9)$$

where  $k$  was found by fitting to the measured NPS at the center of the detector. The detector MTF was calculated with 100 averaged exposures of the tungsten edge. Note that this is a simplified NPS model that assumes a 100% fill fraction.

### 4.2.3 Test-bench data reconstructions

To investigate the performance of the proposed reconstruction algorithm on physical data, we scanned a custom wrist phantom (The Phantom Laboratory, Greenwich, NY). This phantom includes a natural human skeleton of the arm, wrist, and hand bones in a tissue-equivalent plastic including simulated cartilage and tendon features. Projections were obtained over 720 angles in a 360° circular orbit in a C-arm geometry (source to detector distance of 118 cm and source to axis distance of 60 cm). The reconstruction volume was  $600 \times 600 \times 210$  voxels with cubic voxels 0.15 mm to a side. The X-ray tube on the test-bench had two focal spot settings. All projection data for system characterization (except the NPS study) and reconstruction comparisons were acquired with the large focal spot (0.8 specification). However, one acquisition

was also obtained using the small focal spot (0.4 specification). These data were reconstructed using FDK to generate a high-resolution reference image with which to compare images from the various reconstructions of projection data with larger focal spot blur. Data were preprocessed according to the methodology in §3.2.2; however, a few additional calibrations were required for the physical data. Specifically, following traditional gain and offset correction and individual frame normalization of the projection data, the model gain term associated with the primary quanta was estimated. The gain of the system was estimated as a constant equal to the ratio of the mean and variance of an air portion of the normalized projection data (i.e. fitting the Poisson assumption). Data were padded with nearest neighbor values prior to deblurring. Subsequent preprocessing of the data was as described in §3.2.2, with the addition of a thresholding operation on the deblurred data so the minimum was approximately equal to the measurement that would be expected for X-rays attenuated by 40 cm of water.

The data were reconstructed as previously described, using FDK, the uncorrelated noise model, and the correlated noise model. Gaussian approximations for source and scintillator blur were used for deblurring and applying  $\mathbf{K}_L^{-1}$ . For the proposed reconstruction with a correlated noise model,  $\mathbf{C}_c$  had a threshold ( $\epsilon$ ) of zero and padding with zeros. Readout noise was estimated as 1.9 photons. The threshold ( $\epsilon$ ) for  $\mathbf{C}$  and  $\mathbf{C}'$  was  $10^{-2}$  with data padded using nearest neighbor extrapolation. For the  $\mathbf{K}_y$  inversion in the preprocessing section of Algorithm 2, 1000 iterations of the conjugate gradient method were used. In the iterative section, the conjugate gradient method was used for both the inner and outer loops, with 100 iterations for the inner loop and 300 for the outer loop.

Performance evaluation of the physical data reconstructions was conducted using qualitative comparisons to each other and the high resolution reference. Spatial variance was measured in a constant region of a center slice, and used to noise match the reconstructions (by choosing appropriate values for  $\beta$ ) obtained using iterative methods for fair comparison.

## 4.3 Results

### 4.3.1 Simulation studies

Figure 4.4 shows the spatial resolution-variance tradeoff for MBIR reconstructions using the correlated noise model and the uncorrelated noise model as well as ID deblurring in a simulation study with a 0.34 mm FWHM scintillator blur and a 0.70 mm FWHM source blur (system scenario d). Different positions on each curve were obtained by varying regularization strength ( $\beta$  or  $\lambda$ ). When  $\beta$ s are chosen such that the uncorrelated and correlated reconstructions have the same resolution (i.e. the vertically aligned squares in Figure 4.4 are resolution matched), the uncorrelated model yields a variance more than an order of magnitude larger than that of the correlated noise model. Similarly, when  $\beta$ s are chosen such that the variance is the same (i.e. horizontally aligned squares in Figure 4.4 are noise matched), the correlated noise model reconstruction has a smaller edge response than the uncorrelated noise model reconstruction, by about 0.17 mm (i.e. 42% decreased FWHM). In this scenario, the ID deblurring was roughly equivalent to the correlated noise model (discussed below). Non-deblurred FDK is represented by a star demonstrating the traditional spatial resolution limit when no system blur models are adopted. Both the FDK

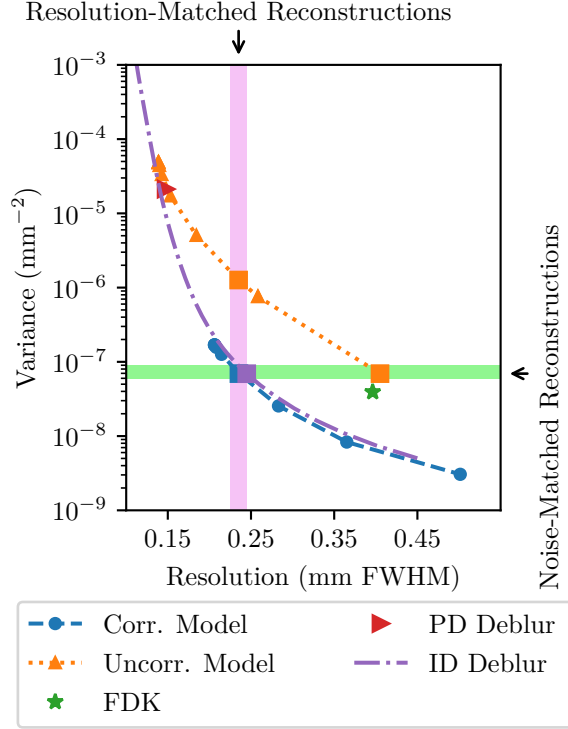


Figure 4.4: Spatial resolution-variance tradeoff for different reconstructions in a simulated tomographic system with a 0.34 mm FWHM scintillator blur and a 0.70 mm FWHM source blur. Variance and spatial resolution are shown for MBIR reconstructions using the correlated and uncorrelated noise models and FDK with no deblurring, PD deblurring, and ID deblurring. The square data points are either noise-matched or resolution-matched to the square data point in the correlated model dataset.

and PD deblurring resolution-variance points are close to the uncorrelated model resolution-variance tradeoff.

Noise- and spatial resolution-matched reconstructions from Figure 4.4 are shown in Figure 4.5(a). These zoomed images show the central portion of the digital phantom with trabecular bone details, as well as an additional zoom inset that shows the line pair object. When the reconstructions are noise-matched, both trabecular details and the line pairs in the uncorrelated reconstruction are blurrier than those in the correlated reconstruction. The ID deblurring appears similar to the correlated noise method, consistent with the resolution-variance plot. To better visualize noise, Figure 4.5(b) shows the difference images where the true image has been subtracted from each reconstruction. In spatial resolution-matched reconstructions, the noise magnitude of the uncorrelated noise reconstruction is larger than that of the correlated noise reconstruction. Note that the noise texture and specific resolution properties also differ between approaches. For example, the correlated noise model and the ID deblurring produce lower frequency noise than the uncorrelated noise model. Thus, despite matching noise in terms of variance, the NPS clearly differ between the three approaches. Similar observations can be made for spatial resolution. While the FWHM edge response is matched, side lobe performance is clearly different between methods. This is particularly evident in the difference images in the trabecular bone and the line pairs.

To get a better understanding of the performance for different levels of source and detector blur, resolution-variance tradeoffs were evaluated for the seven system blur scenarios delineated in Table 4.1, represented graphically by the large dots labeled with letters at the top and left of figures 4.6 and 4.7, respectively. Scenarios a-e



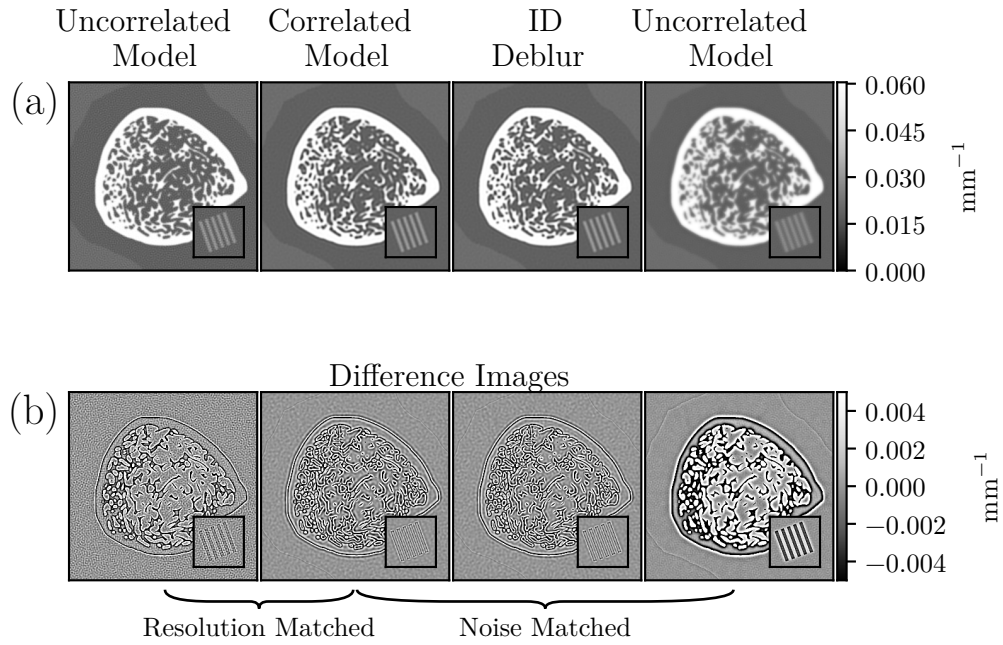


Figure 4.5: (a) Reconstructions from the simulation study corresponding to the noise-matched and resolution-matched data points in Figure 4.4. (b) Difference images show the difference between the reconstruction and truth. Zoomed images focus on the bone in the center of the phantom, with the line pairs inset in the lower right.

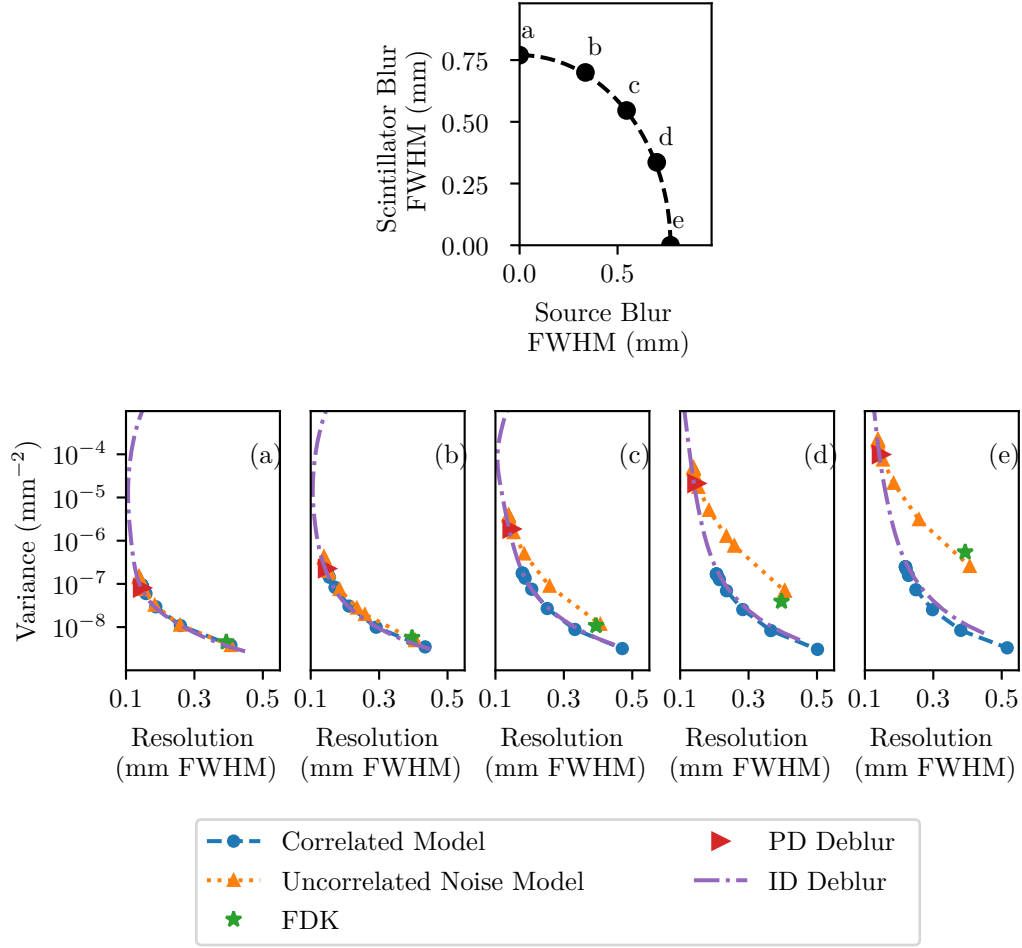


Figure 4.6: Evaluation of reconstruction algorithms for systems with differing source and detector blur. The schematic (top) illustrates the different imaging system scenarios with varying amounts of source and detector blur. These scenarios have a constant total system blur and a varying blur distribution — from detector-dominated (point a) to source-dominated (point e). The subfigures (a-e) show the resolution-variance tradeoff for each of the systems with blur scenarios corresponding to points a-e in the schematic. Note that the correlated noise model shows the greatest advantage over the uncorrelated noise model for the scenario where source blur dominates.

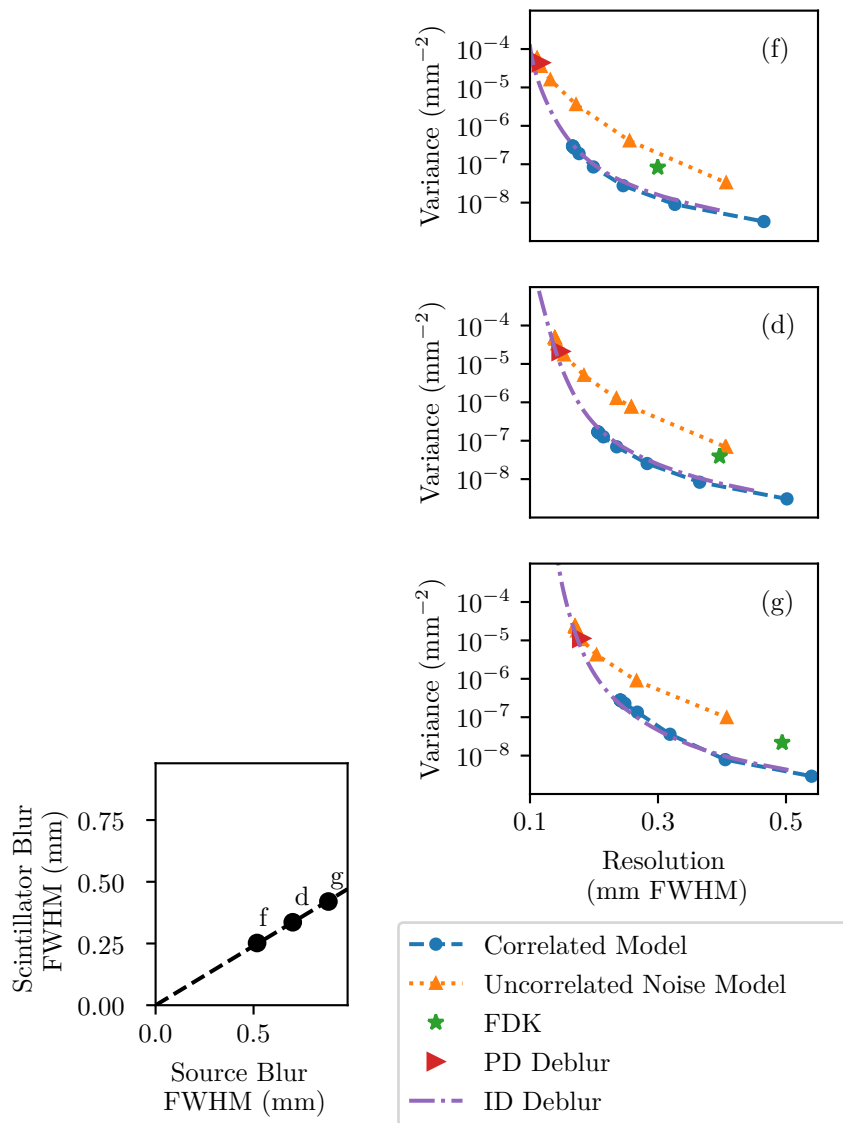


Figure 4.7: Performance evaluation of reconstructions under varying total blur conditions. The points in the left figure show three different system scenarios, each with the same ratio of source to scintillator blur. The different total system blur conditions represented by points f, d, and g correspond to the resolution-variance plots on the right.

(Figure 4.6) represent systems with constant total blur and varying blur distribution. Specifically, system a is dominated by scintillator blur and system e is dominated by source blur. Scenarios f, d, and g (Figure 4.7) represent systems in which the ratio of the source and detector blur is constant, but the total blur changes, with f having the smallest blur and g the largest. The remaining plots in figures 4.6 and 4.7 show the resolution-variance curves for each scenario a-e and f, d, and g, respectively. The FDK points indicate the approximate resolution limit without deblurring. Better imaging performance is found toward the bottom and left of each plot (e.g. lower variance and/or higher resolution).

In all cases, deblurring methods lead to an increase in achievable resolution when compared with non-deblurred FDK. In terms of the resolution-variance tradeoff, the correlated noise model is equivalent to or better than the uncorrelated noise model in all seven cases. When total blur is constant (a-e), the correlated noise model yields the greatest advantage when the blur is due to the source, and yields essentially no advantage when the blur is due only to the scintillator. Intuitively, when source blur is negligible, the deblurring operation is only removing the scintillator blur, thereby whitening the data. In this case, a diagonal covariance matrix becomes an accurate assumption, and the correlated and uncorrelated noise models are essentially equivalent. However, this assumption only holds for low readout noise. As shown in Stayman et al. [92], a system dominated by detector blur will still benefit from a correlated noise model since deblurring will add correlations due to additive readout noise.

When the system has non-negligible source blur, the deblurring of source blur (which, again, in itself does not correlate the noise) adds correlations to the data, which are accounted for in the correlated noise model but not the uncorrelated noise

model, resulting in the advantages seen in figures 4.6(c)–(e). Holding the blur ratio constant while increasing total blur does not have a large effect on the relative performance of the two methods, but does decrease the finest achievable resolution for all methods (figures 4.7(d), (f), (g)).

The FDK and PD deblurring resolution-variance points lie near the uncorrelated model’s resolution-variance curve indicating similar performance. While one often sees an advantage of statistical methods over direct approaches like FDK, the similar performance in this case suggests that the quantum noise modeling<sup>1</sup> does not play a large role in this example (i.e. the dynamic range in variance isn’t particularly large for this object), and it is the correlated noise modeling that is important.

The ID deblurring method is roughly equivalent to the correlated noise model in all cases. The penalty/prior terms between the two methods are equivalent, so the relative performance of the Wiener filter is likely dominated by the noise assumption. While a white noise assumption was used, FBP reconstruction noise is not white and exhibits strong frequency dependence [116]. This suggests that the overall noise magnitude was too low for this discrepancy to matter. Another possibility is that there is a difference between these two methods, but it is not captured by the relatively simple resolution metric used in this study.

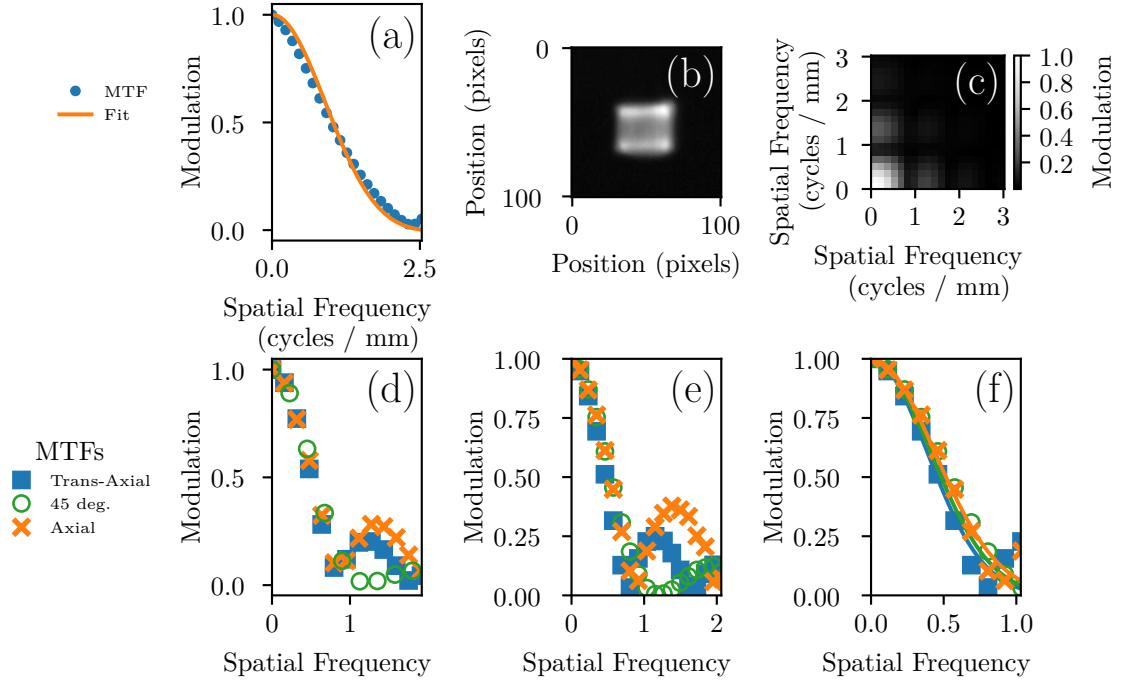


Figure 4.8: (a) Detector MTF measurements and parameterized fit. The model used for fitting was a Gaussian multiplied by a sinc function. (b) Focal spot image from the CBCT test-bench. (c) A source MTF derived from the focal spot image approximately scaled for focal spot blur at the center of rotation. (d) Trans-axial, axial, and  $45^\circ$  profiles of the pinhole-derived source MTF. (e) Source MTFs as estimated from edge responses at the center of rotation. (f) Zoomed version of (e), with solid lines indicating the corresponding profiles of the parameterized fit.

### 4.3.2 Bench characterization

Figure 4.8(a) shows the test-bench detector MTF and the corresponding model approximation. We expect the MTF to be composed of a scintillator MTF and a sinc function (due to pixel sampling). The pixel pitch is 0.388 mm, which would put the first zero of the sinc function at about 2.58 cycles  $\text{mm}^{-1}$ . This is consistent with the measured MTF, which has a first minimum at slightly less than 2.5 cycles  $\text{mm}^{-1}$ . The approximation is a Gaussian multiplied by a sinc of the expected width. The width of the Gaussian in the approximation was found by fitting to the data in the primary lobe. The Gaussian-sinc model is a good approximation to the data at frequencies in this primary lobe.

The pinhole image of the source is shown in Figure 4.8(b). It is approximately a 2D rect function, but a higher order approximation could model the bright horizontal “horns” at the top and bottom of the rect. The pinhole image was Fourier transformed to obtain the 2D MTF shown in Figure 4.8(c). Along the axial and trans-axial directions the modulation intensity appears similar to a sinc function, consistent with the 2D rect model. The bright horizontal horns at the top and bottom introduce the asymmetry between these two profiles. The source MTF is not radially symmetric, with a noticeably different profile along the 45° line. These observations are confirmed in the profiles shown in Figure 4.8(d), in which modulation intensity is plotted as a function of position along the trans-axial, axial, or 45° lines in the 2D MTF.

---

<sup>1</sup>We note that one of the other advantages of model-based approaches is the use of more sophisticated regularization strategies (e.g. non-quadratic penalties). In this chapter we have concentrated on quadratic penalties and the improvements due to system modeling. Thus, the similar performance of FDK and MBIR with a traditional noise model and quadratic penalty is not completely unexpected.

Figures 4.8(e) and (f) show the line profiles of the source MTF acquired using a tungsten edge. The shapes of the MTF profiles are approximately equal to those in Figure 4.8(d). The axial and trans-axial MTFs are similar to each other at frequencies below the first zero, and the axial MTF is larger in the first side lobe, consistent with the profiles in Figure 4.8(d). The first zero appears to be at about  $0.8 \text{ cycles mm}^{-1}$ , which corresponds to a  $1.3 \text{ mm}$  rect function. The  $0.8$  specification of this spot indicates a focal spot size of  $0.8 \text{ mm}$  to  $1.1 \text{ mm}$ , which is close to our estimate [20]. The  $45^\circ$  MTF has its first zero at a higher frequency, which is consistent with a 2D rect function approximation of the focal spot. This approximation would cause the  $45^\circ$  profile to be a squared sinc, resulting in a different shape than the axial and trans-axial profiles, as is seen. The solid lines in Figure 4.8(e) show the Gaussian approximation used for the test-bench data reconstructions. This model captures most of the shape before the first zero, while ignoring the higher frequencies.

Differences between the MTF derived from the pinhole and edge measurements have two main causes. First, because the exact magnification used to acquire the pinhole image was not known, the frequency axes in figures 4.8(c) and (d) were scaled so the zeros approximately matched those in Figure 4.8(e). The MTF derived from the tungsten edge measurement was taken with no source magnification (edge placed at isocenter), so the frequency axis in Figure 4.8(e) should be considered more accurate. Second, the pinhole image and its derived MTFs were not corrected for detector blur nor for blur associated with the pinhole itself (whose diameter was inexactly known).

Figure 4.9 shows the measured vs theoretical NPSs. The widths of the plots are approximately the same, indicating that the correlation length is determined by the



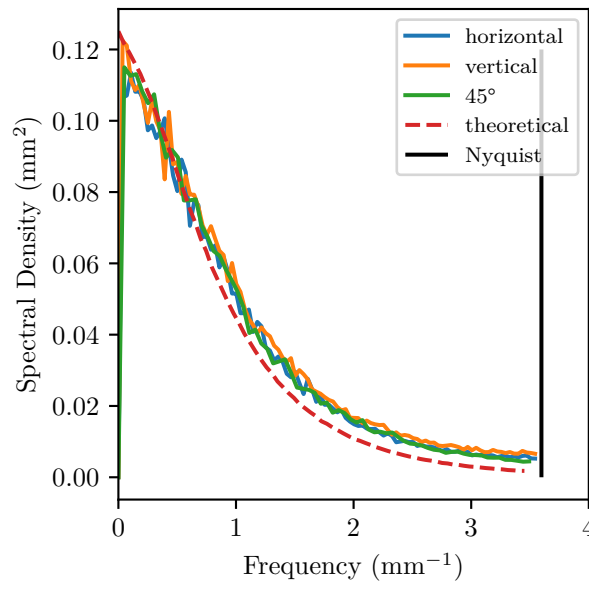


Figure 4.9: This figure shows horizontal, vertical, and 45° slices of the 2D measured NPS at the center of the detector, along with the theoretical 1D NPS (assuming radial symmetry).

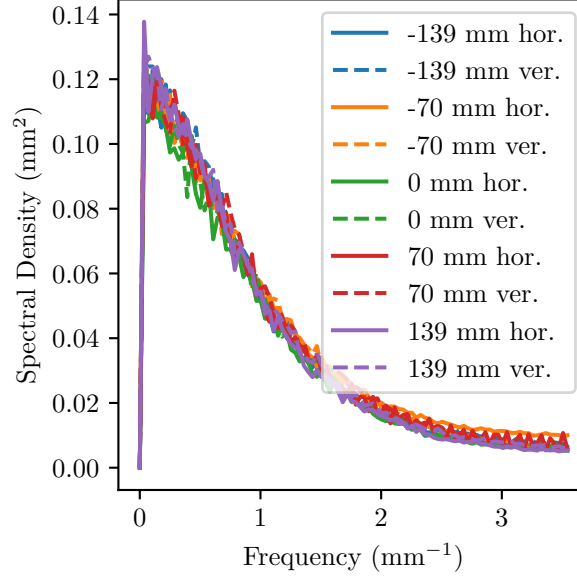


Figure 4.10: Horizontal and vertical NPS slices for NPSs acquired at different positions on the detector, indicated by distance from the center in the horizontal direction.

detector blur. The fact that the horizontal, vertical, and  $45^\circ$  NPSs are the same supports the assumption that scintillator blur is radially symmetric. Note that the theoretical NPS was calculated using the full detector blur (scintillator and pixel aperture), while the MBIR approach only models the scintillator blur as causing correlations. This discrepancy may prove important in systems where pixel aperture is a large effect.

Figure 4.10 shows NPSs acquired at different horizontal positions along the detector. Note that all the NPSs are the same, e.g., are not location dependent, indicating that the underlying detector blur is not SV.

### 4.3.3 Test-bench data reconstructions

The correlated noise model was tested on a wrist phantom imaged using the test-bench. Two Regions of Interest (ROIs) are marked in the high-resolution reference reconstruction (Figure 4.11(a)) with white rectangles. Figure 4.11(d) shows the larger ROI (distal radius) from the same reconstruction. This ROI contains cortical bone surrounding trabecular bone. Within this ROI the phantom also contains cartilage-equivalent plastic on the upper left aspect of the cortical bone (marked by an arrow). Images were reconstructed using the FDK algorithm (Figure 4.11(b)), a combination of PD deblurring and FDK (Figure 4.11(c)), the uncorrelated noise model (Figure 4.11(e)), and the correlated noise model (Figure 4.11(f)). Figures 4.11(e) and (f) are noise-matched in the smaller ROI indicated in Figure 4.11(a), with a variance of  $8.75 \times 10^{-7} \text{ mm}^{-2}$ . The trabecular structure in the FDK reconstruction is present but details are difficult to discern. Deblurring prior to FDK reconstruction results in an unacceptably noisy image. Using the uncorrelated noise model (which includes deblurring) is slightly worse than FDK in terms of resolution at the chosen noise level, although these images are not strictly noise matched. Noting that the uncorrelated MBIR image is both lower resolution and higher noise than FDK underscores the high degree of noise magnification due to the deblurring step. In contrast, the proposed reconstruction method including a correlated noise model recovers more trabecular bone details compared to the noise-matched conventional model-based reconstruction method. We note that the proposed method appears to contain more noise streaks on the upper aspect of the cortical bone. While the exact cause of this increased streaking is unclear and needs additional investigation in future studies, this may be

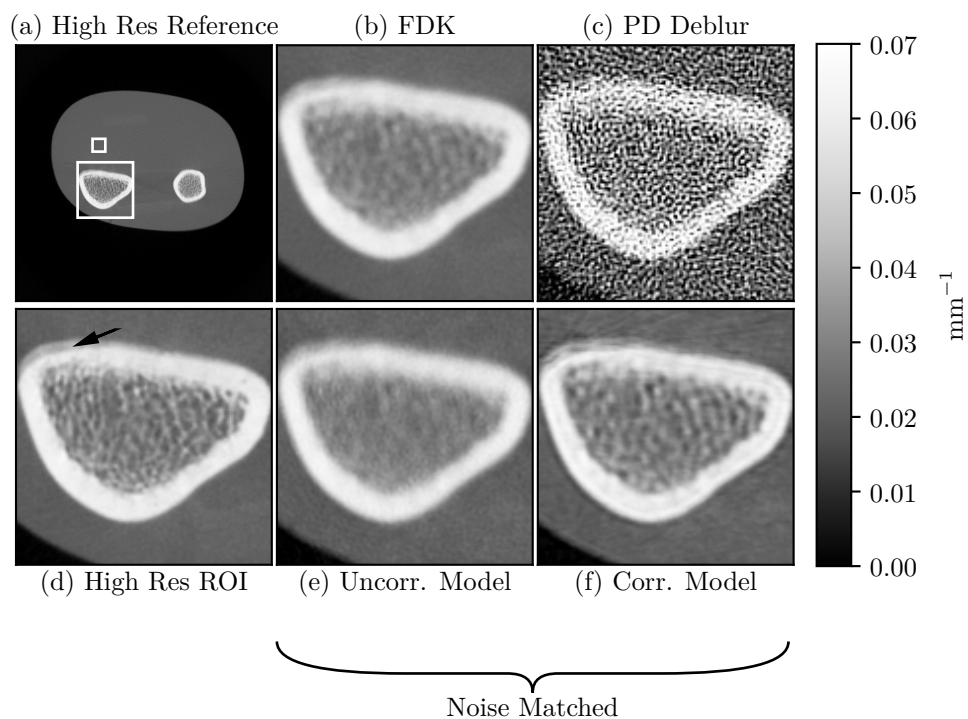


Figure 4.11: Test-bench data reconstructions. (a) High resolution reference image. The large box denotes the ROI used for (b-f). (b) FDK reconstruction. (c) FDK reconstruction on deblurred data. (d) High resolution reference image with an arrow indicating cartilage-equivalent plastic. (e) Reconstruction obtained using the uncorrelated noise model. (f) Reconstruction obtained using the correlated noise model and noise matched with (e).

the result of incomplete physical modeling. Specifically, we note that the data was not corrected for beam hardening nor scatter effects and it is possible that blur modeling (and deconvolution) will exaggerate streaking due to these uncompensated biases.

Figure 4.12 shows the difference between the reconstructions in Figure 4.11(b), (c), (e), (f) and the high-resolution reference reconstruction (Figure 4.11(d)). The correlated noise model reconstruction is the closest to the high-resolution reference with the flattest difference image. The (non-deblurred) FDK and uncorrelated noise model difference images show quite a bit of structure, indicating a resolution mismatch with the reference image. The FDK reconstruction of deblurred data is overwhelmed by noise. The difference images also show a difference in noise texture between the uncorrelated and correlated model reconstructions, similar to that seen in simulation.

To check whether the structure in the correlated MBIR (Figure 4.11(f)) is representative of real anatomy and not mid-frequency noise, this reconstruction was compared with a blurred version of the high-resolution reference image (Figure 4.11(d)). The reference image was convolved with a Gaussian kernel with a width parameter determined by minimizing the Root Mean Squared Error (RMSE) between the blurred reference image and the correlated MBIR reconstruction. The results are in Figure 4.13. The two images are similar, with structures appearing in both images, indicating that these structures represent real anatomy.

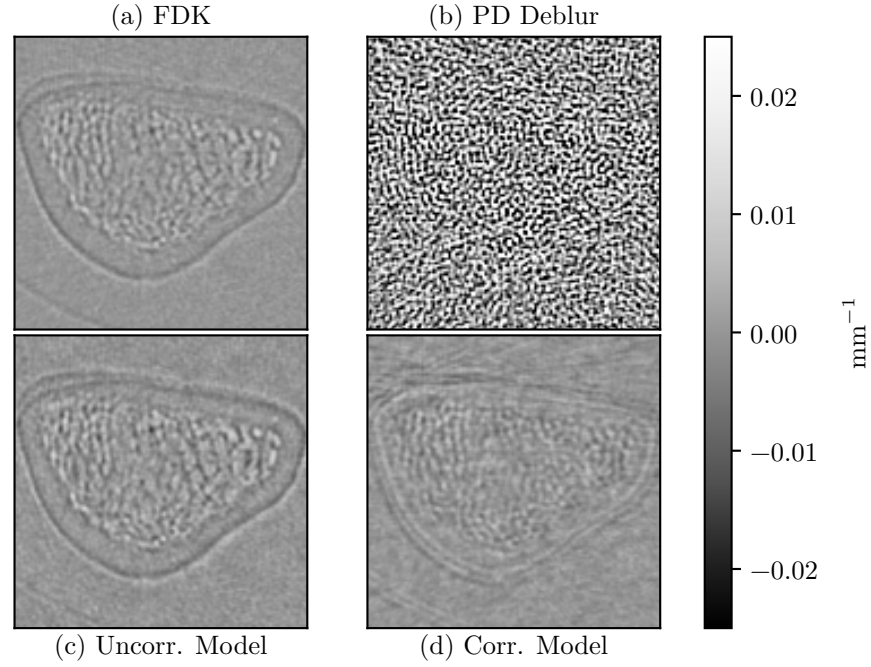


Figure 4.12: Difference images between the high-resolution reference image and the various reconstruction methods: (a) FDK; (b) PD deblur + FDK; (c) uncorrelated MBIR; and (d) correlated MBIR (corresponding to b, c, e, and f in Figure 4.11). The smallest differences from the high-resolution reference are observed in the correlated MBIR reconstruction.

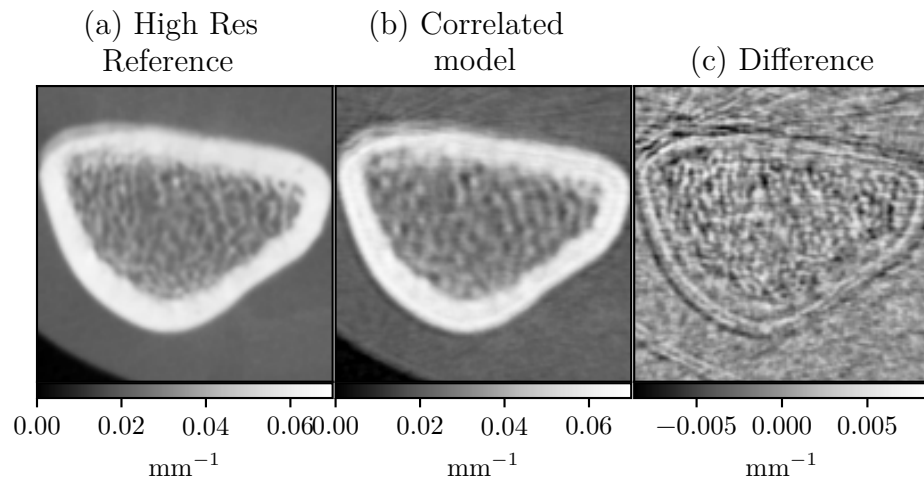


Figure 4.13: (a) Blurred high-resolution reference image. (b) correlated MBIR reconstruction. (c) Difference image between (a) and (b).

## 4.4 Discussion

In this chapter, we have presented a CBCT forward model that accounts for source and detector blur as well as noise correlation in the data. We used an MBIR algorithm from §3.2.2 with a staged data processing chain where projections are first deblurred and log-transformed, data correlations are modeled through both the detection and deblurring processes, and reconstruction is performed through a penalized generalized linear least-squares algorithm with a non-diagonal weighting matrix. We have demonstrated the relative performance of the proposed method in comparison to a traditional MBIR approach without a correlated noise model and a FDK approach with PD deblurring and without deblurring. Experiments in both simulated projections and in CBCT test-bench data demonstrate improved performance of the proposed approach over uncorrelated MBIR and FDK with PD deblurring. Specifically, while any approach that applies deblurring to the projection data permits higher spatial resolution reconstructions, our method can yield significant improvements in noise performance since it maintains an accurate noise model. These improvements vary with the degree of blur and the dominant source of system blur with the greatest advantages for systems with larger focal spot blur.

The proposed method did not offer an advantage over FDK with ID deblurring. This is likely due to the relatively low noise (high photon flux) of the simulation study. At higher noise levels, we expect ID deblurring to perform worse than the proposed method due to noise model mismatch. This may also depend on the choice of image quality metric. The resolution metric used in this chapter makes inherent assumptions about the image estimation process (e.g., local linearity) and may not be a suitable



metric for all reconstruction algorithms or imaging tasks. Additionally, the blur used in the simulation study is relatively simple, and possibly well estimated in the ID. Other types of blur, such as SV focal-spot blur (chapter 6), can not be modeled accurately in the ID, and require integration into an MBIR algorithm. Future work is required to explore the relative performance of the proposed method to various ID deblurring techniques with different noise levels and image quality metrics.

Despite the advantages illustrated in this chapter, there are a number of additional opportunities for future work in the development of reconstruction methods that accommodate system blur and data correlation. For example, one could adopt a similar staged deblur and reconstruction method that deconvolves only the correlating (scintillator) blur, whitening the data, and thereby permitting an objective function that accounts for non-correlating source blur while using an uncorrelated noise model, such as that of Feng, Fessler, and King [54] or Yu, Fessler, and Ficareo [56]. This method would permit use of a nonlinear objective function, permit use of Poisson (or other) noise models, eliminate bias imparted by the log transform, and potentially be more computationally efficient since the statistical weightings are independent. Alternately, one might use the non-staged reconstruction process in §3.2.1, where the entire forward model including system blur is integrated into a nonlinear objective function. Such an approach is attractive since it eliminates any parameter tuning associated with a deblurring step. This is explored in chapter 5. While we have focused on 3D imaging in this paper, the 2D projection noise modeling of the processed measurements might also be applied to 2D restoration with the potential to improve projection radiography.

In addition to algorithm development, further improvement will be more accurate modeling of system blur, especially the higher order (high-frequency) properties of the source blur. The current blur model makes an assumption of shift-invariance. Both the SV nature of the apparent focal spot size and shape, as well as the depth-dependent nature of source blur are a subject of chapter 6.

The bench-data reconstructions shown here suggest applicability to current CBCT systems. However, in addition to different blur properties, different systems and scans will have varying degrees of scatter, patient motion, and gantry jitter. Similarly, in this chapter, we have focused on an extremity imaging example. We would expect other body sites to be potentially more challenging due to increased attenuation and likely increased scatter fractions. Our conjecture is that increased attenuation will predominantly increase noise, while increased scatter will likely reduce contrast but have relatively small effects on high-spatial resolution properties (since scatter effects are largely at low spatial frequencies). These properties will have to be investigated in more detail in future work to determine how they affect reconstruction image quality in real systems, how scatter and other artifact corrections interact with the proposed algorithm, and whether current correction schemes are sufficiently accurate for high resolution reconstructions.

In summary, we have developed a reconstruction method that breaks from the traditional assumption of spatially independent measurement noise. This is important since noise correlation due to FPDs is significant, and accurate noise models are a key element of MBIR methods. We have demonstrated improvements in the resolution-variance tradeoff, opening the opportunity for higher spatial resolution in flat-panel-based CBCT systems, including high-resolution extremities and breast imaging. We

have also conducted preliminary investigations on the system designs that would benefit most from the proposed reconstruction method. This analysis is potentially important for future CBCT system design since the proposed reconstruction method provides an alternate (software-based) route to achieving high spatial resolution. That is, the proposed methodology may permit alternate hardware designs (e.g. the ability to use larger focal spots with higher power limits) while still achieving the desired spatial resolution. Thus, this work has the potential to both extend the clinical performance of existing CBCT systems and improve the tradeoffs and design choices for future clinical systems.

# Chapter 5

## Shift-invariant source and detector blur with a nonlinear forward model

This chapter contains work originally published in

S. Tilley II et al. “Penalized-Likelihood Reconstruction with High-Fidelity Measurement Models for High-Resolution Cone-Beam Imaging”. In: *IEEE Transactions on Medical Imaging* 37.4 (Dec. 4, 2017), pp. 988–999. ISSN: 0278-0062. DOI: 10.1109/TMI.2017.2779406. URL: <https://ieeexplore.ieee.org/document/8125700/>.

Portions of this chapter are © 2017 IEEE. Reproduced here with permission.

### 5.1 Introduction

As in chapter 4, this chapter explores the importance of SI scintillator blur, SI focal-spot blur, and correlated noise modeling in MBIR methods for CBCT resolution recovery. Of particular interest are high resolution clinical tasks such as microcalcification detection in mammography [93, 117] and trabecular bone analysis and quan-

tification in extremities imaging [118, 119], which require resolutions just beyond current system capabilities. In contrast to chapter 4, this chapter uses the nonlinear SQS MBIR algorithm derived in §3.2.1. The optimization algorithm utilizes optimization transfer and separable surrogates, similar to the algorithm in Erdoğan and Fessler [80, 81]. We evaluate the performance of this algorithm in the context of trabecular bone segmentation and derived quantitative metrics such as Trabecular Thickness (Tb.Th.).

MBIR reconstructions in this chapter use a Huber [71] potential function in the penalty term, which may permit sharper edges in the reconstructed image as compared to the quadratic penalty. Using this penalty violates the assumption that the reconstruction is locally linear, and thus prevents us from using the ESF based resolution metric from chapter 4. In other words, a Huber penalty may smooth out high-resolution structures while maintaining sharp edges, and capturing this behavior requires a different image quality metric. In this chapter we focus on a segmentation task. Images are evaluated based on segmentation accuracy and, in the case of trabecular bone segmentation, on the accuracy of derived, clinically relevant trabecular bone metrics.

The nonlinear method is first compared with the linear method studied in chapter 4. The remainder of this chapter evaluates the nonlinear method in simulation and physical test bench studies. Specifically, blur measurements from a prototype extremities quantitative CBCT (qCBCT) test bench [119] were used to construct a simulation study measuring the image quality of reconstructed line-pairs. The nonlinear MBIR algorithm with Blur and Correlated noise modeling (MBIR-BC) is compared with the same algorithm but using simpler forward models, specifically

MBIR-I with no blur in the model (Identity blur) and MBIR-B with Blur but no noise correlations. These MBIR methods are compared to PD deblurring + FDK (dFDK). To emphasize the effects of noise modeling, the simulation study used an elliptical phantom and a much lower dose than the simulation study in chapter 4. The qCBCT test bench was also used to scan a sample of human trabecular bone. Reconstructions of the trabecular bone using FDK, MBIR-I, MBIR-B, and MBIR-BC are compared to each other as well as a registered micro CT ( $\mu$ CT) scan of the same sample. Finally, quantitative metrics of Tb.Th., Trabecular Spacing (Tb.Sp.), and Bone Volume to Total Volume (BV/TV) are compared for each approach [120–122].

## 5.2 Methods

We apply the algorithm in §3.2.1 using a model of focal-spot blur and scintillator blur, where the latter adds spatial correlation to the noise. Both of these types of blur can be represented as factors of the  $\mathbf{B}$  matrix in §3.2.1:

$$\mathbf{B} \triangleq \mathbf{B}_d \mathbf{B}_s D\{\mathbf{g}\} \quad (5.1)$$

where  $\mathbf{B}_s$  is focal-spot blur,  $\mathbf{B}_d$  is scintillator blur, and  $D\{\mathbf{g}\}$  scales the data by the bare-beam photon flux per pixel. The covariance matrix was modeled as

$$\mathbf{K}_Y = \mathbf{B}_d D\{\mathbf{y}\} \mathbf{B}_d^T + D\{\boldsymbol{\sigma}_{ro}^2\} \quad (5.2)$$

where the pre-scintillator quantum noise is estimated with  $\mathbf{y}$  and  $\boldsymbol{\sigma}_{ro}$  is the standard deviation of the readout noise. The weighting matrix  $\mathbf{W}$  is equal to the inverse of  $\mathbf{K}_Y$ ,

which is typically impractical to calculate explicitly. Reconstructions in this chapter use either an iterative solver or the approximation in §3.2.1.3:

$$\mathbf{B}^T \mathbf{W} \mathbf{B} \approx \mathbf{D}\{\mathbf{g}\} \mathbf{B}_s^T \mathbf{D}\{\mathbf{y}^{-1}\} \mathbf{B}_s \mathbf{D}\{\mathbf{g}\}. \quad (5.3)$$

The inverse covariance matrix is also included in the term  $\mathbf{B}^T \mathbf{W} \mathbf{y}$ , which appears in the initialization section of the algorithm. This may be calculated once using an iterative method (e.g. CG).

### 5.2.1 Comparison with linearized method

For comparison with the linear method studied in chapter 4, the phantom in §4.2.1 was reconstructed with the nonlinear SQS method (§3.2.1). A detector blur dominated scenario was examined, specifically scenario b in Figure 4.6. Data were generated as described in §4.2.1. Reconstructions ran for 2000 iterations with 10 subsets and Nesterov acceleration. The reconstruction volume contained 0.1 mm voxels as in §4.2.1. A correlated noise model was used with

$$\mathbf{K}_Y = \mathbf{B}_d \mathbf{D}\{\mathbf{y}\} \mathbf{B}_d^T + \mathbf{D}\{\boldsymbol{\sigma}_{ro}^2\}. \quad (5.4)$$

The approximation in (5.3) was used, and  $\mathbf{B}^T \mathbf{W} \mathbf{y}$  was calculated with 1000 iterations of the preconditioned CG method [41, 123]. The preconditioning matrix was  $\mathbf{D}\{\mathbf{y} + \boldsymbol{\sigma}_{ro}^2\}$ . Resolution and variance were calculated as in §4.2.1.

### 5.2.2 System characterization of a high-resolution prototype extremities scanner

To evaluate the proposed reconstruction method, scintillator and focal-spot blur properties of a prototype extremities qCBCT test bench [119] were first characterized. This characterization was then used to ensure an accurate simulation study (§5.2.3) and to generate accurate blur models for MBIR-BC reconstructions of physical test-bench data (§5.2.4). The test bench uses an IMD RTM37 rotating anode X-ray source (with dual 0.3/0.6 focal spots) and a Teledyne DALSA Xineos-3030HR CMOS X-ray detector (100  $\mu\text{m}$  pixel pitch and CsI scintillator). The geometry emulates that of a prototype extremities qCBCT system, with a source-to-detector distance of 51 cm and a source-to-axis distance of 38 cm. X-ray focal-spot and detector blur were estimated from a pinhole image of the focal spot, ESF measurements at the detector (where focal-spot blur is negligible), and ESF measurements at isocenter. The readout noise ( $\sigma_{ro}$ ) was estimated using dark scans.

Images of a tungsten edge were used to calculate ESFs, which in turn were used to calculate MTFs as described in §4.2.2. MTFs were measured in two directions along the detector: parallel to the axes of rotation (axial) and perpendicular to the axis of rotation (trans-axial). This chapter assumes the detector scintillator MTF is radially symmetric and uses the model of Siewerdsen et al. [124] with an additional Gaussian component to capture observed low frequency characteristics:

$$MTF_d = g e^{-f^2/\sigma^2} + (1 - g)(1 + H f^2)^{-1} \quad (5.5)$$



where  $f$  is frequency and  $g$  is the relative strength of the Gaussian term (between 0 and 1). Combined with pixel sampling, the MTF model at the detector is

$$MTF_{da} = \text{sinc}(fT)MTF_d \quad (5.6)$$

where  $T$  is the pixel pitch. Because the pixels are square and the scintillator MTF is assumed to be radially symmetric, (5.6) models both the horizontal and vertical MTFs. We estimated the parameters  $g$ ,  $\sigma$ , and  $H$  by fitting (5.6) to the MTFs measured at the detector.

Pinhole images of the X-ray focal spot were acquired using a pinhole assembly (Model #07-633 Fluke Electronics, Everett, WA) with a nominal diameter of 0.010 mm. A Point Spread Function (PSF) that models the focal-spot blur experienced by an object at isocenter was found using this pinhole image. Because the pinhole was imaged at a high magnification ( $\sim 34$ ), multiple manipulations were required to obtain the final PSF. First, scale factors were found for each axes to match the shape of the pinhole image to that of the focal-spot PSF at isocenter. We chose the scaling parameters by fitting the axial and trans-axial slices of the pinhole derived MTF to the MTFs measured with the tungsten edge at isocenter. The axial and trans-axial scaling parameters are not necessarily the same due to different SV properties in these two directions, and the possibility that the pinhole was slightly misaligned. The pinhole image was resampled using these scaling parameters to produce a super-sampled PSF of the focal-spot blur at isocenter. In order to account for the aperture of each pixel, the super-sampled PSF was convolved with a  $100\mu\text{m} \times 100\mu\text{m}$  rect function corresponding to the pixel pitch and then binned and normalized to produce a PSF with  $100\mu\text{m}$  pixels (i.e., in native measurement dimensions).

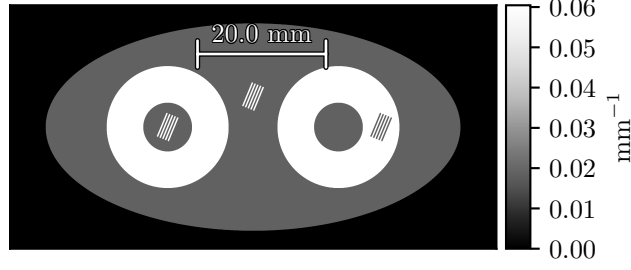


Figure 5.1: Digital phantom with line pairs and bone inserts. The background attenuation value in the oval is  $0.019 \text{ mm}^{-1}$  and the bone attenuation is  $0.060 \text{ mm}^{-1}$ . The line pair attenuation values are either  $0.060 \text{ mm}^{-1}$  (left and center) or  $0.019 \text{ mm}^{-1}$  (right). The line pair frequency is  $2.38 \text{ mm}^{-1}$ . © 2017 IEEE

### 5.2.3 Simulation study

Data were generated using the digital phantom in Figure 5.1 and a simulated system model based on the test bench geometry and characterization. Specifically, the high-resolution phantom was created with  $17.5 \mu\text{m} \times 17.5 \mu\text{m} \times 70 \mu\text{m}$  voxels (with the long axis of the voxel parallel to the axis of rotation) and high contrast line pairs with an attenuation of  $0.060 \text{ mm}^{-1}$  (bone) and a background attenuation of  $0.019 \text{ mm}^{-1}$  (fat). To model nonlinear partial volume effects, this phantom was forward projected onto a  $87.5 \text{ mm}$  detector of subpixels with a small pixel pitch ( $25 \mu\text{m} \times 100 \mu\text{m}$ ) at 720 equally spaced angles using a separable footprints model [50] for the projector. The forward model for data generation used finite integration over the extended focal spot and detector elements:

$$\mathbf{y} = \mathbf{S}\tilde{\mathbf{B}}_d \mathbf{D}\{\tilde{\mathbf{g}}\} \sum_k^{n_k} \omega_k e^{-\mathbf{A}_k \boldsymbol{\mu}} \quad (5.7)$$

where  $\mathbf{A}_k$  is a projection matrix corresponding to an individual sourcelet with relative intensity  $\omega_k$ ,  $\tilde{\mathbf{B}}_d$  is a scintillator blur (5.5) matrix which operators on subpixels,  $\mathbf{D}\{\tilde{\mathbf{g}}\}$  scales the subpixels by the photon flux, and  $\mathbf{S}$  bins the subpixels to  $100\text{ }\mu\text{m} \times 100\text{ }\mu\text{m}$  pixels. To obtain a final photon flux of  $10^3\text{ photons pixel}^{-1}$ ,  $\mathbf{D}\{\tilde{\mathbf{g}}\}$  scaled each subpixel by  $250\text{ photons pixel}^{-1}$ . The scintillator blur matrix was applied functionally using Fourier operations and nearest neighbor substitution at the boundaries. Focal-spot blur was modeled by forward projecting with 354 sourcelets derived from the super-sampled PSF from §5.2.2 (summed to one dimension). The modeled anode angle was  $17.5^\circ$ . Noisy data were generated from a Poisson distribution with the mean equal to the pre-scintillator-blur data (e.g., the vector before application of  $\tilde{\mathbf{B}}_d$ ), and these noisy data were blurred by  $\tilde{\mathbf{B}}_d$ . Finally, we added Gaussian readout noise with a standard deviation of 7.109 equivalent photons (based on bench data dark scan values) to obtain the final measurements.

In all simulation studies the reconstruction volume was  $70\text{ mm} \times 35\text{ mm}$  with  $0.07\text{ mm}$  cubic voxels (i.e., approximately equal to the demagnified pixel size). Data were reconstructed with the presented MBIR-BC algorithm incorporating the blur models derived in §5.2.2. Specifically,  $\mathbf{B}$  in (5.1) was applied, where  $\mathbf{B}_s$  and  $\mathbf{B}_d$  convolve their inputs with the focal-spot PSF (summed to one dimension) and the scintillator blur (5.5), respectively, and  $\mathbf{D}\{\mathbf{g}\}$  scales each value by  $10^3\text{ photons pixel}^{-1}$ .  $\mathbf{B}^T \mathbf{W} \mathbf{y}$  was calculated with 200 iterations of preconditioned CG as described in §5.2.1. With the low photon flux of the simulation study, the measurement data is not substantially higher than readout noise, and (5.3) is not a valid approximation. Therefore, 20 iterations of the preconditioned conjugate gradient method were used to apply  $\mathbf{W}$  every iteration. For comparison, the same optimization strategy was used with two

different forward models. The first, MBIR-B, assumed the noise was uncorrelated (i.e.,  $\mathbf{K} = \mathbf{D}\{\mathbf{y} + \sigma_{ro}^2\}$ ). The second, MBIR-I, also assumed the noise was uncorrelated, and additionally assumed there was no blur (i.e.,  $\mathbf{B} = \mathbf{D}\{\mathbf{g}\}$ ). Finally, the data were also reconstructed using Fourier domain deblurring (using the same blur models as MBIR-B and MBIR-BC) followed by FDK (dFDK) with multiple cutoff frequencies. All model-based reconstructions used the separable footprints projector [50].

Reconstructions were assessed with three metrics: bias, noise, and maximum Jaccard index (mJac) [125]. Bias and noise were chosen as traditional image quality metrics, while mJac was picked as a metric specific to trabecular bone analysis. These metrics were calculated for the set of line pairs in the middle of Figure 5.1. The terms are defined based on the truth image  $\mathbf{t}$  (binned to match voxel size), reconstructions of noiseless data  $\hat{\boldsymbol{\mu}}_{nl}(\beta, \delta)$ , reconstructions of noisy data  $\hat{\boldsymbol{\mu}}(\beta, \delta)$ , and the number of voxels in the ROI ( $N_{roi}$ )

$$\text{bias}(\beta, \delta) = \|\hat{\boldsymbol{\mu}}_{nl}(\beta, \delta) - \mathbf{t}\|/N_{roi} \quad (5.8)$$

$$\text{noise}(\beta, \delta) = \|\hat{\boldsymbol{\mu}}(\beta, \delta) - \hat{\boldsymbol{\mu}}_{nl}(\beta, \delta)\|/N_{roi}. \quad (5.9)$$

These metrics were calculated in an ROI encompassing the central line pairs. To calculate mJac, a truth segmentation  $\mathbf{t}_b$  was calculated by thresholding the truth image  $\mathbf{t}$  at  $0.040 \text{ mm}^{-1}$  (the average attenuation value of fat and bone). The reconstruction  $\hat{\boldsymbol{\mu}}$  was thresholded by a value  $t$  for 101 values of  $t$  between the attenuation values of fat and bone, inclusive. The mJac value for a given reconstruction is the maximum Jaccard index between the truth segmentation and the segmented  $\hat{\boldsymbol{\mu}}$  over all  $t$ :

$$\text{mJac}(\beta, \delta) = \max_t [\text{jaccard}(\hat{\boldsymbol{\mu}}(\beta, \delta) > t, \mathbf{t}_b)]. \quad (5.10)$$

The Jaccard index ranges from zero to one, with one indicating perfect correspondence with the truth segmentation.

### 5.2.3.1 Parameter sweep

This work used a Huber penalty for the regularizer (R) [71] based on (2.48) and a four voxel neighborhood (not the isotropic Huber penalty). The Huber penalty has an additional parameter,  $\delta$ , which is the value below which pixel differences will be penalized quadratically. We conducted a parameter sweep over  $\beta$  and  $\delta$  in order to pick an appropriate value for  $\delta$ . Phantom data were reconstructed using MBIR-BC and MBIR-I. Additionally, two photon fluxes were used:  $10^3$  photons pixel<sup>-1</sup> (low photon flux) to match the simulation study, and  $4 \times 10^4$  photons pixel<sup>-1</sup> (high photon flux) to approximate the bench study. The high photon flux data utilized the covariance matrix approximation in (5.3). Both algorithms used 501 iterations, 10 subsets, and momentum-based acceleration. The mJac metric was calculated for each  $(\beta, \delta)$  pair.

### 5.2.3.2 Algorithm comparison

dFDK, MBIR-I, MBIR-B, and MBIR-BC were compared by analyzing the bias/noise tradeoff and mJac over a range of regularization strengths. A large number of iterations (20 000) were used to ensure nearly converged estimates. We utilized a scheduling approach for acceleration and the number of subsets, with 50 iterations of acceleration and 10 subsets, followed by 50 iterations of acceleration and 5 subsets, 10 000 iterations of acceleration and no subsets, and finally 9000 iterations of no acceleration and no subsets. We used a Huber penalty with  $\delta = 10^{-2}$  mm<sup>-1</sup>. A bias/noise plot and a plot of mJac as a function of  $\beta$  (or cutoff frequency in the case

of dFDK) were analyzed for the center set of line pairs in Figure 5.1 and each of the four reconstruction methods. For direct visual comparison we present reconstructions of the line pairs, along with the corresponding optimum segmentations.

#### 5.2.4 Extremities prototype experiment

To investigate the performance of the proposed algorithm on physical data, a human iliac-crest bone-biopsy core was scanned on the test bench described in §5.2.2. The bone sample comprised both trabecular and cortical bone.  $\mathbf{B}$  was modeled as described previously (5.1), with  $\mathbf{B}_s$  and  $\mathbf{B}_d$  representing applications of the models developed in §5.2.2. Blur matrices were applied functionally as in the simulation study.  $\mathbf{B}_d$  was applied using Fourier methods and  $\mathbf{B}_s$  was applied using convolution. The covariance approximation (5.3) was used.  $D\{\mathbf{g}\}$  was a matrix which scaled the values of each pixel by the estimated bare-beam photon flux and each frame by a normalization factor (details are given in Appendix A). The projection operator  $\mathbf{A}$  used the separable footprints algorithm as in the simulation study. The MBIR methods used the same readout noise value as the simulation study.

Reconstructions were initialized with FDK and ran for 650 iterations with 10 subsets to obtain well-converged estimates.  $\mathbf{B}^T \mathbf{W} \mathbf{y}$  was calculated as in §5.2.1 with 200 iterations. The trabecular bone was also reconstructed with MBIR-I and MBIR-B using the same number of iterations and subsets. Momentum-based acceleration was applied in all cases. A Huber regularization penalty based on (2.48) was used with a range of penalty strengths and  $\delta$  equal to  $1 \times 10^{-3} \text{ mm}^{-1}$  [71]. The penalty neighborhood was the eight nearest voxels. We also computed an FDK reconstruction (frequency cutoff at Nyquist and no additional apodization) for comparison. In all

cases the reconstruction volume was  $60 \text{ mm} \times 60 \text{ mm} \times 30 \text{ mm}$  with  $0.075 \text{ mm}$  voxels (i.e., voxel size was approximately equal to the demagnified pixel size). The projection area was  $120 \text{ mm} \times 25 \text{ mm}$  with  $0.1 \text{ mm}$  pixel pitch and 720 frames.

Reconstructions of qCBCT data were compared with high resolution  $\mu\text{CT}$  data using mJac (5.10), Trabecular Thickness (Tb.Th.), Trabecular Spacing (Tb.Sp.), and Bone Volume to Total Volume (BV/TV) [120–122]. Bench data were acquired at 90 kV and 90.7 mAs. The  $\mu\text{CT}$  data were acquired on a SkyScan 1172 CT scanner (Bruker microCT, Kontich, Belgium) at 65 kV. To find the “true” trabecular bone segmentation with the same voxel size as the reconstructions, the  $\mu\text{CT}$  image of the trabecular bone was first binned from  $0.0076 \text{ mm voxel}^{-1}$  to  $0.0380 \text{ mm voxel}^{-1}$  and then registered with an FDK reconstruction of the qCBCT bench data. The registration algorithm also reduced the voxel size of the  $\mu\text{CT}$  image to match that of the FDK reconstruction (and therefore the model-based reconstructions). The resulting image is referred to as  $\mu\text{CTmv}$  for matched voxel size (mv). The Elastix software package [126] registered the images using the binned  $\mu\text{CT}$  reconstruction as the moving image, a similarity transformation, and the Mutual Information Metric. A mask was used to limit the evaluation of the registration metric to a sub-volume containing only trabecular bone. The  $\mu\text{CTmv}$  image was thresholded to generate the “truth segmentation.” The threshold value was chosen using a visual histogram inspection. The FDK, MBIR-I, MBIR-B, and MBIR-BC reconstructions were thresholded at 101 equally spaced attenuation values between  $0 \text{ mm}^{-1}$  and  $0.07 \text{ mm}^{-1}$ , inclusive, to calculate mJac. The mJac metric was only computed within the trabecular region (using the same mask as the registration). This metric was plotted for each MBIR reconstruction method as a function of regularization strength. The most accurate

segmented reconstruction from each MBIR method was selected as the one with the highest mJac over all regularization strengths, and the most accurate reconstruction was selected as the corresponding pre-thresholded image. The optimal FDK segmentation was defined as the one with the highest mJac over all threshold values. A Tb.Th. map was calculated from the optimal segmented reconstruction for each reconstruction method and the  $\mu$ CTmv image. Tb.Th. and Tb.Sp. were calculated with BoneJ [127], a plug-in for ImageJ [128]. Average Tb.Th., Tb.Sp., and BV/TV were computed over the area defined by the registration/mJac mask. The Tb.Th. and BV/TV of the original  $\mu$ CT image (before binning and registration) were also calculated using the same mask (transformed to the  $\mu$ CT coordinates). (Tb.Sp. was not calculated for this image due to computation constraints.) Slices of the  $\mu$ CT scan and  $\mu$ CT Tb.Th. map were transformed using the registration parameters calculated previously, facilitating visual comparison to the other methods. Optimal reconstructions, optimal segmentations, and Tb.Th. maps for FDK, MBIR-I, MBIR-B, and MBIR-BC were compared with corresponding  $\mu$ CTmv and original  $\mu$ CT images.

## 5.3 Results

### 5.3.1 Comparison with linearized method

The resolution-variance tradeoff between the nonlinear SQS method and the linear method from chapter 4 are shown in Figure 5.2. The two methods are roughly equivalent at the low noise, low resolution side of the plot. The linear method has a resolution limit at about 0.15 mm, likely due to the regularization in the deblurring



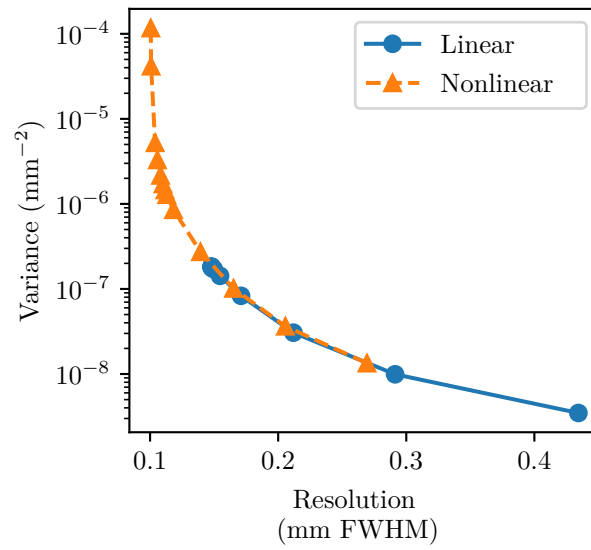


Figure 5.2: Resolution-variance tradeoff of the nonlinear and the linear reconstruction methods.

preprocessing step. In contrast, the nonlinear method has no such limit and is able to achieve much higher resolutions.

### 5.3.2 System characterization of a high-resolution prototype extremities scanner

The system characterization results are shown in Figure 5.3. The measured MTFs are plotted in Figure 5.3A and show that, for the prototype test bench, detector blur is a larger effect than focal-spot blur. Because detector blur (scintillator blur and pixel aperture blur) is the same at the detector and at isocenter, the difference between the isocenter MTF and the detector MTF is due to focal spot blurring. This difference is relatively small, indicating that this system is dominated by detector blur. The axial and trans-axial detector MTFs are almost equivalent, supporting the radially symmetric assumption used in the model. The MTF models (Figure 5.3B) strongly match the measured data.

The focal-spot pinhole image was scaled and resampled to match the magnitude of the blur experienced by an object at isocenter (Figure 5.3). The focal spot has a primary trapezoidal component with a higher intensity on two of the edges, similar to those observed on the rectangular focal spot studied in chapter 4. This focal spot has an additional, lower intensity, trapezoidal component with a different orientation, creating a cross pattern. Because of this complicated structure, we decided to derive a PSF directly from the pinhole image instead of using a mathematical model. The scale bar illustrates that the focal spot blur is relatively small (about the size of a detector pixel) for an object at isocenter.

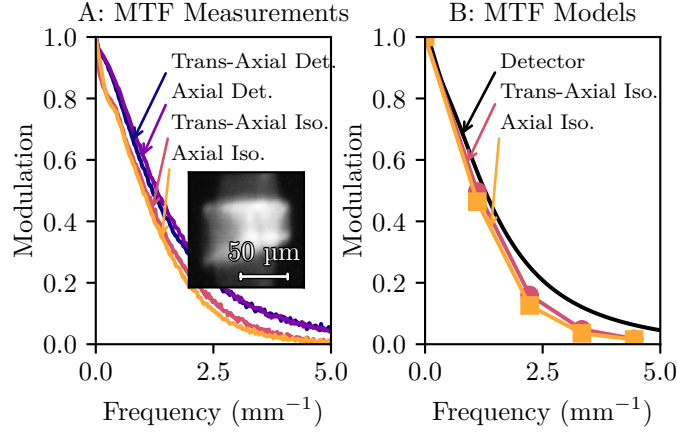


Figure 5.3: System characterization results. A: Measured axial and trans-axial MTF slices derived from tungsten edge responses. Inset: Pinhole image of the X-ray focal spot, resampled to match the PSF of the focal-spot blur experienced by an object at isocenter. B: MTF models. The detector model has the form given in (5.6). The isocenter models are slices of the MTF derived from the final PSF multiplied by the detector MTF model. © 2017 IEEE

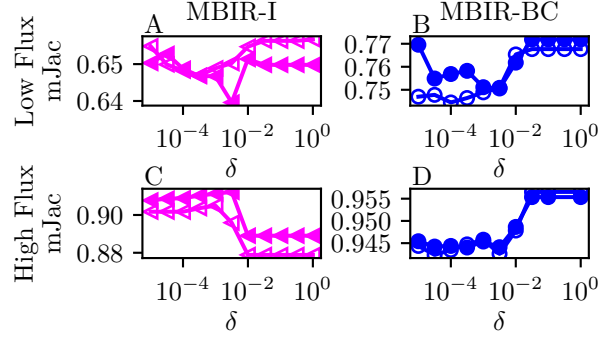


Figure 5.4: Parameter sweep results. Each point is the maximum mJac over  $\beta$  for a given  $\delta$ , reconstruction method, and noise realization. The left column is MBIR-I and the right column is MBIR-BC. The top row is the low photon flux results and the bottom row is the high photon flux results. © 2017 IEEE

### 5.3.3 Simulation study

#### 5.3.3.1 Parameter sweep

Figure 5.4 shows the maximum mJac over  $\beta$  as a function of  $\delta$  for two noise realizations. These results indicate that mJac is relatively insensitive to  $\delta$  (compare the ranges in the plots in Figure 5.4 to those in Figure 5.5). This is potentially due to the fact that mJac is insensitive to edge smoothness. The measurements are relatively noisy at this scale, especially with low gain and low  $\delta$ . For MBIR-BC the optimal  $\delta$  is higher than any contrast in the phantom, indicating a “near” quadratic penalty is ideal. The simulation data were reconstructed with  $\delta = 10^{-2} \text{ mm}^{-1}$  (where mJac values are high and stable) and the bench data with  $\delta = 10^{-3} \text{ mm}^{-1}$  (which potentially gives a slight advantage to MBIR-I).

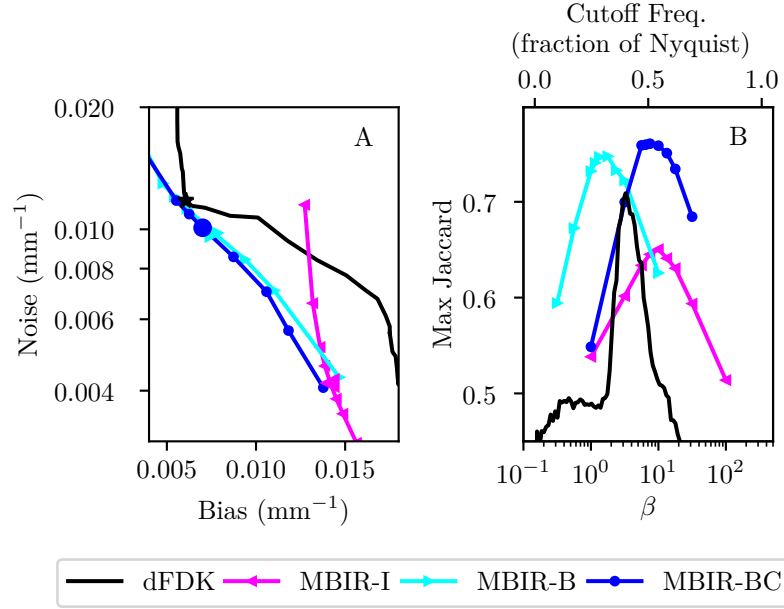


Figure 5.5: Bias/noise (A) and mJac (B) plots. The large markers in (A) correspond to the maximum mJacs in (B). The frequency cutoffs for the dFDK data in B (x-axis) are indicated at the top of the plot. © 2017 IEEE

### 5.3.3.2 Algorithm comparison

Figure 5.5 shows the bias/noise trade-off (A) and maximum Jaccard index (mJac) (B) for the center set of line pairs. Results are similar but less dramatic for the other two sets of line pairs (not shown). At lower regularization strengths, reconstructions of noiseless data are more accurate (lower bias), but reconstructions of noisy data result in noisy reconstructions. On the other hand, for higher regularization strengths, noise is suppressed at the cost of increased smoothing/blurring of the image, imparting bias. Methods with blur modeling (MBIR-BC and MBIR-B) were able to achieve a lower bias than the method without blur modeling (MBIR-I).

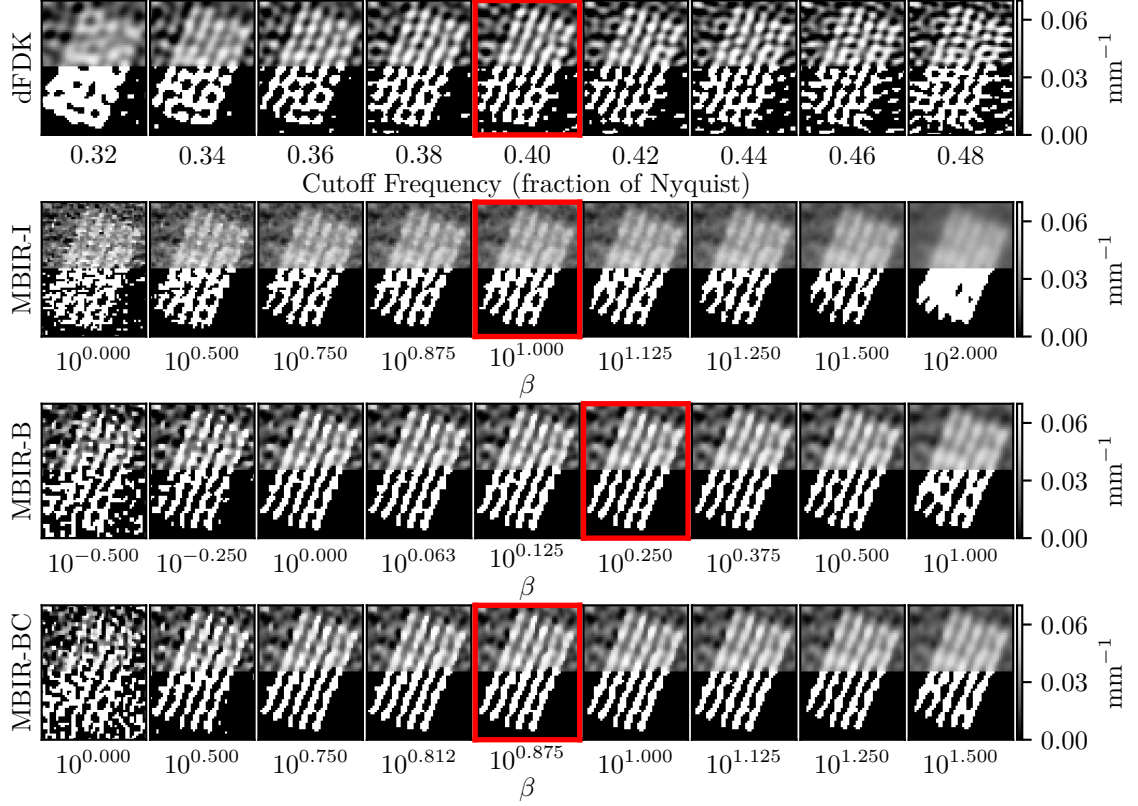


Figure 5.6: The center line pairs from the reconstructions in Figure 5.5. Each row corresponds to a different reconstruction method. Note that different values of  $\beta$  were used for different MBIR methods. The reconstructions with the red border correspond to the ones with the maximum mJac in Figure 5.5(B). The lower half of each image shows the best segmentation for that  $\beta$ /cutoff (i.e., the one resulting in the maximum Jaccard index over threshold values). © 2017 IEEE

MBIR-BC and MBIR-B have a similar bias/noise trade-off, with MBIR-BC showing a slight advantage. Because it does not include a blur model, MBIR-I encounters a bias limit at about  $0.013 \text{ mm}^{-1}$ . dFDK can achieve lower bias reconstructions than MBIR-I, but suffers from increased noise as compared to MBIR-B and MBIR-BC. However, there is a small range (near the best dFDK mJac performance) where dFDK performs comparably to MBIR-B and MBIR-BC.

Figure 5.5B shows similar trends. For each method the “best” reconstruction is defined as the one with the maximum mJac. This maximum mJac value is used to compare the different methods. MBIR-BC results in the best reconstruction, followed by MBIR-B, dFDK, and MBIR-I. The advantage of MBIR-BC over MBIR-B is more apparent in the mJac plot than the bias/noise plot.

Figure 5.6 shows reconstructions of the center line pairs. The bottom half of each image shows the optimal segmentation (i.e., the one resulting in the best mJac). MBIR-I results in the worst performance with low contrast line pairs. The line pairs in the dFDK reconstruction are more distinct but both the line pairs and the background exhibit increased noise. Finally, the MBIR-B and MBIR-BC reconstructions have less noise than the dFDK reconstruction without sacrificing line pair visualization. The difference between the MBIR-BC and MBIR-B reconstructions is subtle, but can be appreciated in the thresholded image, where the MBIR-BC method results in thicker and more uniform line pairs. The noise difference between MBIR-BC/MBIR-B and dFDK is particularly evident in the background of the segmented image, where the dFDK reconstruction contains noisy values above the segmentation threshold, resulting in a “splotchy” segmented background image. Qualitatively, the visually

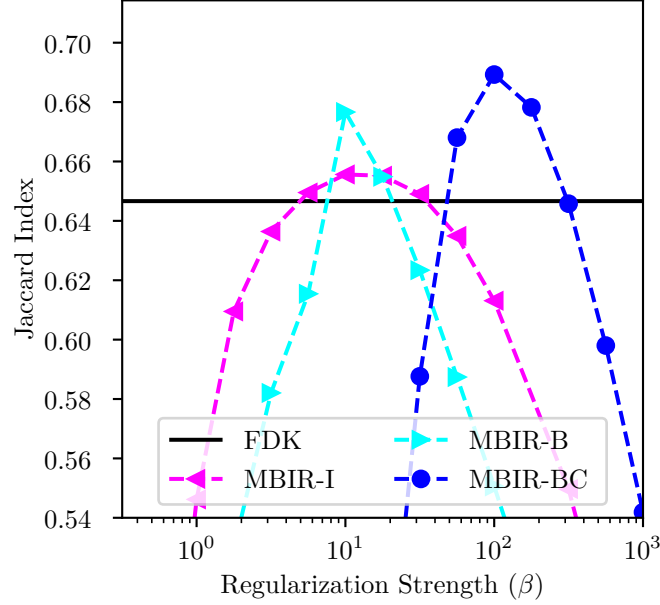


Figure 5.7: Maximum Jaccard (mJac) for each reconstruction method and regularization strength for the test bench-data. © 2017 IEEE

“best” reconstructions correspond to those with the best mJac (indicated by a red outline), confirming the suitability of this metric.

### 5.3.4 Extremities prototype experiment

This section presents the results of the prototype test-bench study with human trabecular bone. The mJac for each reconstruction is shown as a function of regularization strength in Figure 5.7. The MBIR-BC method is able to achieve the highest maximum mJac, followed by MBIR-B, MBIR-I, and FDK (indicated by the black line). The optimal segmentation thresholds for the most accurate MBIR-I, MBIR-B, and MBIR-BC reconstructions (i.e., those with the maximum mJac over regularization



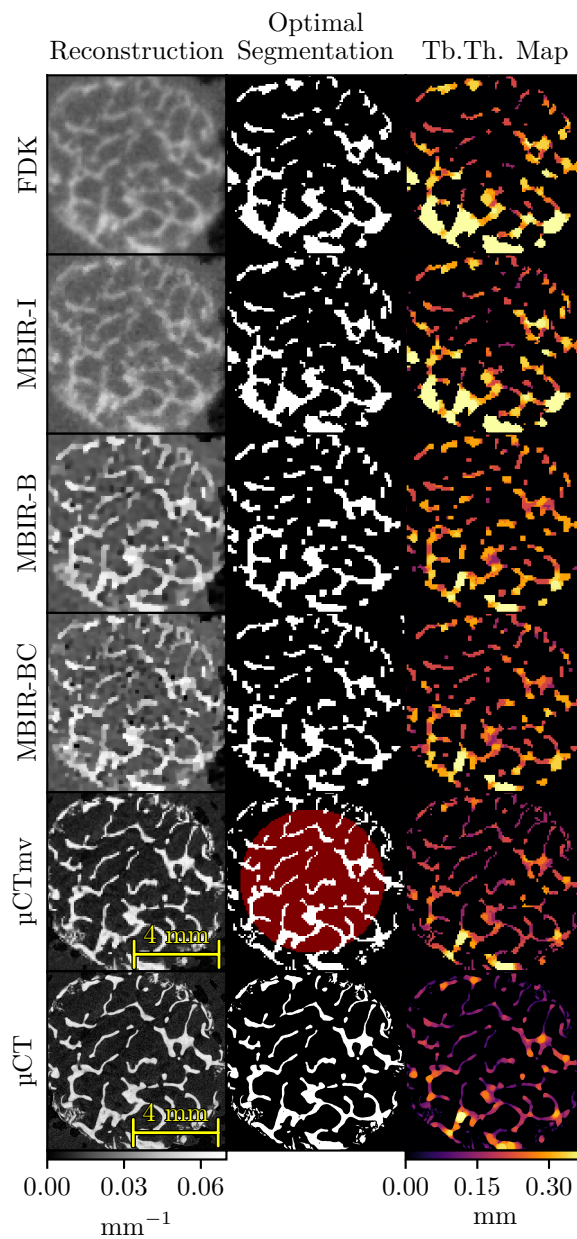


Figure 5.8: Axial slice of trabecular bone reconstructions. Rows correspond to different reconstruction methods. The red background in the  $\mu\text{CTmv}$  segmentation image indicates a slice of the mask used for registration and metric calculation. Note the attenuation values of the  $\mu\text{CT}$  and  $\mu\text{CTmv}$  scans are arbitrary and do not correspond to the gray-level map on the bottom. © 2017 IEEE

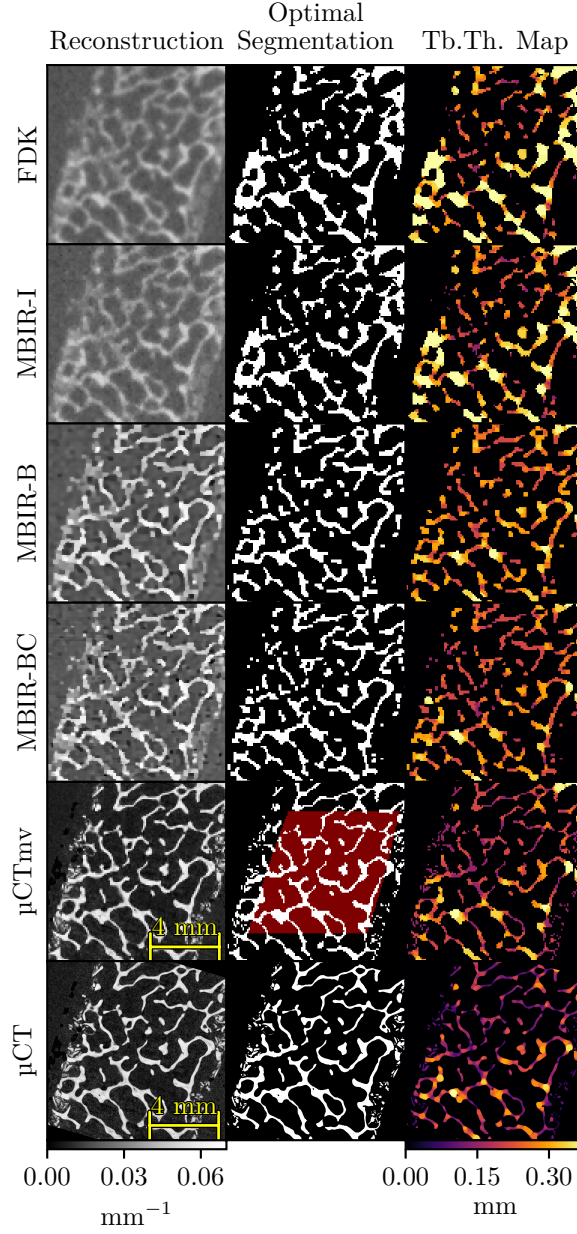


Figure 5.9: Trans-axial slice of trabecular bone reconstructions.  $\mu\text{CT}$  and  $\mu\text{CTmv}$  attenuation units are arbitrary. © 2017 IEEE

strength, corresponding to the maxima in Figure 5.7) are  $0.0322 \text{ mm}^{-1}$ ,  $0.0385 \text{ mm}^{-1}$ , and  $0.0378 \text{ mm}^{-1}$ , respectively.

The most accurate reconstructions are shown in Figure 5.8 and Figure 5.9, along with the corresponding segmented trabecular bone images (using the optimal thresholds) and Tb.Th. maps. The FDK reconstruction, the registered  $\mu$ CT reconstruction with Matched Voxel size ( $\mu$ CTmv), and the registered  $\mu$ CT reconstruction slices with the original  $\mu$ CT voxel size ( $\mu$ CT) are also included. While the  $\mu$ CT reconstruction is the best approximation of the true image volume, the  $\mu$ CTmv image is a better approximation of the best achievable reconstruction at the chosen voxel size.

The MBIR-BC reconstruction has improved resolution as compared to the MBIR-B, MBIR-I, and FDK reconstructions, with sharper trabecular bone boundaries. Consequently, MBIR-BC results in a more accurate trabecular segmentation. This is particularly evident when comparing to FDK and MBIR-I, where the segmentation images contain less detailed trabeculae. This effect is well illustrated in the Tb.Th. maps. The FDK and MBIR-I maps show fewer, thicker trabeculae, while the MBIR-BC map is similar to the  $\mu$ CTmv and  $\mu$ CT maps with thinner and more numerous trabeculae. The MBIR-B map is more similar to the MBIR-BC map, but still contains thicker trabeculae. The mean Tb.Th. calculations (Table 5.1) confirm this observation, with MBIR-BC resulting in a Tb.Th. value closer to those of  $\mu$ CTmv and  $\mu$ CT than do FDK, MBIR-I, and MBIR-B. In contrast, MBIR-BC shows no advantage with respect to Tb.Sp. and BV/TV. BV/TV values are similar for all methods, suggesting the loss of fine trabecular structures and the increase in apparent trabecular thickness tend to cancel each other out in terms of BV/TV. The same mechanism is a potential cause for the better accuracy of the FDK and MBIR-I mean Tb.Sp. val-

Table 5.1: Trabecular bone metric results. © 2017 IEEE

	mean Tb.Th. (mm)	mean Tb.Sp. (mm)	BV/TV
FDK	0.335	0.860	0.214
MBIR-I	0.309	0.824	0.216
MBIR-B	0.271	0.785	0.224
MBIR-BC	0.255	0.775	0.219
$\mu$ CTmv	0.232	0.826	0.189
$\mu$ CT	0.193	—	0.190

ues: the spacing lost to thicker trabeculae is recovered by the loss of fine trabeculae. In contrast, MBIR-BC does a better job in general at recovering small trabeculae, but still reconstructs trabeculae as thicker than they should be, reducing the mean Tb.Sp. Optimizing reconstructions based on one of these metrics instead of mJac may improve metric accuracy, or show that MBIR-BC is ill-suited to that metric.

## 5.4 Discussion

In this chapter we studied the generalized reconstruction algorithm from §3.2.1 in a scintillator blur dominated scenario in simulation and on a prototype CBCT test bench. These studies show that high fidelity modeling with this MBIR-BC method can improve resolution and produce more accurate reconstructions as compared to more traditional models and FDK approaches. The improved accuracy of the trabecular bone segmentation and Tb.Th. measurement suggest that MBIR-BC can increase the accuracy of quantitative metrics used to study trabecular bone health [14, 129, 130]. Additionally, the improved bias/noise trade-off suggests that MBIR-BC produces more accurate attenuation values than dFDK and MBIR-I,

which is critical for quantitative CT [131] (however, note that bias includes both attenuation value error and blurring).

The nonlinear method discussed in this chapter is preferable to the linear method in chapter 4 for high resolution reconstructions. It is likely the frequency cutoff in the preprocessing step in chapter 4 makes resolution recovery difficult or impossible beyond a certain point. Whether to use the linear or the nonlinear method depends on the target resolution, imaging task, preprocessing technique, and computation constraints. Future work could expand upon the preliminary comparison in this chapter by varying these parameters (e.g., using wiener filter deblurring) and increasing the number of iterations in each method to ensure converged estimates.

As algorithms enable increased resolution, proper choice of voxel size will be critical [132]. If one were not attempting resolution recovery, the ideal voxel size would be about the size of the demagnified system blur (0.33 mm for this system). (The large system blur relative to pixel pitch results in most CBCT systems binning projection data to increase effective pixel pitch.) In this work voxel size was approximately equal to the demagnified pixel pitch (i.e., much smaller than the limit imposed by system blur). Angular sampling also effects voxel size. CT data is almost always angularly undersampled. To limit the effect of undersampling we acquire data in half angle increments (double the sampling of traditional CBCT). In summary, we believe the choices of voxel size and angular sampling in this work are appropriate for the system blur studied, and allow a fair comparison of the different MBIR system models.

While not a focus of this study, we note that incorporating blur into the model decreases the convergence rate. In order to compare nearly converged solutions, many iterations were used. (This is particularly important for regularization sweeps, as dif-

ferent regularization strengths may require different numbers of iterations.) However, we believe that tuning the subset/acceleration schedule can improve the convergence rate in practice. With the current (only partially optimized) implementation, the bench data reconstructions took approximately 10 min to 15 min per iteration. (Note the reconstruction volume was much larger than the ROI shown.) When the ROI is small, as in this chapter, a multi-resolution reconstruction method may be employed to decrease iteration time [133].

The main limitation of the objective function presented is the application of the inverse covariance matrix, which may be computationally expensive if noise correlations are modeled. In the bench data study, we make assumptions to avoid computing this inversion every iteration, but such assumptions will not always be valid (as in the simulation study). In such cases, one may need to make additional approximations to reduce computation time. Additionally, patient motion may be a resolution limiting factor on high-resolution systems. However, if patient motion is properly estimated, it may be incorporated into the system matrix to reduce this image degradation without altering the presented algorithm [134].

The success of MBIR methods illustrates the importance of high-fidelity modeling in CT reconstruction. Accurate modeling of CBCT systems, enabled by the proposed method, improves image quality and permits high-resolution tasks such as microcalcification detection and analysis of trabecular bone morphology. In addition to improving the capabilities of current CBCT systems, this method has the potential to alter the trade-offs between hardware/geometry choices and image quality, potentially effecting future CBCT system designs, including those that aren't necessarily aiming for high resolution.

# Chapter 6

## Shift-variant focal-spot blur and gantry-motion blur

This chapter contains work originally published in

Steven Tilley II et al. “Modeling Shift-Variant X-Ray Focal Spot Blur for High-Resolution Flat-Panel Cone-Beam CT”. in: *Proc. 4th Intl. Mtg. on Image Formation in X-Ray CT*. 2016,

Steven Tilley II, Wojciech Zbijewski, and J. Webster Stayman. “High-Fidelity Modeling of Shift-Variant Focal-Spot Blur for High-Resolution CT”. in: *Int’l Mtg. Fully 3D Image Recon. in Radiology and Nuc. Med.* Xi’an, China, June 18, 2017,

and

Steven Tilley II et al. “High-Fidelity Modeling of Detector Lag and Gantry Motion in CT Reconstruction”. In: *Proc. 5th Intl. Mtg. on Image Formation in X-Ray CT*. vol. submitted. 2018.

Reproduced here with permission.

## 6.1 Introduction

As has been shown in previous chapters, modeling physical effects with MBIR has the potential to dramatically improve resolution and image quality. Some effects, such as focal-spot blur and gantry motion blur, result in location-dependent, or Shift Variant (SV), image quality properties. SV blur precludes traditional convolutional modeling, complicating analysis and deblurring. Application specific CT systems are becoming more widespread, and can vary dramatically in geometry and hardware choices. SV blur modeling may be particularly important in some of these systems, particularly those with high magnification. For example, smaller, more economic systems may opt for a fixed-anode X-ray tube to decrease cost, often resulting in a larger focal-spot and more dramatic SV blur properties. In this chapter we model and analyze SV imaging properties of high-resolution CT systems caused by focal-spot blur and gantry motion blur. MBIR is used to improve image quality by incorporating models of these effects into the reconstruction algorithm.

The X-ray source can be a significant source of location-dependent image quality in CBCT. X-ray tubes emit X-rays from a small area (focal spot) on a tungsten anode. To enable better heat dissipation (and permit higher current settings for lowering noise or decreasing acquisition time), larger focal spots are often employed. However, the anode is angled such that the focal spot has a small cross-sectional area when viewed from isocenter. Due to this angulation, the apparent size and shape of the focal spot can vary dramatically with location, contributing different amounts of blur to data depending on location. The location-dependence is more pronounced for larger cone- and fan-angles. Modeling SV focal-spot properties due



to anode angulation may therefore be important for systems with high-magnification and objects that cover a large fan/cone angle. Additionally, blur induced by the focal spot is subject to variable magnification for positions parallel to the source-detector axis. This effect will be most pronounced in systems where the object has a large extent along this axis (relative to the source-detector distance). Thus, source blur due to the X-ray focal spot is complex with significant potential shift-variance throughout the FOV. Previous work has incorporated SV focal-spot blur models into MBIR in 2D simulation studies [51, 55, 56].

Gantry motion blur is due to movement of the gantry during X-ray exposure and detection. This blur occurs within a single measurement — effectively integrating an arc of projection images based on how far the source and detector have rotated during an integration period. Such blur exhibits as an azimuthal smearing of the CT volume and is most pronounced toward the edge of the FOV. Gantry motion effects have been addressed in hardware (e.g., collecting data with a step-and-shoot protocol or more complicated methods [138]) and in software (e.g., incorporating a blur model into a linearized forward model for MBIR [57]).

This chapter contains multiple experiments to assess the impact of SV blur on image quality and the advantages gained with advanced modeling and MBIR. For focal-spot blur, simulation and bench studies are conducted using a simplified SV model that ignores depth dependence. A simulation study is then conducted using a small phantom to simplify computation while assessing image quality at various points throughout a 3D volume with different X-ray tube orientations. This model includes depth dependent effects. A full sourcelets model is then applied to physical data of a line pair phantom to assess improvements on a real system. For gantry

motion blur, a SV model is incorporated into MBIR and used to improve image quality in a simulation study and a physical data study.

All MBIR reconstructions in this chapter use the nonlinear method in §3.2.1 with the mean forward model

$$\bar{\mathbf{y}} = \mathbf{B} \exp(-\mathbf{A}\boldsymbol{\mu}). \quad (6.1)$$

## 6.2 Focal-spot blur modeling

Three focal spot blur models were assessed multiple systems. The three focal-spot blur studies use different modeling approximations. The first study only models blur parallel to the detector (Projection Domain (PD) blur), and ignores variable magnification. It also assumes the focal-spot distribution is rectangular and uniform. The second assumes the imaged object is small relative to the shift-variance, permitting a SI approximation for each projection angle. The third approach uses a full sourcelets model with a custom projector to model both PD blur and variable magnification for arbitrarily sized objects. The models in the second and third studies permit arbitrary focal-spot distributions.

### 6.2.1 Methods

#### 6.2.1.1 Projection Domain blur modeling

**6.2.1.1.1 Mathematical derivation** In this section we model the SV focal-spot blur along directions parallel to the detector. The model approximates a depth-independent blur. Therefore, the blur model can be included in the  $\mathbf{B}$  term in (6.1). This approximation is appropriate when the object covers a wide fan/cone angle but

is small relative to the source-detector distance. To estimate a continuous source-blur model for discrete inputs and outputs, we use nearest neighbor interpolation to create a continuous approximation of the input image, integrate with a location-dependent impulse response, then discretize the signal using a rectangular kernel with the dimensions of a pixel and sampling at pixel centers. The full operation is:

$$g[k, l] = \int_{x,y} \int_{\xi,\eta} \sum_{i,j} f[i, j] \text{rect}\left(\frac{\xi - iT_x}{T_x}, \frac{\eta - jT_y}{T_y}\right) T_x T_y h(x, y; \xi, \eta) \text{rect}\left(\frac{x - lT_x}{T_x}, \frac{y - kT_y}{T_y}\right) d\xi d\eta dx dy \quad (6.2)$$

where  $f$  and  $g$  are the input and output images,  $T_x$  and  $T_y$  are the pixel widths along the corresponding directions and  $h(\cdot, \cdot; \xi, \eta)$  is the impulse response of a point source at  $\xi, \eta$ . Equation (6.2) can be approximated by discretizing variables and assuming  $h$  is constant over small displacements. We sample  $x$  and  $\xi$  at intervals of  $T_x/s$  and  $y$  and  $\eta$  at intervals of  $T_y/s$ , where the sampling factor  $s$  is an odd integer (the number of samples is equal to  $2s-1$ ). Applying these approximations and simplifying leads to:

$$g[k, l] \approx \sum_{j,i,a,b} f[i, j] |1 - a| |1 - b| h((a + l)T_x, (b + k)T_y; iT_x, jT_y) T_x T_y / s^2 \quad (6.3)$$

where  $a$  and  $b$  range from  $-(s-1)/s$  to  $(s-1)/s$  in increments of  $1/s$ . The transpose operation (e.g. for  $\mathbf{B}^T$ ) requires switching the indices for  $f$  and  $g$ , and summing over  $k, l$  instead of  $i, j$ .

The impulse response ( $h$ ) centered at a given point  $(u_c, v_c)$  is assumed to be a binary function, with values either equal to 0 or  $k = \text{area}(h(\cdot, \cdot; u_c, v_c))^{-1}$ . To determine the value of  $h(u, v; u_c, v_c)$ , the point  $(u, v)$  is backprojected through a

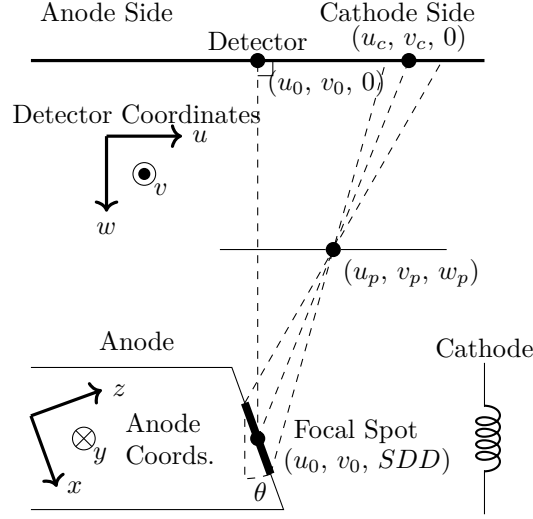


Figure 6.1: Geometry used to calculate the focal-spot blur impulse response. The focal spot is represented by the bold line on the side of the anode. All coordinates are in detector coordinates. The origin of the anode coordinate system is at  $(u_0, v_0, SDD)$ .

pinhole onto the anode. A two dimensional cross section of the geometry is illustrated in Figure 6.1. The pinhole is placed a distance  $w_p$  from the detector and along the line connecting  $(u_c, v_c)$  with the center of the focal spot. If the backprojected point is in the rectangular focal spot,  $h(u, v; u_c, v_c) = k$ , otherwise  $h(u, v; u_c, v_c) = 0$ . The area of  $h$  was found by forward projecting the corners of the focal spot through the pinhole, and applying Bretschneider's formula to the resulting points [139].

**6.2.1.1.2 Simulation study** Data were generated using the digital extremities phantom in Figure 6.2. Line integrals were generated from a high-resolution truth image ( $3300 \times 2300$  image of  $30 \mu\text{m}$  voxels) projected onto a one-dimensional detector with 8192 subpixels and a  $48.5 \mu\text{m}$  pixel pitch. A high-magnification geometry was

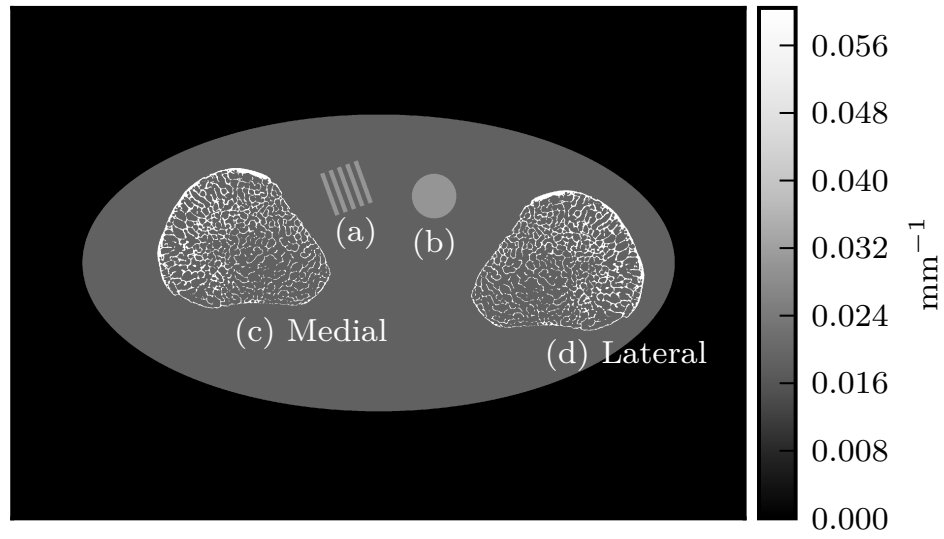


Figure 6.2: Digital extremities phantom with medial (c) and lateral (d) bones, line pairs (a), and a uniform disc (b).

used, with a source-detector distance of 1200 mm, a source-axis distance of 250 mm, and an angular spacing of  $0.5^\circ$ . These line integrals were downsampled by a factor of four to give a simulated pixel pitch of  $194\text{ }\mu\text{m}$ . Measurements were generated from the downsampled line integrals ( $\ell$ ) according to:

$$\bar{\mathbf{y}} = \mathbf{B}_s I_0 \exp(-\ell) \quad (6.4)$$

$$\mathbf{y} = \bar{\mathbf{y}} + \mathcal{N}(0, \mathbf{D}\{\bar{\mathbf{y}}\}) + \mathcal{N}(0, \mathbf{D}\{\boldsymbol{\sigma}_{ro}^2\}) \quad (6.5)$$

where  $I_0$  is  $10^4$  photons pixel $^{-1}$ ,  $\mathbf{B}_s$  is the focal-spot blur operator (we assume there is no detector blur), and the readout-noise standard deviation ( $\boldsymbol{\sigma}_{ro}$ ) is 3.32 equivalent photons for each measurement. The focal-spot was modeled as a  $5\text{ mm} \times 0.8\text{ mm}$  rectangle on a  $14^\circ$  anode with the anode-cathode axis parallel to the detector row. The sampling factor ( $s$ ) was equal to 41. (Note that  $\mathbf{B}_s I_0$  is equivalent to  $\mathbf{B}$  in (6.1).) Data were generated using two short scans (short-1 and short-2) spaced  $180^\circ$  apart, and a full scan. The short-1 scan placed the medial bone (Figure 6.2c) predominately on the anode side, and the lateral bone (6.2d) predominately on the cathode side. The reverse is true for the short-2 scan.

Data from each scan were reconstructed using the nonlinear SQS algorithm with three models for focal-spot blur: identity (no blur), SI blur, and SV blur. The sampling factor ( $s$ ) used in reconstructions was 11. Data were reconstructed into a  $1650 \times 1150$  volume of  $60\text{ }\mu\text{m}$  voxels using a Huber penalty ( $\delta = 10^{-4}$ ). The covariance matrix was modeled as  $\mathbf{D}\{\mathbf{y} + \boldsymbol{\sigma}_{ro}^2\}$ . Nesterov acceleration was used with 20 ordered subsets.

The accuracy of trabeculae segmentation in the medial and lateral bones was used as a measure of image quality. The truth segmentation for each bone was found by downsampling the high-resolution phantom to match the reconstruction volume dimensions and thresholding at the average attenuation of bone and fat. Data were reconstructed at several penalty strengths and thresholded at regularly spaced values between the attenuation values of fat and bone. Accuracy was quantified as the mutual overlap between the thresholded truth image,  $t$ , and the thresholded reconstruction,  $r$  [140]:

$$\text{mutual overlap}(t, r) = 2(\sum tr)(\sum(t + r))^{-1}. \quad (6.6)$$

**6.2.1.1.3 Focal-spot measurement** To apply the approach to physical data, we characterized the focal-spot blur of a CBCT test bench consisting of a Rad-94 x-ray tube (Varian, Salt Lake City UT), a PaxScan 4343CB flat-panel detector (Varian, Palo Alto CA), and a SDD of 108 cm. In this work we focus on two-dimensional reconstructions, and therefore only measure one dimensional MTFs along the  $u$  axis. MTFs were measured using a tungsten edge placed at isocenter (40 cm from the source) and translated in the  $\pm u$  directions. The detector MTF was measured by placing the edge at the detector. We assume the detector MTF is SI and fit it to the following model [124]:

$$|MTF_d(f_u)| = \left| \frac{\text{sinc}(f_u T_x)}{1 + H f_u^2} \right| \quad (6.7)$$

where  $f_u$  is the spatial frequency in  $\text{mm}^{-1}$  and  $H$  is a constant blur parameter. The focal-spot MTF at each position  $u_p$  was modeled as a rect function with an apparent

length  $L(u_p)$ , resulting in the combined MTF:

$$|MTF_{sd}|(f_u; u_p) = |\text{sinc}(f_u L(u_p)) MTF_d(f_u)| \quad (6.8)$$

Theoretical apparent blur lengths from anode angle ( $\theta$ ) and focal-spot length ( $L$ ) were fit to the measured lengths to yield estimates for  $\theta$  and  $L$ .

**6.2.1.1.4 Resolution phantom study** A cylindrical resolution phantom (CatPhan CTP528 High Resolution Module, Phantom Laboratory, Salem, NY) with variable frequency line pairs was scanned on the CBCT test bench. The source-detector and source-axis distances were 108 cm and 40 cm respectively. A full scan of 720 projections was collected at 80 kVp and 0.504 mAs per projection. Data were reconstructed using the identity and SV blur models, as well as three SI blur models. The three SI blur models were the blur at the center of the detector (as in the simulation study) and the blur at either edge of the detector. The presented MBIR algorithm was used with 800 iterations to ensure a nearly converged solution. The reconstruction volume was  $170 \text{ mm} \times 170 \text{ mm}$  with  $100 \mu\text{m}$  voxels. The blur model used the focal-spot length and anode angle from §6.2.1.1.3 and a subset parameter ( $s$ ) of 5. We assume that detector blur is negligible and do not model it in the reconstruction algorithm.

#### 6.2.1.2 Trabecular probe study

We would like to characterize high-resolution CT system performance with highly accurate forward models both in the simulation of data and incorporation into advanced reconstruction methods. Performing this characterization over the entire FOV is a computational challenge due to the small pixel sizes, small voxel sizes, focal-spot



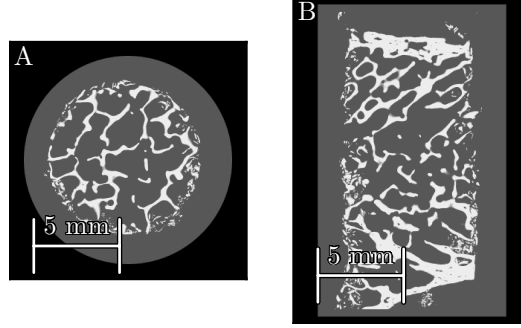


Figure 6.3: Axial (A) and Coronal (B) slice of trabecular bone phantom. The phantom consists of bone ( $0.060 \text{ mm}^{-1}$ ) surrounded by fat ( $0.019 \text{ mm}^{-1}$ ).

complexities (shift-variance, depth-dependence), etc. Thus, a strategy for local investigation within the larger FOV was devised. This strategy is discussed below.

**6.2.1.2.1 Phantom and data generation** A  $\mu$ CT scan of a human iliac crest biopsy sample was thresholded and used to create a realistic and clinically pertinent digital phantom (Figure 6.3). The volume was binned to  $0.038 \text{ mm}$  cubic voxels prior to propagation through the imaging chain model. The digital phantom is intentionally small, serving as a high-resolution “probe” that can be scanned in various positions throughout the entire FOV. The small support of the digital phantom permits both computationally efficient data generation and reconstruction for a detailed analysis of regional performance.

For a realistic system characterization, a pinhole image of an X-ray focal spot from an IMD RTM 37 source (IMD, Grassobbio, Italy) was used to form a two-dimensional focal-spot model for simulation. This X-ray tube has a  $17.5^\circ$  anode angle and a nominal focal spot of  $0.6 \text{ mm}$ . The source distribution on the anode is shown in Figure 6.4. This model was used to generate the SV apparent focal-spot

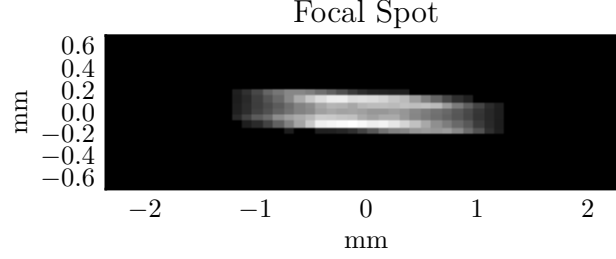


Figure 6.4: Focal spot model for data generation. Each pixel represents a sourcelet, and the relative intensity indicates the relative weight of that sourcelet’s measurements. Due to the anode angle, fewer samples were required along the long axis of the focal spot, resulting in anisotropic sourcelets.

distributions based on position within the FOV. Sampling of the source distribution into “sourcelets” for projection and scaling by regional focal-spot intensity was anisotropic ( $0.096 \text{ mm} \times 0.058 \text{ mm}$ ) with finer sampling along the short axis of the source and coarser sampling on the long axis since oblique views of the source result in finer sampling of the apparent focal spot.

Measurement data were generated according the following forward model:

$$\mathbf{y} = \mathbf{B}_d \text{Poisson} \left( I_0 \mathbf{S} \left[ \sum_k w_k \exp(-\mathbf{A}_k \boldsymbol{\mu}) \right] \right) + \mathcal{N}(\mathbf{0}, \boldsymbol{\sigma}_{ro}) \quad (6.9)$$

where  $\mathbf{B}_d$  is the scintillator blur,  $I_0$  is the bare-beam source intensity,  $\mathbf{S}$  is a data binning operator,  $w_k$  is the relative intensity of sourcelet  $k$ , and  $\mathbf{A}_k$  is a system matrix with the focal spot centered at sourcelet  $k$ . In short, at the core of (6.9), a volume of attenuation values,  $\boldsymbol{\mu}$ , is forward projected (on a fine grid of sub-pixels) for each focal-spot sourcelet,  $k$ . The results are subsequently summed to form pre-detection projections. These finely sampled projections are binned using the operator

**S** (representing pixel aperture and sampling) to account for nonlinear partial-volume effects. In this section, data were binned by a factor of two in each direction, for a detector pixel pitch of 0.1 mm. Pre-detection, incoming photons are presumed to be Poisson-distributed and undergo a detector blur based on the operator  $\mathbf{B}_d$ . This blur operation presumes a scintillator blur whose MTF is modeled by a Gaussian-Lorentzian mixture given by

$$H = a \exp(-q^2/\sigma^2) + (1 - a)(1 + Hq^2)^{-1}. \quad (6.10)$$

Lastly, measurements are subject to an additive uniform Gaussian readout noise.

**6.2.1.2.2 Reconstruction** While various reconstruction methods are explored, in all cases, data were reconstructed with 0.0767 mm voxels. The phantom was placed 20 mm, 40 mm, 60 mm and 80 mm from the axis of rotation and offset from the positive  $x$  axis  $0^\circ$  to  $355^\circ$  in  $5^\circ$  increments (rotated about the  $y$  axis, see Figure 6.11a). At the center of the short scan, the focal spot was at  $z = 381.0$  mm and the detector was at  $z = -132.0$  mm. The source and detector rotated about the  $y$  axis during scans. We conducted this experiment at three planes: the central plane ( $y = 0$  mm) and 60 mm above and below the central plane ( $y = \pm 60$  mm). FDK reconstructions used a ramp filter with no apodization and a cutoff at the Nyquist frequency. Additionally, the X-ray tube's anode-cathode axis was modeled in two different orientations: *Transaxial* with the anode-cathode axis parallel to the plane of rotation; and *Axial* with the anode-cathode axis parallel to the axis of rotation.

We also reconstructed the phantom with three MBIR methods: MBIR-I, MBIR-SI, and MBIR-SV. Each MBIR method used the nonlinear SQS method in §3.2.1,

which uses the forward model in (6.1), with the covariance matrix given by

$$\mathbf{K}_Y = \mathbf{B}_d \mathbf{D}\{\mathbf{y}\} \mathbf{B}_d^T + \mathbf{D}\{\boldsymbol{\sigma}_{ro}\}. \quad (6.11)$$

and

$$\mathbf{B} \triangleq \mathbf{B}_d \mathbf{B}_s I_0 \quad (6.12)$$

where  $\mathbf{B}_d$  is the scintillator blur,  $\mathbf{B}_s$  is the source blur, and  $I_0$  is the photon flux. A standard reconstruction system matrix ( $\mathbf{A}$ , without sourcelets) is used.

Each reconstruction approach uses a different approximation of system blur. The blur models used for each MBIR method are summarized in Table 6.1. MBIR-I did not include blur and is similar to a traditional MBIR approach presuming uncorrelated Gaussian noise. MBIR-SI and MBIR-SV model scintillator blur, matched with that used in the data generation step, and focal-spot blur, with convolution kernels based on simulated impulse responses at particular locations. The impulse responses were generated using sourcelets as in the data generation step, but with sourcelet sampling reduced by a factor of two in each dimension. Specifically, impulse responses ( $\mathbf{h}$ ) were found by calculating the line integrals through a single voxel for each sourcelet, weighting each line integral by the sourcelet intensity, and summing over sourcelets:

$$\mathbf{h} = \sum_k w_k \mathbf{A}_k \boldsymbol{\mu} \quad (6.13)$$

where  $\boldsymbol{\mu}$  is a length one vector with value 1. MBIR-SI's focal-spot blur model used a single blur kernel calculated from an impulse placed at isocenter (origin in Figure 6.11A). MBIR-SV used a different blur kernel for each projection. Specifically,

Table 6.1: Summary of blur models

	$\mathbf{B}_s$	$\mathbf{B}_d$
MBIR-I	Identity (no blur)	Identity
MBIR-SI	Blur kernel from isocenter impulse response	Equation (6.10)
MBIR-SV	Different blur kernels for each projection, calculated from impulse at phantom location	Equation (6.10)

the location of the impulse corresponded to the center of the phantom probe location. The blur kernel changes for every projection due to 1) change in magnification at the impulse location as a function of angle and 2) change in apparent focal-spot shape due to varying obliquity of the ray from the source to the impulse. The focal-spot blur model for each projection is SI, but because a different blur model (impulse response) was used for each projection, the overall effect of this blur model is SV when reconstruction is applied.

All of these assumptions are a mismatch with the source model in data generation to varying degrees. However, the MBIR-SV model is an excellent approximation for a small ROI since location-dependent effects are marginal and the variable magnification and angular-dependence of the apparent focal spot are handled by the view-dependent blur. Thus, the MBIR-SV investigation is a good indicator of regionally optimized performance, and potentially a good approximation of performance should a more sophisticated reconstruction with a global model for SV blur be adopted (e.g., a full sourcelets model).

The inverse covariance ( $\mathbf{K}_Y^{-1}$ ) was applied using an iterative solution for MBIR-SI and MBIR-SV. Similarly, readout noise was assumed negligible in certain computation steps to avoid application of  $\mathbf{K}_Y^{-1}$  every iteration, as described in §3.2.1.3. The term

$\mathbf{K}_Y^{-1}\mathbf{y}$  was precomputed using 200 iterations of the preconditioned CG method. All MBIR methods used a Huber Penalty [71] with  $\delta = 10^{-5}$  and were optimized in terms of RMSE over a range of penalty strengths ( $\beta$ 's). Each reconstruction ran for 500 iterations using 10 subsets and Nesterov acceleration [83, 85]. The phantom was reconstructed using the three MBIR methods at the locations indicated by circles in Figure 6.11A (80 mm from isocenter;  $0^\circ$ ,  $90^\circ$ ,  $180^\circ$ , and  $360^\circ$  about the  $y$  axis;  $y = 0$  mm and  $y = 60$  mm; and using both tube orientations).

### 6.2.1.3 Bench data reconstructions with full sourcelets model

Focal-spots were measured and modeled on two CBCT test benches, one with an axially oriented X-ray tube and one with a transaxially oriented X-ray tube. A line pair phantom was scanned and reconstructed on the transaxial bench using a full sourcelets model. Specifically, the mean forward model was

$$\bar{\mathbf{y}} = \mathbf{D}\{\mathbf{g}\} \sum_k w_k \exp(-\mathbf{A}_k \boldsymbol{\mu}) \quad (6.14)$$

where  $\mathbf{A}_k$  is the system matrix associated with sourcelet  $k$  and  $w_k$  is the relative intensity of that sourcelet. This may be written in matrix form demonstrating it is consistent with (6.1)

$$\bar{\mathbf{y}} = \underbrace{\mathbf{D}\{\mathbf{g}\} \begin{bmatrix} \mathbf{I}w_1 & \mathbf{I}w_2 & \dots & \mathbf{I}w_k \end{bmatrix}}_{\mathbf{B}} \exp \left( \underbrace{\begin{bmatrix} \mathbf{A}_1 \\ \mathbf{A}_2 \\ \vdots \\ \mathbf{A}_k \end{bmatrix}}_{\mathbf{A}} \boldsymbol{\mu} \right). \quad (6.15)$$

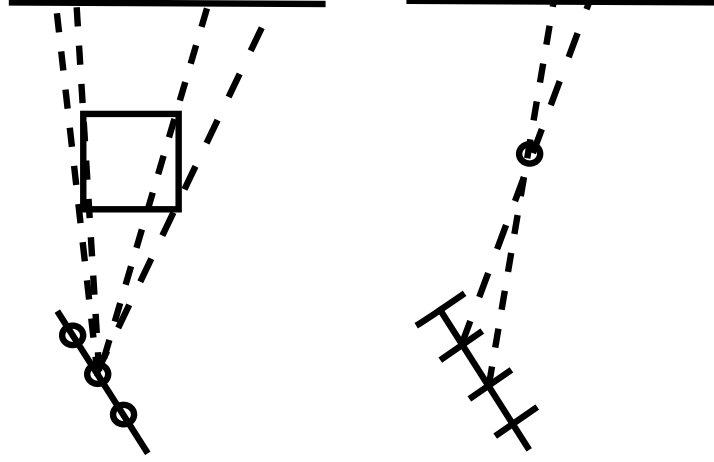


Figure 6.5: Sourcelet modeling illustration with two different types of projector. On the left, the sourcelets are modeled as point sources, and the voxels as rectangles/cubes. On the right, the sourcelets are modeled as lines/rectangles, and the voxels are modeled as points.

**6.2.1.3.1 Focal-spot modeling and measurement** Matrix  $\mathbf{A}$  in (6.15) may be implemented with multiple applications of a standard projector, such as separable footprints [50], which assumes the focal spot is a point source. Each  $\mathbf{A}_k$  matrix would model the focal-spot at the center of the corresponding sourcelet. However, this requires fine sampling of the focal spot (i.e., many sourcelets) to prevent sampling artifacts, and therefore requires many expensive projection operations. To reduce sampling requirements, we developed a novel projector which models the sourcelets as rectangles with separable projections on the detector. The voxels in this model are point sources, moving the sampling requirements from the focal-spot domain to the volume domain. The schematic in Figure 6.5 illustrates these different assumptions.

This model is suitable when focal-spot blur is large relative to voxel size. The separable sourcelets projector is derived in Appendix B. Simulated impulse responses of a simple digital focal spot were computed using (6.13) with varying levels of sampling to compare this new projector to the separable footprints projector.

The focal spot was measured on two X-ray benches, one with an axially oriented X-ray tube and one with a transaxially oriented X-ray tube. Each bench had two focal spots. For this study the large focal-spots were used for measuring, modeling, and reconstruction. On the axial bench, a 07-633 pinhole assembly (Fluke Electronics, Everett, WA, 0.010 mm) diameter was attached to a pan-tilt stage and a translation stage. Pinhole images from multiple view angles were acquired by translating the pinhole on the horizontal axis and angling the pinhole towards the source with the pan-tilt stage. Vertical translations were achieved by moving both the source and detector vertically relative to the pinhole. The approximate center of each pinhole image was found, and used to estimate the magnification by comparing pinhole image translation distances on the detector with the distances moved by the stages. The focal-spot distribution on the anode was estimated from the pinhole image acquired near the center of the detector using the estimated magnification. The anode angle was assumed to be  $14^\circ$  based on the source specifications. This focal-spot model was then used to generate simulated pinhole images using (6.13). These were compared with the measured pinhole images at each position on the detector to verify the accuracy of the model.

The axial bench did not have a pan-tilt stage, so only a single pinhole image was acquired. In order to estimate the pinhole magnification, multiple MTFs were acquired by translating a tungsten edge along the horizontal dimension of the de-



tector. The magnification was found by calculating the focal-spot distribution at a given magnification using the single pinhole image, simulating pinhole images at the measured MTF locations on the detector, and fitting the horizontal component of the simulated-pinhole derived MTFs to the horizontal MTFs acquired with the tungsten edge. The magnification resulting in the best fit was used to derive the final focal-spot distribution. While we assumed a specific anode angle, this method could be modified to solve for anode angle as well as magnification.

**6.2.1.3.2 Multiresolution forward model** Reconstruction with a full sourcelets model is expensive, requiring a projection operation for each sourcelet. While the separable sourcelets projector reduces the number of projection operations by reducing the number of sourcelets, a full volume reconstruction may still be quite slow. Additionally, small voxels are required both to ensure voxel size does not limit resolution and to meet the requirements of the separable sourcelets projector. In many clinical applications, only a small ROI needs to be studied at high-resolution (e.g., trabecular bone) while other portions of the image may be reconstructed at a lower-resolution (e.g., soft tissue). (While FDK is capable of reconstructing only a subset of the scanned object, the reconstruction volume in MBIR must be large enough to account for all the projection data.) Many multiresolution techniques have been explored [133, 141–144]. In this chapter we use a technique based on Cao et al. [133] where different ROIs are reconstructed with different voxel sizes. This may be written as

$$\mathbf{y} = \begin{bmatrix} \mathbf{y}_1 \\ \mathbf{y}_2 \end{bmatrix} = \begin{bmatrix} \mathbf{B}_1 & 0 \\ 0 & \mathbf{B}_2 \end{bmatrix} \exp \left( - \begin{bmatrix} \mathbf{A}_{1,lr} & 0 \\ \mathbf{A}_{2,lr} & \mathbf{A}_{2,hr} \end{bmatrix} \begin{bmatrix} \boldsymbol{\mu}_{lr} \\ \boldsymbol{\mu}_{hr} \end{bmatrix} \right) \quad (6.16)$$

where  $\boldsymbol{\mu}_{hr}$  is the high resolution ROI and  $\boldsymbol{\mu}_{lr}$  is the low resolution ROI (i.e., the remainder of the volume). The measurement data is divided into two regions as well:  $\mathbf{y}_2$  is a subset of the measurement data which contains all the projections from the high-resolution ROI, and  $\mathbf{y}_1$  is the remainder of the measured data. In other words, any measurement whose path from source to pixel intersects the high-resolution ROI must be included in  $\mathbf{y}_2$ . Equation 6.16 contains three system matrices, mapping the low- and high-resolution images to the appropriate projection domain pixels. Note that by design, the high-resolution ROI does not contributed to  $\mathbf{y}_1$ . Finally, each region of the measurement data has an associated  $\mathbf{B}$  matrix. In this chapter the high-resolution ROI was a box and  $\mathbf{y}_2$  was composed of rectangular ROIs for simplicity.

Equation 6.16 not only permits different voxel sizes in the low- and high-resolution ROIs, but different forward models as well. For example,  $\mathbf{B}_1$  could be a diagonal matrix while  $\mathbf{B}_2$  models scintillator blur. In this chapter, we apply the full sourcelets model only to the high-resolution ROI and  $\mathbf{y}_2$ . Specifically, we may expand (6.16) as

$$\mathbf{y} = \begin{bmatrix} \mathbf{y}_1 \\ \mathbf{y}_2 \end{bmatrix} = \begin{bmatrix} \mathbf{B}_1 & 0 & 0 & \dots & 0 \\ 0 & w_1 \mathbf{I} & w_2 \mathbf{I} & \dots & w_k \mathbf{I} \end{bmatrix} \exp \left( - \begin{bmatrix} \mathbf{A}_{1,lr} & 0 \\ \mathbf{A}_{2,lr} & \mathbf{A}_{2,hr,1} \\ \mathbf{A}_{2,lr} & \mathbf{A}_{2,hr,2} \\ \vdots & \vdots \\ \mathbf{A}_{2,lr} & \mathbf{A}_{2,hr,k} \end{bmatrix} \begin{bmatrix} \boldsymbol{\mu}_{lr} \\ \boldsymbol{\mu}_{hr} \end{bmatrix} \right) \quad (6.17)$$

where  $\mathbf{A}_{2,hr,k}$  is the system matrix from  $\boldsymbol{\mu}_{hr}$  to  $\mathbf{y}_2$  with sourcelet  $k$ . The same system matrix ( $\mathbf{A}_{2,lr}$ ) mapping  $\boldsymbol{\mu}_{hr}$  to  $\mathbf{y}_1$  is used for each sourcelet, so focal-spot blur is *not* modeled in the  $\mathbf{y}_1$  measurements. Note that while  $\mathbf{A}_{2,lr}$  appears multiple times, it

only needs to be evaluated once for each application of the forward model. While (6.17) still contains one projection operation for each focal-spot (plus two projection operations for the low-resolution ROI), each of these operates on much fewer voxels and pixels, dramatically reducing computation time. Equation 6.17 is consistent with (6.1), permitting use of the nonlinear SQS algorithm derived in §3.2.1.

Care must be taken with regards to the penalty function when using this approach. One option is to regularize across the boundary of the low- and high-resolution regions, using upsampling and binning operations, while another option is to regularize each region separately. Details about regularizing across boundaries can be found in Cao et al. [133]. In this chapter ROIs were regularized across the boundary.

**6.2.1.3.3 Reconstruction** A  $\approx 15$  cm water phantom containing a custom line pair target was scanned on the bench with the transaxially oriented X-ray tube. The line pair phantom contained alternating sheets of aluminum and plastic, each 0.4 mm thick, glued together with epoxy. The phantom was placed off center on the X-ray bench, with the line pairs near the edge of the phantom and the field of view ( $\approx 12$  cm from the center of rotation). The line pairs were oriented such that X-rays passed parallel to the aluminum and plastic sheets when the line pairs were near the edge of the FOV. Data were acquired at 80 kVp and 0.5 mAs per frame with  $1^\circ$  rotational sampling. The source-detector distance was 115 cm and the source-axis distance was 87 cm. The measurements were divided into two short scans, one with the line pairs predominately on the anode side of the detector and one with the line pairs predominately on the cathode side. Each short scan covered  $210^\circ$ .

Data were reconstructed using the multiresolution strategy described in §6.2.1.3.2, with  $0.05 \text{ mm} \times 0.05 \text{ mm} \times 0.05 \text{ mm}$  voxels in the high-resolution ROI (containing the

line pairs) and  $0.5 \text{ mm} \times 0.5 \text{ mm} \times 0.5 \text{ mm}$  voxels in the low resolution ROI. Three focal-spot blur models were used: an Identity model which assumed no focal-spot blur, a SI model (modeled in  $\mathbf{B}_2$  in (6.16)), and a sourcelets model using the separable sourcelets projector. The SI blur kernel was a simulated pinhole image using the derived focal-spot model and the source-detector distance/source-axis distance used for data acquisition. The SI model was only applied to the  $\mathbf{y}_2$  data. Data were acquired and reconstructed with the smaller focal spot to provide a “truth” image. This reconstruction did not model any blur. The isotropic Huber penalty (§3.3) was used with  $\delta = 10^{-3}$ . Regularization strength was varied in the high-resolution ROI ( $\beta = 10^i$  where  $i = -2, -1.75, -1.5, -1.25, -1, -0.75, -0.5$  and  $-0.25$ ), but was constant in the low resolution ROI ( $\beta = 10^3$ ). Reconstructions used 300 iterations with Nesterov acceleration and 10 subsets.

Reconstructions were compared qualitatively with approximately noise matched reconstructions. Noise was measured as the standard deviation in a region of the high-resolution reconstruction surrounding the line pairs (indicated in Figure 6.6). The contrast of the reconstructed line pairs was also calculated for each model/regularization strength. To calculate contrast, 11 slices of the reconstruction were first averaged together. The resulting line pair image was then averaged over 125 rows, resulting in a 1D profile. Contrast was calculated as the average of the peak values minus the average of the trough values. Peak and trough values were calculated as the max or min values in predefined ranges of the 1D profile. This is illustrated in Figure 6.6. The contrast-noise tradeoff was plotted for each reconstruction method and scan type.

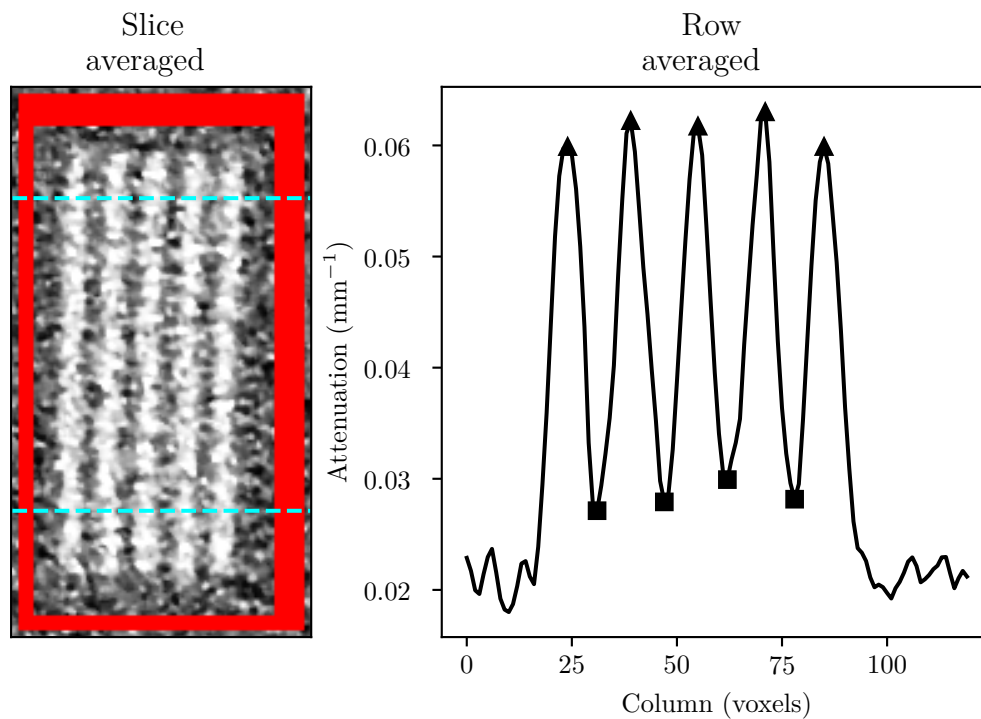


Figure 6.6: Demonstration of the line-pair contrast calculation. The reconstruction was averaged over slices to reduce noise (left). The rows were averaged between the dotted lines, resulting in the profile on the right. The mean of the peak values (triangles) and trough values (squares) were found and subtracted to get the final contrast measurement. A slice of the mask used for noise calculation is shown in red.

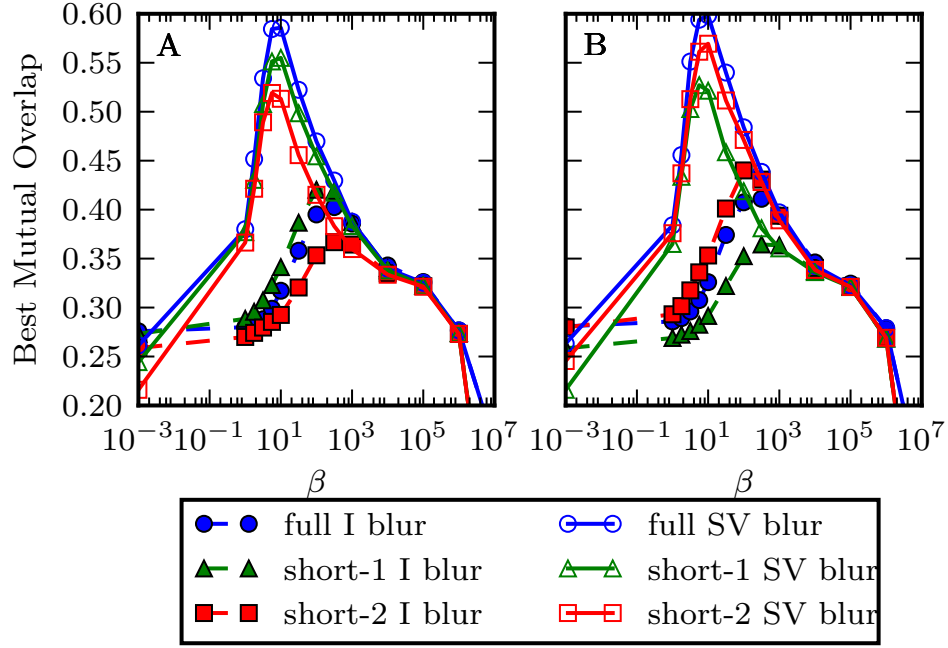


Figure 6.7: Best mutual overlap versus  $\beta$ . A) Medial and B) Lateral bone.

## 6.2.2 Results

### 6.2.2.1 Projection Domain blur modeling

**6.2.2.1.1 Simulation study** The best mutual overlap values (over all threshold values) for each ( $\beta$ ) are shown in Figure 6.7. Results are shown for reconstructions with an Identity (I) blur model and the SV blur model. Each line represents a blur model and scan type combination, and each point represents a reconstruction. A higher best mutual overlap indicates that a segmentation based on that reconstruction is closer to the truth segmentation, and the reconstruction is therefore more accurate. All methods that used the SV model were more accurate than those that used the

I model, which is evident by comparing the maximum of each line. With the I model, the best quality segmentation of the medial bone is achieved with data from the short-1 scan, which placed the medial bone projections primarily on the high-resolution (anode) side of the detector. The lowest quality was the short-2 scan, which placed the projections primarily on the low-resolution (cathode) side. The full scan reconstructions with the I model rank between the reconstructions from the two short scans. Neglecting a blur model is equivalent to assuming that classically redundant projections in the full scan (i.e., those with the same integration path but reversed direction) contain the same information, despite the fact that they are subject to different degrees of blurring, which results in a reconstruction whose image quality is a compromise between that of the two short scan reconstructions. Predictably, the lateral bone reconstructions are best when using the short-2 scan and worst when using the short-1 scan, in which the lateral bone projection data was on the high- and low-resolution sides of the detector, respectively.

When using the SV model, the full scan provides the best reconstruction of both bones, followed by the short-1 scan and then the short-2 scan in the case of the medial bone, and the short-2 scan and then the short-1 scan for the lateral bone. The better image quality of the full scan images over the corresponding high-resolution short-scan reconstructions can be attributed to the additional (low-resolution) data. The SV model can use this additional information to improve the reconstruction without losing details provided by the high-resolution data. In effect, rather than averaging the redundant data, the low-frequency data is used to reduce noise while the high-frequency data maintains spatial resolution. The corresponding low-resolution scan for each bone (short-2 for the medial bone and

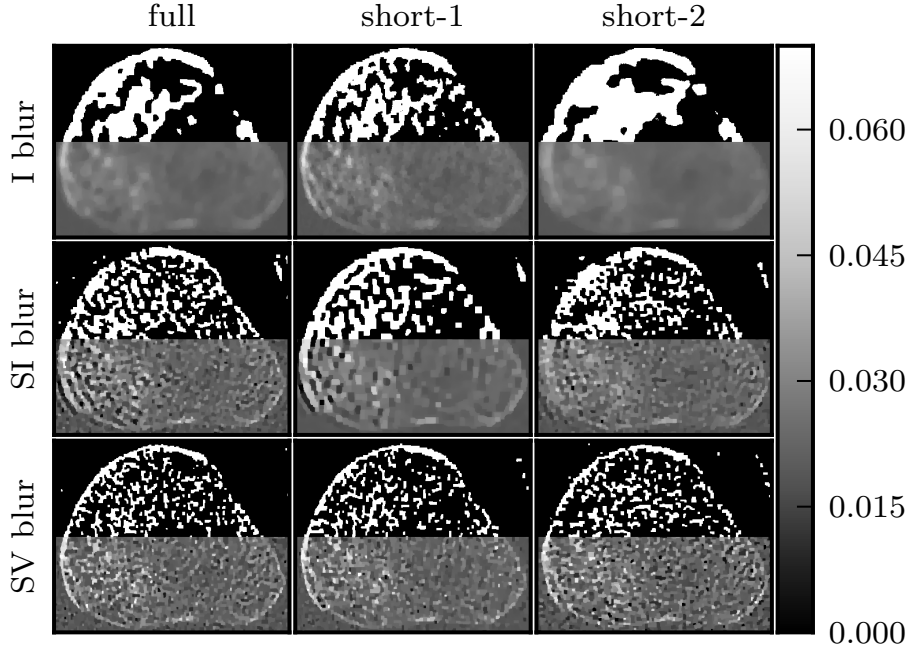


Figure 6.8: Reconstructions of the medial bone with the highest mutual overlap over all thresholds and  $\beta$ 's. The top half of each reconstruction is thresholded at the optimum threshold value.

short-1 for the lateral bone) results in the lowest quality reconstructions due to the increased difficulty in deblurring the data.

Figure 6.8 shows the medial-bone reconstructions (bottom of each image) and segmentations (top of each image) corresponding to the best possible mutual overlap (optimal threshold and  $\beta$  values) with each scan type and blur model combination. All SV reconstructions depict more trabecular structure than the SI or I models. The difference in image quality among I reconstructions is readily apparent in these images, with the short-1 scan resulting in the most trabecular detail. Finally, the SI



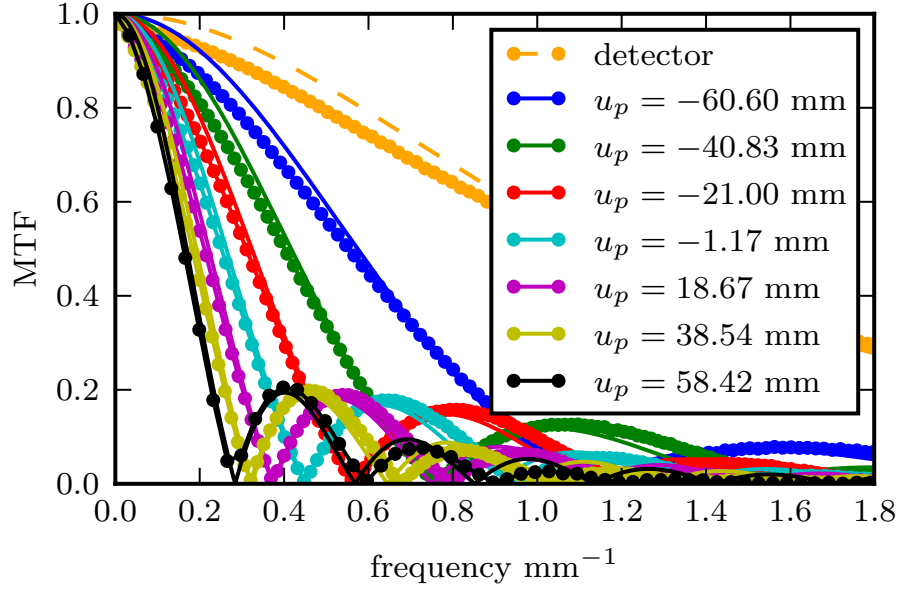


Figure 6.9: MTFs and fits for the detector and the detector+source blur at different displacements from the center of rotation.

images depict more detail than the I model but less detail than the SV reconstructions. However, the SI model results in a ringing artifact, particularly evident on the lower left aspect of the medial bone in the full scan reconstruction. This is likely due to blur/model mismatch (the SI model is accurate at the center of the detector but less accurate at the edges).

**6.2.2.1.2 Focal-spot measurement** The detector MTF and the combined focal-spot and detector MTFs at different positions are shown in Figure 6.9. The magnification in this system was about 2.7, so that the focal-spot blur dominates over the detector blur. Each combined focal-spot and detector MTF is labeled by the distance of the tungsten edge from the central ray. At positive positions, the edge is

on the cathode side, and at negative positions the edge is on the anode side. There is a dramatic difference in MTFs at different positions due to the angulation of the anode. Fits for each MTF are also shown. These fits give the apparent length of the focal spot at each position, which was used to estimate the actual length of the focal spot and the angle of the anode. The focal-spot length was found to be 5.23 mm and the anode angle was  $14.3^\circ$ .

**6.2.2.1.3 Resolution phantom study** Figure 6.10 shows the same ROI of five reconstructions, each of which used a different blur model. The three SI blur models are the apparent focal-spot size at the center, anode side, and cathode side of the detector. The reconstructions have approximately the same amount of noise (estimated by computing standard deviation in a flat region at the center of the phantom). The line pairs in the SV (Figure 6.10c) and center SI (Figure 6.10b) reconstructions are much sharper than those in the I reconstruction (Figure 6.10a). That the SI reconstruction line-pairs are roughly as sharp as those of the SV reconstruction suggests that at this distance from isocenter (approximately 4.75 cm) the SI approximation is fairly accurate. However, at the edge of the phantom (approximately 7.5 cm from isocenter), this assumption breaks down, and the resulting mismatch between the model and the actual blur results in a “ringing” artifact. The anode-side SI blur model (6.10d) underestimates the blur over most of the detector, reducing ringing compared to the center SI blur model but also reducing the sharpness of the line pairs. The cathode-side SI blur model (6.10e) overestimates the blur over much of the detector, increasing the ringing artifact.

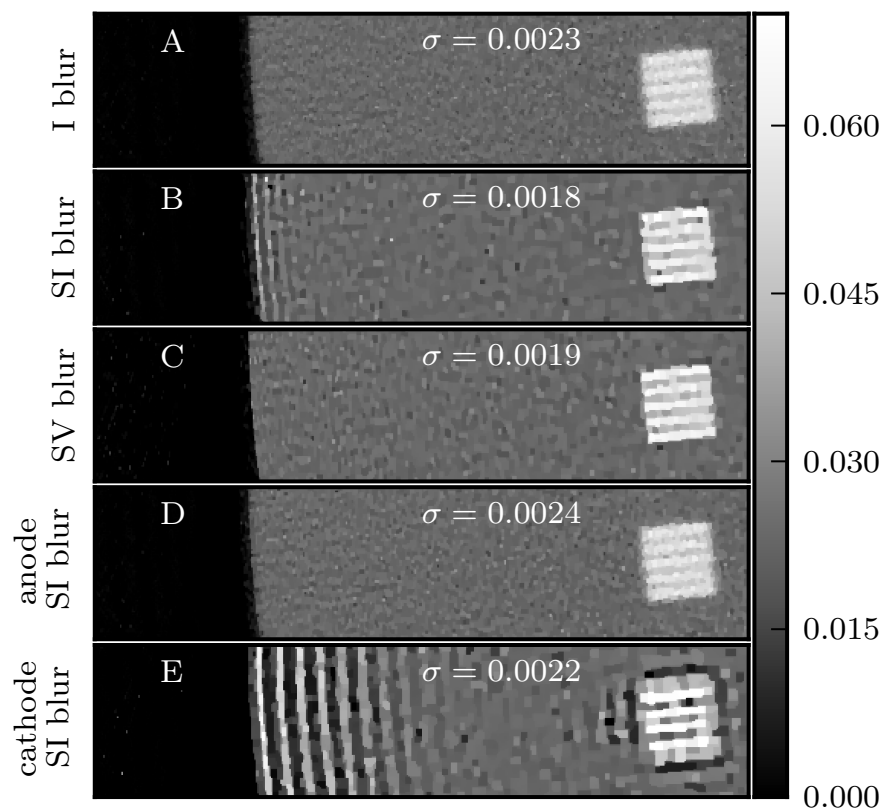


Figure 6.10: Physical CBCT reconstructions. Each subfigure shows a portion of the phantom from the edge to one of the line pairs. Each reconstruction has approximately the same noise level (indicated in each subplot in units of  $\text{mm}^{-1}$  and denoted by  $\sigma$ ).

### 6.2.2.2 Trabecular probe study

**6.2.2.2.1 FDK short scan maps** The results of the FDK sweep can be seen in Figure 6.11. Figure 6.11A is a schematic of the locations sampled, with each circular path corresponding to a constant radius in one of the plots in Figure 6.11B-G. The  $y = \pm 60$  mm planes (Figure 6.11B-C,F-G) have a substantially higher RMSE than the  $y = 0$  mm plane (Figure 6.11D-E). Because this RMSE increase occurs with both X-ray tube orientations and is similar in magnitude above and below  $y = 0$  mm, most of this image quality decrease is likely due to the large cone angle (e.g., incomplete sampling and cone-beam artifacts).

Within the  $y = 0$  mm plane, the transaxial orientation (Figure 6.11D) exhibits more variance in image quality as compared to the axial orientation (Figure 6.11E). This is mainly a spatial resolution effect since the focal-spot blur shift-variance is predominately along the anode-cathode axis, which is in-plane in D (parallel to the  $x$  axis at middle of the scan) but perpendicular to the plane in E (parallel to the  $y$  axis). For the transaxial orientation, the RMSE varies more along the  $x$  axis than the  $z$  axis, as expected, with the lowest RMSE on the left side of the image, corresponding to the side with a smaller apparent focal-spot blur (i.e., the anode side). In other words, as the source travels around isocenter, the apparent focal spot at the negative  $x$  axis is generally smaller than at isocenter. The exception to this being when the source is at the extremes of the scan, specifically, in the negative  $z$  half plane. However, this is a minority of the projection angles, and the net result is a smaller blur at an object on the  $-x$  axis than at isocenter. The axial orientation (Figure 6.11E) shows little variation along the  $x$  axis. Figure 6.11D-E also show depth-dependent effects, with the minimum RMSE offset in the positive  $z$  direction. As the source orbits isocenter,

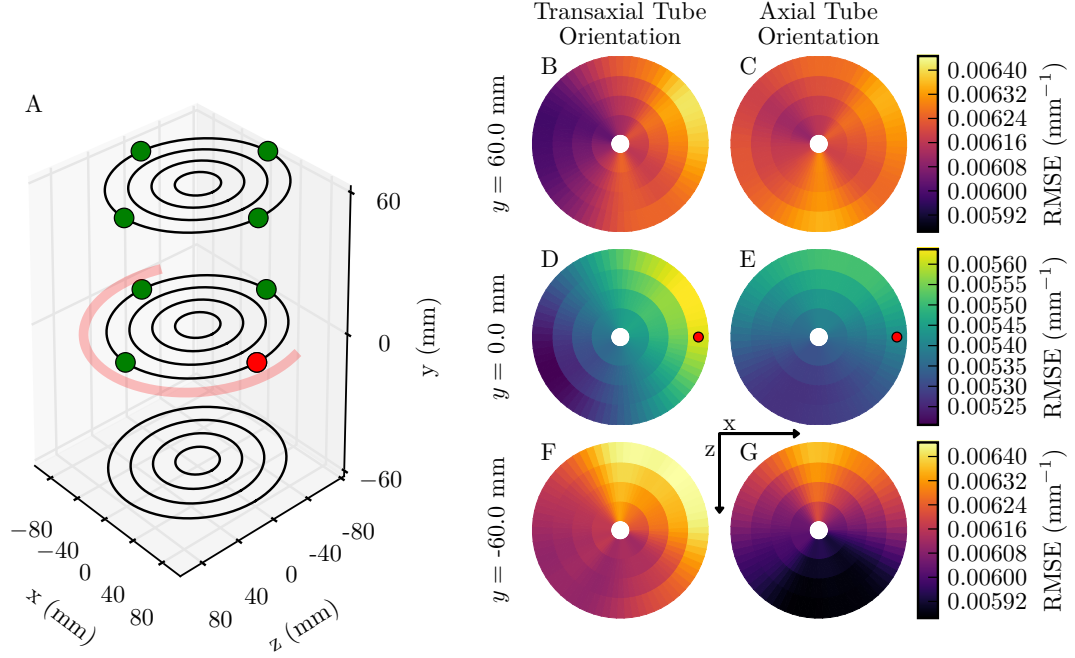


Figure 6.11: A: Schematic of the FOV sampling. Each ring was sampled using the FDK algorithm. For a given sample point (for example the red dot), the phantom was placed at that location and scanned using a short scan with the source centered at  $(0, 0, 381.0)$  and the detector centered at  $(0, 0, -132.0)$ . The angular range covered by the source is represented by the red arc. The data were then reconstructed using FDK. B-G: RMSE of FDK reconstructions for each sample point. Data at a constant radius corresponds to sampling along one of the black circles in A. The red dots indicate the corresponding location in A.

the apparent focal-spot blur size will change as magnification changes. However, even though increasing magnification increases focal-spot blur, it also decreases the effect of detector blur (scintillator blur and pixel sampling). Thus there is an optimum magnification where these two effects are balanced. Placing the phantom at locations with an average magnification close to this optimum should result in superior image quality. In this system, this optimum magnification appears to be more than the magnification at isocenter. Thus, with a transaxial tube orientation, the best image quality is achieved by placing the phantom as far to the anode side of the FOV as possible, and potentially offset in  $z$ , while the optimum position with an axial orientation is along the  $z$  axis, with the optimal location along the axis dependent on the tradeoff between focal-spot blur, scintillator blur, and pixel sampling.

With the transaxial orientation, the  $y = \pm 60$  mm planes exhibit a similar pattern, favoring the  $-x$  direction to reduce focal-spot blur. The axial orientation shows a dramatic difference between these two planes, due to the anode-cathode axis being parallel to the  $y$  axis. The overall RMSE is lower in Figure 6.11G ( $0.006\,05\text{ mm}^{-1}$ ) than Figure 6.11C ( $0.006\,22\text{ mm}^{-1}$ ), consistent with the fact that the apparent focal spot is smaller below the  $y = 0$  mm plane. The RMSE values in Figure 6.11G also vary dramatically as compared to Figure 6.11C, as apparent focal-spot size is more sensitive to magnification ( $z$  position) on the anode side of the anode-cathode axis (i.e.,  $y < 0$ ) as compared to the cathode side.

With both orientations, the minimum RMSE location is partially dependent on the optimum magnification, which is a function of focal-spot blur, scintillator blur, and pixel sampling. With a transaxial tube orientation, position along the anode-cathode axis is particularly important, resulting in large in-plane variance in RMSE.

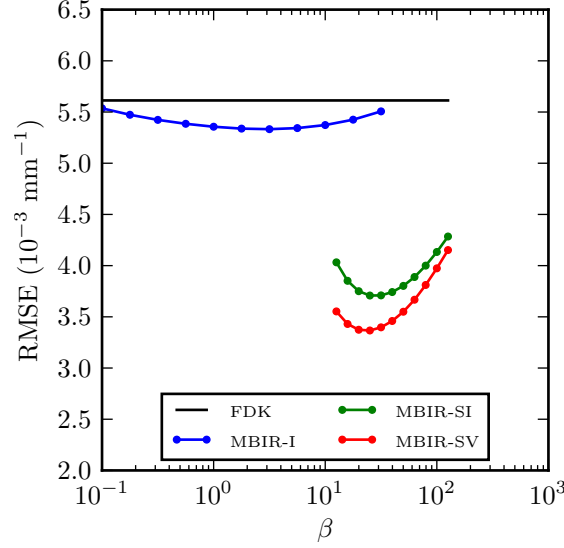


Figure 6.12: Example  $\beta$  sweep results at the red dot in Figure 6.11A with a transaxial focal-spot orientation.

Moving out of the central plane reduces image quality due to cone-beam artifacts and incomplete sampling. With an axial orientation, in-plane variance is reduced. However, image quality at different locations above and below the central plane is effected by shift-variant blur along the anode-cathode axis as well as cone beam effects. Thus, the optimum position may be slightly off the  $y = 0$  mm plane (in this case in the negative  $y$  direction) because of the reduction in focal-spot blur.

**6.2.2.2.2 MBIR** Figure 6.12 shows the results of a  $\beta$  sweep in the  $y = 0$  mm plane with a transaxial orientation. Comparing the minimum RMSE for each reconstruction method, MBIR-SV results in the best image quality, followed by MBIR-SI, MBIR-I, and finally FDK.

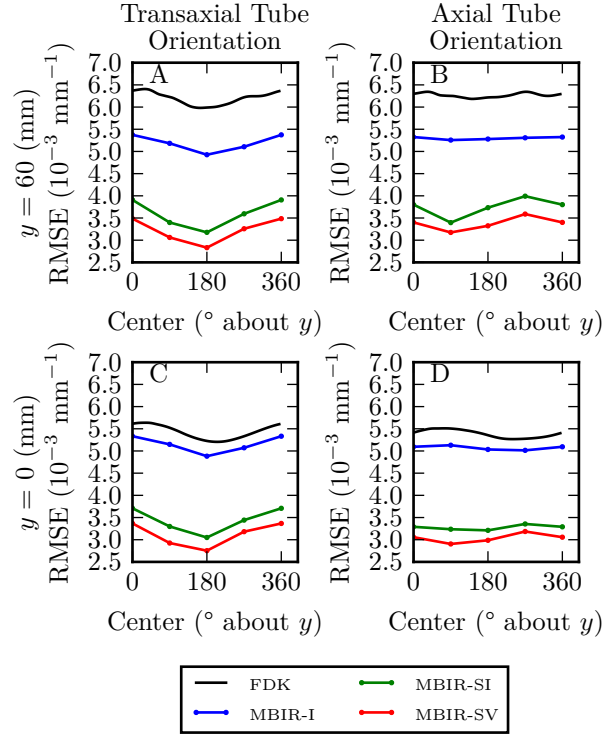


Figure 6.13: Minimum RMSE from each  $\beta$  sweep along with the FDK RMSE values. Data is wrapped around at  $360^\circ$  (i.e., the  $360^\circ$  data are the same as the  $0^\circ$  data). Subfigures A-D correspond to B-E, respectively, in Figure 6.11.



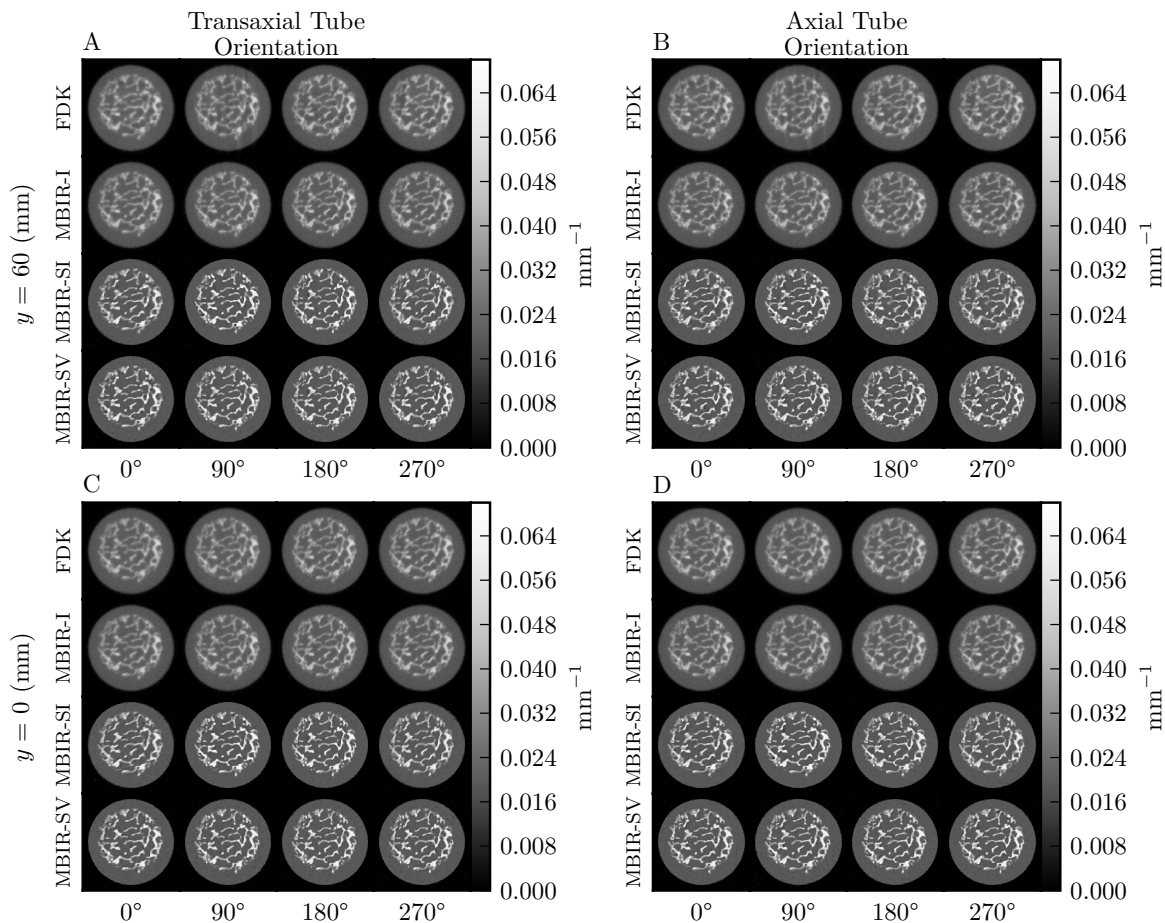


Figure 6.14: Axial slices of reconstructions. Each set of 16 reconstruction corresponds to a X-ray tube orientation (columns) and plane in the FOV (rows). Within each set, columns correspond to the location of the phantom (in degrees rotated about the  $y$  axis) and rows to reconstruction method.

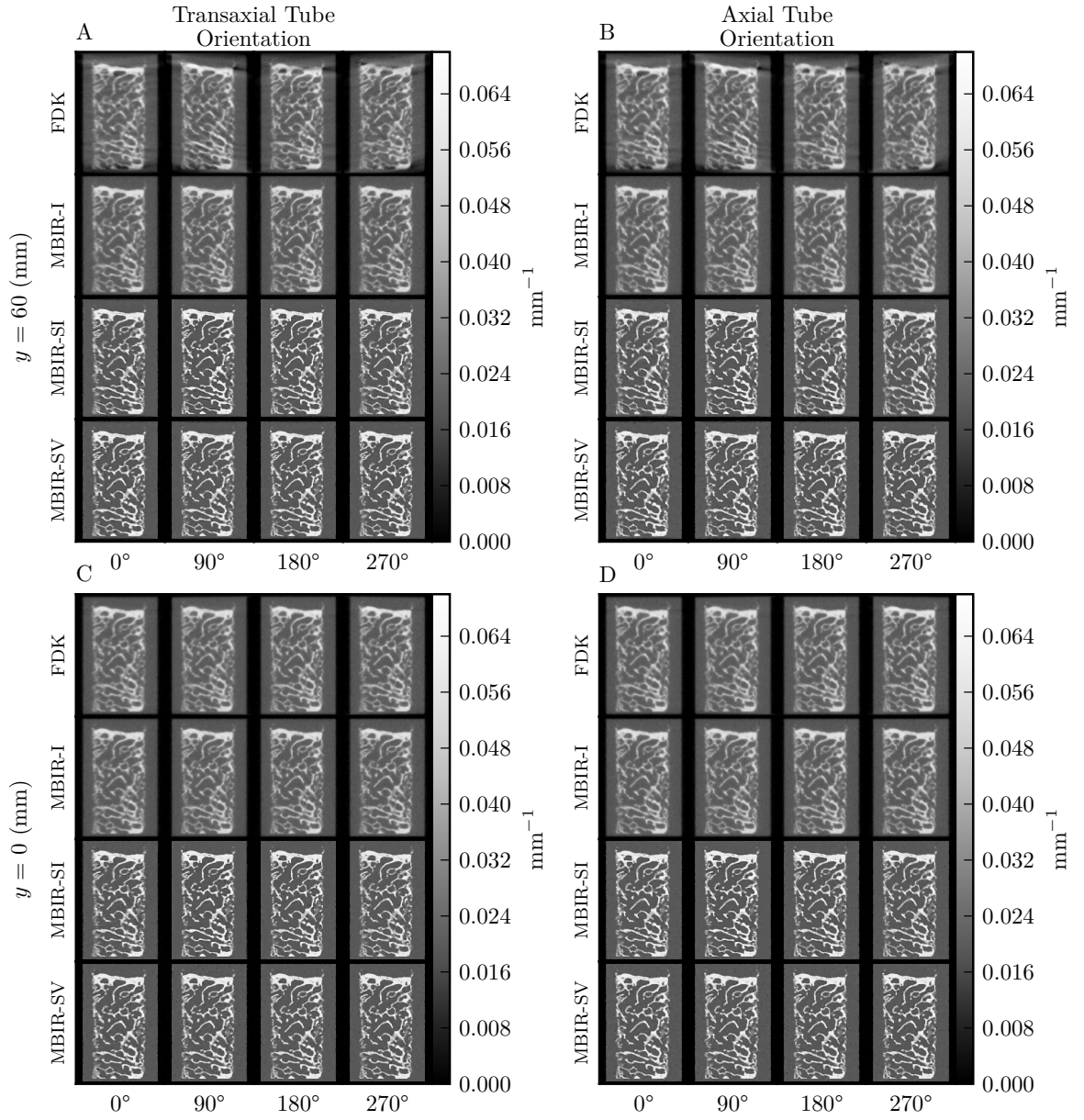


Figure 6.15: Coronal slices of reconstructions. Images are arranged as in Figure 6.14.

We conducted  $\beta$  sweeps similar to Figure 6.12 for both X-ray tube orientations at 80 mm from the axis of rotation in the  $y = 0$  mm and 60 mm planes and at  $0^\circ$ ,  $90^\circ$ ,  $180^\circ$ , and  $270^\circ$  rotations (i.e., the green/red circles in Figure 6.11A). The minimum RMSE across  $\beta$ 's was plotted as a function of angle (Figure 6.13), along with the FDK reconstruction RMSEs. In all cases, the rank ordering of performance across reconstruction methods is the same as in Figure 6.12, with MBIR-SV providing the best image quality. The most dramatic improvement is between MBIR-I and MBIR-SI, due to the introduction of the blur model. Improving the accuracy of the blur model with MBIR-SV further improves image quality as compared to MBIR-SI.

Unlike FDK, the MBIR methods result in similar RMSE values in the  $y = 0$  mm plane (Figure 6.13C,D) and the  $y = 60$  mm plane (Figure 6.13A,B). This is likely due to the advantages of the Huber regularizer which better handles the incomplete data at high cone angles.

With the axial orientation and in the  $y = 60$  mm plane (Figure 6.13B), the blur at the axis of rotation is larger than at isocenter. Therefore at  $0^\circ$  and  $180^\circ$  MBIR-SI generally underestimates the blur, causing MBIR-SI to have reduced image quality as compared to MBIR-SV. At  $90^\circ$ , the blur is reduced relative to the blur at  $0^\circ$  and  $180^\circ$  due to a decrease in magnification, decreasing RMSE in both MBIR-SI and MBIR-SV. Additionally, the MBIR-SI blur model is more accurate at this location, resulting in the similar performance of MBIR-SI and MBIR-SV. At  $270^\circ$  the reverse occurs, and the RMSE values of both methods increase. While MBIR-SI further underestimates the blur, in this experiment there was not a substantial increase in the RMSE difference between MBIR-SI and MBIR-SV at  $270^\circ$  as compared to  $0^\circ$ .

and  $180^\circ$ . MBIR-I and FDK both exhibited less variance in RMSE with angle than MBIR-SI and MBIR-SV.

The RMSE results are supported by a qualitative analysis of the reconstructions (Figure 6.14 and Figure 6.15). The reconstructions show the dramatic improvement due to incorporation of the blur model. In all cases (both tube orientations and both planes), the FDK and MBIR-I reconstructions (top two rows), have substantially more blur than the MBIR-SI and MBIR-SV reconstructions (bottom two rows). The FDK coronal slices in the  $y = 60$  mm plane (Figure 6.15A-B) have substantial cone-beam artifacts near the top of the phantom, as compared to the MBIR coronal slices. In the  $y = 0$  mm plane with the transaxial orientation (Figure 6.14C and Figure 6.15C), the FDK reconstruction at  $180^\circ$  is sharper than the reconstruction at  $0^\circ$ , consistent with the RMSE results. Differences between MBIR-SI and MBIR-SV are subtle, but are apparent when comparing how the performance of these two methods vary with angle. For example, with an axial tube orientation and in the  $y = 60$  mm plane (Figure 6.14B and Figure 6.15B), MBIR-SI produces the sharpest reconstruction at  $90^\circ$  (consistent with the RMSE results). On the other hand, the MBIR-SV method produces visually similar reconstructions. This is particularly evident in the coronal slices (Figure 6.15B).

In general, axial tube orientations result in more uniform image quality, while transaxial tube orientations result in better image quality in a specific region of interest, at the cost of reduced image quality elsewhere. MBIR and blur modeling were able to improve image quality as compared to FDK in all cases, with more accurate models resulting in more accurate reconstructions. Even without blur modeling, MBIR-I was able to reduce cone-beam artifact and improve image quality at high

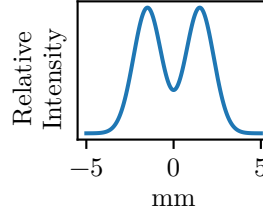


Figure 6.16: Simple 1D focal-spot distribution used to test focal-spot sampling properties with different projectors.

cone angles as compared to FDK, resulting in more uniform image quality as a function of slice. However, the best results were obtained with the accurate, SV model of focal-spot blur.

### 6.2.2.3 Bench data reconstructions with full sourcelets model

**6.2.2.3.1 Focal-spot modeling and measurement** Impulse responses of the digital focal-spot distribution in Figure 6.16 were generated using the separable footprints projector and the presented separable sourcelets projector with different numbers of sourcelets (i.e., different focal-spot sampling). The results are shown in Figure 6.17. As the number of sourcelets decreases, the impulses acquired with the separable footprints projector contain more high-frequency sampling artifacts. In contrast, the separable sourcelets projector can tolerate fewer sourcelets without artifacts. At the lowest number of sourcelets (11), the separable sourcelets projector results in a slightly misshapen impulse response. However, most of the shape is preserved, and the distortion is much less than the severe high-frequency artifacts in the separable footprints response.

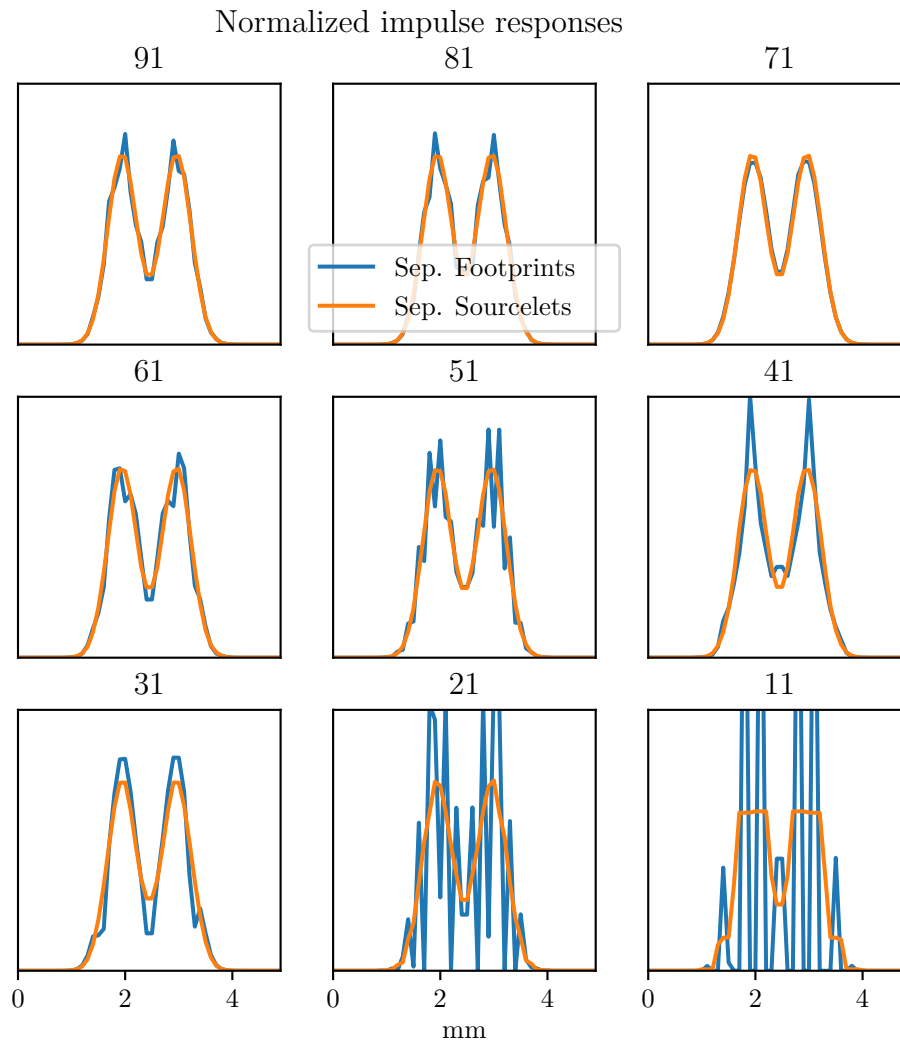


Figure 6.17: Simulated impulse responses using the focal spot in Figure 6.16 and either the separable footprints projector (blue) or the proposed separable sourcelets projector (orange). For each plot a different number of sourcelets were sampled from the distribution in Figure 6.16 (indicated at the top of each plot).

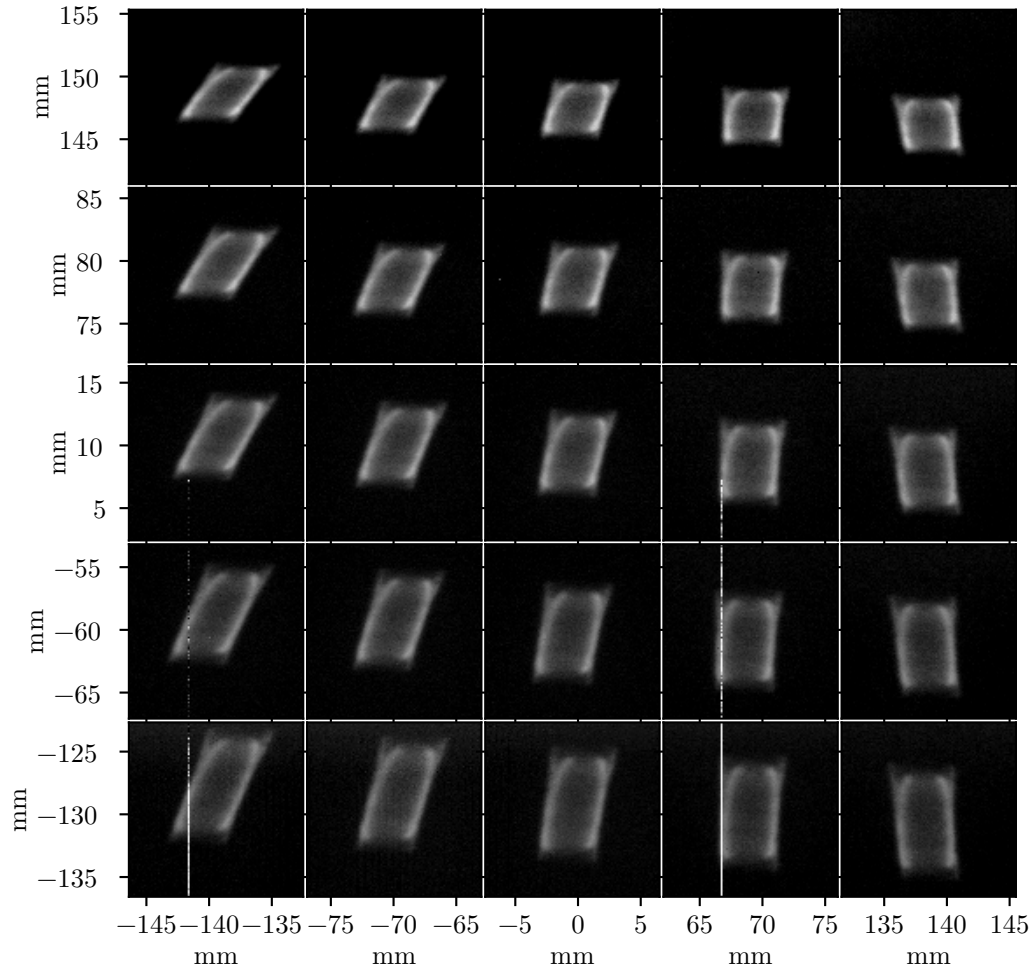


Figure 6.18: Pinhole measurements at different positions on the detector with the axial bench. There are some residual artifacts (vertical streaks) due to bad pixels. Approximate position relative to the piercing point (the point on the detector closest to the focal spot) is given in mm.

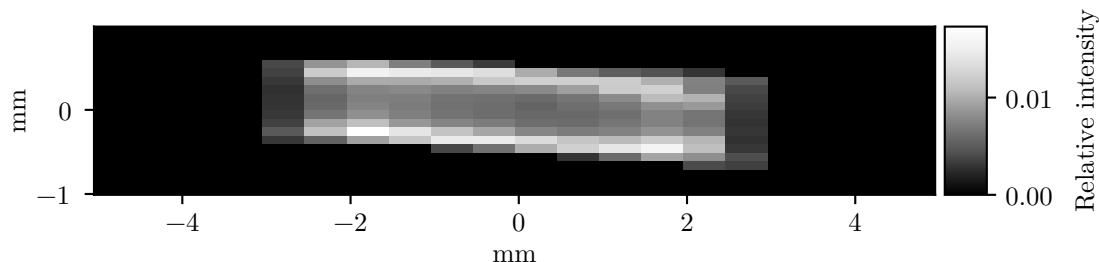


Figure 6.19: Focal spot model for the axial bench. Each pixel in the image is a sourcelet and represents an area on the anode that emits X-rays. The intensity of each pixel indicates the relative intensity of the corresponding sourcelet. The coordinates indicate the position on the anode surface.

Figure 6.18 shows the pinhole measurements at different positions on the detector for the bench with the axially oriented X-ray tube. The images are magnified by about a factor of 5. This focal spot is oriented axially, so the primary SV is in the vertical direction. Towards the top of the detector (the anode side), the focal spot has a smaller vertical extent, while towards the bottom of the detector (cathode side) the focal spot appears larger. Moving horizontally along the detector shears the pinhole images, but doesn't change the overall size as dramatically as movement in the vertical direction.

Figure 6.19 shows the modeled focal-spot distribution on the anode. The focal spot is approximately a trapezoid, with higher intensity horns as seen previously. The fact that the model is a trapezoid and not a rectangle may reflect the true focal spot, or may be the model compensating for a slightly rotated X-ray tube. However,



Table 6.2: Noise levels in each of the four reconstructions in Figure 6.23

	Small focal spot $\mu\text{m}^{-1}$	Identity $\mu\text{m}^{-1}$	SI $\mu\text{m}^{-1}$	Sourcelets $\mu\text{m}^{-1}$
Anode side	9.93	9.37	12.6	8.74
Cathode side	9.37	8.91	12.2	11.9

this discrepancy is not critical so long as the simulated pinhole images match the measured pinhole images. The focal spot is sampled more coarsely along its long axis, as this axis will appear smaller due to the anode angle.

The simulated pinhole measurements are shown in Figure 6.20. These capture the shape of the true pinhole images from Figure 6.18 very well, indicating that the focal-spot model is accurate. While many pinhole images were acquired, the focal-spot model is based on a single pinhole image and the magnification. Therefore, only one pinhole image of the transaxial X-ray bench focal-spot was acquired to develop the model for that bench. The transaxial X-ray bench focal-spot model is shown in Figure 6.21, and the blur kernel for the SI model is shown in Figure 6.22.

**6.2.2.3.2 Reconstruction** Figure 6.23 shows reconstructions from each scan type and blur model. On the high-resolution anode side, the identity model is able to resolve the line pairs, while on the low resolution side the line pairs are more difficult to visualize. A comparison to the other blur models is difficult, partially due to imperfect noise matching. However, the anode side line pairs with SI modeling appear sharper than the identity method and the sourcelets method (although the SI model has higher noise as well, as indicated in table 6.2). On this side of the detector the SI model overestimates the focal-spot blur, which may cause artificial contrast

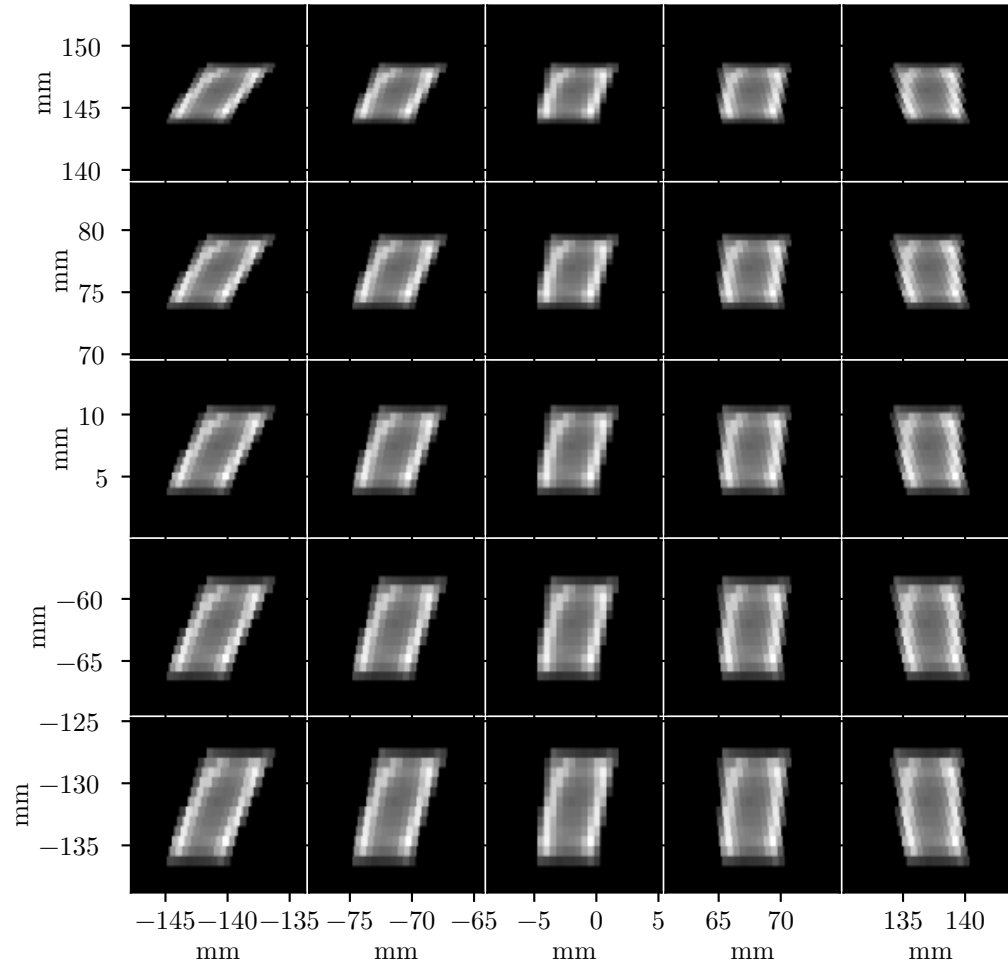


Figure 6.20: Simulated pinhole measurements for the axial bench based on the focal-spot model and separable sourcelets projector.

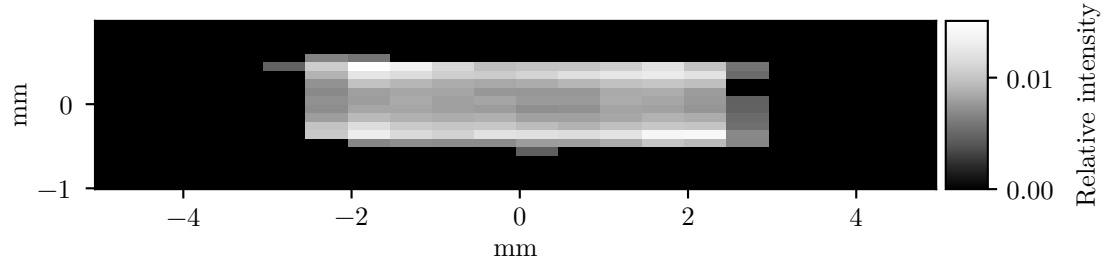


Figure 6.21: Focal spot model for the transaxial bench.

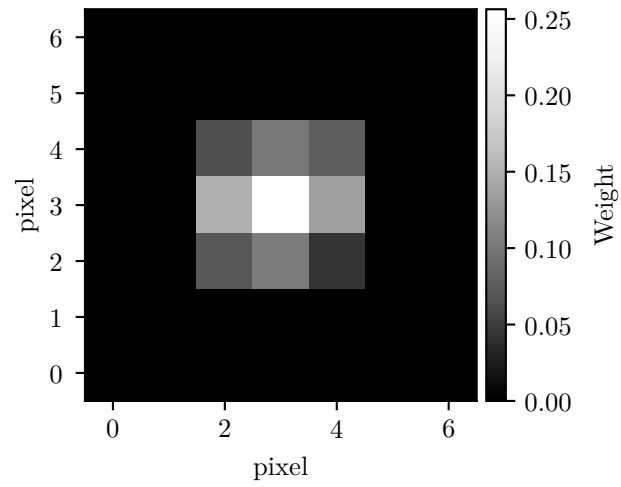


Figure 6.22: SI blur kernel for the transaxial bench.

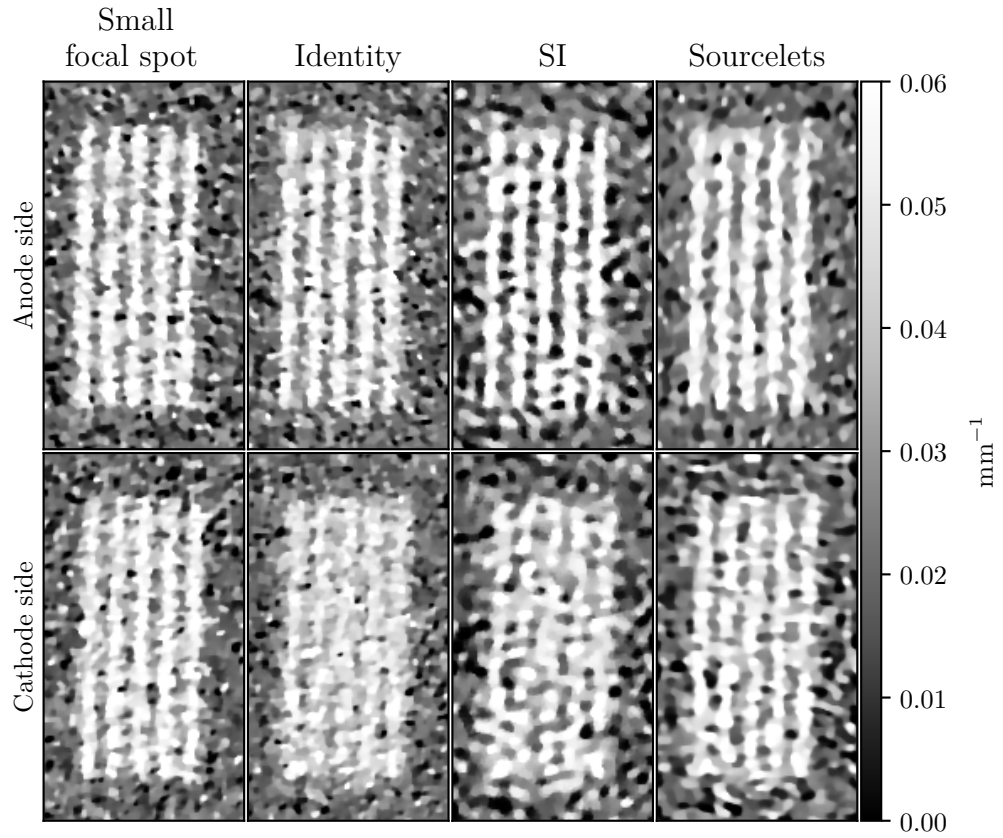


Figure 6.23: Reconstructions from each scan type (rows) and blur model (columns) for the transaxial bench. The reconstructions are approximately noise matched. The noise for each reconstruction is give in Table 6.2.

enhancement (i.e., more contrast than the true object). On the cathode side, the two methods with blur modeling are closely noise matched, but the sourcelets model produces line pairs that are easier to visualize. Each reconstruction method (except for the small focal-spot reconstruction) used the same geometry for fair comparison. Note that the small focal-spot reconstruction still contains scintillator blur and focal-spot blur due to the small focal spot.

Figure 6.24 shows the contrast-noise tradeoff for each scan type and reconstruction method. Better image quality is at the top left of the plots (high contrast, low noise). On the anode (high-resolution) side, the identity and small focal-spot reconstructions are roughly the same, as focal-spot blur is small and the identity model is fairly accurate. The sourcelets model slightly increases contrast as compared to the identity model and small focal spot-reconstruction, and the SI model dramatically increases contrast. Because the SI model overestimates the focal-spot blur on the anode side, one would expect contrast at certain frequencies to be larger than the true values. However, because the small focal-spot reconstruction still contains blur, it is unclear whether this contrast improvement is due to over-deblurring or if the SI model is undoing real blur which is present in the image. We note that scintillator blur is present but not modeled, so depending on the amount of scintillator blur overestimating focal-spot blur may actually be advantageous. The sourcelets model also contains higher contrast than small focal-spot reconstruction, although the difference is much less. Further studies are required to determine if the SI model (and possibly the sourcelets model) are over-deblurring the data and artificially boosting contrast.

On the cathode (low-resolution) side, the small focal-spot reconstruction has higher contrast at almost all noise levels, and the identity model is among the lowest

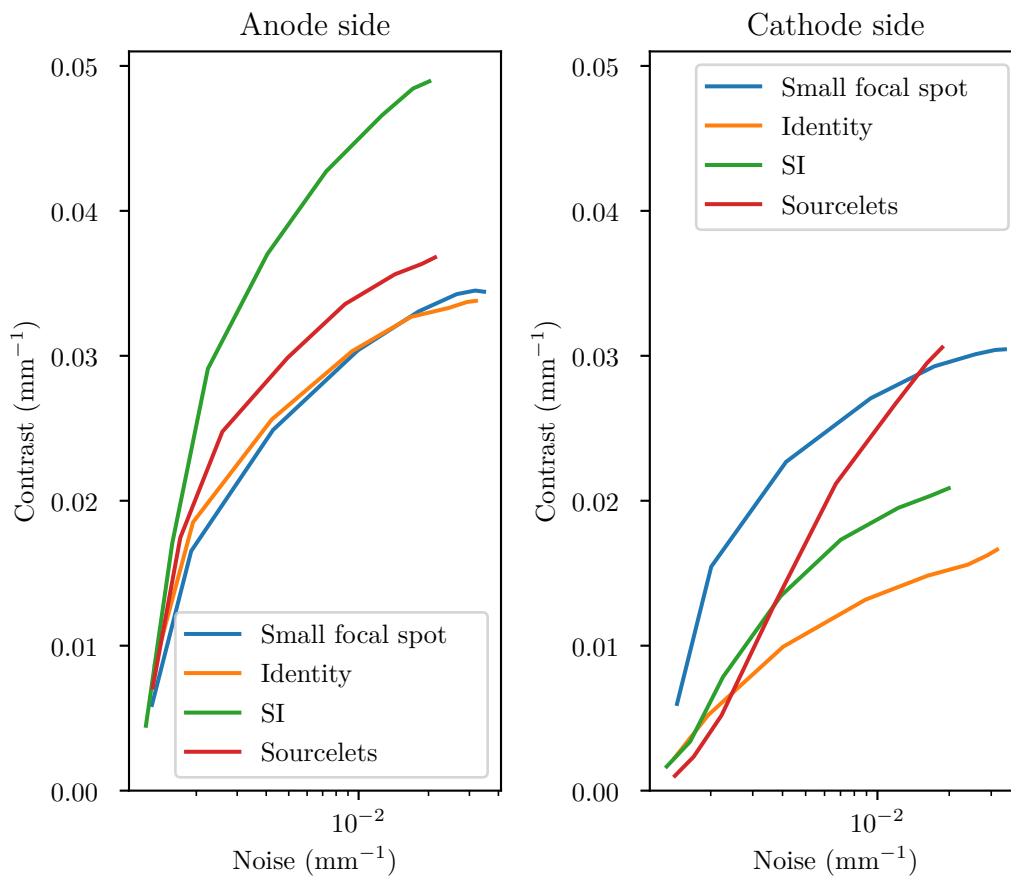


Figure 6.24: Contrast-noise plots for each scan type and reconstruction method for the transaxial bench reconstructions.

contrasts at all noise levels. At low noise levels, the high regularization prevents the SI and sourcelets models from recovering contrast. As regularization decreases, both models provide improved contrast. However, the SI model underestimates the blur, and is unable to match the contrast level of the sourcelets model. At high noise levels, the sourcelets model has higher contrast than small focal-spot reconstruction. This may be due to the fact that the small focal-spot reconstruction still contains some focal-spot blur, although future studies are required to properly assess this.

## 6.3 Gantry motion blur modeling

In this section we assess the importance of gantry motion modeling in a simulated MDCT system and with physical test bench data.

### 6.3.1 Methods

#### 6.3.1.1 Model

Gantry motion blur is the result of a continuous integration over angle, and may be modeled as

$$\bar{\mathbf{y}}_i = \mathbf{B}_2 \int_{\psi=\theta_i-\Delta\theta/2}^{\theta_i+\Delta\theta/2} \exp(-\mathbf{A}_\psi \boldsymbol{\mu}) d\psi \quad (6.18)$$

where  $\bar{\mathbf{y}}_i$  is the mean measurement vector at projection  $i$  and gantry angle  $\theta_i$ ,  $\Delta\theta$  is the angular distance over which data is collected for projection  $i$ , and  $\mathbf{A}_\psi$  is the projection matrix at angle  $\psi$ . A discrete approximation is achieved by oversampling

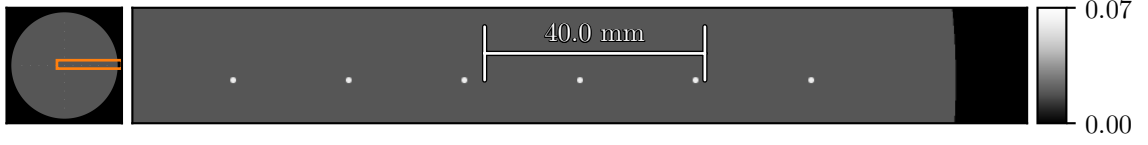


Figure 6.25: The digital phantom used in the motion blur study. The ROI indicated by the orange box in the left image is shown on the right. The left most circle in this ROI is at the center of the phantom. The circles are separated by 20 mm.

in projection angle and summing the results to obtain the measurement sampling:

$$\bar{\mathbf{y}}_i = \mathbf{B}_2 J^{-1} \sum_{j=0}^J \exp(-\mathbf{A}_\psi \boldsymbol{\mu}) \quad (6.19)$$

$$\psi(j) = \theta_i + \Delta\theta (j/J - 1/2) \quad (6.20)$$

where  $J$  is the angular oversampling factor.  $\mathbf{B}$  from (6.1) contains  $\mathbf{B}_2$  and the summation term in (6.19), and  $\mathbf{A}$  contains all the  $\mathbf{A}_\psi$  used in (6.19). For example, if the measurement data contains 360 projections and  $J$  is 3, then  $\mathbf{A}$  results in 1080 projections, and every three consecutive projections are summed together as part of  $\mathbf{B}$ .

#### 6.3.1.2 Simulation study

A circular simulation phantom (Figure 6.25) with a diameter of 25 cm and multiple round ROIs at different distances from the center of rotation was used to evaluate the proposed algorithm. A continuous motion system was simulated with a 500 mm source-to-axis distance, a 1000 mm source-to-detector distance, and 1000 projections per rotation. This geometry was chosen to approximate high-resolution MDCT systems. Data were generated from a phantom with  $0.1 \text{ mm} \times 0.1 \text{ mm}$  voxels



and a detector with 0.125 mm pixel pitch. We projected the data at 51 000 equally spaced angles over a  $360^\circ$  rotation. Poisson noise was added prior to binning to 1000 projections and spatially binning to 0.25 mm pixels. The photon flux after binning was  $10^5$  photons pixel<sup>-1</sup>. Finally, readout noise was added to the data ( $\sigma_{ro} = 7.11$  equivalent photons).

Data were reconstructed with  $0.2 \text{ mm} \times 0.2 \text{ mm}$  voxels. We used two blur models: an identity blur model (no blur,  $\mathbf{A}$  produces 1000 projections), and a gantry motion blur model with an angular oversampling factor of  $J = 5$  ( $\mathbf{A}$  produces 5000 projections). We used an uncorrelated noise model, the isotropic Huber penalty from §3.3 ( $\delta = 10^{-3}$ ) [71], and the separable footprints projector [50]. Nesterov acceleration was used with 1000 iterations and 10 subsets. Bias/noise measurements were calculated for each ROI. Bias was computed as the RMSE between a noiseless reconstruction and truth at the ROI, and noise was computed as the RMSE between a noisy reconstruction and a noiseless reconstruction in a nearby region. Bias and noise were calculated for multiple penalty strengths to obtain a bias/noise curve for each method.

### 6.3.1.3 Test bench study

A “harp” phantom (Figure 6.26) consisting of 25 vertically oriented spans of wire submerged in water was scanned on a CBCT test bench. The phantom was scanned with a 109 cm source-to-detector distance, a 82 cm source-to-axis distance, and  $0.139 \text{ mm} \times 0.139 \text{ mm}$  pixels. The FPD on the test bench is not designed for continuous exposure, so a continuous operation was emulated by oversampling in angle by a factor of 10 and binning the results. Specifically, 3600 projections were acquired in  $0.1^\circ$  increments, which were then binned to 360 projections. The

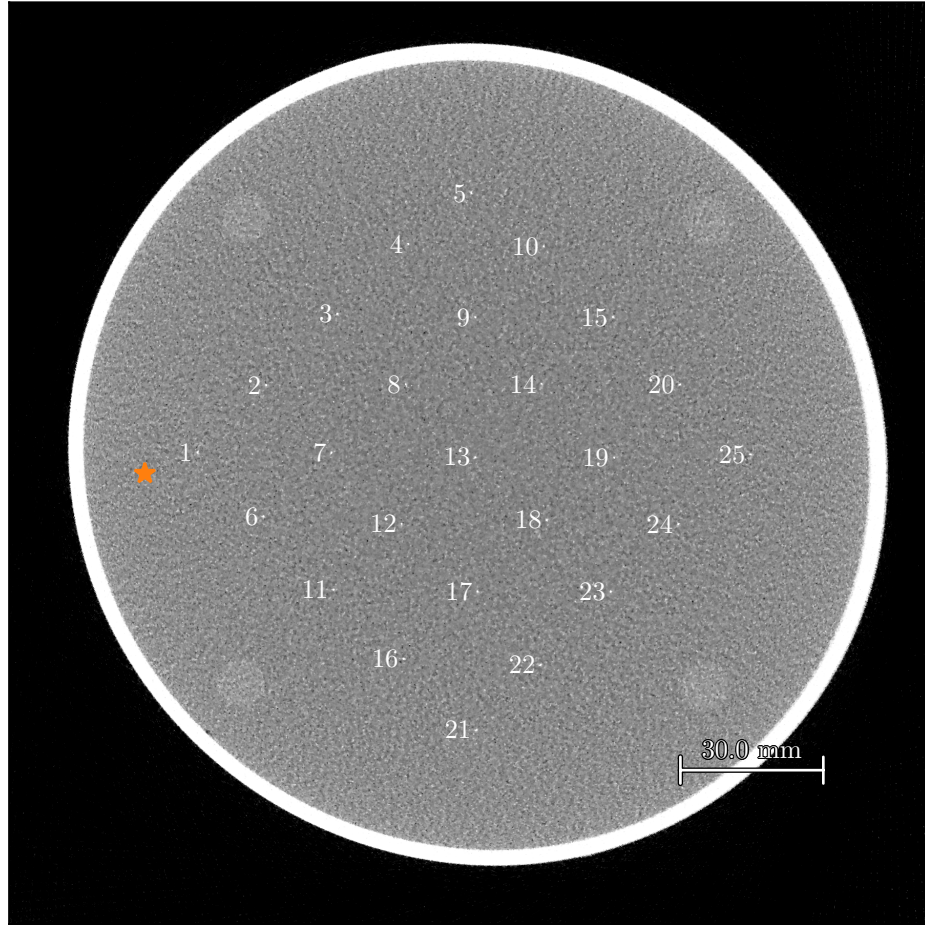


Figure 6.26: “Harp” phantom containing 25 spans of wire (labeled 1–25). The phantom was positioned off-center, with the center of rotation indicated by the star.

phantom was positioned off-center in the FOV, such that the edge of the phantom approached the edge of the FOV. The center of rotation is indicated in Figure 6.26.

Data were reconstructed with  $0.1\text{ mm} \times 0.1\text{ mm} \times 0.1\text{ mm}$  voxels using the non-linear SQS algorithm, 1000 iterations, 10 subsets, Nesterov acceleration, and the isotropic Huber penalty ( $\delta = 10^{-3}$ ). Two models were used for reconstruction, an identity model ( $J = 1$ ) and a blur model ( $J = 5$ ). Reconstructions were compared qualitatively at a single regularization strength ( $\beta = 10$ ).

## 6.3.2 Results

### 6.3.2.1 Simulation study

Gantry motion simulation results are summarized in Figure 6.27. The bias/noise tradeoff is shown for each ROI at varying distances from the center of rotation. The identity model suffers from increased bias at large distances from the center of rotation, while the blur model bias is relatively unchanged (suggesting a recovery of spatial resolution). The identity model appears to outperform the blur model at 20 mm to 40 mm from the center of rotation, although the difference is small.

These results are confirmed in the reconstructions in Figure 6.27. These reconstructions were approximately noise matched at the ROI furthest from the center of rotation by altering penalty strength (noise is  $2.719 \times 10^{-4}$  mm for the identity model and  $2.622 \times 10^{-4}$  mm for the blur model). The circles in the identity model reconstruction get blurrier along the direction of rotation as distance from the center increases. However, with the blur model the circles are accurately reconstructed.

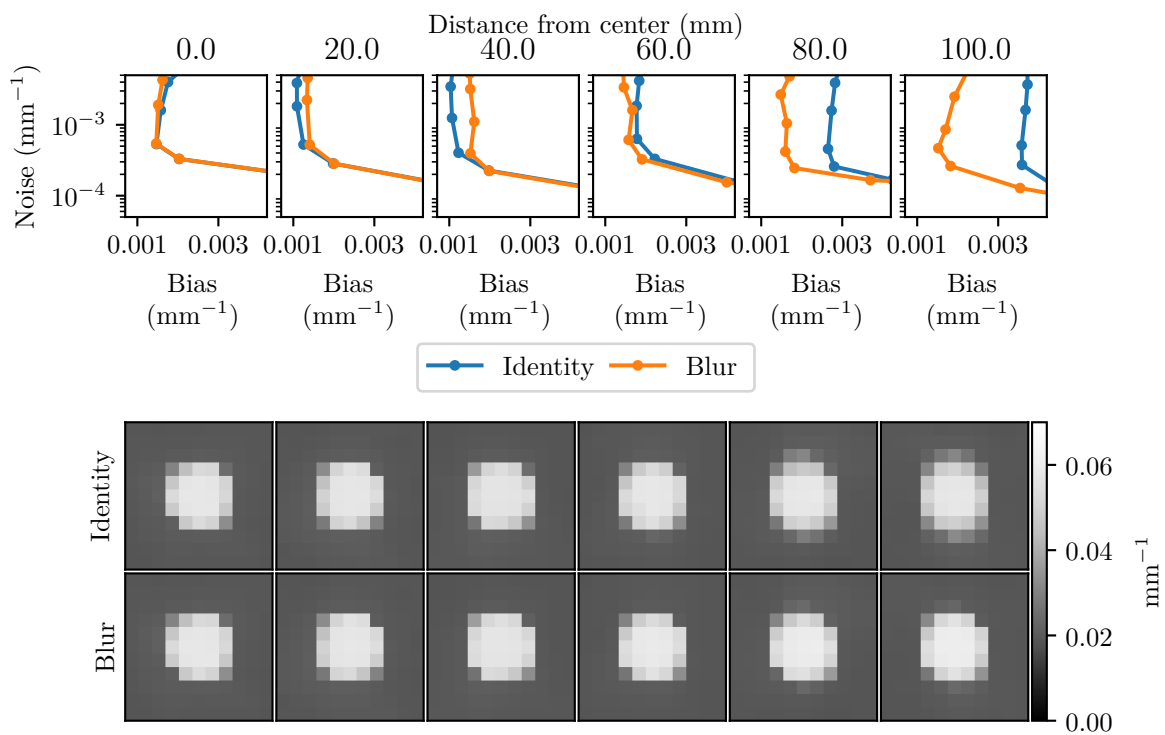


Figure 6.27: Bias/noise curves (top) and reconstructions (bottom) for each ROI in Figure 6.25. Each column corresponds to a distance from the center of rotation. The top row reconstructions use the identity model and the bottom row reconstructions use the gantry motion blur model.

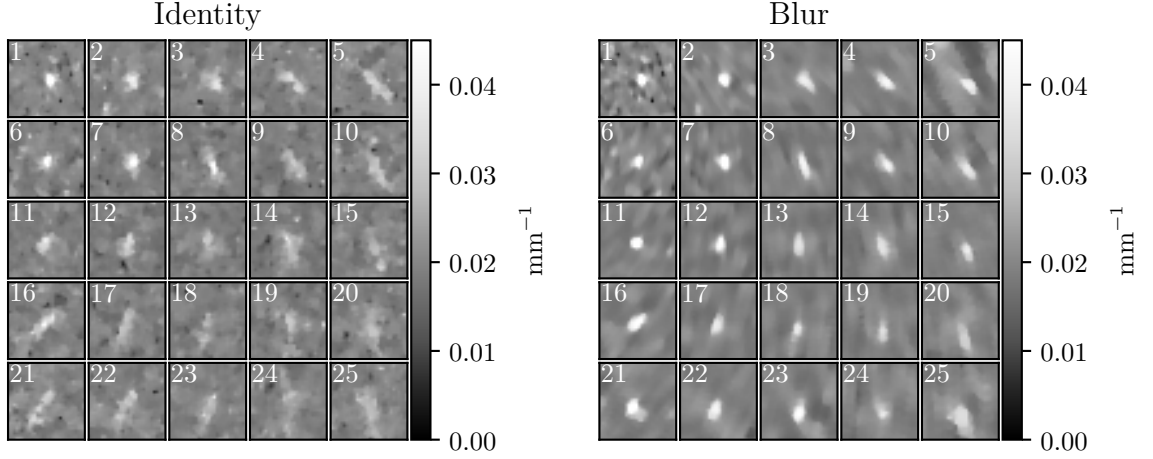


Figure 6.28: “Harp” phantom reconstructions for the identity model (left) and blur model (right). Each ROI corresponds to one of the wires in Figure 6.26.

### 6.3.2.2 Test bench study

The “harp” phantom reconstructions are shown in Figure 6.28. With the identity blur model, the wires near the center of rotation (e.g., ROI 1) are reconstructed well, but wires far from the center of rotation (e.g., ROI 25) are blurred out almost entirely. With this model contrast decreases as distance from the center of rotation increases. The blur model is able to reconstruct all the wires fairly well, and with better contrast than the identity model at locations far from the center of rotation. The noise properties throughout the blur model reconstruction vary considerably, with much less noise towards the edge of the FOV. This method may benefit considerably from position-dependent regularization [145].

## 6.4 Discussion

MBIR with SV blur modeling can provide improved image quality over SI models by making more efficient use of the acquired data. Such modeling can enable MBIR to use high-resolution data where available (e.g., on the anode side of the detector) while using low-resolution data to reduce noise. Disregarding this resolution difference can lead to an averaging effect, where high-resolution information is lost, or ringing artifacts due to inaccurate modeling at certain locations.

By modeling multiple CBCT imaging systems we have shown that SV blur can cause image quality to vary with position throughout a FOV. Understanding these properties can aid design of application and system specific acquisition protocols. For example, when imaging a small object with a short scan and reconstructing using FDK, the best image quality will be obtained with a transaxial X-ray tube orientation and the object at the edge of the FOV on the anode side of the anode–cathode axis ( $-x$  in 6.11). Similarly, placing the object at the cathode side should be avoided. On the other hand, when scanning a large object which requires image-quality uniformity, an axial X-ray tube orientation should be used. The results show that MBIR methods may alter these trade-offs depending on the incorporated blur models. For example, in the trabecular probe study with an axial X-ray tube orientation and an object in the  $y = 60$  mm plane, position of the object is more important when using a SI model as compared to an identity model or FDK when minimizing RMSE.

When modeling SV blur, the wrong approximation can lead to drastically reduced image quality. In particular, modeling a highly SV blur as SI may lead to a mismatch between the true blur and the model. If the blur is underestimated, resolution recovery

will be limited, while if the blur is overestimated, ringing artifacts may occur. Without SV blur modeling, these two effects may appear at different locations in the same reconstruction. Overestimating the blur could also lead to contrast boosting (i.e., artificially high contrast that does not reflect the true object). This is likely what was observed in the sourcelets study. While in many cases contrast enhancement may be desirable, it presents problems when accurate quantification is required. Future studies are required to determine if this is the effect seen in the sourcelets study, and the degree to which blur mismatch may effect quantification in various clinical scenarios.

MBIR often results in location-dependent resolution and noise properties throughout the FOV [145]. Incorporating SV blur modeling may exacerbate this effect, as shown in the gantry motion bench study. One solution is location dependent penalty strengths as shown in Fessler and Rogers [145]. Such a solution may need to be modified to account for more advanced blur modeling. Uniform resolution and noise properties in the context of SV blur modeling are a potential subject of future work.

SV blur modeling can be computationally expensive. In this chapter we explored simplifications such as ignoring depth-dependence and multiresolution reconstruction. Whether such high-fidelity modeling is worth the computational cost will depend on the system properties and clinical task. High-fidelity SV modeling may also be used to reconstruct “gold-standard” images to validate or train more efficient techniques (MBIR with less accurate models, convolutional neural network denoising, etc.).

Through analysis of shift-variant blur properties of multiple systems, we have demonstrated how understanding location-dependent blur can improve acquisition protocol design (e.g., favoring the anode side of the X-ray source) and system design (e.g., axial tube orientation for uniformity, transaxial for ROI imaging). It was

also shown that proper modeling of shift-variant blur properties with MBIR leads to improved image quality. As CT systems target increasingly high-resolution applications, understanding and accounting for SV system blur may be essential to providing better accuracy and improved clinical outcomes.



# Chapter 7

## Model-based material decomposition

This chapter contains work originally published in

Steven Tilley et al. “A General CT Reconstruction Algorithm for Model-Based Material Decomposition”. In: *Proc. SPIE. Medical Imaging 2018: Physics of Medical Imaging*. Vol. 10573. Houston, TX: International Society for Optics and Photonics, Mar. 9, 2018, pp. 10573–7. DOI: 10.1117/12.2293776. URL: <https://www.spiedigitallibrary.org/conference-proceedings-of-spie/10573/105731E/A-general-CT-reconstruction-algorithm-for-model-based-material-decomposition/10.1117/12.2293776.short> (visited on 05/15/2018)

and

S. Tilley II, Wojciech Zbijewski, and J. Webster Stayman. “Model-Based Material Decomposition with a Penalized Nonlinear Least-Squares CT Reconstruction Algorithm”. In: *Physics in Medicine and Biology* (2018). ISSN: 1361-6560. DOI: 10.1088/1361-6560/aaf973. URL:

<http://iopscience.iop.org/10.1088/1361-6560/aaf973> (visited on 01/01/2019).

Reproduced here with permission.

## 7.1 Introduction

Spectral CT has found clinical application in a number of imaging scenarios, including contrast enhanced applications such as anthrography [148, 149], angiography [150], and lung ventilation [151], as well as urinary stone classification [152] and bone marrow lesion detection [153]. Spectral CT permits separation of different materials (material decomposition) which may have similar attenuation values by exploiting differences in their spectral properties. For example, while iodinated contrast agents and calcified plaques can appear similar in traditional CT angiography, they can be distinguished in spectral CT [150]. Additionally, material decomposition results in density estimates for each material, as compared to overall attenuation in traditional CT, which are often more physiologically relevant than attenuation — e.g. in bone mineral density studies [131]. Finally, spectral CT facilitates reduction of beam hardening artifacts, which are caused by monoenergetic model assumptions in traditional CT.

Material decomposition utilizes multiple types, or channels, of measurements with different spectral properties. Such channels can be obtained in many ways. Strategies include multiple energy bins in photon counting detectors [154] and data acquired with different incident X-ray spectra, either via different tube voltages [60, 155, 156] or differential filtering [58, 157–159]. Combining this multi-channel data with knowledge

of the X-ray spectra and the attenuation properties of the materials being imaged enables reconstruction of individual material density images.

Traditionally, material decomposition is performed separately from the reconstruction. In Projection Domain Decomposition (PDD) [160] material specific line integrals are estimated from the measurements using a polyenergetic forward model. Because this is done independently for each integration path (i.e., each “ray” through the object from source to detector), this method requires multiple channels for each ray. In other words, the different energy channels need to be geometrically matched so they correspond to the same integration paths through the object. This is the case in photon counting detectors, where each detector element has multiple energy bins. However, other approaches may not meet this criteria — e.g., kV switching [60] — or only meet this criteria after re-binning — e.g., split filter with sufficient sampling [159]. In Image Domain Decomposition (IDD), the spectral channels are reconstructed independently, and material density images are estimated from the reconstructions [161–163]. The IDD method is capable of using unmatched measurements, but because the channels are reconstructed separately, each channel needs sufficient sampling. Additionally, IDD may require separate correction for spectral effects such as beam-hardening [164].

MBMD techniques perform the decomposition and the reconstruction simultaneously. MBMD is a form of MBIR, which minimizes an objective function derived from a physical and statistical model of the measurement process. MBMD includes a polyenergetic forward model which relates material densities to the measurement data, allowing direct estimation of the material image volumes. Such a direct approach has many advantages as compared to traditional methods. MBMD does not

require matched data as in PDD, and does not necessarily require each channel to be sufficiently sampled as in IDD (because the densities are reconstructed from all channels simultaneously). Because MBMD uses a polyenergetic forward model, beam hardening effects can be eliminated (in contrast to traditional IDD, where removing beam-hardening artifacts requires a pre-correction). Lastly, regularization in MBMD acts jointly on both the decomposition and reconstruction, as opposed to traditional methods which either only regularize the reconstruction (potentially resulting in noisy decomposition) or require separate regularization for each step (increasing the number of free parameters). Multiple MBMD methods have been developed [58–65, 165]. Additionally, Zhang et al. [166] have developed a hybrid approach, in which the noise properties of the initial PDD (e.g., correlation between material line integrals) are modeled in the subsequent MBIR reconstruction.

The mathematical model used to derive the nonlinear SQS algorithm in §3.2.1 is sufficiently general to accommodate a polyenergetic forward model, and can therefore be used for MBMD. This approach differs from the aforementioned MBMD methods in that it is the only penalized weighted least-squares MBMD method (Gaussian noise model) utilizing optimization transfer and operating on pre-log data.

In this chapter we provide an in-depth description on how to apply the general MBIR method in §3.2.1 to material decomposition, resulting in the proposed MBMD method. We compare this MBMD method to IDD and PDD in a simulated CBCT kV-switching scenario decomposing water and calcium. Both fast and slow kV-switching schemes are explored. (While this work uses CBCT systems, all reconstructions are at or near the central plane, so cone beam artifacts are minimal.) We also compare MBMD to IDD in a simulated CBCT kV-switching scenario with water-iodine

decomposition, focusing on the sensitivity of each method to iodine concentration. We then use MBMD to decompose water, iodine, and gadolinium in both a CBCT simulation study and in a CBCT test bench study with a unique acquisition protocol: combining a split filter with kV-switching to obtain four spectral channels. The test bench data was also used to evaluate a novel tiled filter acquisition, which has four spectral channels but more challenging sampling properties than the split filter.

## 7.2 Methods

### 7.2.1 Reconstruction algorithm

All MBIR methods generally consist of a forward model, which is a mathematical description of the measurement process and associated statistical properties, and a corresponding objective function, which is a goodness-of-fit measure between the measurements and an image volume estimate. The reconstruction process seeks to find an optimal volume estimate for this objective function. In this section we demonstrate how to adapt the general MBIR approach described in §3.2.1 to a MBMD estimation framework.

In §3.2.1, we presented a general algorithm for image estimation with the following forward model:

$$\bar{\mathbf{y}} = \mathbf{B} \exp(-\mathbf{M}\mathbf{x}) \quad (7.1a)$$

$$\mathbf{y} \sim \mathcal{N}(\bar{\mathbf{y}}, \mathbf{K}) \quad (7.1b)$$

where  $\mathbf{y}$  denotes a vector of measurements and  $\mathbf{x}$  is the (image) vector to be estimated.

To accommodate the MBMD objective, one must relate densities of specific materials to the tomographic measurements. Moreover, since material decomposition relies on energy-dependent attenuation differences between materials, the forward model must encompass the polyenergetic nature of the measurement process and the mechanisms of spectral discrimination. Towards this end, we define the following data model. For simplicity, we present the mean model in terms of an individual measurement,  $\bar{\mathbf{y}}_i$ :

$$\bar{\mathbf{y}}_i = \int_E S^{(i)}(E) \exp \left[ - \sum_{m=1}^{N_m} \mu^{(m)}(E) \sum_j \mathbf{A}_{ij} \boldsymbol{\rho}_j^{(m)} \right] dE. \quad (7.2)$$

This forward model presumes the object is composed of  $N_m$  basis materials. For each material ( $m$ ), a (image volume) vector of material density values ( $\boldsymbol{\rho}^{(m)}$ ) is forward projected using a system matrix ( $\mathbf{A}$ ). For each energy ( $E$ ), line integrals for that basis material are multiplied by the material-specific mass attenuation coefficient ( $\mu^{(m)}(E)$ ) to obtain material- and energy-dependent line integrals. After summing over basis materials, Beer's law is applied to the energy-dependent line integrals, and the result is scaled by the energy-dependent system response ( $S^{(i)}(E)$ ). The expected value of each measurement is obtained by integrating over energy. The system response is a general function that permits modeling of both source spectra (including filtration) as well as detector response. Note that  $S^{(i)}(E)$  is also indexed by the measurement ( $i$ ), which allows modeling of a wide variety of spectral CT strategies including multiple spectral filters, view-dependent energies (e.g., kV switching), and energy-discriminating detector bins. The number of spectral channels of an acquisition is the number of unique normalized spectral responses. For example, in a simple kV-switching acquisition, all the  $S^{(i)}$  for even numbered projections would be equal,

Table 7.1: Notation summary.

Variable	Description	Units	Size
$N_j$	Number of voxels in the image	—	—
$N_i$	Number of measurements	—	—
$N_m$	Number of materials	—	—
$N_E$	Number of energies	—	—
$\mathbf{A}$	System matrix	mm	$N_i \times N_j$
$\boldsymbol{\rho}^{(m)}$	Vector of densities for material $m$	$\text{g mm}^{-3}$	$N_j \times 1$
$\mu^{(m)}(E)$	Mass attenuation coefficient of material $m$ at energy $E$	$\text{mm}^2 \text{g}^{-1}$	
$S^{(i)}(E)$	System spectral response of measurement $i$ at energy $E$	$\text{photons kV}^{-1}$	
$\mathbf{x}$	Concatenated density vectors of all materials	$\text{g mm}^{-3}$	$(N_m \cdot N_j) \times 1$
$\mathbf{M}$		$\text{mm}^3 \text{g}^{-1}$	$(N_E \cdot N_i) \times (N_m \cdot N_j)$
$\mathbf{B}$		photons	$N_i \times (N_E \cdot N_i)$

and likewise for odd numbered projections, resulting in two spectral channels. All of the pertinent variables of this forward model are summarized in Table 7.1. In this paper we adopt a version of (7.2) that is discretized in energy:

$$\bar{\mathbf{y}}_i = \sum_{k=1}^{N_E} S^{(i)}(E_k) \Delta E \exp \left[ - \sum_{m=1}^{N_m} \mu^{(m)}(E_k) \sum_j \mathbf{A}_{ij} \boldsymbol{\rho}_j^{(m)} \right] \quad (7.3)$$

where  $N_E$  is the number of energy bins and  $\Delta E$  is the width of each bin (in this work 1 kV). One may also scale by mass attenuation coefficients and sum over materials prior to the forward projection, but this would result in  $N_E$  forward projections as opposed to  $N_m$  forward projections. In this work  $N_E$  is much larger than  $N_m$ , so performing projection operations first is more efficient.

Equation 7.3 can be written in the form of (7.1a), permitting use of the previously developed MBIR algorithm. Denoting  $\mathbf{I}^{(n)}$  as an  $n \times n$  identity matrix, we may write the terms in (7.1a) as

$$\mathbf{x} \equiv \begin{bmatrix} \boldsymbol{\rho}^{(1)} \\ \vdots \\ \boldsymbol{\rho}^{(N_m)} \end{bmatrix} \quad (7.4)$$

$$\mathbf{M} \equiv \begin{bmatrix} \mu^{(1)}(E_1)\mathbf{I}^{(N_i)} & \dots & \mu^{(N_m)}(E_1)\mathbf{I}^{(N_i)} \\ \vdots & \ddots & \vdots \\ \mu^{(1)}(E_{N_E})\mathbf{I}^{(N_i)} & \dots & \mu^{(N_m)}(E_{N_E})\mathbf{I}^{(N_i)} \end{bmatrix} \begin{bmatrix} \mathbf{A} & \mathbf{0} \\ & \ddots \\ \mathbf{0} & \mathbf{A} \end{bmatrix} \quad (7.5)$$

$$\mathbf{B} \equiv \Delta E \begin{bmatrix} S(E_1, 1) & 0 & 0 & \dots & S(E_{N_E}, 1) & 0 & 0 \\ 0 & \ddots & 0 & & 0 & \ddots & 0 \\ 0 & 0 & S(E_1, N_i) & \dots & 0 & 0 & S(E_{N_E}, N_i) \end{bmatrix}. \quad (7.6)$$

The outputs of the MBMD algorithm with these substitutions are images of the local density of each base material ( $\boldsymbol{\rho}^{(m)}$ ), as opposed to images of attenuation values as in traditional methods. While some multienergy methods produce images of attenuation values at different energies (e.g., monoenergetic reconstructions), the MBMD approach estimates material density values directly.

Note that explicit formation of these matrices is not required, nor desirable for implementation due to their size. For computational implementation, a functional approach is adopted — computing the result of each matrix multiplication without explicitly creating the matrix. For example, to apply  $\mathbf{B}$ , each element of the input is scaled by the appropriate term in  $S$ , and then the result is summed over energy.



Though the noise model is general, in this work, we presume uncorrelated measurement noise such that

$$\mathbf{K} = \mathbf{D} \{ \mathbf{y} \} + \mathbf{I}^{(N_i)} \sigma_{ro}^2 \quad (7.7)$$

where  $\mathbf{D} \{ \cdot \}$  forms a diagonal matrix with its argument on the diagonal, and  $\sigma_{ro}$  is the equivalent readout noise standard deviation in photons. In order to utilize existing penalty functions, the penalty is applied separately for each material density image

$$\mathbf{R}(\mathbf{x}) = \sum_m^{N_m} \beta^{(m)} \mathbf{R}_\rho(\boldsymbol{\rho}^{(m)}) \quad (7.8)$$

where  $\beta^{(m)}$  is the penalty strength for material  $m$  and  $\mathbf{R}_\rho$  is a penalty function for an individual material density image.

### 7.2.2 Image domain decomposition

We used the following IDD approach for comparison with MBMD. Each energy channel is reconstructed with standard MBIR with system matrix  $\mathbf{M} = \mathbf{A}$  and a simple  $\mathbf{B} = \mathbf{D} \{ I_0 \}$  that accommodates a gain due to photon flux ( $I_0$  photons per pixel). These assumptions are typical for MBIR, and implicitly assume a monoenergetic spectrum. IDD is then applied to these reconstructions. Traditionally, IDD is applied to analytical reconstructions (e.g., FDK). However, in this work MBIR is used as a more fair comparison to MBMD. A comparison between different reconstruction methods with IDD can be found in Zbijewski et al. [149]. We used the following model for each voxel in the reconstructions of  $N_c$  spectral channels:

$$\mathbf{r} = \hat{\mathbf{U}} \boldsymbol{\tau} \quad (7.9)$$

where  $\hat{\mathbf{U}}$  is a  $N_c \times N_m$  matrix of effective attenuation values,  $\mathbf{r}$  is a  $N_c \times 1$  vector of voxel attenuation values from each spectral channel reconstruction, and  $\boldsymbol{\tau}$  is a  $N_m \times 1$  vector of material densities for that voxel. (In this work only two materials were estimated using IDD from two spectral channels, so there was no need to incorporate a volume constraint.) Each effective attenuation value is defined as the average mass attenuation value weighted by energy [161]

$$\hat{U}_{cm} \equiv \frac{\sum_k^{N_E} S^{(c)}(E_k) \mu^{(m)}(E_k)}{\sum_k^{N_E} S^{(c)}(E_k)} \quad (7.10)$$

where  $S^{(c)}$  is the system spectral response of channel  $c$ . The normal equations are used to find a least squares estimate for  $\boldsymbol{\tau}$

$$\hat{\boldsymbol{\tau}} = \left[ \hat{\mathbf{U}}^T \hat{\mathbf{U}} \right]^{-1} \hat{\mathbf{U}}^T \mathbf{r}. \quad (7.11)$$

This estimation process is applied to each voxel separately.

### 7.2.3 Water/calcium simulation study

A digital cylindrical water phantom with  $0.125 \text{ mm} \times 0.125 \text{ mm}$  voxels was created containing three calcium inserts, two with  $600 \text{ mg mL}^{-1}$  Ca and the other with  $100 \text{ mg mL}^{-1}$ . Data were generated from this phantom using (7.3) with a source-detector distance of 120 cm, a source-axis distance of 60 cm, and a detector with  $0.097 \text{ mm}$  pixels. Two X-ray spectra were used, 60 kVp and 120 kVp, with the latter containing additional filtration (4 mm of aluminum and 0.254 mm of silver) [23]. Each energy response curve was normalized to sum to one, and then scaled by  $2.5 \times 10^5 \text{ photons pixel}^{-1}$ . Finally, we added Poisson noise to the data, binned it by a

factor of four (resulting in a photon flux of  $10^6$  photons pixel<sup>-1</sup>), and added readout noise equivalent to 2.8 photons. Kilovolt switching was simulated by alternating the spectrum as a function of projection angle, resulting in 180 projections acquired with the 60 kVp spectrum and 180 with the 120 kVp spectrum, with consecutive projections separated by 1°. Two kV-switching schemes were used: switching every other frame (KV1:1), and switching every 10 frames (KV10:10).

Data were reconstructed using three methods: PDD, IDD, and MBMD. For PDD, (7.3) was used to generate a map from pairs of measurements to pairs of line integrals using interpolation [160]. This relationship was used to estimate ideal line-integrals for each material (i.e.,  $\mathbf{A}\boldsymbol{\rho}^{(m)}$  in (7.3)). In order to obtain matched projection data, the 60 kVp data and the 120 kVp data were upsampled to 360 projections each using linear interpolation. Because of the required interpolation, we only applied PDD to the KV1:1 case. The decomposed line integrals were then used to generate ideal (i.e., monoenergetic) measurements, which were reconstructed using MBIR. The nonlinear SQS MBIR method (§3.2.1) was used with  $\mathbf{B} = \mathbf{D}\{I_0\}$  where  $I_0 = 10^6$  photons and  $\mathbf{M}$  was the system matrix, using the notation from (7.1a). IDD was calculated as in §7.2.2. To ensure nearly converged reconstructions, all MBIR algorithms ran for 20 000 iterations using 10 subsets. Additionally, Nesterov momentum acceleration[83, 85] was used for the first 15 000 iterations. A Huber penalty[71] was used with  $\delta = 10^{-3}$ . For each method the penalty strength was the same between each channel/material (e.g., all  $\beta^{(m)}$  were the same for a given reconstruction).

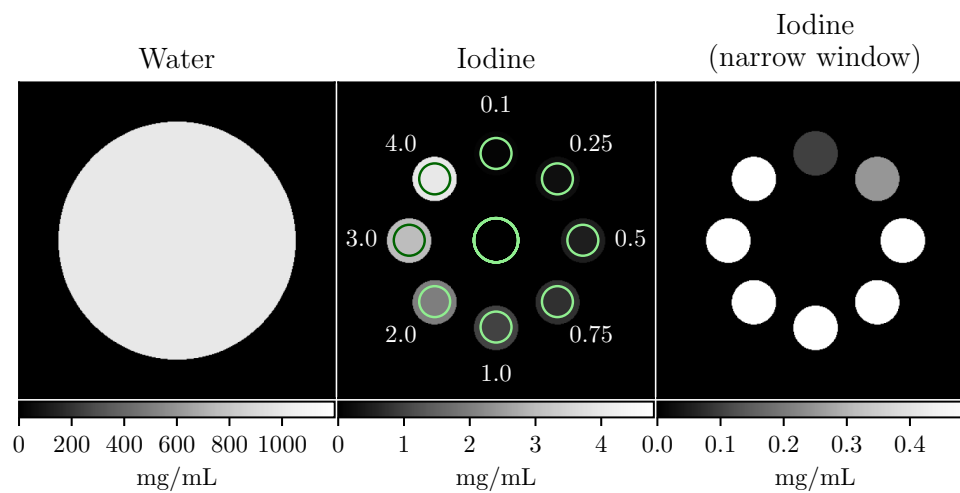


Figure 7.1: Iodine sensitivity phantom. The numbers indicate the iodine concentration in each adjacent ROI in  $\text{mg mL}^{-1}$ . ROI specific CNR was calculated as the ratio of the mean in the regions indicated by the circles along the edge of the phantom to the standard deviation in the inner circle.

### 7.2.4 Iodine sensitivity simulation study

We compared the sensitivity of IDD and MBMD to iodine concentration using the digital phantom in Figure 7.1. Data were generated using a kV-switching scheme [60, 155, 156, 167] with 80 kVp and 140 kVp spectra alternating every frame. This experiment investigates whether MBMD offers improvements over traditional methods with standard acquisition schemes.

The phantom was created with  $0.25 \text{ mm} \times 0.25 \text{ mm}$  voxels. Data were generated according to (7.1a) with a 60 cm source-to-isocenter distance, a 120 cm source-to-detector distance, a 0.278 mm pixel pitch, and 360 projections in  $1^\circ$  increments. The data were binned to 0.556 mm pixels to model nonlinear partial volume effects. The bare-beam intensity was  $10^4$  photons/pixel after binning. Lastly, Poisson noise and readout noise ( $\sigma_{ro} = 7.109$  equivalent photons/pixel) were added to the data.

Mass attenuation coefficients were obtained from NIST [24], and emitted X-ray spectra were calculated using Spektr [23] with an inherent filtration of 1.6 mm of aluminum. Mass attenuation curves were interpolated to match the energy sampling of the spectra (one sample per kV from 5 kV to 140 kV). Emitted spectra had peak kVs of 80 and 140 and were both modified by filtration with 2.0 mm of aluminum and 0.2 mm of copper. Peak kV was switched every projection ( $1^\circ$ ). The CsI scintillator in the indirect detector was modeled with 0.6 mm thickness.

Data were reconstructed with both MBMD and MBIR with the monoenergetic model (for IDD) with  $0.5 \text{ mm} \times 0.5 \text{ mm}$  voxels, 2000 iterations, 9 ordered subsets, and momentum-based acceleration [83, 85]. Monoenergetic MBIR for IDD was initialized with a FDK reconstruction [35]. MBMD reconstructions also used a FDK reconstruc-

tion, which was segmented to determine the support of the object. The support was assumed to be uniformly water with constant density. MBMD was initialized with this water-only image.

A quadratic regularizer was used for all reconstructions (2.40). Both IDD and MBMD require two regularization strengths (either for each energy reconstruction or for each material density image, respectively). A two-dimensional sweep was performed for each method, and the optimal reconstruction was determined as the one with the minimum RMSE over the entire reconstruction ( $\mathbf{x}$  in (7.1a)). The Contrast-to-Noise Ratio (CNR) for each ROI from these optimal reconstructions was calculated as the average value in the ROI divided by the standard deviation in the center of the image (ROI locations are indicated in Figure 7.1). CNR values were compared to evaluate the sensitivity of each method to iodine concentration.

### 7.2.5 Kilovolt-switching with split-filtration simulation studies

We evaluate the application of this MBMD approach in another simulated spectral CT scenario that uses a combination of kV-switching and split-filters to obtain different spectral channels (illustrated in Figure 7.2). Kilovolt-switching [60, 155, 156, 167] and split-filters [159, 168, 169] may be used to acquire multiple channels of spectral data by altering the incident spectra temporally or spatial, respectively. Each technique presents different sampling trade-offs, either reducing angular sampling (kV-switching) or spatial sampling (split-filters). Both techniques result in non-coincident rays, precluding PDD (without interpolation/re-binning). By combining both tech-

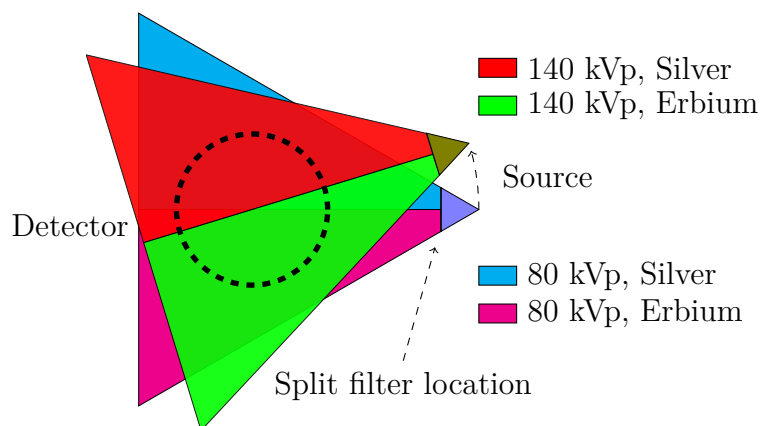


Figure 7.2: Schematic of the kV-switching/split-filter acquisition protocol. The kVp was switched every projection (i.e., every  $1^\circ$ ).

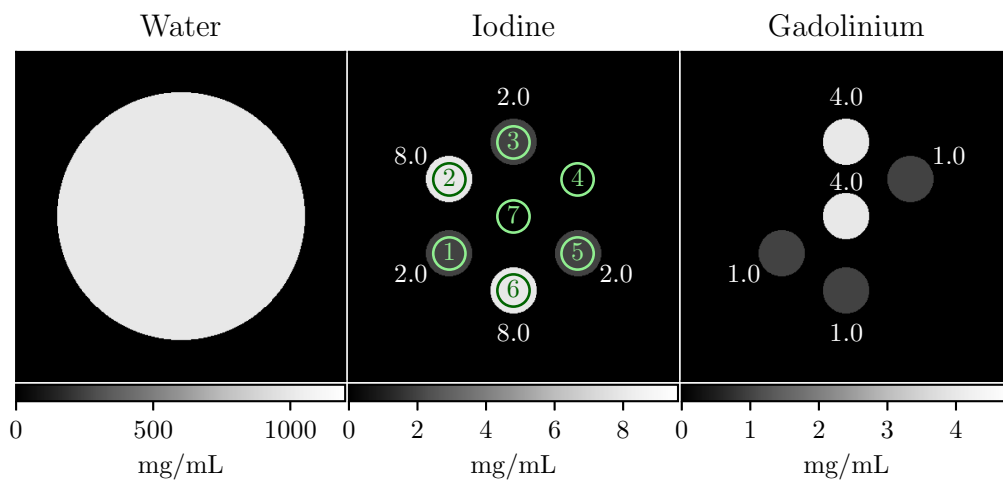


Figure 7.3: Digital water, iodine, and gadolinium phantom. Inserts are numbered in the iodine image, and corresponding ROIs for metric evaluation are indicated with circles. Iodine and gadolinium concentrations are next to each ROI in  $\text{mg mL}^{-1}$ .

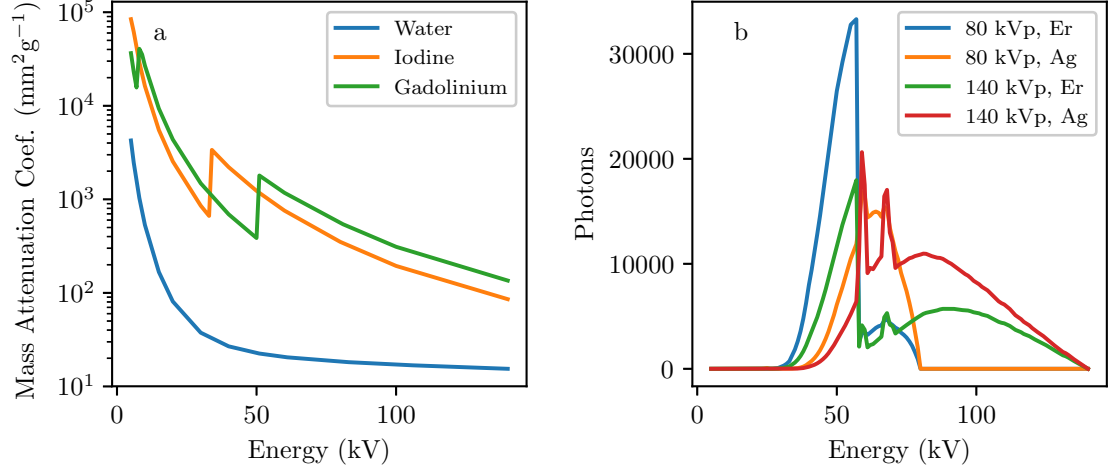


Figure 7.4: (a) Mass attenuation coefficients. (b) Spectral responses ( $S$ ) for the kV-switching/split-filter simulation study.

niques, both the number of spectral channels and the sampling challenges are compounded, providing a unique scenario with which to evaluate the MBMD method.

Two filters and two kVp settings were used to produce four spectral channels, from which three basis materials were reconstructed. Data were generated as in the previous study (§7.2.4), but used a different, 3-material phantom (Figure 7.3) and the additional split filter. The phantom contains ROIs with different concentrations and mixtures of iodine and gadolinium. Half of the beam was filtered with 0.25 mm of erbium, and the other half was filtered with 0.254 mm of silver. The spectra were normalized such that the bare beam intensity after the erbium filter was  $5 \times 10^5$  photons/pixel ( $2.5 \times 10^5$  photons/pixel bare beam before binning). Mass attenuation curves for the different materials and spectral responses for each channel are shown in Figure 7.4.



Data were reconstructed using MBMD as in the previous study. However, simplifying assumptions were made to avoid a three-dimensional parameter sweep in penalty strengths. Specifically, the ratio of regularization strength for each material image ( $\beta^{(m)}$  in (7.8)) to the regularization strength for the water image was set to the (approximate) ratio of the density of water to the maximum density of that material: 100 for iodine and 200 for gadolinium. For example, if the regularization strength for water was  $10^3$ , it was  $10^5$  for iodine and  $2 \times 10^5$  for gadolinium. Therefore, the reconstruction method had only one degree of freedom, which was varied to select a reconstruction with an acceptable level of noise. Reconstructions were initialized as in the previous study.

### 7.2.6 Kilovolt-switching with filtration physical test bench studies

The proposed MBMD algorithm was also evaluated in physical data. Specifically, we conducted spectral CT data acquisitions using a CBCT test bench emulating a setup similar to the kV-switching/split-filter simulation study. The phantom (Figure 7.5) consisted of four vials of different mixtures of iodine ( $0 \text{ mg mL}^{-1}$  to  $75 \text{ mg mL}^{-1}$ ) and gadolinium ( $0 \text{ mg mL}^{-1}$  to  $20 \text{ mg mL}^{-1}$ ). Iodine and gadolinium solutions were obtained by diluting Omnipaque ( $300 \text{ mg mL}^{-1}$  iodine, GE Healthcare, Chicago, IL.) and Magnevist ( $469.01 \text{ mg mL}^{-1}$  gadopentetate dimeglumine, Bayer, Leverkusen, Germany), respectively. The vials were placed in a 10 cm plastic cylinder. Data were acquired with a Varian (Salt Lake City, UT) PaxScan 4343CB detector (0.278 mm pixel pitch, 0.6 mm CsI scintillator), 120 cm source-to-detector distance, and 72.7 cm source-to-axis distance. The x-ray beam was filtered with 0.25 mm erbium and

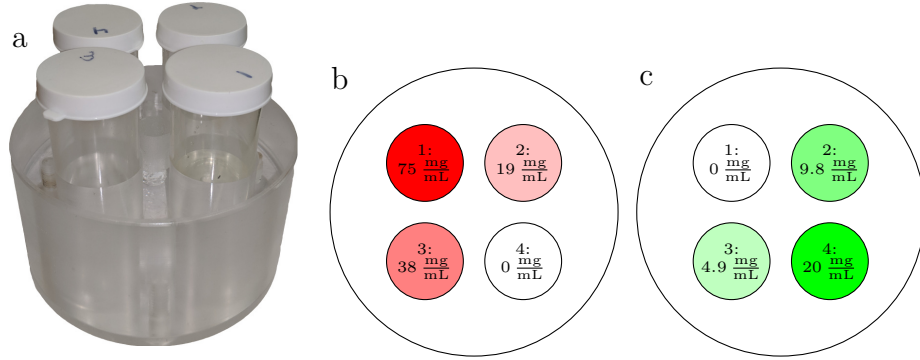


Figure 7.5: (a) Iodine/gadolinium phantom. Each vial contains different mixtures of iodine- and gadolinium-based contrast agents. In (b) and (c) we show a schematic of the phantom identifying insert/ROI labels. The concentration of iodine in each vial is indicated in (b), and the concentration of gadolinium in each vial is in (c).

0.254mm silver, at both 80 kVp and 130 kVp. These four data sets were acquired separately, and then combined in post-processing to emulate the kV-switching/split-filter protocol. The data were reconstructed as in the previous study, using a quadratic penalty and the same material penalty strength ratios. The reconstructions were initialized with a segmented FDK reconstruction as in the previous studies. Readout noise was estimated from dark scans for each channel and averaged. Data were reconstructed at multiple penalty strengths, and a reconstruction with an acceptable noise level was chosen for further analysis.

To further stress robustness to unique sampling properties, we also emulated a tiled filtered acquisition [170]. The tiled filtered consisted of repeating elements of erbium and silver, each 8 pixels wide on the detector. The filter was translated 1 pixel every frame to improve sampling. A tiled filter permits more than two materials, as opposed to the split filter design, increasing the number of spectral channels. However,

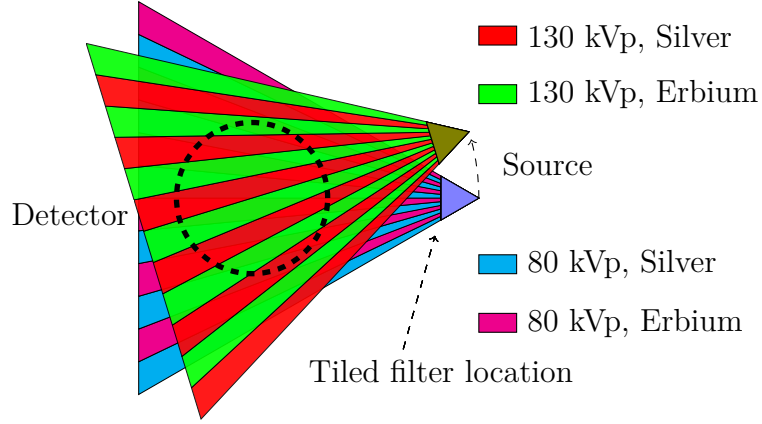


Figure 7.6: Schematic of tiled filter acquisition. The filter was translated each frame to improve sampling (not shown).

in this work only two materials were used, but with kV-switching. As with the split-filter data, the tiled filter data was emulated in post-processing. The tiled-filter acquisition is illustrated in Figure 7.6.

We developed a spectral response model of the test bench by fitting to the transmissivity of each vial from the phantom in Figure 7.5. Specifically, we obtained projections of the vials (without the plastic cylinder) arranged such that each ray only passed through one vial. We used spectra from Spektr modified with aluminum, copper, tungsten, and glass filters. CMA-ES [171] was used to estimate the thicknesses of these filters by matching simulated transmissivities with physical transmissivities through the center of each vial.

## 7.3 Results

### 7.3.1 Water/calcium simulation study

Figures 7.7 and 7.8 summarize decomposition performance. PDD and MBMD produced the best reconstructions in terms of concentration accuracy and artifact reduction. Because IDD does not model the full spectrum through the phantom, it was unable to remove beam hardening artifacts in the center insert (visible in the zoomed image of insert 2 for the IDD in Figure 7.7). The average concentration values in each insert ROI are compared in Figure 7.8. PDD and MBMD produced the most accurate concentration values, while IDD underestimated calcium concentration and overestimated water concentration, particularly for the  $600 \text{ mg mL}^{-1}$  inserts. MBMD also produced accurate concentration values in the challenging KV10:10 case.

### 7.3.2 Iodine sensitivity simulation study

A two-dimensional penalty-strength sweep was performed for each reconstruction method to find the optimal reconstruction (in terms of RMSE) and examine the relationship between penalty strengths. The RMSEs for each method are shown in Figure 7.9. For IDD, the penalty strengths resulting in the lowest RMSE were  $10^6$  for the 80 kVp channel and  $10^6$  for the 140 kVp channel (indicated by the star in Figure 7.9a). For MBMD, the optimal penalty strengths were  $10^8$  for the water image and  $10^{12}$  for the iodine image.

Figure 7.9a has a line of low RMSE values along the diagonal, indicating that the two penalty strengths should be equal for IDD in this scenario. In MBMD the optimal

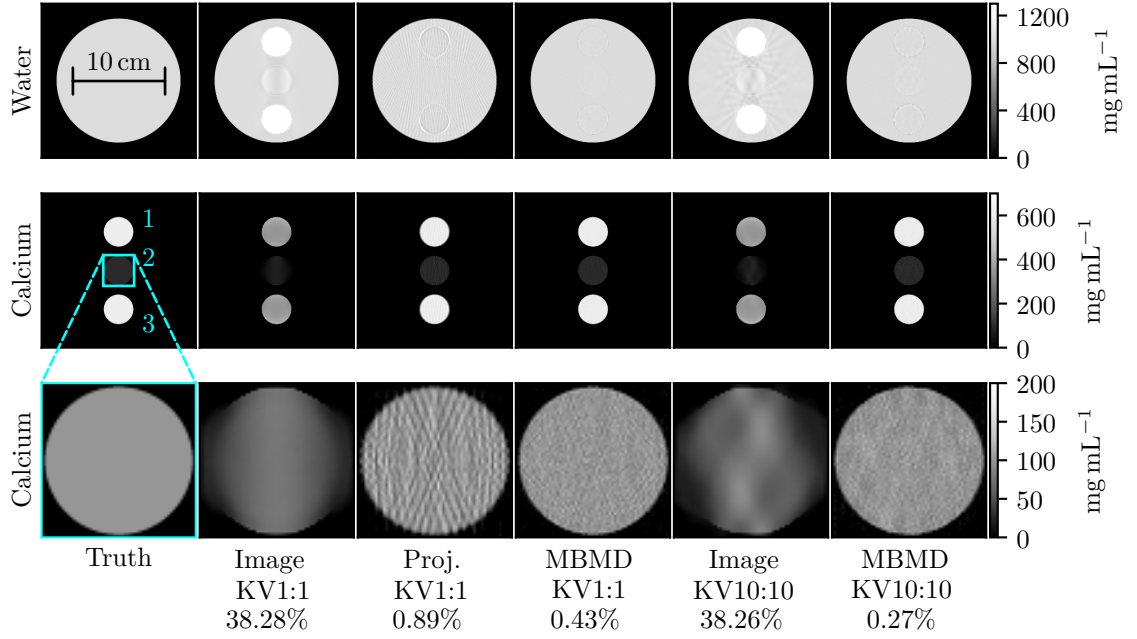


Figure 7.7: Water/calcium simulation reconstructions. The insert ROIs are numbered from top to bottom. The standard deviations of the calcium concentrations in insert 1 are  $7.82 \text{ mg mL}^{-1}$  for IDD KV1:1,  $12.41 \text{ mg mL}^{-1}$  for PDD KV1:1,  $8.11 \text{ mg mL}^{-1}$  for MBMD KV1:1,  $8.42 \text{ mg mL}^{-1}$  for IDD KV10:10, and  $8.71 \text{ mg mL}^{-1}$  for MBMD KV10:10. The percentages indicate the root mean squared fractional errors in the calcium ROIs.

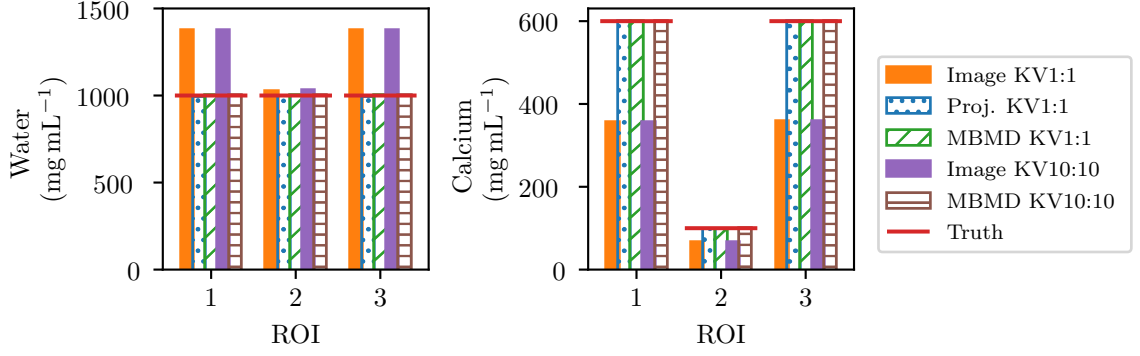


Figure 7.8: Average concentration in each insert in Figure 7.7 for water (left) and calcium (right).

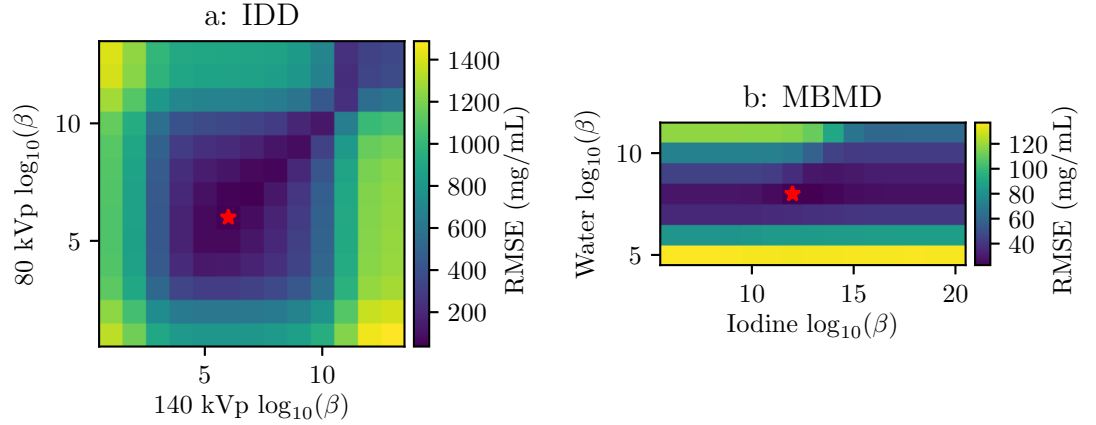


Figure 7.9: RMSE for each penalty strength combination for the (a) IDD and (b) MBMD methods. The minimum RMSE in each plot is indicated with a star.

iodine image penalty strength is  $10^4$  times the water image penalty strength. This is the ratio of the density of water to the density of iodine in the lowest concentration ROI. Because the density of the water image is much greater than the densities in the iodine image, changing the water image penalty strength has a more dramatic effect on RMSE than changing the iodine penalty strength by the same amount.

Figure 7.10 shows the minimum RMSE reconstructions for each method. The IDD reconstructions contain more noise than the MBMD reconstructions. The noise difference may be explained by the fact that MBMD regularizes the material density images (the values of interest), while IDD regularizes the intermediate individual-channel attenuation images, prior to an unregularized decomposition step which can amplify noise in the density estimates. Low concentration regions are more discernible in the MBMD reconstruction, although concentrations below  $0.5 \text{ mg mL}^{-1}$  cannot be visualized with either reconstruction method. Differences between the MBMD and IDD reconstructions also include the presence of a ring in the MBMD iodine image and biases in the MBMD water image at the high iodine concentration ROIs. These differences are likely due to the quadratic penalty smoothing objects in one material image, and the MBMD algorithm compensating by changing the density of the other material at that location. For example, the smoothed edge in the water image results in less overall attenuation due to water, which is compensated for with the ring in the iodine image.

The CNR values in each ROI are plotted in Figure 7.11. MBMD has higher CNR at all concentrations. If we define a detectable concentration as having a CNR of at least two (indicated by the black line), then MBMD is sensitive to iodine concentrations as low as  $0.5 \text{ mg mL}^{-1}$ , while IDD is only sensitive to concentrations as low as

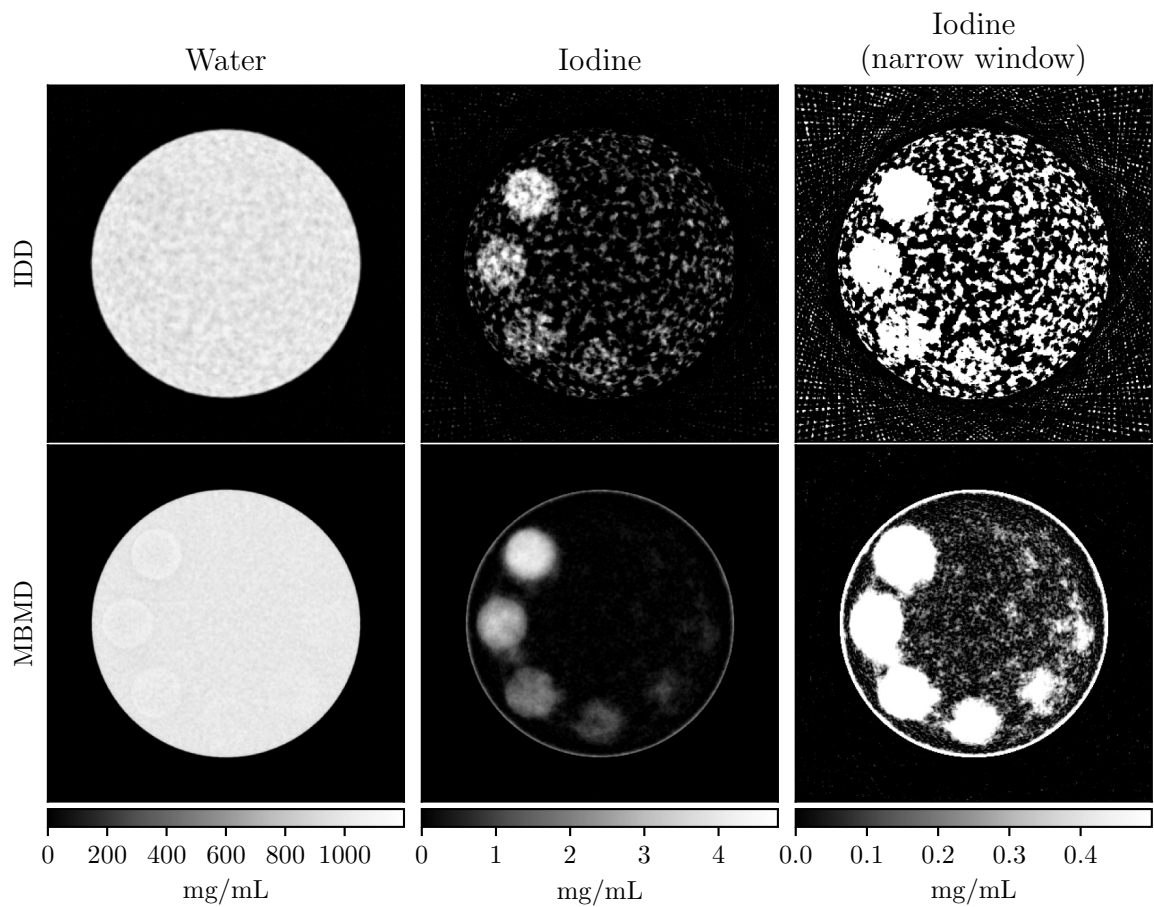


Figure 7.10: IDD (top) and MBMD (bottom) reconstructions of water (left) and iodine (middle and right) concentrations. The right column is the same as the center but with a tighter window to better visualize the low concentration ROIs.



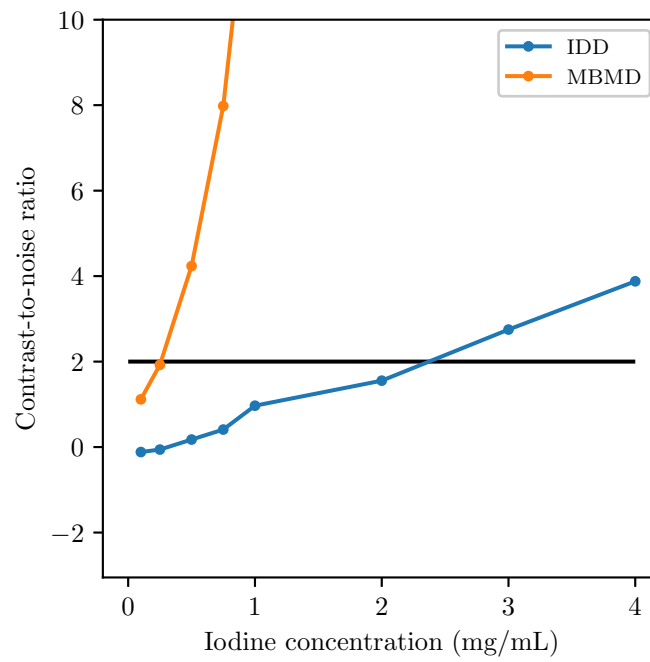


Figure 7.11: CNR values in each ROI from the optimal reconstruction with each method.

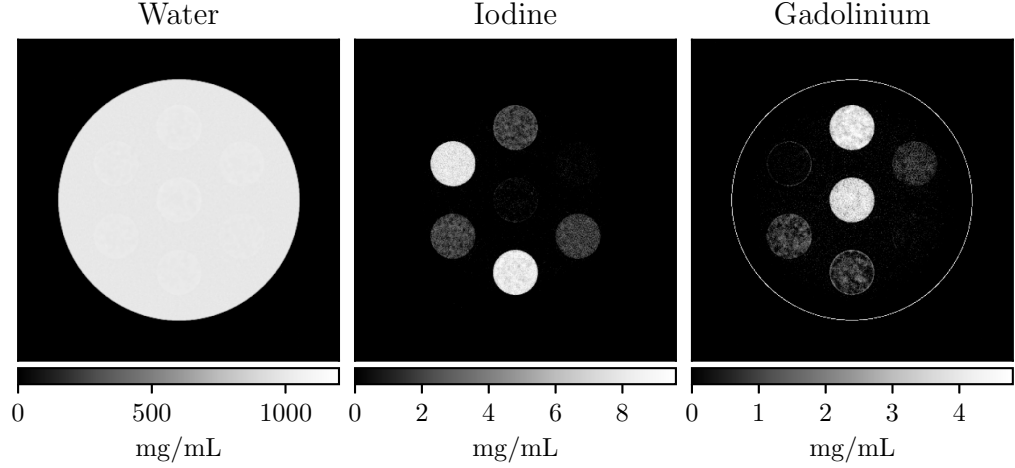


Figure 7.12: Digital iodine/gadolinium phantom reconstructions. Each column is a different material density image.

$3 \text{ mg mL}^{-1}$ . This result is specific to comparing the minimum RMSE reconstructions, and choosing the reconstructions from each method using a different metric might improve the relative performance of IDD. For example, noise-matching the reconstructions would likely increase IDD CNR relative to MBMD but reduce resolution. We chose minimum RMSE because it captures both resolution and noise effects and is straightforward to apply to the two-dimensional parameter sweeps.

### 7.3.3 Kilovolt-switching with split-filtration simulation studies

The reconstruction from the kV-switching/split-filter simulation study is shown in Figure 7.12. The reconstruction appears similar to the true phantom in Figure 7.3, with accurate relative iodine and gadolinium concentration estimates. The gadolin-

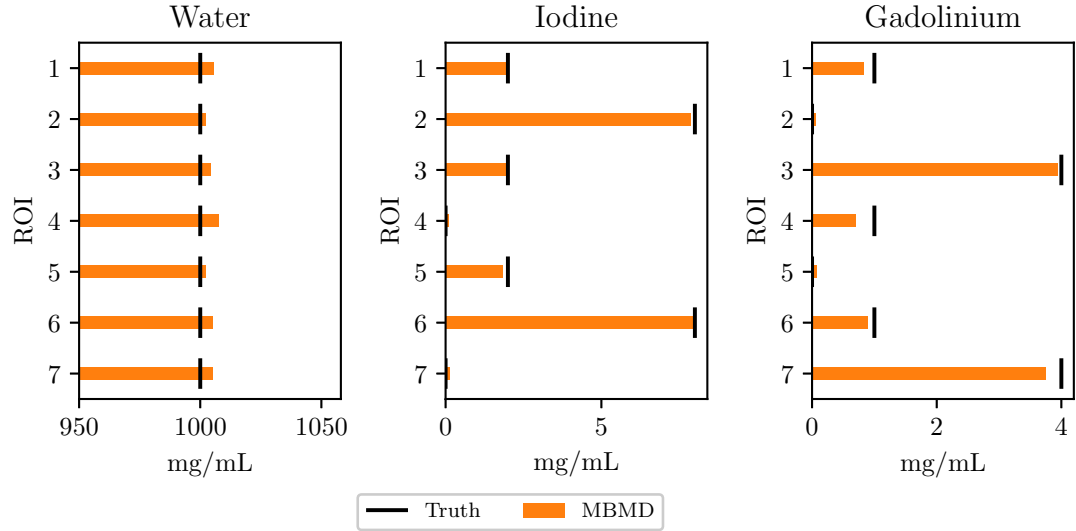


Figure 7.13: Concentrations of each material (columns) and ROI in the digital iodine/gadolinium phantom. The true concentrations are indicated by vertical lines. ROI numbers correspond to those in Figure 7.3.

ium image contains a ring at the edge of the phantom as in the iodine image in the previous study.

Estimated concentration values are presented in Figure 7.13. These estimates are fairly accurate, although gadolinium is slightly underestimated and water is slightly overestimated. RMSE concentration values for each material are  $4.86 \text{ mg mL}^{-1}$ ,  $0.108 \text{ mg mL}^{-1}$ , and  $0.170 \text{ mg mL}^{-1}$  for water, iodine, and gadolinium, respectively.

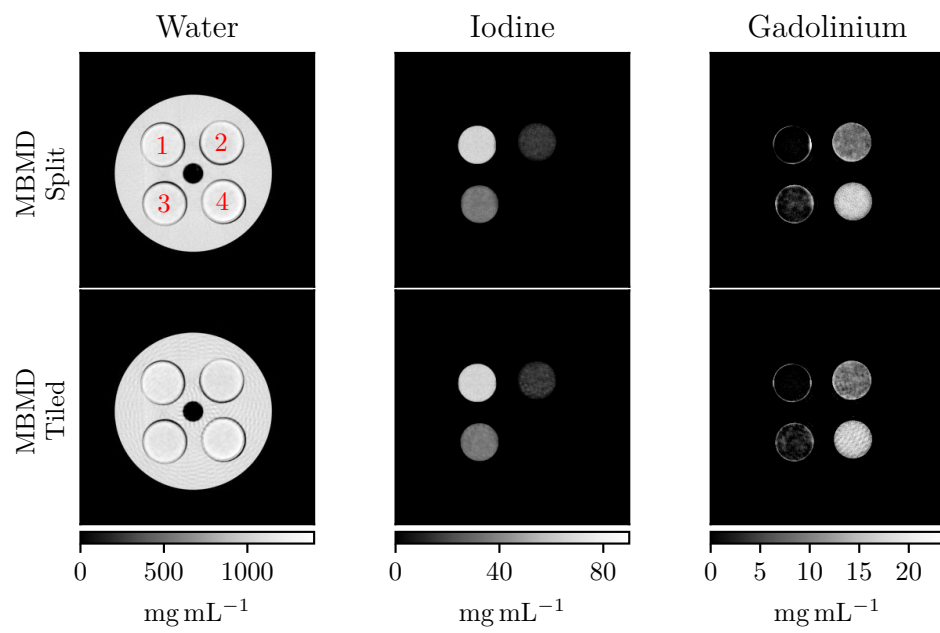


Figure 7.14: Iodine and gadolinium estimates for the physical test bench experiment. The top row shows the split filter results and the bottom shows the tiled filtered results.

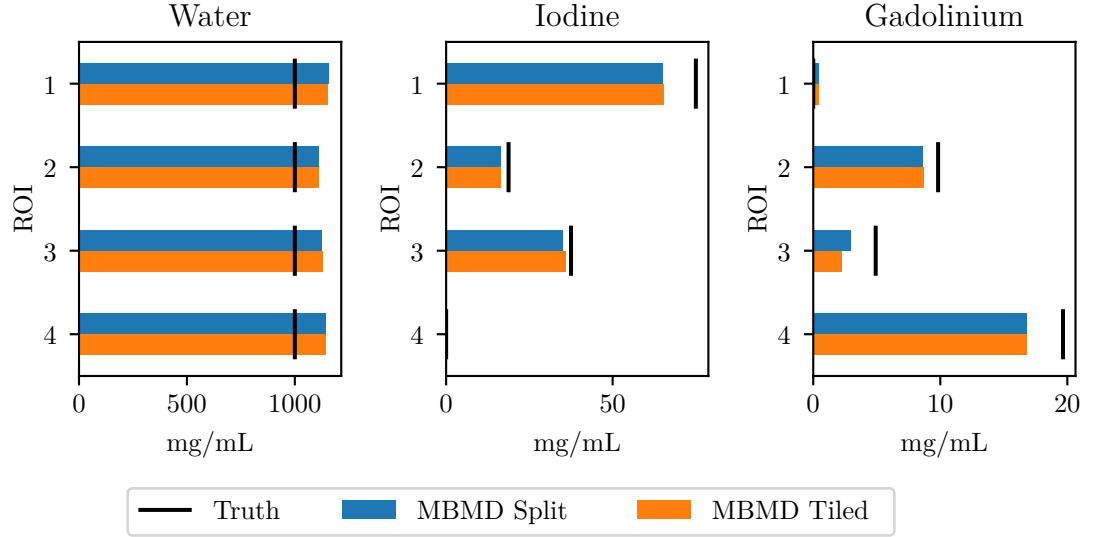


Figure 7.15: Concentration values for each material and ROI in the physical iodine/gadolinium phantom. Insert/ROI locations are indicated in Figure 7.5.

### 7.3.4 Kilovolt-switching with filtration physical test bench studies

Figure 7.14 shows the reconstructions for the physical iodine/gadolinium phantom in Figure 7.5. The results are similar to the simulation study results, although the gadolinium image contains strong ring artifacts around ROIs 1 and 3, and does not contain a ring artifact at the boundary of the phantom. The tiled filter results are similar to the split filter results, indicating MBMD is robust against different sampling. However, the tiled filter does result in more high-frequency artifacts.

The concentration values from the physical phantom reconstructions are shown in Figure 7.15. Iodine and gadolinium concentration values are slightly underestimated

while water concentration is slightly overestimated, although the relative concentrations among ROIs for each material is preserved. With the split filter, the RMSE for each material is  $134 \text{ mg mL}^{-1}$ ,  $5.26 \text{ mg mL}^{-1}$ , and  $1.85 \text{ mg mL}^{-1}$  for water, iodine, and gadolinium, respectively. With the tiled filter, the RMSEs are  $134 \text{ mg mL}^{-1}$ ,  $5.11 \text{ mg mL}^{-1}$ , and  $2.05 \text{ mg mL}^{-1}$ .

## 7.4 Discussion

With a conventional kV-switching acquisition protocol, MBMD maintained a CNR greater than two for iodine concentrations as low as  $0.5 \text{ mg mL}^{-1}$ . This was more sensitive than a traditional IDD method, indicating that MBMD is a suitable candidate for traditional acquisition schemes with the potential to extend low concentration limits. Additionally, MBMD was able to remove beam-hardening artifacts that were present in IDD reconstructions. However, we note that IDD may potentially be improved by using different effective attenuation values in (7.11), a non-negativity constraint, beam hardening pre-correction, and/or a nonlinear decomposition [163, 172]. Common IDD techniques include preprocessing projection data to correct for beam hardening [163], and using effective attenuation coefficients obtained with a calibration step, which can also mitigate beam hardening effects [173]. Bench reconstructions may be improved with a more accurate spectral model. In this work we proposed a simple spectral calibration procedure using transmissivity measurements of the base materials to estimate effective filtration of the X-ray system. MBMD achieved satisfactory decomposition accuracy of K-edge contrast materials (iodine and gadolinium) and water with the resulting spectral model. However, errors in the

spectral model lead to biases in the material decompositions, with larger biases occurring in harder decomposition problems. Future work will explore more sophisticated modeling and calibration methods to improve decomposition accuracy [174].

MBMD produced accurate concentration estimates using unique acquisition protocols combining kV-switching and filtration. This suggests that MBMD may be used with other non-traditional acquisition protocols such as unconventional filtration [170, 175, 176], multiple limited angle scans [64], and systems with multiple axially oriented X-ray sources [177]. Related work has applied the MBMD approach to X-ray beam spectral filtering [170] scenarios. This study further supports the robustness of this approach, demonstrating its application in additional acquisition strategies. All of these methods preclude the use of PDD due to unmatched measurement data (although in specific scenarios matched data may be acquired via re-binning). Similarly, IDD may be infeasible for these methods depending on the sampling of each channel. For example, reconstructing multiple limited angle scans separately would result in artifacts if the rotation angle of each scan were less than  $180^\circ$  plus the fan angle. Furthermore, MBMD may enable new acquisition protocols that are impractical with traditional methods. Applying MBMD to more unique acquisition protocols is a focus of future work.

Another future consideration is regularization design and strength. Because the search space is large, we may require better techniques to select regularization strengths, or relative regularization strengths, *a priori* (similar to the work by Zhang et al. [178] in prior image reconstruction). Regularization type is also likely to be important in future applications. For example, the ring artifacts in the MBMD reconstructions are probably caused by the quadratic penalty, and may be prevented

with edge-preserving or low rank penalties [70, 71]. Future work will also explore regularizers that enforce low rank jointly across material density images, thereby taking advantage of the common structure among these images [179].

This chapter primarily focused on discrimination of K-edge contrast agents. MBMD may also be used to decompose materials without a K-edge (e.g., the water/calcium simulation study in §7.2.3). Such decomposition can be more challenging due to the similarity of energy-dependent attenuation but may still be accommodated in the MBMD approach with appropriate material basis selection. Previous work [165, 180] has shown elemental decomposition can be effective in modeling spectral dependencies and estimating density across many tissue types. That strategy may be extended to MBMD which could offer further improvements. Future work will explore application of the methods discussed in this chapter to a larger number of materials with more similar attenuation properties.

Because the MBMD method is derived from a general MBIR forward model, it is straightforward to include models of more physical effects in the reconstruction, such as those modeled in previous chapters. Such changes can be made without altering the underlying reconstruction algorithm. Future work will take advantage of the generality of the presented MBMD algorithm for high-resolution material decomposition.

We have presented a material decomposition algorithm that is capable of modeling a wide variety of systems, including those with unique spectral acquisitions. In addition to improving the sensitivity of material density estimates, this method may enable novel multi-spectral systems and acquisition protocols, ultimately increasing access to material decomposition in pre-clinical and clinical applications.



# Chapter 8

## Conclusion

### 8.1 Summary

In this dissertation we have improved the image quality and accuracy of CT reconstructions by combining high-fidelity models of measurement physics and statistics with MBIR. A generalized MBIR framework was presented in chapter 3 that is capable of incorporating a wide range of physical effects. This framework is an important contribution to the field in that it enables advanced physical modeling without deriving custom reconstruction algorithms. We then measured and modeled many physical effects, and demonstrated that including these models in the MBIR framework improved image quality. Specifically

**Chapters 4 and 5** modeled focal-spot and scintillator blur with noise correlations using a SI model. In addition to demonstrating improvements due to blur modeling, these results show that modeling noise correlations due to scintillator blur is also important for high-resolution reconstruction. To our knowledge, this is the first

time noise correlations have been incorporated into MBIR for physical CT data reconstruction.

**Chapter 6** demonstrated that some types of blur are SV and result in location-dependent blurring of the image. Two types of SV blur were explored, focal-spot blur and gantry motion blur. Focal-spot blur was extensively measured and modeled in a variety of ways suitable for different applications. By incorporating these models into MBIR we showed that certain systems require SV modeling to efficiently use the measurement data for high-resolution reconstructions. Gantry motion blur was also modeled and included in the MBIR framework to correct this radially dependent effect, restoring resolution at the edge of the FOV.

**Chapter 7** applied the MBIR framework to model-based material decomposition. First, we demonstrated that the framework presented in chapter 3 is sufficiently general to model the polyenergetic nature of CT systems. We then incorporated this polyenergetic model into the framework to accurately decompose different materials as part of the reconstruction process. This method was applied to data with unique spatial/spectral sampling properties, and proved robust to various types of spectral data acquisition.

Additionally, we have presented a novel sourcelet projector that enables efficient focal-spot modeling, and derived a surrogate function for the isotropic Huber penalty for use with existing SQS methods.

## 8.2 Future work

This dissertation provides many opportunities for future work, including comparing MBIR with high-fidelity modeling to more methods, improving the presented algorithm, and applying the presented approaches to numerous applications.

In this work we compared MBIR methods with different models and more traditional approaches. However, some questions remain unanswered. For example, the ID deblurring in chapter 4 performed about as well as the MBIR method with correlated noise modeling. We expect that MBIR will outperform ID deblurring in the presence of higher noise, less circular phantoms (leading to more heterogeneous measurements and noise properties), and different image quality metrics. For example, one could apply ID deblurring to the line-pair phantom in chapter 5 and evaluate performance with the maximum Jaccard, bias, and noise metrics. However, certain SV blurs such as focal-spot blur cannot be accurately modeled in the ID due to the view-dependent nature of the effect.

While SV blur was studied in numerous scenarios in chapter 6, some aspects were not explored. Specifically, full sourcelet reconstructions with an axially oriented X-ray tube were not presented. Additionally, another simulation study could clarify some of the observations of the physical data reconstructions with the transaxially oriented X-ray tube, specifically whether contrast is artificially increased with the SI blur model. The gantry motion bench study suggests that location dependent regularization strength may be important when modeling SV blur, but this needs to be explored further.

In chapter 7 we presented preliminary results using a tiled spectral filter. Because these filters have yet to be built, the data was emulated in post-processing, which ignores many effects that may be present in real systems. For example, the projection of the filter will be effected by focal-spot blur, resulting in blurred spectral properties in the measurements. This and other potential challenges creating physical tiled filters are subjects of ongoing work [181].

The nonlinear SQS algorithm presented in chapter 3 was designed to model a wide range of physical effects. Many of these effects, particularly blur and energy-dependent attenuation, can dramatically alter the convergence properties of the reconstruction. This seems particularly true for MBMD. This dissertation focused primarily on the modeling and image quality aspects of the reconstruction. Thus, there are opportunities to study the convergence properties of the presented algorithm with different models and different techniques to decrease reconstruction time (e.g., preconditioning).

Instead of being used directly in commercial CT systems, the presented methods may be used to provide “gold standard” reconstructions to test the tradeoffs between image quality and algorithm/model selection. For example, the techniques in chapter 6 may be used to determine whether a system would benefit from SV blur modeling. These “gold standards” may also be used to train deep-learning based reconstruction or image restoration techniques [182], potentially permitting these algorithms to learn the relevant physical effects for a given system.

The algorithms, models, and techniques presented in this work provide a means to ensure CT measurement data is used as efficiently as possible by incorporating detailed knowledge of the imaging physics. The resulting improvements in image

quality may permit CT to be used for clinical applications that were previously out of reach, such as analyzing fine trabecular structure. By increasing resolution and image quality, high-fidelity modeling and MBIR have the potential to improve the study and diagnosis of disease, ultimately leading to better patient outcomes.

# Appendix A

## Test-Bench Gain Estimation

This section describes a strategy for gain estimation in physical bench data.

To accommodate nonuniform illumination of the FP detector, photon flux may be modeled with the following equations [18]:

$$\mathbf{g}_i = \mathbf{p}_i \mathbf{f}_i \tag{A.1}$$

$$\mathbf{f}_i \sim \text{Poisson}(I_0 \cos^3(\boldsymbol{\theta}_i)) \tag{A.2}$$

where  $\mathbf{g}_i$  is a random variable representing an offset corrected gain (bare-beam) scan value for pixel  $i$ ,  $I_0$  is a constant value representing the photon flux at the piercing point,  $\mathbf{p}_i$  is the detector gain for pixel  $i$  (detector units per photon), and  $\boldsymbol{\theta}_i$  is the angle between pixel  $i$  and the piercing ray. The parameters  $I_0$  and  $\mathbf{p}_i$  may be estimated using the mean and noise properties of offset corrected gain scans. Measurements can then be corrected for detector gain (i.e., divided by  $\mathbf{p}_i$ ) to obtain measurements in photon units. To account for focal-spot intensity variations, a normalization factor  $\mathbf{n}_v$  may be calculated for each frame ( $v$ ) using an unobstructed (bare-beam) region

of the projection data. Using this method,  $D\{\mathbf{g}\}$  is a matrix which scales the value of each pixel  $i$  by  $I_0 \cos^3(\boldsymbol{\theta}_i)$  and the values in each frame  $v$  by  $\mathbf{n}_v$ .

# Appendix B

## Separable Sourcelet Projector

Here we derive the separate sourcelet projector used in this work. The geometry and definition of coordinates for the trans-axially oriented x-ray source are shown in Figure B.1. (The axially oriented geometry is similar, except the anode coordinates are rotated 90 degrees about  $z$ .)

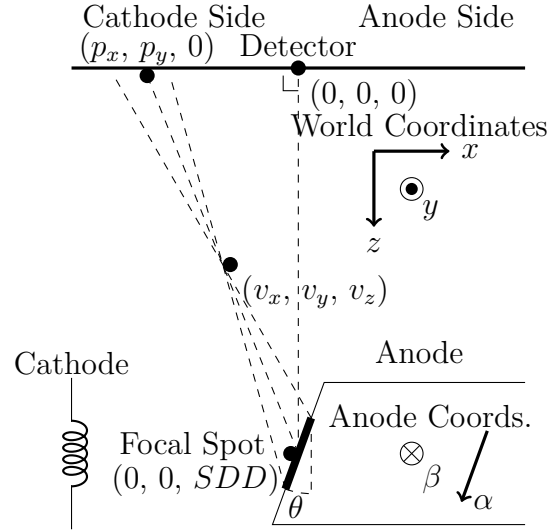


Figure B.1: Geometry and coordinates for a transaxial oriented x-ray source.



## B.1 Derivation

The transformation from anode coordinates ( $\alpha$  and  $\beta$ ) to world coordinates ( $x, y, z$ ) of a point  $f$  on the anode is given by

$$f_x = -\sin(\theta)f_\alpha \quad (\text{B.1})$$

$$f_y = -f_\beta \quad (\text{B.2})$$

$$f_z = \cos(\theta)f_\alpha + SDD \quad (\text{B.3})$$

for a trans-axial orientation and

$$f_x = f_\beta \quad (\text{B.4})$$

$$f_y = -\sin(\theta)f_\alpha \quad (\text{B.5})$$

$$f_z = \cos(\theta)f_\alpha + SDD \quad (\text{B.6})$$

for an axial orientation.

We model the intensity distribution on the anode as a collection of rectangular sourcelets, and proceed with the derivation for an individual sourcelet. This sourcelet has an indicator function  $h$  that is 1 inside the sourcelet and 0 otherwise. Sourcelet intensity is accounted for outside the exponential in a separate step (see (6.15)).

For an individual sourcelet the line integral  $g$  of an object  $f$  at a point  $p$  on the detector is given by

$$g(p_x, p_y) = \int_{f_\alpha, f_\beta} \int_{v_x, v_y, v_z} f(v_x, v_y, v_z) h(f_\alpha, f_\beta) \delta\left(v_x - \frac{p_x(f_z - v_z) + f_x v_z}{f_z}\right) \delta\left(v_y - \frac{p_y(f_z - v_z) + f_y v_z}{f_z}\right) dv_x dv_y dv_z df_\alpha df_\beta \quad (\text{B.7})$$

where  $\delta$  is the Dirac delta function.

Integrating over  $v_x$  and  $v_y$  eliminates the delta functions to yield

$$g(p_x, p_y) = \int_{f_\alpha, f_\beta} \int_{v_z} f\left(\frac{p_x(f_z - v_z) + f_x v_z}{f_z}, \frac{p_y(f_z - v_z) + f_y v_z}{f_z}, v_z\right) h(f_\alpha, f_\beta) dv_z df_\alpha df_\beta. \quad (\text{B.8})$$

We approximate the imaging volume  $f$  as a collection of points:

$$\hat{f}(v_x, v_y, v_z) = \sum_{a,b,c} f(a\Delta_x, b\Delta_y, c\Delta_z) \Delta_x \Delta_y \Delta_z \delta(v_x - a\Delta_x) \delta(v_y - b\Delta_y) \delta(v_z - c\Delta_z). \quad (\text{B.9})$$

Substituting  $\hat{f}$  for  $f$  and integrating over  $v_z$  yields

$$g(p_x, p_y) \approx \int_{f_\alpha, f_\beta} \sum_{a,b,c} f(a\Delta_x, b\Delta_y, c\Delta_z) \Delta_x \Delta_y \Delta_z \delta\left(\frac{p_x(f_z - c\Delta_z) + f_x c\Delta_z}{f_z} - a\Delta_x\right) \delta\left(\frac{p_y(f_z - c\Delta_z) + f_y c\Delta_z}{f_z} - b\Delta_y\right) h(f_\alpha, f_\beta) df_\alpha df_\beta. \quad (\text{B.10})$$

Note that this approximation assumes the projected voxel size is relatively small as compared to the projected sourcelet size.

We define  $\tilde{g}$  as the discrete approximation of  $g$  obtained by integrating over pixel areas, yielding

$$\tilde{g}[i, j] = \int_{i'=i-0.5}^{i'=i+0.5} \int_{j'=j-0.5}^{j'=j+0.5} g(p_x(i', j'), p_y(i', j')) (\Delta u \Delta v)^{-1} di' dj' \quad (\text{B.11})$$

$$\begin{aligned} \tilde{g}[i, j] \approx & \int_{i'=i-0.5}^{i'=i+0.5} \int_{j'=j-0.5}^{j'=j+0.5} \int_{f_\alpha, f_\beta} \sum_{a, b, c} f(a\Delta_x, b\Delta_y, c\Delta_z) \Delta_x \Delta_y \Delta_z \\ & \delta\left(\frac{p_x(i', j')(f_z - c\Delta_z) + f_x c\Delta_z}{f_z} - a\Delta_x\right) \\ & \delta\left(\frac{p_y(i', j')(f_z - c\Delta_z) + f_y c\Delta_z}{f_z} - b\Delta_y\right) \\ & h(f_\alpha, f_\beta) (\Delta u \Delta v)^{-1} df_\alpha df_\beta di' dj'. \end{aligned} \quad (\text{B.12})$$

Let

$$\phi \triangleq \frac{p_x(i', j')(f_z - c\Delta_z) + f_x c\Delta_z}{f_z} - a\Delta_x \quad (\text{B.13})$$

$$\psi \triangleq \frac{p_y(i', j')(f_z - c\Delta_z) + f_y c\Delta_z}{f_z} - b\Delta_y. \quad (\text{B.14})$$

We now convert the integrations over  $f_\alpha$  and  $f_\beta$  to integrations over  $\phi$  and  $\psi$ .

$$\begin{aligned} g[i, j] \approx & \int_{i'=i-0.5}^{i'=i+0.5} \int_{j'=j-0.5}^{j'=j+0.5} \int_{\psi, \phi} \sum_{a, b, c} f(a\Delta_x, b\Delta_y, c\Delta_z) \Delta_x \Delta_y \Delta_z \delta(\phi) \delta(\psi) \\ & h(f_\alpha, f_\beta) (\Delta u \Delta v)^{-1} |\mathbf{J}|^{-1} d\psi d\phi di' dj' \end{aligned} \quad (\text{B.15})$$

where

$$\mathbf{J} = \begin{bmatrix} \frac{\partial \phi}{\partial f_\alpha} & \frac{\partial \phi}{\partial f_\beta} \\ \frac{\partial \psi}{\partial f_\alpha} & \frac{\partial \psi}{\partial f_\beta} \end{bmatrix}. \quad (\text{B.16})$$

Integrating over  $\phi$  and  $\psi$  yields

$$g[i, j] \approx \int_{i'=i-0.5}^{i'=i+0.5} \int_{j'=j-0.5}^{j'=j+0.5} \sum_{a,b,c} f(a\Delta_x, b\Delta_y, c\Delta_z) \Delta_x \Delta_y \Delta_z h(f_\alpha^*, f_\beta^*) (\Delta_u \Delta_v)^{-1} |\mathbf{J}|^{-1} di' dj' \quad (\text{B.17})$$

where  $f_\alpha^*$  and  $f_\beta^*$  are the zeros of  $\phi$  and  $\psi$ .

If we assume  $h$  is separable,  $\frac{\partial \phi}{\partial j} \approx 0$ , and  $\frac{\partial \psi}{\partial i} \approx 0$  (i.e., minimal panel rotation), then

$$g[i, j] \approx \sum_{a,b,c} f(a\Delta_x, b\Delta_y, c\Delta_z) \Delta_x \Delta_y \Delta_z (\Delta_u \Delta_v)^{-1} |\mathbf{J}|^{-1} \int_{i'=i-0.5}^{i'=i+0.5} h_\alpha(f_\alpha^*) di' \int_{j'=j-0.5}^{j'=j+0.5} h_\beta(f_\beta^*) dj' \quad (\text{B.18})$$

for a trans-axial tube orientation and

$$g[i, j] \approx \sum_{a,b,c} f(a\Delta_x, b\Delta_y, c\Delta_z) \Delta_x \Delta_y \Delta_z (\Delta_u \Delta_v)^{-1} |\mathbf{J}|^{-1} \int_{i'=i-0.5}^{i'=i+0.5} h_\beta(f_\beta^*) di' \int_{j'=j-0.5}^{j'=j+0.5} h_\alpha(f_\alpha^*) dj' \quad (\text{B.19})$$

for an axial tube orientation.

Because the projected sourcelet is approximated as separable in each dimension, it is relatively straightforward to calculate the integral of this projection for each pixel. The pseudocode for a transaxial orientation is in §B.2.

## B.2 Algorithm

This section presents the algorithm used to calculate the projections for a single sourcelet. In this algorithm,  $\tilde{f}$  is the voxelized representation of  $f$ , and  $P_i(f_\alpha - 0.5\Delta_\alpha, f_\beta, a, b, c)$  calculates the  $i$  pixel coordinate of the point on the detector that marks the intersection of the detector plane and the line connecting  $(a\Delta_x, b\Delta_y, c\Delta_z)$  and  $(f_\alpha - 0.5\Delta_\alpha, f_\beta)$ .

**function** SEPARABLE SOURCELET PROJECTION

**for all**  $(a, b, c)$  **do**

$$f_{scaled} \leftarrow \tilde{f}[a, b, c] |\mathbf{J}|^{-1} \Delta_x \Delta_y \Delta_z (\Delta_u \Delta_v)^{-1}$$

$$i_1 \leftarrow P_i(f_\alpha - 0.5\Delta_\alpha, f_\beta, a, b, c)$$

$$i_2 \leftarrow P_i(f_\alpha - 0.5\Delta_\alpha, f_\beta, a, b, c)$$

$$j_1 \leftarrow P_j(f_\alpha, f_\beta - 0.5\Delta_\beta, a, b, c)$$

$$j_2 \leftarrow P_j(f_\alpha, f_\beta - 0.5\Delta_\beta, a, b, c)$$

$$i_1, i_2 \leftarrow \text{sort}(i_1, i_2)$$

$$j_1, j_2 \leftarrow \text{sort}(j_1, j_2)$$

**if**  $i_1 + 0.5$  is an integer **then**

$$i_{min} \leftarrow i_1 - 0.5 \quad \triangleright \text{Ensure the starting pixel edge is outside projection}$$

**else**

$$i_{min} \leftarrow \text{round}(i_1)$$

**if**  $j_{min} + 0.5$  is an integer **then**

$$j_{min} \leftarrow j_1 - 0.5$$

**else**

$$j_{min} \leftarrow \text{round}(j_1)$$

---

```

 $i_{max} \leftarrow \text{round}(i_2)$ 
 $j_{max} \leftarrow \text{round}(j_2)$ 
for  $i = \max(i_{min}, 0) .. \min(i_{max}, N_i - 1)$  do
  for  $j = \max(j_{min}, 0) .. \min(j_{max}, N_j - 1)$  do
     $out \leftarrow f_{scaled}$ 
    if  $i == i_{min}$  and  $i == i_{max}$  then    ▷ 1D projection entirely within pixel
       $out \leftarrow out * (i_2 - i_1)$ 
    else if  $i == i_{min}$  then                ▷ Projection partially in pixel
       $out \leftarrow out * (i + 0.5 - i_1)$ 
    else if  $i == i_{max}$  then                ▷ Projection partially in pixel
       $out \leftarrow out * (i_2 + 0.5 - i)$ 
    else                                     ▷ Entire pixel in projection (in this dimension)
      Do nothing
    if  $j == j_{min}$  and  $j == j_{max}$  then
       $out \leftarrow out * (j_2 - j_1)$ 
    else if  $j == j_{min}$  then
       $out \leftarrow out * (j + 0.5 - j_1)$ 
    else if  $j == j_{max}$  then
       $out \leftarrow out * (j_2 + 0.5 - j)$ 
    else
      Do nothing
   $\tilde{g}[i, j] \leftarrow out$ 

```

## B.3 Jacobian Calculation

In this section we calculate the determinant of the Jacobian matrix, which contributes to the scale factor in the above algorithm.

First, using the chain rule, we have

$$\frac{\partial \phi}{\partial f_\alpha} = \frac{\partial \phi}{\partial f_x} \frac{\partial f_x}{\partial f_\alpha} + \frac{\partial \phi}{\partial f_z} \frac{\partial f_z}{\partial f_\alpha} \quad (\text{B.20})$$

$$\frac{\partial \phi}{\partial f_\beta} = \frac{\partial \phi}{\partial f_x} \frac{\partial f_x}{\partial f_\beta} + \frac{\partial \phi}{\partial f_z} \frac{\partial f_z}{\partial f_\beta} \quad (\text{B.21})$$

$$\frac{\partial \psi}{\partial f_\alpha} = \frac{\partial \psi}{\partial f_y} \frac{\partial f_y}{\partial f_\alpha} + \frac{\partial \psi}{\partial f_z} \frac{\partial f_z}{\partial f_\alpha} \quad (\text{B.22})$$

$$\frac{\partial \psi}{\partial f_\beta} = \frac{\partial \psi}{\partial f_y} \frac{\partial f_y}{\partial f_\beta} + \frac{\partial \psi}{\partial f_z} \frac{\partial f_z}{\partial f_\beta} \quad (\text{B.23})$$

where

$$\frac{\partial \phi}{\partial f_x} = \frac{c\Delta v_z}{f_z} \quad (\text{B.24})$$

$$\frac{\partial \phi}{\partial f_z} = \frac{c\Delta v_z(p_x(i', j') - f_x)}{f_z^2} \quad (\text{B.25})$$

$$\frac{\partial \psi}{\partial f_y} = \frac{c\Delta v_z}{f_z} \quad (\text{B.26})$$

$$\frac{\partial \psi}{\partial f_z} = \frac{c\Delta v_z(p_y(i', j') - f_y)}{f_z^2}. \quad (\text{B.27})$$

The other portions of the derivative depend on whether we're using the transaxial or axial coordinate system.

### B.3.1 Transaxial coordinate system

With a transaxial coordinate system we have

$$\frac{\partial \phi}{\partial f_\alpha} = -\frac{c\Delta v_z}{f_z} \sin(\theta) + \frac{c\Delta v_z(p_x(i', j') - f_x)}{f_z^2} \cos(\theta) \quad (\text{B.28})$$

$$= \frac{c\Delta v_z(p_x(i', j') \cos(\theta) - f_x \cos(\theta) - f_z \sin(\theta))}{f_z^2} \quad (\text{B.29})$$

$$= \frac{c\Delta v_z(p_x(i', j') \cos(\theta) + f_\alpha \sin \theta \cos(\theta) - f_\alpha \cos(\theta) \sin(\theta) - SDD \sin(\theta))}{(f_\alpha \cos(\theta) + SDD)^2} \quad (\text{B.30})$$

$$= \frac{c\Delta v_z(p_x(i', j') \cos(\theta) - SDD \sin(\theta))}{(f_\alpha \cos(\theta) + SDD)^2} \quad (\text{B.31})$$

$$\approx \frac{c\Delta v_z(p_x(i', j') \cos(\theta) - SDD \sin(\theta))}{SDD^2} \quad (\text{B.32})$$

$$\approx \frac{c\Delta v_z p_x(i', j') \cos(\theta)}{SDD^2} - \frac{c\Delta v_z \sin(\theta)}{SDD} \quad (\text{B.33})$$

$$\approx \frac{(M(c) - 1)}{M} (p_x(i', j') \cos(\theta) SDD^{-1} - \sin(\theta)) \quad (\text{B.34})$$

where  $M(c)$  is the magnification and is equal to

$$M = \frac{SDD - c\Delta v_z}{SDD}. \quad (\text{B.35})$$



Because  $\frac{\partial \phi}{\partial f_\beta} = 0$ , there is no need to calculate  $\frac{\partial \psi}{\partial f_\alpha}$  for the Jacobian determinant. The remaining term is then

$$\frac{\partial \psi}{\partial f_\beta} = -\frac{c\Delta v_z}{f_z} \quad (\text{B.36})$$

$$\approx -\frac{c\Delta v_z}{SDD} \quad (\text{B.37})$$

$$\approx -\frac{M(c) - 1}{M(c)}. \quad (\text{B.38})$$

Therefore

$$|\mathbf{J}| = \left( \frac{(M(c) - 1)}{M} \right)^2 (p_x(i', j') \cos(\theta) SDD^{-1} - \sin(\theta)). \quad (\text{B.39})$$

### B.3.2 Axial coordinate system

Because  $\frac{\partial \psi}{\partial f_\beta} = 0$ , there is no need to calculate  $\frac{\partial \phi}{\partial f_\alpha}$ .

The remaining terms are similar to the transaxial coordinate system:

$$\frac{\partial \phi}{\partial f_\beta} = \frac{c\Delta v_z}{f_z} \quad (\text{B.40})$$

$$\approx \frac{M(c) - 1}{M(c)} \quad (\text{B.41})$$

and

$$\frac{\partial \psi}{\partial f_\alpha} = -\frac{c\Delta v_z}{f_z} \sin(\theta) + \frac{c\Delta v_z(p_y(i', j') - f_y)}{f_z^2} \cos(\theta) \quad (\text{B.42})$$

$$\approx \frac{(M(c) - 1)}{M} (p_y(i', j') \cos(\theta) SDD^{-1} - \sin(\theta)). \quad (\text{B.43})$$

Therefore, the Jacobian determinant has a very similar form:

$$|\mathbf{J}| = \left( \frac{(M(c) - 1)}{M} \right)^2 (p_y(i', j') \cos(\theta) S D D^{-1} - \sin(\theta)). \quad (\text{B.44})$$

## References

- [1] Eric Jones, Travis Oliphant, Pearu Peterson, and Others. “SciPy: Open Source Scientific Tools for Python”. In: (2001). URL: <http://www.scipy.org/>.
- [2] J D Hunter. “Matplotlib: A 2D Graphics Environment”. In: *Computing In Science & Engineering* 9.3 (2007), pp. 90–95.
- [3] Ronald G. Evens. “Chapter 16: Computed Tomography”. In: *A History of the Radiological Sciences: DIAGNOSIS*. Radiology Centennial, Inc, 1996, pp. 402–411. URL: [http://www.arrs.org/publications/HRS/diagnosis/RCI\\_D\\_c16.pdf](http://www.arrs.org/publications/HRS/diagnosis/RCI_D_c16.pdf).
- [4] G. N. Hounsfield. “Computerized Transverse Axial Scanning (Tomography): Part 1. Description of System”. In: *The British Journal of Radiology* 46.552 (1, 1973), pp. 1016–1022. ISSN: 0007-1285. DOI: 10.1259/0007-1285-46-552-1016. URL: <https://www.birpublications.org/doi/abs/10.1259/0007-1285-46-552-1016>.
- [5] J. T. Littleton and M. L. Durizch Littleton. “Chapter 15: Conventional Tomography”. In: *A History of the Radiological Sciences: DIAGNOSIS*. Radiology Centennial, Inc, 1996, pp. 368–401. URL: [http://www.arrs.org/publications/HRS/diagnosis/RCI\\_D\\_c15.pdf](http://www.arrs.org/publications/HRS/diagnosis/RCI_D_c15.pdf).

- [6] *SOMATOM Force*. URL: <https://usa.healthcare.siemens.com/computed-tomography/dual-source-ct/somatom-force/technical-specifications>.
- [7] *Revolution CT | GE Healthcare*. URL: <https://www.gehealthcare.com/en/products/computed-tomography/revolution-family/revolution-ct>.
- [8] *SOMATOM Go.Now Brochure*. URL: [https://static.healthcare.siemens.com/siemens\\_hwem-hwem\\_ssxa\\_websites-context-root/wcm/idc/groups/public/@global/@imaging/@ct/documents/download/mda2/ntm4/~edisp/siemens-healthineers\\_somatom-go-now\\_product-brochure-03537399.pdf](https://static.healthcare.siemens.com/siemens_hwem-hwem_ssxa_websites-context-root/wcm/idc/groups/public/@global/@imaging/@ct/documents/download/mda2/ntm4/~edisp/siemens-healthineers_somatom-go-now_product-brochure-03537399.pdf).
- [9] *Aquilion Precision CT Scanner | Computed Tomography | CT System | Canon Medical Systems USA*. URL: <https://us.medical.canon/products/computed-tomography/aquilion-precision/>.
- [10] J Bamba, K Araki, A Endo, and T Okano. "Image Quality Assessment of Three Cone Beam CT Machines Using the SEDENTEXCT CT Phantom". In: *Dentomaxillofacial Radiology* 42.8 (1, 2013), p. 20120445. ISSN: 0250-832X. DOI: 10.1259/dmfr.20120445. URL: <http://www.birpublications.org/doi/10.1259/dmfr.20120445>.
- [11] W. Zbijewski, P. De Jean, P. Prakash, Y. Ding, J. W. Stayman, N. Packard, R. Senn, D. Yang, J. Yorkston, A. Machado, J. A. Carrino, and J. H. Siewerdsen. "A Dedicated Cone-Beam CT System for Musculoskeletal Extremities Imaging: Design, Optimization, and Initial Performance Characterization". In: *Med-*

- ical Physics* 38.8 (2011), p. 4700. ISSN: 00942405. DOI: 10.1118/1.3611039. pmid: 21928644.
- [12] P. Mozzo, C. Procacci, A. Tacconi, P. Tinazzi Martini, and I. A. Bergamo Andreis. “A New Volumetric CT Machine for Dental Imaging Based on the Cone-Beam Technique: Preliminary Results”. In: *European Radiology* 8.9 (23, 1998), pp. 1558–1564. ISSN: 0938-7994, 1432-1084. DOI: 10.1007/s0033000050586. URL: <http://link.springer.com/10.1007/s0033000050586>.
  - [13] David A Jaffray, Jeffrey H Siewerdsen, John W Wong, and Alvaro A Martinez. “Flat-Panel Cone-Beam Computed Tomography for Image-Guided Radiation Therapy”. In: *International Journal of Radiation Oncology\*Biology\*Physics* 53.5 (1, 2002), pp. 1337–1349. ISSN: 0360-3016. DOI: 10.1016/S0360-3016(02)02884-5. URL: <http://www.sciencedirect.com/science/article/pii/S0360301602028845>.
  - [14] James F. Griffith and Harry K. Genant. “New Imaging Modalities in Bone”. In: *Current Rheumatology Reports* 13.3 (2011), pp. 241–250. ISSN: 15233774. DOI: 10.1007/s11926-011-0174-x. pmid: 21369797.
  - [15] Xing Gong, Aruna A Vedula, and Stephen J Glick. “Microcalcification Detection Using Cone-Beam CT Mammography with a Flat-Panel Imager.” In: *Physics in Medicine and Biology* 49.11 (2004), pp. 2183–2195. ISSN: 0031-9155. DOI: 10.1088/0031-9155/49/11/005. pmid: 15248571.
  - [16] Philippe Lambin, Emmanuel Rios-Velazquez, Ralph Leijenaar, Sara Carvalho, Ruud G. P. M. van Stiphout, Patrick Granton, Catharina M. L. Zegers, Robert Gillies, Ronald Boellard, André Dekker, and Hugo J. W. L. Aerts. “Radiomics:

- Extracting More Information from Medical Images Using Advanced Feature Analysis”. In: *European Journal of Cancer* 48.4 (1, 2012), pp. 441–446. ISSN: 0959-8049. DOI: 10.1016/j.ejca.2011.11.036. URL: <http://www.sciencedirect.com/science/article/pii/S0959804911009993>.
- [17] C E Cann. “Quantitative CT for Determination of Bone Mineral Density: A Review.” In: *Radiology* 166.2 (1, 1988), pp. 509–522. ISSN: 0033-8419. DOI: 10.1148/radiology.166.2.3275985. URL: <http://pubs.rsna.org/doi/abs/10.1148/radiology.166.2.3275985>.
- [18] Jerry L. Prince and Jonathan Links. *Medical Imaging Signals and Systems*. 1 edition. Upper Saddle River, NJ: Prentice Hall, 25, 2005. 496 pp. ISBN: 978-0-13-065353-6.
- [19] Jiang Hsieh. *Computed Tomography Principles, Design, Artifacts, and Recent Advances*. 2nd. Bellingham, Washington: Wiley Inter-Science, 2009. ISBN: 978-0-470-56353-3.
- [20] Jerrold T. Bushberg, Anthony J. Seibert, Edwin M. Leidholdt Jr, and John M. Boone. *The Essential Physics of Medical Imaging*. 3rd. Philadelphia, PA: Lippincott Williams & Wilkins, 2012.
- [21] E. Sato, M. Sagae, K. Takahashi, A. Shikoda, T. Oizumi, Y. Hayasi, Y. Tamakawa, and T. Yanagisawa. “10 kHz Microsecond Pulsed X-Ray Generator Utilising a Hot-Cathode Triode with Variable Durations for Biomedical Radiography”. In: *Medical & Biological Engineering & Computing* 32.3 (1994), pp. 295–301. ISSN: 0140-0118, 1741-0444. DOI: 10.1007/BF02512525. URL: <http://link.springer.com/10.1007/BF02512525>.

- [22] Henry Stark and John W. Woods. *Probability and Random Processes with Applications to Signal Processing*. Third. Upper Saddle River, New Jersey: Prentice Hall, 2002. ISBN: 0-13-020071-9.
- [23] J. Punnoose, J. Xu, A. Sisniega, W. Zbijewski, and J. H. Siewerdsen. “Technical Note: Spektr 3.0—A Computational Tool for x-Ray Spectrum Modeling and Analysis”. In: *Medical Physics* 43 (8Part1 1, 2016), pp. 4711–4717. ISSN: 2473-4209. DOI: 10.1118/1.4955438. URL: <http://onlinelibrary.wiley.com/doi/10.1118/1.4955438/abstract>.
- [24] J. H. Hubbell and S. M. Seltzer. *X-Ray Mass Attenuation Coefficients*. 2004. URL: <http://physics.nist.gov/xaamdi>.
- [25] J. K. Gong, J. S. Arnold, and S. H. Cohn. “Composition of Trabecular and Cortical Bone”. In: *The Anatomical Record* 149.3 (1, 1964), pp. 325–331. ISSN: 1097-0185. DOI: 10.1002/ar.1091490303. URL: <https://onlinelibrary.wiley.com/doi/abs/10.1002/ar.1091490303>.
- [26] V. V. Nagarkar, T. K. Gupta, S. R. Miller, Y. Klugerman, M. R. Squillante, and G. Entine. “Structured CsI(Tl) Scintillators for X-Ray Imaging Applications”. In: *IEEE Transactions on Nuclear Science* 45.3 (1998), pp. 492–496. ISSN: 0018-9499. DOI: 10.1109/23.682433.
- [27] Efrat Shefer, Ami Altman, Rolf Behling, Raffy Goshen, Lev Gregorian, Yalon Roterman, Igor Uman, Naor Wainer, Yoad Yagil, and Oren Zarchin. “State of the Art of CT Detectors and Sources: A Literature Review”. In: *Current Radiology Reports* 1.1 (1, 2013), pp. 76–91. ISSN: 2167-4825. DOI: 10.1007/s40134-012-0006-4. URL: <https://doi.org/10.1007/s40134-012-0006-4>.

- [28] J. H. Siewerdsen, L. E. Antonuk, Y. el Mohri, J. Yorkston, W. Huang, J. M. Boudry, and I. A. Cunningham. “Empirical and Theoretical Investigation of the Noise Performance of Indirect Detection, Active Matrix Flat-Panel Imagers (AMFPIs) for Diagnostic Radiology”. In: *Medical Physics* 24.1 (1997), pp. 71–89. ISSN: 0094-2405. DOI: 10.1118/1.597919. pmid: 9029542.
- [29] *PaxScan 4030CB Flat Panel Detector*. Varex Imaging. URL: <https://www.vareximaging.com/file/4030cbpdsdpdf-0>.
- [30] *PaxScan 4343CB Flat Panel Detector*. Varex Imaging. URL: <https://www.vareximaging.com/file/4343cbpdsdpdf-0>.
- [31] Adam S. Wang, J. Webster Stayman, Yoshito Otake, Sebastian Vogt, Gerhard Kleinszig, A. Jay Khanna, Gary L. Gallia, and Jeffrey H. Siewerdsen. “Low-Dose Preview for Patient-Specific, Task-Specific Technique Selection in Cone-Beam CT”. In: *Medical Physics* 41.7 (2014), p. 071915. ISSN: 2473-4209. DOI: 10.1118/1.4884039. URL: <https://aapm.onlinelibrary.wiley.com/doi/abs/10.1118/1.4884039>.
- [32] *1207, 1512, 2307, 2315 and 2923 CMOS Flat Panel Detectors*. Varex Imaging. URL: <https://www.vareximaging.com/file/cmos-12071512230723152923pdf-3>.
- [33] Jared Starman, Josh Star-Lack, Gary Virshup, Edward Shapiro, and Rebecca Fahrig. “Investigation into the Optimal Linear Time-Invariant Lag Correction for Radar Artifact Removal”. In: *Medical Physics* 38.5 (2011), pp. 2398–2411. ISSN: 0094-2405. DOI: 10.1118/1.3574873. pmid: 21776774.



- [34] A. C. Kak and Malcolm Slaney. *Principles of Computerized Tomographic Imaging*. IEEE Press, 1988. URL: <http://www.slaney.org/pct/>.
- [35] L A Feldkamp, L C Davis, and J W Kress. “Practical Cone-Beam Algorithm”. In: *J. Opt. Soc. Am. A* 1.6 (1984), pp. 612–619. DOI: 10.1364/JOSAA.1.000612. URL: <http://josaa.osa.org/abstract.cfm?URI=josaa-1-6-612>.
- [36] Hao Dang, J. W Stayman, A Sisniega, J Xu, W Zbijewski, X Wang, D. H Foos, N Aygun, V Koliatsos, and J. H Siewerdsen. “Statistical Reconstruction for Cone-Beam CT with a Post-Artifact-Correction Noise Model: Application to High-Quality Head Imaging”. In: *Physics in Medicine and Biology* 60.16 (2015), pp. 6153–6175. ISSN: 0031-9155. DOI: 10.1088/0031-9155/60/16/6153.
- [37] T. Hebert and R. Leahy. “A Generalized EM Algorithm for 3-D Bayesian Reconstruction from Poisson Data Using Gibbs Priors”. In: *IEEE Transactions on Medical Imaging* 8.2 (1989), pp. 194–202. ISSN: 0278-0062. DOI: 10.1109/42.24868.
- [38] D S Lalush and B M W Tsui. “A Generalized Gibbs Prior for Maximum a Posteriori Reconstruction in SPECT”. In: *Physics in Medicine and Biology* 38.6 (1, 1993), pp. 729–741. ISSN: 0031-9155, 1361-6560. DOI: 10.1088/0031-9155/38/6/007. URL: <http://stacks.iop.org/0031-9155/38/i=6/a=007?key=crossref.2f26e1acca7e18c282e4911eacc96228>.
- [39] Jonas Adler and Ozan Öktem. “Deep Bayesian Inversion”. In: (14, 2018). arXiv: 1811.05910 [cs, math, stat]. URL: <http://arxiv.org/abs/1811.05910>.

- [40] J. M. Hammersley and P. Clifford. *Markov Fields on Finite Graphs and Lattices*. 1971. URL: <http://www.statslab.cam.ac.uk/~grg/books/hammfest/hamm-cliff.pdf>.
- [41] Magnus Rudolph Hestenes and Eduard Stiefel. “Methods of Conjugate Gradients for Solving Linear Systems”. In: *Journal of Research of the National Bureau of Standards* 49.6 (1952), pp. 409–436.
- [42] Patrick J La Rivière, Junguo Bian, and Phillip A Vargas. “Penalized-Likelihood Sinogram Restoration for Computed Tomography.” In: *IEEE Transactions on Medical Imaging* 25.8 (2006), pp. 1022–36. ISSN: 0278-0062. pmid: 16894995. URL: [http://ieeexplore.ieee.org/xpls/abs\\_all.jsp?arnumber=1661697&tag=1](http://ieeexplore.ieee.org/xpls/abs_all.jsp?arnumber=1661697&tag=1).
- [43] Benjamin M W Tsui, Hong Bin Hu, David R. Gilland, and Grant T. Gullberg. “Implementation of Simultaneous Attenuation and Detector Response Correction in Spect.” In: *IEEE Transactions on Nuclear Science* 35.1 (1987), pp. 778–783. ISSN: 00189499. DOI: 10.1109/23.12831.
- [44] Jinyi Qi, R. M. Leahy, Chinghan Hsu, T. H. Farquhar, and S. R. Cherry. “Fully 3D Bayesian Image Reconstruction for the ECAT EXACT HR+”. In: *IEEE Transactions on Nuclear Science* 45.3 (1998), pp. 1096–1103. ISSN: 0018-9499. DOI: 10.1109/23.681985.
- [45] Jinyi Qi, Richard M. Leahy, Simon R. Cherry, Arion Chatziioannou, and Thomas H. Farquhar. “High-Resolution 3D Bayesian Image Reconstruction Using the microPET Small-Animal Scanner”. In: *Physics in Medicine and Bi-*

- ology* 43.4 (1998), p. 1001. ISSN: 0031-9155. DOI: 10.1088/0031-9155/43/4/027. URL: <http://stacks.iop.org/0031-9155/43/i=4/a=027>.
- [46] A. R. Formiconi, A. Pupi, and A. Passeri. “Compensation of Spatial System Response in SPECT with Conjugate Gradient Reconstruction Technique”. In: *Physics in Medicine and Biology* 34.1 (1989), p. 69. ISSN: 0031-9155. DOI: 10.1088/0031-9155/34/1/007. URL: <http://stacks.iop.org/0031-9155/34/i=1/a=007>.
- [47] A. M. Alessio, P. E. Kinahan, and T. K. Lewellen. “Modeling and Incorporation of System Response Functions in 3-D Whole Body PET”. In: *IEEE Transactions on Medical Imaging* 25.7 (2006), pp. 828–837. ISSN: 0278-0062. DOI: 10.1109/TMI.2006.873222.
- [48] Jean-Baptiste Thibault, Ken D. Sauer, Charles A. Bouman, and Jiang Hsieh. “A Three-Dimensional Statistical Approach to Improved Image Quality for Multislice Helical CT”. In: *Medical Physics* 34.11 (2007), p. 4526. ISSN: 00942405. DOI: 10.1118/1.2789499. URL: <http://link.aip.org/link/MPHYA6/v34/i11/p4526/s1&Agg=doi>.
- [49] Bruno De Man and Samit Basu. “Distance-Driven Projection and Backprojection in Three Dimensions”. In: *Physics in Medicine & Biology* 49.11 (2004), p. 2463. ISSN: 0031-9155. DOI: 10.1088/0031-9155/49/11/024. URL: <http://stacks.iop.org/0031-9155/49/i=11/a=024>.
- [50] Yong Long, Jeffrey A Fessler, and James M Balter. “3D Forward and Back-Projection for X-Ray CT Using Separable Footprints.” In: *IEEE Transactions on Medical Imaging* 29.11 (2010), pp. 1839–50. ISSN: 1558-254X. DOI: 10.1109/

TMI.2010.2050898. pmid: 20529732. URL: <http://www.pubmedcentral.nih.gov/articlerender.fcgi?artid=2993760&tool=pmcentrez&rendertype=abstract>.

- [51] K. J. Little and P. J. La Rivière. “An Algorithm for Modeling Non-Linear System Effects in Iterative CT Reconstruction”. In: *2012 IEEE Nuclear Science Symposium and Medical Imaging Conference Record (NSS/MIC)*. 2012 IEEE Nuclear Science Symposium and Medical Imaging Conference Record (NSS/MIC). 2012, pp. 2174–2177. DOI: 10.1109/NSSMIC.2012.6551496.
- [52] G. H. Glover and N. J. Pelc. “Nonlinear Partial Volume Artifacts in X-ray Computed Tomography”. In: *Medical Physics* 7.3 (1, 1980), pp. 238–248. ISSN: 2473-4209. DOI: 10.1118/1.594678. URL: <https://aapm.onlinelibrary.wiley.com/doi/abs/10.1118/1.594678>.
- [53] K. Zeng, B. De Man, J. Thibault, Z. Yu, C. Bouman, and K. Sauer. “Spatial Resolution Enhancement in CT Iterative Reconstruction”. In: *2009 IEEE Nuclear Science Symposium Conference Record (NSS/MIC)*. 2009 IEEE Nuclear Science Symposium Conference Record (NSS/MIC). 2009, pp. 3748–3751. DOI: 10.1109/NSSMIC.2009.5401880.
- [54] Bing Feng, Jeffrey A. Fessler, and Michael A. King. “Incorporation of System Resolution Compensation (RC) in the Ordered-Subset Transmission (OSTR) Algorithm for Transmission Imaging in SPECT.” In: *IEEE Transactions on Medical Imaging* 25.7 (2006), pp. 941–9. ISSN: 0278-0062. pmid: 16827494.
- [55] Jolyon A. Browne, John M Boone, and Timothy J Holmes. “Maximum-Likelihood x-Ray Computed-Tomography Finite-Beamwidth Considera-

- tions”. In: *Applied optics* 34.23 (10, 95), pp. 5199–5209. URL: [https://www.osapublishing.org/DirectPDFAccess/9B5E7CE5-A2E0-B63C-8F59423CF1A269ED\\_45467/ao-34-23-5199.pdf?da=1&id=45467&seq=0&mobile=no](https://www.osapublishing.org/DirectPDFAccess/9B5E7CE5-A2E0-B63C-8F59423CF1A269ED_45467/ao-34-23-5199.pdf?da=1&id=45467&seq=0&mobile=no).
- [56] D F Yu, J A Fessler, and E P Ficaro. “Maximum-Likelihood Transmission Image Reconstruction for Overlapping Transmission Beams.” In: *IEEE Transactions on Medical Imaging* 19.11 (2000), pp. 1094–105. ISSN: 0278-0062. DOI: 10.1109/42.896785. pmid: 11204847.
- [57] Jeroen Cant, Willem Jan Palenstijn, Gert Behiels, and Jan Sijbers. “Modeling Blurring Effects Due to Continuous Gantry Rotation: Application to Region of Interest Tomography”. In: *Medical Physics* 42.5 (2015), pp. 2709–2717. ISSN: 2473-4209. DOI: 10.1118/1.4914422. pmid: 25979069.
- [58] Y Long, J Fessler, and J Balter. “WE-C-110-06: Two-Material Decomposition from a Single CT Scan Using Statistical Image Reconstruction”. In: *Medical Physics*. Vol. 38. 4, 2011, pp. 3810–3810. DOI: 10.1118/1.3613345. URL: <http://onlinelibrary.wiley.com/doi/10.1118/1.3613345/abstract>.
- [59] Y. Long and J. A. Fessler. “Multi-Material Decomposition Using Statistical Image Reconstruction for Spectral CT”. In: *IEEE Transactions on Medical Imaging* 33.8 (2014), pp. 1614–1626. ISSN: 0278-0062. DOI: 10.1109/TMI.2014.2320284.
- [60] W. Huh, J. A. Fessler, A. M. Alessio, and P. E. Kinahan. “Fast kVp-Switching Dual Energy CT for PET Attenuation Correction”. In: *2009 IEEE Nuclear Science Symposium Conference Record (NSS/MIC)*. 2009 IEEE Nuclear Sci-

- ence Symposium Conference Record (NSS/MIC). 2009, pp. 2510–2515. DOI: 10.1109/NSSMIC.2009.5402036.
- [61] Rina Foygel Barber, Emil Y. Sidky, Taly Gilat Schmidt, and Xiaochuan Pan. “An Algorithm for Constrained One-Step Inversion of Spectral CT Data”. In: *Physics in Medicine & Biology* 61.10 (2016), p. 3784. ISSN: 0031-9155. DOI: 10.1088/0031-9155/61/10/3784. URL: <http://stacks.iop.org/0031-9155/61/i=10/a=3784>.
- [62] Thomas Weidinger, Thorsten M. Buzug, Thomas Flohr, Steffen Kappler, and Karl Stierstorfer. *Polychromatic Iterative Statistical Material Image Reconstruction for Photon-Counting Computed Tomography*. 2016. URL: <https://www.hindawi.com/journals/ijbi/2016/5871604/abs/>.
- [63] Korbinian Mechlem, Sebastian Ehn, Thorsten Sellerer, Eva Braig, Daniela Munzel, Franz Pfeiffer, and Peter B. Noel. “Joint Statistical Iterative Material Image Reconstruction for Spectral Computed Tomography Using a Semi-Empirical Forward Model”. In: *IEEE transactions on medical imaging* (13, 2017). ISSN: 1558-254X. DOI: 10.1109/TMI.2017.2726687. pmid: 28715327.
- [64] Buxin Chen, Zheng Zhang, Emil Y. Sidky, Dan Xia, and Xiaochuan Pan. “Image Reconstruction and Scan Configurations Enabled by Optimization-Based Algorithms in Multispectral CT”. In: *Physics in Medicine & Biology* 62.22 (2017), p. 8763. ISSN: 0031-9155. DOI: 10.1088/1361-6560/aa8a4b. URL: <http://stacks.iop.org/0031-9155/62/i=22/a=8763>.
- [65] B. De Man, J. Nuyts, P. Dupont, G. Marchal, and P. Suetens. “An Iterative Maximum-Likelihood Polychromatic Algorithm for CT”. In: *IEEE Transac-*

- tions on Medical Imaging* 20.10 (2001), pp. 999–1008. ISSN: 0278-0062. DOI: 10.1109/42.959297.
- [66] Qiaoqiao Ding, Yong Long, Xiaoqun Zhang, and Jeffrey A. Fessler. “Statistical Image Reconstruction Using Mixed Poisson-Gaussian Noise Model for X-Ray CT”. In: (19, 2018). arXiv: 1801.09533 [physics]. URL: <http://arxiv.org/abs/1801.09533>.
  - [67] Mehmet Yavuz and Jeffrey A. Fessler. “Statistical Image Reconstruction Methods for Randoms-Precorrected PET Scans”. In: *Medical Image Analysis* 2.4 (1, 1998), pp. 369–378. ISSN: 1361-8415. DOI: 10.1016/S1361-8415(98)80017-0. URL: <http://www.sciencedirect.com/science/article/pii/S1361841598800170>.
  - [68] Hua Zhang, Luo Ouyang, Jianhua Ma, Jing Huang, Wufan Chen, and Jing Wang. “Noise Correlation in CBCT Projection Data and Its Application for Noise Reduction in Low-Dose CBCT.” In: *Medical Physics* 41.3 (2014), p. 031906. ISSN: 0094-2405. DOI: 10.1118/1.4865782. pmid: 24593724.
  - [69] J. Zheng, J. A. Fessler, and H. Chan. “Detector Blur and Correlated Noise Modeling for Digital Breast Tomosynthesis Reconstruction”. In: *IEEE Transactions on Medical Imaging* 37.1 (2018), pp. 116–127. ISSN: 0278-0062. DOI: 10.1109/TMI.2017.2732824.
  - [70] Emil Y Sidky and Xiaochuan Pan. “Image Reconstruction in Circular Cone-Beam Computed Tomography by Constrained, Total-Variation Minimization.” In: *Physics in Medicine and Biology* 53.17 (2008), pp. 4777–4807. ISSN: 0031-9155. DOI: 10.1088/0031-9155/53/17/021. pmid: 18701771.

- [71] Peter J. Huber. *Robust Statistics*. New York: Wiley, 1981. ISBN: 0-471-41805-6.
- [72] Q. Xu, H. Yu, X. Mou, L. Zhang, J. Hsieh, and G. Wang. “Low-Dose X-Ray CT Reconstruction via Dictionary Learning”. In: *IEEE Transactions on Medical Imaging* 31.9 (2012), pp. 1682–1697. ISSN: 0278-0062. DOI: 10.1109/TMI.2012.2195669.
- [73] Hao Dang, J. Webster Stayman, Jennifer Xu, Wojciech Zbijewski, Alejandro Sisniega, Michael Mow, Xiaohui Wang, David H. Foos, Nafi Aygun, Vassilis E. Koliatsos, and Jeffrey H. Siewerdsen. “Task-Based Statistical Image Reconstruction for High-Quality Cone-Beam CT”. In: *Physics in Medicine & Biology* 62.22 (2017), p. 8693. ISSN: 0031-9155. DOI: 10.1088/1361-6560/aa90fd. URL: <http://stacks.iop.org/0031-9155/62/i=22/a=8693>.
- [74] D. Wu, K. Kim, G. El Fakhri, and Q. Li. “Iterative Low-Dose CT Reconstruction With Priors Trained by Artificial Neural Network”. In: *IEEE Transactions on Medical Imaging* 36.12 (2017), pp. 2479–2486. ISSN: 0278-0062. DOI: 10.1109/TMI.2017.2753138.
- [75] J. Webster Stayman, Hao Dang, Yifu Ding, and Jeffrey H. Siewerdsen. “PIRPLE: A Penalized-Likelihood Framework for Incorporation of Prior Images in CT Reconstruction”. In: *Physics in Medicine and Biology* 58.21 (2013), p. 7563. URL: <http://iopscience.iop.org/article/10.1088/0031-9155/58/21/7563/meta>.
- [76] H. Dang, A. S. Wang, Marc S. Sussman, J. H. Siewerdsen, and J. W. Stayman. “dPIRPLE: A Joint Estimation Framework for Deformable Registration and Penalized-Likelihood CT Image Reconstruction Using Prior Images”. In:



- Physics in Medicine and Biology* 59.17 (2014), p. 4799. ISSN: 0031-9155. DOI: 10.1088/0031-9155/59/17/4799. URL: <http://stacks.iop.org/0031-9155/59/i=17/a=4799>.
- [77] Guang-Hong Chen, Jie Tang, and Shuai Leng. “Prior Image Constrained Compressed Sensing (PICCS): A Method to Accurately Reconstruct Dynamic CT Images from Highly Undersampled Projection Data Sets”. In: *Medical Physics* 35.2 (1, 2008), pp. 660–663. ISSN: 2473-4209. DOI: 10.1118/1.2836423. URL: <https://aapm.onlinelibrary.wiley.com/doi/abs/10.1118/1.2836423>.
- [78] Steven Tilley II, Jeffrey H. Siewerdsen, and J. Webster Stayman. “Model-Based Iterative Reconstruction for Flat-Panel Cone-Beam CT with Focal Spot Blur, Detector Blur, and Correlated Noise”. In: *Physics in Medicine and Biology* 61.1 (2016), p. 296. ISSN: 0031-9155. DOI: 10.1088/0031-9155/61/1/296. URL: <http://stacks.iop.org/0031-9155/61/i=1/a=296>.
- [79] S. Tilley II, M. Jacobson, Q. Cao, M. Brehler, A. Sisniega, W. Zbijewski, and J. W. Stayman. “Penalized-Likelihood Reconstruction with High-Fidelity Measurement Models for High-Resolution Cone-Beam Imaging”. In: *IEEE Transactions on Medical Imaging* 37.4 (4, 2017), pp. 988–999. ISSN: 0278-0062. DOI: 10.1109/TMI.2017.2779406. URL: <https://ieeexplore.ieee.org/document/8125700/>.
- [80] H Erdoğan and J. A. Fessler. “Ordered Subsets Algorithms for Transmission Tomography”. In: *Physics in Medicine and Biology* 2835 (1999). URL: <http://iopscience.iop.org/0031-9155/44/11/311>.

- [81] H Erdoğan and J A Fessler. “Monotonic Algorithms for Transmission Tomography.” In: *IEEE Transactions on Medical Imaging* 18.9 (1999), pp. 801–14. ISSN: 0278-0062. DOI: 10.1109/42.802758. pmid: 10571385.
- [82] Alvaro R. De Pierro. “On the Relation between the ISRA and the EM Algorithm for Positron Emission Tomography”. In: *IEEE Transactions on Medical Imaging* 12.2 (1993), pp. 328–333. ISSN: 02780062. DOI: 10.1109/42.232263. pmid: 18218422.
- [83] Donghwan Kim, Sathish Ramani, and Jeffrey A Fessler. “Combining Ordered Subsets and Momentum for Accelerated X-Ray CT Image Reconstruction”. In: *IEEE Transactions on Medical Imaging* 34.1 (2015), pp. 167–178.
- [84] M. W. Jacobson and J. A. Fessler. “An Expanded Theoretical Treatment of Iteration-Dependent Majorize-Minimize Algorithms”. In: *IEEE Transactions on Image Processing* 16.10 (2007), pp. 2411–2422. ISSN: 1057-7149. DOI: 10.1109/TIP.2007.904387.
- [85] Yurri Nesterov. “Smooth Minimization of Non-Smooth Functions”. In: *Mathematical Programming Journal, Series A* 103 (2005), pp. 127–152.
- [86] K. Sauer and C. Bouman. “A Local Update Strategy for Iterative Reconstruction from Projections”. In: *IEEE Transactions on Signal Processing* 41.2 (1993), pp. 534–548. ISSN: 1053587X. DOI: 10.1109/78.193196. URL: <http://ieeexplore.ieee.org/lpdocs/epic03/wrapper.htm?arnumber=193196>.
- [87] Jeffrey A Fessler. “Hybrid Poisson/Polynomial Objective Functions for Tomographic Image Reconstruction from Transmission Scans”. In: *IEEE Transactions on Image Processing* 4.10 (1995), pp. 1439–1450.

- [88] C. Radhakrishna Rao. *Linear Statistical Inference and Its Applications*. 2nd. New York: John Wiley & Sons, Inc., 1973. 527–528. ISBN: 0-471-70823-2.
- [89] Steven J. Benbow. “Solving Generalized Least-Squares Problems with LSQR”. In: *SIAM Journal on Matrix Analysis and Applications* 21.1 (1999), pp. 166–177. ISSN: 0895-4798. DOI: 10.1137/S0895479897321830. URL: <http://epubs.siam.org/doi/abs/10.1137/S0895479897321830>.
- [90] K Lange and J a Fessler. “Globally Convergent Algorithms for Maximum a Posteriori Transmission Tomography.” In: *IEEE transactions on image processing : a publication of the IEEE Signal Processing Society* 4.10 (1995), pp. 1430–8. ISSN: 1057-7149. DOI: 10.1109/83.465107. PMID: 18291974.
- [91] Steven Tilley II, Jeffrey H Siewerdsen, and J Webster Stayman. “Iterative CT Reconstruction Using Models of Source and Detector Blur and Correlated Noise”. In: *Proc. 3rd Intl. Mtg. on Image Formation in X-Ray CT*. 2014, pp. 363–367. URL: <http://www.ucair.med.utah.edu/CTmeeting/ProceedingsCTMeeting2014.pdf>.
- [92] J Webster Stayman, Wojciech Zbijewski, Steven Tilley II, and Jeffrey Siewerdsen. “Generalized Least-Squares CT Reconstruction with Detector Blur and Correlated Noise Models”. In: *Proc. SPIE*. San Diego, CA, 2014, pp. 903335–903335–6. ISBN: 4-10-955111-0. DOI: 10.1117/12.2043067. URL: <http://dx.doi.org/10.1117/12.2043067>.
- [93] Chao-Jen Lai, Chris C Shaw, Lingyun Chen, Mustafa C Altunbas, Xinming Liu, Tao Han, Tianpeng Wang, Wei T Yang, Gary J Whitman, and Shu-Ju Tu. “Visibility of Microcalcification in Cone Beam Breast CT: Effects of X-Ray

- Tube Voltage and Radiation Dose.” In: *Medical Physics* 34.7 (2007), pp. 2995–3004. ISSN: 00942405. DOI: 10.1118/1.2745921. pmid: 17822008.
- [94] A A Muhit, S Arora, M Ogawa, Y Ding, W Zbijewski, J W Stayman, G Thawait, N Packard, R Senn, D Yang, J Yorkston, C O Bingham, K Means, J A Carrino, and J H Siewerdsen. “Peripheral Quantitative CT (pQCT) Using a Dedicated Extremity Cone-Beam CT Scanner”. In: *Proc. SPIE* 8672 (2013), pp. 867203–867207. ISSN: 16057422. DOI: 10.1117/12.2006939. pmid: 25076823. URL: <http://dx.doi.org/10.1117/12.2006939>.
- [95] J Hsieh, R C Molthen, C a Dawson, and R H Johnson. “An Iterative Approach to the Beam Hardening Correction in Cone Beam CT.” In: *Medical physics* 27.1 (2000), pp. 23–29. ISSN: 00942405. DOI: 10.1118/1.598853. pmid: 10659734.
- [96] Ruola Ning, Xiangyang Tang, and David Conover. “X-Ray Scatter Correction Algorithm for Cone Beam CT Imaging.” In: *Medical physics* 31.5 (2004), pp. 1195–1202. ISSN: 00942405. DOI: 10.1118/1.1711475. pmid: 15191309.
- [97] J H Siewerdsen, M J Daly, B Bakhtiar, D J Moseley, S Richard, H Keller, and D a Jaffray. “A Simple, Direct Method for x-Ray Scatter Estimation and Correction in Digital Radiography and Cone-Beam CT.” In: *Medical Physics* 33.1 (2006), pp. 187–197. ISSN: 00942405. DOI: 10.1118/1.2148916. pmid: 16485425.
- [98] Lei Zhu, Jing Wang, and Lei Xing. “Noise Suppression in Scatter Correction for Cone-Beam CT.” In: *Medical Physics* 36.3 (2009), pp. 741–752. ISSN: 00942405. DOI: 10.1118/1.3063001. pmid: 19378735.

- [99] A Sisniega, W Zbijewski, J Xu, H Dang, J W Stayman, J Yorkston, N Aygun, V Koliatsos, and J H Siewerdsen. “High-Fidelity Artifact Correction for Cone-Beam CT Imaging of the Brain”. In: *Physics in Medicine and Biology* 60.4 (2015), p. 1415. URL: <http://stacks.iop.org/0031-9155/60/i=4/a=1415>.
- [100] Idris A. Elbakri and Jeffrey A. Fessler. “Statistical Image Reconstruction for Polyenergetic X-Ray Computed Tomography”. In: *IEEE Transactions on Medical Imaging* 21.2 (2002), pp. 89–99. ISSN: 02780062. DOI: 10.1109/42.993128. pmid: 11929108.
- [101] Joshua D. Evans, Bruce R. Whiting, David G. Politte, Joseph a. O’Sullivan, Paul F. Klahr, and Jeffrey F. Williamson. “Experimental Implementation of a Polyenergetic Statistical Reconstruction Algorithm for a Commercial Fan-Beam CT Scanner”. In: *Physica Medica* 29.5 (2013), pp. 500–512. ISSN: 11201797. DOI: 10.1016/j.ejmp.2012.12.005. pmid: 23343747. URL: <http://dx.doi.org/10.1016/j.ejmp.2012.12.005>.
- [102] Jing Wang, Tianfang Li, and Lei Xing. “Iterative Image Reconstruction for CBCT Using Edge-Preserving Prior.” In: *Medical Physics* 36.1 (2009), pp. 252–260. ISSN: 00942405. DOI: 10.1118/1.3036112. pmid: 19235393.
- [103] Adam S Wang, J Webster Stayman, Yoshito Otake, Gerhard Kleinszig, Sebastian Vogt, Gary L Gallia, A Jay Khanna, and Jeffrey H Siewerdsen. “Soft-Tissue Imaging with C-Arm Cone-Beam CT Using Statistical Reconstruction”. In: *Physics in Medicine and Biology* 59.4 (2014), pp. 1005–1026. ISSN: 0031-9155. DOI: 10.1088/0031-9155/59/4/1005. URL: <http://stacks.iop.org/0031-9155/59/i=4/a=1005?key=crossref.a57fdd600f4403e76d37fb25998fc364>.

- [104] Tao Sun, Nanbo Sun, Jing Wang, and Shan Tan. “Iterative CBCT Reconstruction Using Hessian Penalty”. In: *Physics in Medicine and Biology* 60.5 (2015), pp. 1965–1987. ISSN: 0031-9155. DOI: 10.1088/0031-9155/60/5/1965. URL: <http://stacks.iop.org/0031-9155/60/i=5/a=1965?key=crossref.fae03739cf2c0ae9eaf09f3bca1d2395>.
- [105] Adam Alessio, Ken Sauer, and Charles A. Bouman. “MAP Reconstruction From Spatially Correlated PET Data”. In: *IEEE Transactions on Nuclear Science* 50.5 (2003), pp. 1445–1451.
- [106] Alex Sawatzky, Qiaofeng Xu, Carsten O. Schirra, and Mark A. Anastasio. “Proximal ADMM for Multi-Channel Image Reconstruction in Spectral X-Ray CT”. In: *IEEE Transactions on Medical Imaging* 33.8 (2014), pp. 1657–1668. ISSN: 1558254X. DOI: 10.1109/TMI.2014.2321098. pmid: 24802167.
- [107] Kevin M. Brown, Stanislav Žabić, and Gilad Shechter. “Impact of Spectral Separation in Dual-Energy CT with Anti-Correlated Statistical Reconstruction”. In: *The 13th International Meeting on Fully Three-Dimensional Image Reconstruction in Radiology and Nuclear Medicine*. Newport, RI, 2015, pp. 491–494.
- [108] Yan Liu and Zhou Yu. “A Joint Iterative Reconstruction Algorithm for Dual Energy CT Using ADMM”. In: *The 13th International Meeting on Fully Three-Dimensional Image Reconstruction in Radiology and Nuclear Medicine*. 2015, pp. 511–514.
- [109] S Y Chun, J a Fessler, and Y K Dewaraja. “Correction for Collimator-Detector Response in SPECT Using Point Spread Function Template”. In: *IEEE Transactions on Medical Imaging* 32.2 (2013), pp. 295–305.

- [110] Christian Hofmann, Michael Knaup, and Marc Kachelrieß. “Effects of Ray Profile Modeling on Resolution Recovery in Clinical CT”. In: *Medical Physics* 41.2 (1, 2014), n/a–n/a. ISSN: 2473-4209. DOI: 10.1118/1.4862510. URL: <http://onlinelibrary.wiley.com/doi/10.1118/1.4862510/abstract>.
- [111] Jing Wang, Tianfang Li, Hongbing Lu, and Zhengrong Liang. “Penalized Weighted Least-Squares Approach to Sinogram Noise Reduction and Image Reconstruction for Low-Dose X-Ray Computed Tomography”. In: *IEEE Transactions on Medical Imaging* 25.10 (2006), pp. 1272–1283. ISSN: 02780062. DOI: 10.1109/TMI.2006.882141. pmid: 17024831.
- [112] J P Moy. “Signal-to-Noise Ratio and Spatial Resolution in x-Ray Electronic Imagers: Is the MTF a Relevant Parameter?” In: *Medical physics* 27.1 (2000), pp. 86–93. ISSN: 00942405. DOI: 10.1118/1.598859. pmid: 10659741.
- [113] John Nickolls, Ian Buck, Michael Garland, and Kevin Skadron. “Scalable Parallel Programming with CUDA”. In: *Queue* 6.2 (2008), pp. 40–53. ISSN: 15427730. DOI: 10.1145/1365490.1365500.
- [114] Ehsan Samei, Michael J. Flynn, and David A. Reimann. “A Method for Measuring the Presampled MTF of Digital Radiographic Systems Using an Edge Test Device”. In: *Medical Physics* 25.1 (1998), p. 102. ISSN: 00942405. DOI: 10.1118/1.598165. URL: <http://scitation.aip.org/content/aapm/journal/medphys/25/1/10.1118/1.598165>.
- [115] J H Siewerdsen, I A Cunningham, and D A Jaffray. “A Framework for Noise-Power Spectrum Analysis of Multidimensional Images.” In: *Medical Physics*

- 29.2002 (2002), pp. 2655–2671. ISSN: 00942405. DOI: 10.1118/1.1513158. pmid: 12462733.
- [116] M. F. Kijewski and P. F. Judy. “The Noise Power Spectrum of CT Images”. In: *Physics in Medicine & Biology* 32.5 (1987), p. 565. ISSN: 0031-9155. DOI: 10.1088/0031-9155/32/5/003. URL: <http://stacks.iop.org/0031-9155/32/i=5/a=003>.
- [117] Alexander L C Kwan, John M Boone, Kai Yang, and Shih-Ying Huang. “Evaluation of the Spatial Resolution Characteristics of a Cone-Beam Breast CT Scanner.” In: *Medical Physics* 34.1 (2007), pp. 275–281. ISSN: 00942405. DOI: 10.1118/1.2400830. pmid: 17278513.
- [118] John A Carrino, Abdullah Al Muhit, Wojciech Zbijewski, Gaurav K Thawait, J Webster Stayman, Nathan Packard, Robert Senn, Dong Yang, David H Foos, John Yorkston, and Jeffrey H Siewerdsen. “Dedicated Cone-Beam CT System for Extremity Imaging.” In: *Radiology* 270.3 (2014), pp. 816–24. ISSN: 1527-1315. DOI: 10.1148/radiol.13130225. pmid: 24475803.
- [119] Eugenio Marinetto, Michael Brehler, Alejandro Sisniega, Qian Cao, J. Webster Stayman, J. Yorkston, Jeffrey H. Siewerdsen, and Wojciech Zbijewski. “Quantification of Bone Microarchitecture in Ultrahigh Resolution Extremities Conebeam CT with a CMOS Detector and Compensation of Patient Motion”. In: *Computer Assisted Radiology 30th International Congress and Exhibition*. Computer Assisted Radiology 30th International Congress and Exhibition. Heidelberg, Germany, 2016, S20–S21.



- [120] M Ding and I Hvid. “Quantification of Age-Related Changes in the Structure Model Type and Trabecular Thickness of Human Tibial Cancellous Bone”. In: *Bone* 26.3 (2000), pp. 291–295. ISSN: 8756-3282. DOI: 10.1016/S8756-3282(99)00281-1. URL: <http://www.sciencedirect.com/science/article/pii/S8756328299002811>.
- [121] T. Hildebrand and P. Rüegsegger. “A New Method for the Model-Independent Assessment of Thickness in Three-Dimensional Images”. In: *Journal of Microscopy* 185.1 (1, 1997), pp. 67–75. ISSN: 1365-2818. DOI: 10.1046/j.1365-2818.1997.1340694.x. URL: <http://onlinelibrary.wiley.com/doi/10.1046/j.1365-2818.1997.1340694.x/abstract>.
- [122] Mary L Bouxsein, Stephen K Boyd, Blaine A Christiansen, Robert E Guldberg, Karl J Jepsen, and Ralph Müller. “Guidelines for Assessment of Bone Microstructure in Rodents Using Micro-Computed Tomography”. In: *Journal of Bone and Mineral Research* 25.7 (2010), pp. 1468–1486. ISSN: 08840431. DOI: 10.1002/jbmr.141. URL: <http://doi.wiley.com/10.1002/jbmr.141>.
- [123] Jorge Nocedal and Stephen J Wright. *Numerical Optimization*. 2nd. Springer Series in Operation Research and Financial Engineering. New York, NY, USA: Springer, 2006. ISBN: 978-0-387-30303-1.
- [124] J. H. Siewerdsen, L. E. Antonuk, Y. El-Mohri, J. Yorkston, W. Huang, and I. A. Cunningham. “Signal, Noise Power Spectrum, and Detective Quantum Efficiency of Indirect-Detection Flat-Panel Imagers for Diagnostic Radiology”. In: *Medical Physics* 25.5 (1, 1998), pp. 614–628. ISSN: 0094-2405. DOI: 10.1118/1.598243. URL: <http://scitation.aip.org/content/aapm/journal/medphys/25/5/10.1118/1.598243>.

- [125] Paul Jaccard. “The Distribution of the Flora in the Alpine Zone.1”. In: *New Phytologist* 11.2 (1, 1912), pp. 37–50. ISSN: 1469-8137. DOI: 10.1111/j.1469-8137.1912.tb05611.x. URL: <http://onlinelibrary.wiley.com/doi/10.1111/j.1469-8137.1912.tb05611.x/abstract>.
- [126] S. Klein, M. Staring, K. Murphy, M. A. Viergever, and J. P. W. Pluim. “Elastix: A Toolbox for Intensity-Based Medical Image Registration”. In: *IEEE Transactions on Medical Imaging* 29.1 (2010), pp. 196–205. ISSN: 0278-0062. DOI: 10.1109/TMI.2009.2035616.
- [127] Michael Doube, Michał M. Kłosowski, Ignacio Arganda-Carreras, Fabrice P. Cordelières, Robert P. Dougherty, Jonathan S. Jackson, Benjamin Schmid, John R. Hutchinson, and Sandra J. Shefelbine. “BoneJ: Free and Extensible Bone Image Analysis in ImageJ”. In: *Bone* 47.6 (2010), pp. 1076–1079. ISSN: 8756-3282. DOI: 10.1016/j.bone.2010.08.023. URL: <http://www.sciencedirect.com/science/article/pii/S8756328210014419>.
- [128] Caroline A. Schneider, Wayne S. Rasband, and Kevin W. Eliceiri. “NIH Image to ImageJ: 25 Years of Image Analysis”. In: *Nature Methods* 9.7 (2012), pp. 671–675. ISSN: 1548-7091. DOI: 10.1038/nmeth.2089. URL: <http://www.nature.com/nmeth/journal/v9/n7/full/nmeth.2089.html>.
- [129] G. Mohan, E. Perilli, I. H. Parkinson, J. M. Humphries, N. L. Fazzalari, and J. S. Kuliwaba. “Pre-Emptive, Early, and Delayed Alendronate Treatment in a Rat Model of Knee Osteoarthritis: Effect on Subchondral Trabecular Bone Microarchitecture and Cartilage Degradation of the Tibia, Bone/Cartilage Turnover, and Joint Discomfort”. In: *Osteoarthritis and Cartilage* 21.10 (2013),

- pp. 1595–1604. ISSN: 10634584. DOI: 10.1016/j.joca.2013.06.020. pmid: 23827368. URL: <http://dx.doi.org/10.1016/j.joca.2013.06.020>.
- [130] Ahi S. Issever, Thomas M. Link, Marie Kentenich, Patrik Rogalla, Andrew J. Burghardt, Galateia J. Kazakia, Sharmila Majumdar, and Gerd Diederichs. “Assessment of Trabecular Bone Structure Using MDCT: Comparison of 64- and 320-Slice CT Using HR-pQCT as the Reference Standard”. In: *European Radiology* 20.2 (27, 2009), pp. 458–468. ISSN: 0938-7994, 1432-1084. DOI: 10.1007/s00330-009-1571-7. URL: <http://link.springer.com/article/10.1007/s00330-009-1571-7>.
- [131] C E Cann. “Quantitative CT for Determination of Bone Mineral Density: A Review.” In: *Radiology* 166.2 (1, 1988), pp. 509–522. ISSN: 0033-8419. DOI: 10.1148/radiology.166.2.3275985. URL: <http://pubs.rsna.org/doi/abs/10.1148/radiology.166.2.3275985>.
- [132] Emil Y. Sidky, Yuval Duchin, Xiaochuan Pan, and Christer Ullberg. “A Constrained, Total-Variation Minimization Algorithm for Low-Intensity x-Ray CT”. In: *Medical Physics* 38.S1 (1, 2011), S117–S125. ISSN: 2473-4209. DOI: 10.1118/1.3560887. URL: <http://onlinelibrary.wiley.com/doi/10.1118/1.3560887/abstract>.
- [133] Qian Cao, Wojciech Zbijewski, Alejandro Sisniega, John Yorkston, Jeffrey H. Siewerdsen, and J. Webster Stayman. “Multiresolution Iterative Reconstruction in High-Resolution Extremity Cone-Beam CT”. In: *Physics in Medicine and Biology* 61.20 (2016), p. 7263. ISSN: 0031-9155. DOI: 10.1088/0031-9155/61/20/7263. URL: <http://stacks.iop.org/0031-9155/61/i=20/a=7263>.

- [134] Alejandro Sisniega, J. Webster Stayman, J. Yorkston, J. H. Siewerdsen, and Wojciech Zbijewski. “Motion Compensation in Extremity Cone-Beam CT Using a Penalized Image Sharpness Criterion.” In: *Physics in Medicine and Biology (accepted)* (2017). DOI: 10.1088/1361-6560/aa6869.
- [135] Steven Tilley II, W. Zbijewski, J. H. Siewerdsen, and J. Webster Stayman. “Modeling Shift-Variant X-Ray Focal Spot Blur for High-Resolution Flat-Panel Cone-Beam CT”. In: *Proc. 4th Intl. Mtg. on Image Formation in X-Ray CT*. 2016.
- [136] Steven Tilley II, Wojciech Zbijewski, and J. Webster Stayman. “High-Fidelity Modeling of Shift-Variant Focal-Spot Blur for High-Resolution CT”. In: *Int’l Mtg. Fully 3D Image Recon. in Radiology and Nuc. Med.* Xi’an, China, 18, 2017.
- [137] Steven Tilley II, Alejandro Sisniega, Jeffrey H. Siewerdsen, and J. Webster Stayman. “High-Fidelity Modeling of Detector Lag and Gantry Motion in CT Reconstruction”. In: *Proc. 5th Intl. Mtg. on Image Formation in X-Ray CT*. Vol. submitted. 2018.
- [138] Tristan Nowak, Martin Hupfer, Felix Althoff, Robert Brauweiler, Fabian Eisa, Christian Steiding, and Willi A. Kalender. “Time-Delayed Summation as a Means of Improving Resolution on Fast Rotating Computed Tomography Systems”. In: *Medical Physics* 39.4 (1, 2012), pp. 2249–2260. ISSN: 2473-4209. DOI: 10.1118/1.3697533. URL: <http://onlinelibrary.wiley.com/doi/10.1118/1.3697533/abstract>.

- [139] Eric W. Weisstein. *Bretschneider's Formula*. URL: <http://mathworld.wolfram.com/BretschneidersFormula.html>.
- [140] Milan Sonka, Vaclav Hlavac, and Roger Boyle. "Chapter 6: Segmentation 1". In: *ISE Image Processing, Analysis and Machine Vision*. Student Ed edition. Nelson Engineering, 18, 2007. ISBN: 978-0-495-24438-7.
- [141] P. J. La Riviere. "Monotonic Iterative Reconstruction Algorithms for Targeted Reconstruction in Emission and Transmission Computed Tomography". In: *2006 IEEE Nuclear Science Symposium Conference Record*. 2006 IEEE Nuclear Science Symposium Conference Record. Vol. 5. 2006, pp. 2924–2928. DOI: 10.1109/NSSMIC.2006.356488.
- [142] Benoit Hamelin, Yves Goussard, Jean-Pierre Dussault, Guy Cloutier, Gilles Beaudoin, and Gilles Soulez. "Design of Iterative ROI Transmission Tomography Reconstruction Procedures and Image Quality Analysis". In: *Medical Physics* 37.9 (2010), pp. 4577–4589. ISSN: 0094-2405. DOI: 10.1118/1.3447722. pmid: 20964175.
- [143] B. Hamelin, Y. Goussard, and J. Dussault. "Penalized-Likelihood Region-of-Interest CT Reconstruction by Local Object Supersampling". In: *2007 29th Annual International Conference of the IEEE Engineering in Medicine and Biology Society*. 2007 29th Annual International Conference of the IEEE Engineering in Medicine and Biology Society. 2007, pp. 739–742. DOI: 10.1109/IEMBS.2007.4352396.
- [144] Zhou Yu, Ken Sauer, and Jiang Hsieh. "Edge-Localized Iterative Reconstruction for Computed Tomography". In: (), p. 5.

- [145] J. A. Fessler and W. L. Rogers. “Spatial Resolution Properties of Penalized-Likelihood Image Reconstruction: Space-Invariant Tomographs”. In: *IEEE Transactions on Image Processing* 5.9 (1996), pp. 1346–1358. ISSN: 1057-7149. DOI: 10.1109/83.535846.
- [146] Steven Tilley, Wojciech Zbijewski, Jeffrey H. Siewerdsen, and J. Webster Stayman. “A General CT Reconstruction Algorithm for Model-Based Material Decomposition”. In: *Proc. SPIE. Medical Imaging 2018: Physics of Medical Imaging*. Vol. 10573. Houston, TX: International Society for Optics and Photonics, 9, 2018, pp. 10573–7. DOI: 10.1117/12.2293776. URL: <https://www.spiedigitallibrary.org/conference-proceedings-of-spie/10573/105731E/A-general-CT-reconstruction-algorithm-for-model-based-material-decomposition/10.1117/12.2293776.short>.
- [147] S. Tilley II, Wojciech Zbijewski, and J. Webster Stayman. “Model-Based Material Decomposition with a Penalized Nonlinear Least-Squares CT Reconstruction Algorithm”. In: *Physics in Medicine and Biology* (2018). ISSN: 1361-6560. DOI: 10.1088/1361-6560/aaf973. URL: <http://iopscience.iop.org/10.1088/1361-6560/aaf973>.
- [148] Jee Won Chai, Jung-Ah Choi, Ja-Young Choi, Sujin Kim, Sung Hwan Hong, and Heung Sik Kang. “Visualization of Joint and Bone Using Dual-Energy CT Arthrography with Contrast Subtraction: In Vitro Feasibility Study Using Porcine Joints”. In: *Skeletal Radiology* 43.5 (1, 2014), pp. 673–678. ISSN: 0364-2348, 1432-2161. DOI: 10.1007/s00256-014-1817-6. URL: <https://link.springer.com/article/10.1007/s00256-014-1817-6>.

- [149] W. Zbijewski, G. J. Gang, J. Xu, A. S. Wang, J. W. Stayman, K. Taguchi, J. A. Carrino, and J. H. Siewerdsen. “Dual-Energy Cone-Beam CT with a Flat-Panel Detector: Effect of Reconstruction Algorithm on Material Classification”. In: *Medical Physics* 41.2 (1, 2014), n/a–n/a. ISSN: 2473-4209. DOI: 10.1118/1.4863598. URL: <http://onlinelibrary.wiley.com/doi/10.1118/1.4863598/abstract>.
- [150] David N. Tran, Matus Straka, Justus E. Roos, Sandy Napel, and Dominik Fleischmann. “Dual-Energy CT Discrimination of Iodine and Calcium: Experimental Results and Implications for Lower Extremity CT Angiography”. In: *Academic Radiology* 16.2 (1, 2009), pp. 160–171. ISSN: 1076-6332, 1878-4046. DOI: 10.1016/j.acra.2008.09.004. pmid: 19124101. URL: [http://www.academicradiology.org/article/S1076-6332\(08\)00535-7/fulltext](http://www.academicradiology.org/article/S1076-6332(08)00535-7/fulltext).
- [151] Eun Jin Chae, Joon Beom Seo, Hyun Woo Goo, Namkug Kim, Koun-Sik Song, Sang Do Lee, Soo-Jong Hong, and Bernhard Krauss. “Xenon Ventilation CT with a Dual-Energy Technique of Dual-Source CT: Initial Experience”. In: *Radiology* 248.2 (2008), pp. 615–624. ISSN: 1527-1315. DOI: 10.1148/radiol.2482071482. pmid: 18641254.
- [152] Paul Stolzmann, Marko Kozomara, Natalie Chuck, Michael Müntener, Sebastian Leschka, Hans Scheffel, and Hatem Alkadhi. “In Vivo Identification of Uric Acid Stones with Dual-Energy CT: Diagnostic Performance Evaluation in Patients”. In: *Abdominal Imaging* 35.5 (2010), pp. 629–635. ISSN: 1432-0509. DOI: 10.1007/s00261-009-9569-9. pmid: 19727931.
- [153] Gregor Pache, Bernhard Krauss, Peter Strohm, Ulrich Saueressig, Philipp Blanke, Stefan Bulla, Oliver Schäfer, Peter Helwig, Elmar Kotter, Mathias

- Langer, and Tobias Baumann. “Dual-Energy CT Virtual Noncalcium Technique: Detecting Posttraumatic Bone Marrow Lesions—Feasibility Study”. In: *Radiology* 256.2 (1, 2010), pp. 617–624. ISSN: 0033-8419. DOI: 10.1148/radiol.10091230. URL: <http://pubs.rsna.org/doi/10.1148/radiol.10091230>.
- [154] X. Wang, D. Meier, S. Mikkelsen, G. E. Maehlum, D. J. Wagenaar, B. M. W. Tsui, B. E. Patt, and E. C. Frey. “MicroCT with Energy-Resolved Photon-Counting Detectors”. In: *Physics in Medicine & Biology* 56.9 (2011), p. 2791. ISSN: 0031-9155. DOI: 10.1088/0031-9155/56/9/011. URL: <http://stacks.iop.org/0031-9155/56/i=9/a=011>.
- [155] Dan Xu, David A. Langan, Xiaoye Wu, Jed D. Pack, Thomas M. Benson, J. Eric Tkaczky, and Andrea M. Schmitz. “Dual Energy CT via Fast kVp Switching Spectrum Estimation”. In: *Medical Imaging 2009: Physics of Medical Imaging*. Vol. 7258. International Society for Optics and Photonics, 14, 2009, 72583T. DOI: 10.1117/12.811650. URL: <https://www.spiedigitallibrary.org/conference-proceedings-of-spie/7258/72583T/Dual-energy-CT-via-fast-kVp-switching-spectrum-estimation/10.1117/12.811650.short>.
- [156] M. Grasruck, S. Kappler, M. Reinwand, and K. Stierstorfer. “Dual Energy with Dual Source CT and kVp Switching with Single Source CT: A Comparison of Dual Energy Performance”. In: *Medical Imaging 2009: Physics of Medical Imaging*. Vol. 7258. International Society for Optics and Photonics, 14, 2009, 72583R. DOI: 10.1117/12.811534. URL: <https://www.spiedigitallibrary.org/conference-proceedings-of-spie/7258/72583R/Dual-energy->



with-dual-source-CT-and-kVp-switching-with/10.1117/12.811534.  
short.

- [157] R. T. Ritchings and B. R. Pullan. “A Technique for Simultaneous Dual Energy S”. In: *Journal of Computer Assisted Tomography* 3.6 (1979). ISSN: 0363-8715.
- [158] R. Taschereau, R. W. Silverman, and A. F. Chatziioannou. “Dual-Energy Attenuation Coefficient Decomposition with Differential Filtration and Application to a microCT Scanner”. In: *Physics in Medicine and Biology* 55.4 (11, 2009). DOI: 10.1088/0031-9155/55/4/016. URL: <http://iopscience.iop.org/article/10.1088/0031-9155/55/4/016/meta>.
- [159] Brian Rutt and Aaron Fenster. “Split-Filter Computed Tomography: A Simple Technique for Dual Energy Scanning”. In: *Journal of Computer Assisted Tomography* 4.4 (1980), pp. 501–509. ISSN: 0363-8715.
- [160] R. E. Alvarez and A. Macovski. “Energy-Selective Reconstructions in X-Ray Computerised Tomography”. In: *Physics in Medicine & Biology* 21.5 (1976), p. 733. ISSN: 0031-9155. DOI: 10.1088/0031-9155/21/5/002. URL: <http://stacks.iop.org/0031-9155/21/i=5/a=002>.
- [161] Rodney A. Brooks. “A Quantitative Theory of the Hounsfield Unit and Its Application to Dual Energy Scanning”. In: *Journal of Computer Assisted Tomography* 1.4 (1977), pp. 487–493. ISSN: 0363-8715.
- [162] M. M. Goodsitt, D. I. Rosenthal, W. R. Reinus, and J. Coumas. “Two Postprocessing CT Techniques for Determining the Composition of Trabecular Bone”. In: *Investigative radiology* 22 (1987). URL: [https://www.researchgate.net/profile/Daniel\\_Rosenthal3/publication/19603821\\_Two\\_](https://www.researchgate.net/profile/Daniel_Rosenthal3/publication/19603821_Two_)

Postprocessing\_CT\_Techniques\_for\_Determining\_the\_Composition\_of\_Trabecular\_Bone/links/5460bd360cf295b56163769f.pdf.

- [163] Clemens Maaß, Matthias Baer, and Marc Kachelrieß. “Image-Based Dual Energy CT Using Optimized Precorrection Functions: A Practical New Approach of Material Decomposition in Image Domain”. In: *Medical Physics* 36.8 (1, 2009), pp. 3818–3829. ISSN: 2473-4209. DOI: 10.1118/1.3157235. URL: <http://onlinelibrary.wiley.com/doi/10.1118/1.3157235/abstract>.
- [164] P. M. Joseph and R. D. Spital. “A Method for Correcting Bone Induced Artifacts in Computed Tomography Scanners”. In: *Journal of Computer Assisted Tomography* 2.1 (1978), pp. 100–108. ISSN: 0363-8715. pmid: 670461.
- [165] Chenyang Shen, Bin Li, Yifei Lou, Ming Yang, Linghong Zhou, and Xun Jia. “Multienergy Element-Resolved Cone Beam CT (MEER-CBCT) Realized on a Conventional CBCT Platform”. In: *Medical Physics* 45.10 (1, 2018), pp. 4461–4470. ISSN: 2473-4209. DOI: 10.1002/mp.13169. URL: <https://aapm.onlinelibrary.wiley.com/doi/abs/10.1002/mp.13169>.
- [166] R. Zhang, J. B. Thibault, C. A. Bouman, K. D. Sauer, and J. Hsieh. “Model-Based Iterative Reconstruction for Dual-Energy X-Ray CT Using a Joint Quadratic Likelihood Model”. In: *IEEE Transactions on Medical Imaging* 33.1 (2014), pp. 117–134. ISSN: 0278-0062. DOI: 10.1109/TMI.2013.2282370.
- [167] Yu Zou and Michael D. Silver. “Analysis of Fast kV-Switching in Dual Energy CT Using a Pre-Reconstruction Decomposition Technique”. In: *Medical Imaging 2008: Physics of Medical Imaging*. Medical Imaging 2008: Physics of Medical Imaging. Vol. 6913. International Society for Optics and Photon-

- ics, 18, 2008, p. 691313. DOI: 10.1117/12.772826. URL: <https://www.spiedigitallibrary.org/conference-proceedings-of-spie/6913/691313/Analysis-of-fast-kV-switching-in-dual-energy-CT-using/10.1117/12.772826.short>.
- [168] André Euler, Anushri Parakh, Anna L. Falkowski, Sebastian Manneck, David Dashti, Bernhard Krauss, Zsolt Szucs-Farkas, and Sebastian T. Schindera. “Initial Results of a Single-Source Dual-Energy Computed Tomography Technique Using a Split-Filter: Assessment of Image Quality, Radiation Dose, and Accuracy of Dual-Energy Applications in an In Vitro and In Vivo Study”. In: *Investigative Radiology* 51.8 (2016), pp. 491–498. ISSN: 0020-9996. DOI: 10.1097/RLI.0000000000000257. URL: <https://insights.ovid.com/crossref?an=00004424-201608000-00003>.
- [169] G. S. K. Fung, K. Stierstorfer, M. Fuld, S. Kawamoto, E. K. Fishman, B. M. W. Tsui, and K. Taguchi. “Spectrum Optimization in Split-Filter Dual-Energy CT for Iodine Quantification and Virtual-Non-Contrast Imaging”. In: *Proc. 4th Intl. Mtg. on Image Formation in X-Ray CT*. 2016, pp. 53–56.
- [170] J. Webster Stayman and Steven Tilley II. “Model-Based Multi-Material Decomposition Using Spatial-Spectral Filters”. In: *Proc. 5th Intl. Mtg. on Image Formation in X-Ray CT*. International Conference on Image Formation in X-Ray Computed Tomography. Salt Lake City, Utah, US, 2018, accepted.
- [171] N. Hansen and A. Ostermeier. “Completely Derandomized Self-Adaptation in Evolution Strategies”. In: *Evolutionary Computation* 9.2 (2001), pp. 159–195. ISSN: 1063-6560. DOI: 10.1162/106365601750190398. pmid: 11382355.

- [172] A. J. Coleman and M. Sinclair. “A Beam-Hardening Correction Using Dual-Energy Computed Tomography”. In: *Physics in Medicine & Biology* 30.11 (1985), p. 1251. ISSN: 0031-9155. DOI: 10.1088/0031-9155/30/11/007. URL: <http://stacks.iop.org/0031-9155/30/i=11/a=007>.
- [173] Huy Q. Le and Sabee Molloy. “Segmentation and Quantification of Materials with Energy Discriminating Computed Tomography: A Phantom Study”. In: *Medical Physics* 38.1 (1, 2011), pp. 228–237. ISSN: 2473-4209. DOI: 10.1118/1.3525835. URL: <https://aapm.onlinelibrary.wiley.com/doi/abs/10.1118/1.3525835>.
- [174] Emil Y. Sidky, Lifeng Yu, Xiaochuan Pan, Yu Zou, and Michael Vannier. “A Robust Method of X-Ray Source Spectrum Estimation from Transmission Measurements: Demonstrated on Computer Simulated, Scatter-Free Transmission Data”. In: *Journal of Applied Physics* 97.12 (15, 2005), p. 124701. ISSN: 0021-8979. DOI: 10.1063/1.1928312. URL: <http://aip.scitation.org/doi/abs/10.1063/1.1928312>.
- [175] Yan Xi, Wenxiang Cong, Daniel Harrison, and Ge Wang. “Grating Oriented Line-Wise Filtration (GOLF) for Dual-Energy X-Ray CT”. In: *Sensing and Imaging* 18.1 (1, 2017), p. 27. ISSN: 1557-2064, 1557-2072. DOI: 10.1007/s11220-017-0174-7. URL: <https://link.springer.com/article/10.1007/s11220-017-0174-7>.
- [176] Lifeng Yu, Shuai Leng, and Cynthia H. McCollough. “Dual-Source Multi-Energy CT with Triple or Quadruple X-Ray Beams”. In: *Proceedings of SPIE—the International Society for Optical Engineering* 9783 (2016). ISSN: 0277-

- 786X. DOI: 10.1117/12.2217446. pmid: 27330237. URL: <https://www.ncbi.nlm.nih.gov/pmc/articles/PMC4912217/>.
- [177] Grace J. Gang, Wojciech Zbijewski, Mahadevappa Mahesh, Gaurav Thawait, Nathan Packard, John Yorkston, Shadpour Demehri, and Jeffrey H. Siewerdsen. “Image Quality and Dose for a Multisource Cone-Beam CT Extremity Scanner”. In: *Medical Physics* 45.1 (1, 2018), pp. 144–155. ISSN: 2473-4209. DOI: 10.1002/mp.12659. URL: <http://onlinelibrary.wiley.com/doi/10.1002/mp.12659/abstract>.
- [178] Hao Zhang, Hao Dang, Grace J Gang, and J Webster Stayman. “Prospective Regularization Analysis and Design for Prior-Image-Based Reconstruction of X-Ray CT”. In: *Proc. The 14th Fully Three-Dimensional Image Reconstruction in Radiology and Nuclear Medicine*. Vol. 14. 2017, pp. 417–423. URL: <http://onlinelibrary.fully3d.org/papers/2017/Fully3D.2017-11-3101003.pdf>.
- [179] David S. Rigie and Patrick J. La Rivière. “Joint Reconstruction of Multi-Channel, Spectral CT Data via Constrained Total Nuclear Variation Minimization”. In: *Physics in Medicine & Biology* 60.5 (2015), p. 1741. ISSN: 0031-9155. DOI: 10.1088/0031-9155/60/5/1741. URL: <http://stacks.iop.org/0031-9155/60/i=5/a=1741>.
- [180] Chenyang Shen, Bin Li, Liyuan Chen, Ming Yang, Yifei Lou, and Xun Jia. “Material Elemental Decomposition in Dual and Multi-Energy CT via a Sparsity-Dictionary Approach for Proton Stopping Power Ratio Calculation”. In: *Medical Physics* 45.4 (1, 2018), pp. 1491–1503. ISSN: 2473-4209. DOI:

10.1002/mp.12796. URL: <https://aapm.onlinelibrary.wiley.com/doi/abs/10.1002/mp.12796>.

- [181] M. Tivnan, S. Tilley II, and J. W. Stayman. “Physical Modeling and Performance of Spatial-Spectral Filters for CT Material Decomposition”. In: *SPIE Medical Imaging 2019 (Accepted)*. 2019.
- [182] *AiCE Deep Learning Reconstruction*. URL: [https://global.medical.canon/products/computed-tomography/aice\\_dlr](https://global.medical.canon/products/computed-tomography/aice_dlr).

# CURRICULUM VITAE

## The Johns Hopkins University School of Medicine

Steven Tilley II

January 18th, 2019

### Educational History

Ph.D. expected	2019	Program in Biomedical Engineering Mentor: J. Webster Stayman	Johns Hopkins School of Medicine
B.S.	2012	Biological Engineering	Cornell University

### Other Professional Experience

Research Rotation	2013	I-STAR Lab Mentor: Wojciech Zbijewski	Johns Hopkins School of Medicine
Research Rotation	2012-2013	Trayanova Lab Mentor: Natalia Trayanova	Johns Hopkins University
Temporary Service Technician	2012	Schaffer Lab Supervisor: Chris B. Schaffer	Cornell University
Undergraduate Researcher	2009-2012	Schaffer Lab Mentor: Chris B. Schaffer	Cornell University

### Funding and Awards

2017-2019	F31 EB023783 ~\$87,000	National Institute of Biomedical Imaging and Bioengineering <i>Model-based reconstruction for high-spatial resolution cone-beam computed tomography</i>
2017	Travel Award	14th International Conference on Fully Three- Dimensional Image Reconstruction in Radiology and Nuclear Medicine
2015	Travel Award	13th International Conference on Fully Three- Dimensional Image Reconstruction in Radiology and Nuclear Medicine
2012-2014	T32 EB010021 ~\$44,000	National Institute of Biomedical Imaging and Bioengineering <i>Training program in translational research in imaging</i>
2010	Undergraduate Research Award	Engineering Learning Initiatives <i>Design and construction of a four-channel two- photon excited fluorescence microscope</i>

## Academic Honors

2012

Graduated with honors

Cornell University

## Publications, peer reviewed

- Tilley II, S.**, Zbijewski, W., and Stayman, J. W. (2018) “Model-based material decomposition with a penalized nonlinear least-squares CT reconstruction algorithm” *Physics in Medicine and Biology*
- Tilley II, S.**, Jacobson, M., Cao, Q., Brehler, M., Sisniega, A., Zbijewski, W., and Stayman, J. W. (2017) “Penalized-likelihood reconstruction with high-fidelity measurement models for high-resolution cone-beam imaging” *IEEE Transactions on Medical Imaging* Vol: 37, pp: 988-999
- Tilley II, S.**, Siewerdsen, J. H., and Stayman, J. W. (2016) “Model-based iterative reconstruction for flat-panel cone-beam CT with focal spot blur, detector blur, and correlated noise” *Physics in Medicine and Biology* Vol: 61, pp: 296

## Conference publications

- Tivnan, M., Wang, W., **Tilley II, S.**, Siewerdsen, J. H., and Stayman, J. W. (2019) “Optimized Spatial-Spectral CT for Multi-Material Decomposition” *Intl. Mtg. Fully 3D Image Recon. in Radiology and Nuc. Med. (submitted)*
- Wang, W., **Tilley II, S.**, Tivnan, M., and Stayman, J. W. (2019) “Local response prediction in model-based CT material decomposition” *Intl. Mtg. Fully 3D Image Recon. in Radiology and Nuc. Med. (submitted)*
- Liu, S., **Tilley II, S.**, Cao, Q., Siewerdsen, J. H., Stayman, J. W., and Zbijewski, W. (2019) “Known-component model-based material decomposition for dual energy imaging of bone composition in the presence of metal hardware” *Intl. Mtg. Fully 3D Image Recon. in Radiology and Nuc. Med. (submitted)*
- Mahmood, F., Borders, D., Chen, R., Nishioka, N. S., **Tilley II, S.**, Stayman, J. W., and Durr, N. J. (2019) “Robust photometric stereo endoscopy via deep learning trained on synthetic data” *SPIE Photonics West BIOS (accepted)*
- Tivnan, M., **Tilley II, S.**, and Stayman, J. W. (2019) “Physical modeling and performance of spatial-spectral filters for CT material decomposition” *SPIE Medical Imaging (accepted)*
- Tilley II, S.**, Sisniega, A., Siewerdsen, J. H., and Stayman, J. W. (2018) “High-fidelity modeling of detector lag and gantry motion in CT reconstruction” *Proc. 5th Intl. Mtg. on Image Formation in X-ray CT* pp: 318-322
- Stayman, J. W. and **Tilley II, S.** (2018) “Model-based multi-material decomposition using spatial-spectral filters” *Proc. 5th Intl. Mtg. on Image Formation in X-ray CT* pp: 102-105



- Cao, Q., Brehler, M., Sisniega, A., **Tilley II, S.**, Bhruwani, M. M. S., Stayman, J. W., Yorkston, J., Siewerdsen, J. H., and Zbijewski, W. (2018) "High-resolution extremity cone-beam CT with a CMOS detector: evaluation of a clinical prototype in quantitative assessment of bone microarchitecture" *SPIE Medical Imaging* Vol: 10573
- Tilley II, S.**, Zbijewski, W., and Stayman, J. W. (2018) "A general CT reconstruction algorithm for model-based material decomposition" *SPIE Medical Imaging* Vol: 10573
- Tilley II, S.**, Zbijewski, W., and Stayman, J. W. (2017) "High-fidelity modeling of shift-variant focal-spot blur for high-resolution CT" *Intl. Mtg. Fully 3D Image Recon. in Radiology and Nuc. Med.* pp: 752-759
- Zhang, X., **Tilley II, S.**, Xu, S., Mathews, A., McVeigh, E. R., and Stayman, J. W. (2017) "Deformable known component model-based reconstruction for coronary CT angiography" *SPIE Medical Imaging* Vol: 10132
- Bares, A., Pender, M. A., Mejjooli, M. A., **Tilley II, S.**, Chen, K. E., Dong, J., Doerschuk, P. C., and Schaffer, C. B. (2016) "Hyperspectral imaging in live mouse cortex using a 48-channel multiphoton microscope" *Frontiers in Optics* pp: FTh5D.5
- Mathews, A. J., **Tilley II, S.**, Gang, G., Kawamoto, S., Zbijewski, W., Siewerdsen, J. H., Levinson, R., and Stayman, J. W. (2016) "Design of dual multiple aperture devices for dynamical fluence field modulated CT" *Proc. 4th Intl. Mtg. on Image Formation in X-ray CT*
- Tilley II, S.**, Zbijewski, W., Siewerdsen, J. H., and Stayman, J. W. (2016) "Modeling shift-variant X-ray focal spot blur for high-resolution flat-panel cone-beam CT" *Proc. 4th Intl. Mtg. on Image Formation in X-ray CT*
- Tilley II, S.**, Siewerdsen, J. H., Zbijewski, W., and Stayman, J. W. (2016) "Nonlinear statistical reconstruction for flat-panel cone-beam CT with blur and correlated noise models" *SPIE Medical Imaging* Vol: 9783
- Bares, A., **Tilley II, S.**, Doerschuk, P. S., and Schaffer, C. B. (2015) "Hyperspectral multiphoton microscopy: demonstration of 48-channel imaging in vivo" *Frontiers in Optics* pp: FTu2D.5
- Zbijewski, W., Cao, Q., **Tilley II, S.**, Sisniega, A., Stayman, J. W., Yorkston, J., and Siewerdsen, J. H. (2015) "Quantitative assessment of bone and joint health on a dedicated extremities cone-beam CT system" *International Journal of Computer Assisted Radiology and Surgery* Vol: 10, pp: S29-S31
- Tilley II, S.**, Siewerdsen, J. H., and Stayman, J. W. (2015) "Generalized penalized weighted least-squares reconstruction for deblurred flat-panel CBCT" *Intl. Mtg. Fully 3D Image Recon. in Radiology and Nuc. Med.* pp: 236-239

- Tilley II, S.**, Siewerdsen, J. H., and Stayman, J. W. (2014) “Iterative CT reconstruction using models of source and detector blur and correlated noise” *Proc. 3rd Intl. Mtg. on Image Formation in X-ray CT* pp: 363-367
- Stayman, J. W., Zbijewski, W., **Tilley II, S.**, and Siewerdsen, J. (2014) “Generalized least-squares CT reconstruction with detector blur and correlated noise models” *SPIE Medical Imaging* Vol: 9033
- Stayman, J. W., **Tilley II, S.**, and Siewerdsen, J. H. (2014) “Integration of component knowledge in penalized-likelihood reconstruction with morphological and spectral uncertainties” *Proc. 3rd Intl. Mtg. on Image Formation in X-ray CT* pp: 111-115
- Zbijewski, W., Xu, J., **Tilley II, S.**, Stayman, J. W., Taguchi, K., Fredenberg, E., and Siewerdsen, J. H. (2013) “Volumetric imaging with sparse arrays of photon counting silicon strip detectors” *Intl. Mtg. Fully 3D Image Recon. in Radiology and Nuc. Med.* pp: 276-279

#### **Abstracts, Posters, and Talks**

- Tilley II, S.** and Stayman, J. W. (2018) “Model-based material decomposition for acquisitions with relaxed spectral and spatial sampling” *The American Association of Physicists in Medicine Annual Meeting*
- Tilley II, S.** (2018) “Improving image quality and accuracy in flat-panel cone-beam CT using model-based iterative reconstruction with high-fidelity system and noise models” *Center for Imaging Science Seminar Series, Johns Hopkins University*
- Tilley II, S.** (2018) “A general CT reconstruction algorithm for model-based material decomposition” *BME Student Seminar Series, Johns Hopkins University*
- Zbijewski, W., Cao, Q., Brehler, M., **Tilley II, S.**, Sisniega, A., Stayman, J. W., and Siewerdsen, J. H. (2018) “High-resolution imaging of bone health” *Bulletin of the American Physical Society*
- Zbijewski, W., Cao, Q., **Tilley II, S.**, Brehler, M., Sisniega, A., Stayman, J. W., and Siewerdsen, J. H. (2018) “Quantitative cone-beam CT: new technologies, algorithms, and applications in orthopedic imaging” *SIAM Conference on Imaging Science*
- Bares, A. J., **Tilley II, S.**, Mejjooli, M. A., Pender, M. A., Doerschuk, P. C., and Schaffer, C. B. (2016) “In vivo imaging of multiple cell types in murine cortex using 48-channel hyperspectral multiphoton microscopy” *SPIE Photonics Europe*
- Tilley II, S.**, Siewerdsen, J. H., and Stayman, J. W. (2015) “High resolution CBCT with blur and correlated noise models in a non-linear reconstruction algorithm” *The 5th Annual Hopkins Imaging Conference, Johns Hopkins University*

**Tilley II, S.** and Schaffer, C. B. (2011) “Construction of a high efficiency four channel 2 photon excited fluorescence microscope” *26th Annual Undergraduate Spring Research Forum, Cornell University*

## Patents

2018	Spatial-spectral filters for multi-material decomposition in computed tomography	Application number 62/750,328
2018	Hyperspectral multiphoton microscope for biomedical applications	US20180196246A1

## Service and Leadership

### Peer Review

2018 IEEE Transactions on Biomedical Engineering

### Leadership

2013 Director of the 3rd Annual Hopkins Imaging Conference, Baltimore, MD

### Teaching Experience

2016	Teaching Assistant	Imaging Instrumentation Department of Biomedical Engineering Johns Hopkins University, Baltimore, MD
2015	Teaching Assistant	Models and Simulations Department of Biomedical Engineering Johns Hopkins University, Baltimore, MD

### Volunteering and Outreach

2013	Classroom Volunteer	Friendship Academy of Science and Technology, Baltimore, MD
------	---------------------	---

### Memberships

2018	Institute of Electrical and Electronics Engineers
2018	American Association of Physicists in Medicine
2016	The International Society for Optics and Photonics